

A Validation Study on the Novel Three-Dimensional Spiral Injection Scheme with the Electron Beam for Muon $g - 2$ /EDM Experiment



Muhammad Abdul Rehman

Department of Accelerator Science

School of High Energy Accelerator Science

The Graduate University for Advanced Studies, SOKENDAI

A thesis submitted for the degree of

Doctor of Philosophy

2020

Supervisor: Prof. Kazuro Furukawa (KEK/ACCL)

Reviewers: Assoc. Prof. Hiromi Iinuma (Ibaraki University)
Prof. Takuya Kamitani (KEK/ACCL)
Assoc. Prof. Tsutomu Mibe (KEK/IPNS)
Prof. Kenichi Sasaki (KEK/IPNS)
Assis. Prof. Hiroshi Sugimoto (KEK/ACCL)
Senior Scientist Yasuhiro Kondo (JAEA)

Abstract

The muon anomalous magnetic moment $(g - 2)_\mu$ is one of the most important measurements in elementary particle physics. The most recent measurement of $(g - 2)_\mu$ at Brookhaven National Laboratory (BNL) results in more than 3σ discrepancy compared with the equally precise Standard Model prediction. This disparity could be indicative of new physics beyond the standard model. To resolve this discrepancy, a new muon's $g - 2$ /EDM (E34) experiment at J-PARC aims to measure $(g - 2)_\mu$ to a precision of 0.1 ppm and electric dipole moment (EDM) down to the sensitivity of 1.5×10^{-21} e.cm. The key objective of measuring $(g - 2)_\mu$ is to store spin polarized μ^+ beam in a magnetic field and evaluate the evolution of the spin precession vector. In the E34 experiment, a muon beam with an emittance less than 0.5π mm mrad and a momentum of 300 MeV/c from a muon accelerator will be injected into a compact 3-T solenoid magnet. The muon beam will be stored on a 0.66 m diameter orbit. The solenoid magnet will provide an unprecedented local field uniformity of 0.1 ppm (peak to peak).

A new three-dimensional spiral injection scheme has been invented to inject the beam into the MRI-type magnet. This new injection scheme will enhance injection efficiency and overcome technical challenges related to the small storage orbit diameter. In the spiral injection scheme, the beam will be injected at a vertical angle into the storage magnet. The radial field of the solenoid will decrease the vertical angle of the beam as it approaches the midplane of the magnet. Finally, a magnetic kicker will guide the beam to the storage volume where the beam will be stored under a weak focusing field. However, the injection of the accelerated beam into such a small storage orbit is unprecedented; therefore, a demonstration experiment to establish the feasibility of this new injection scheme is inevitable. The purpose of this research is to develop a scale down Spiral Injection Test Experiment (SITE) with an electron beam to demonstrate the ideology behind this new injection scheme.

An electron beamline of a length of 2 m has been designed and constructed for the SITE. The beamline consists of a triode-type thermionic electron gun with a **LaB₆** cathode to generate a DC electron beam of 80 keV with a beam current of approximately 100 μ A. Subsequently, a magnetic lens was placed to prevent the growth of the beam. A collimator with a diameter of 3 mm and a depth of 5 mm was placed at a distance of 0.7 m from the electron gun. The main function of the collimator is to produce a differential pumping for the gas monitor, as well as to cut the beam halo. A pair of air-core steering coils has been installed to control the transverse position of the 80 keV electron beam. Next, three rotation quadrupole magnets were installed to control the beam phase space for the spiral injection. The emittance of the electron beam after collimation was measured by the quadrupole scan method. The emittance value in the horizontal direction was estimated 0.61 ± 0.05 mm mrad and in the vertical direction, it was 0.41 ± 0.04 mm mrad. In order to estimate the beam transverse coupling strength a simple procedure was developed. The coupling strength of the beam after the collimator was estimated to 0.17 ± 0.6 . This small value of coupling means decoupled beam after the collimator.

A normal conducting solenoid-type storage magnet of field strength 82.5 Gauss was designed

and constructed to store the electron beam in an orbit with a diameter of 0.24 m. In the case of SITE, the field index value n (strength of weak focusing: $0 < n < 1$) of 1.65×10^{-2} was set. This higher value of the field index relaxes the phase space requirement and vertical kicker parameters for SITE.

A non-invasive gas monitor was used to detect the electron beam track in the storage magnet. A charge-coupled device (CCD) camera was used to observe fluorescent light originating from the gas monitor. An electron beam track of four turns in the vacuum chamber of the storage magnet was confirmed by this gas monitor, which is a good qualitative tool to efficiently verify the electron beam track inside the storage magnet. However, a gas monitor lacks the ability to provide quantitative information about the position of the beam and the profile in the storage magnet. Therefore, a special type of wire scanner for determining the beam position and measuring the profile in the solenoid magnet was designed and constructed for the SITE. Two wire scanners were installed on the storage magnet to measure the beam profile and beam evolution in the storage magnet.

Due to the axial symmetric field of the solenoid magnet, a strongly XY-coupled beam is required. To produce the required phase space for the solenoid-type storage magnet, a beam transport line consisting of three rotatable quadrupole magnets has been designed and built for SITE. The vertical beam size reduction by means of phase space matching and other geometrical information have been successfully measured by the wire scanners and confirmed by the simulation. The vertical beam size had been reduced to 25.68 ± 0.31 mm with the phase matching as compared to vertical beam growth of 78.41 ± 0.83 mm without any rotatable quadrupole magnets.

To store the beam at the center of the storage magnet, a pulsed magnetic kicker was designed and simulated. From simulation studies, the best design parameters for the magnetic kicker have been determined. As explained earlier in the case of SITE, the field index value of 1.65×10^{-2} was used. This value of the field index allowed to use pulse width of 50 ns for the kicker. In addition, it also provides a weak focusing trap of ± 50 mm at storage region. A tracking simulation with the best beam phase space that can be achieved by the three rotatable quadrupole magnets has been performed. And it was estimated that injection efficiency of 81% can be achieved for SITE.

The purpose of this study was to prove the ideology of 3-D spiral injection scheme with the electron beam. The qualitative and quantitative details of the vertical and horizontal beam profiles and positions inside the solenoid storage magnet are one of the most important requisites for the successful 3-D spiral injection. Therefore, a wire scanner type beam position and profile monitor was developed for the SITE. The knowledge and experience of wire scanner development to extract the beam profile and position for the SITE storage magnet greatly helped to understand the beam behavior inside the solenoid storage magnet. Moreover, it paved the way for the development of a similar quantitative monitor for the successful 3-D spiral injection in the case of E34. The method to measure the transverse beam coupling developed at the SITE will also be implanted at E34 to estimate the coupling strength at the matching point.

Contents

List of Figures	10
List of Tables	20
1 Introduction	23
1.1 Structure of this thesis	24
1.2 Muon's Anomalous Magnetic Dipole Moment	24
1.3 Muon's Electric Dipole Moment	27
1.4 Historical Glimpse of Muon $g - 2$ Experiments	27
1.5 The BNL Muon's $g - 2$ Experiment (E821)	28
1.5.1 Principle of Measurement	29
1.6 J-PARC Muon's $g - 2$ /EDM Experiment	31
2 Three-Dimensional Spiral Injection Scheme	35
2.1 Why Three-Dimensional Spiral Injection?	35
2.2 Basic idea of Spiral Injection Scheme	37
2.3 Vertical Kicker System	37
2.4 Weak Focusing System	40
2.5 Beam Phase Space Requirements	43
2.5.1 Concepts in beam dynamics	44
2.5.2 Emittance and Twiss parameters	46
2.5.3 Beam matrix	48
2.5.4 Beam Phase Space Requirements for 3-D Spiral Injection	49
3 Spiral Injection Test Experiment (SITE) with Electron Beam	51
3.1 Experimental Setup of SITE	51
3.2 Electron Gun	53
3.2.1 Emission Process	57
3.2.2 Electron Gun Stability	58
3.3 Magnetic Lens	59
3.4 Electric Chopper	60
3.5 Collimator	63
3.6 Rotatable Quadrupole Magnets	64

3.6.1	Field Measurement	66
3.7	Dipole Magnet	70
3.7.1	Dipole Magnet 1	70
3.7.2	Dipole Magnet 2	73
3.8	Storage Magnet	75
3.8.1	Field Measurement	75
4	Development of Beam Monitors for SITE's Storage Magnet	79
4.1	Gas Monitor	79
4.1.1	Gas Monitor Setup	81
4.1.2	Optical System	81
4.1.3	Light Reflection Suppression	82
4.1.4	Performance of the Gas Monitor	85
4.2	Wire Scanner	87
4.2.1	Basic Principle and Design of Wire Scanner	87
4.2.2	Mechanical Design	91
4.2.3	Data Acquisition System	97
5	Beam Commissioning with DC Beam	99
5.1	Emittance Measurement By Quadrupole Scan	99
5.2	Emittance Measurement at SITE Beamline	101
5.2.1	Image Analysis	101
5.2.2	Misalignment of Quadrupole Magnets	103
5.3	Results	108
5.3.1	Beam Phase Space at the Collimator	117
5.4	Coupling Measurement	122
5.4.1	Results	124
6	Experimental Results of Phase Space Matching	129
6.1	Beam Phase-Space Requirements	129
6.1.1	Coordinates System	129
6.1.2	A Method to Calculate the Beam Phase-Space Requirements at the Matching Point	132
6.1.3	Errors on the Beam Phase-Space Slopes	138
6.2	The Matching Beamline	141
6.3	Three Rotatable Quadrupole Magnets Solution	143
6.3.1	Beamline	143
6.4	Results	147
6.4.1	Injection without Rotatable Quadrupole Magnets	147
6.4.2	Injection with Normal Quadrupole Magnets	154

6.4.3	Injection with Rotatable Quadrupole Magnets	155
6.5	Discussions and Summary	162
7	Kicker System for SITE	165
7.1	Vertical Magnetic Kicker for SITE	167
7.2	Design of the kicker Coils	173
7.3	Eddy Current Considerations	176
7.4	Kicker Power Supply	180
7.5	Injection Efficiency	182
7.5.1	Injection Inefficiencies	186
7.6	Summary	186
8	Conclusions	189
A	Appendix	195
A.1	Wire Scanner Data Acquisition System Code (C#)	195
B	Appendix	201
B.1	The beam Injection with other settings	201
C	Appendix	205
C.1	Pulsed Magnetic Kicker Tracking Code (Mathematica)	205
	Bibliography	211

List of Figures

1.1	Feynman diagrams for a_μ^{SM} . From left to right: first order QED contribution, lowest order weak and hadronic contribution [3].	26
1.2	The comparison between the SM model prediction value from different groups and the latest value of the muon $g - 2$ measurement from E821 [7].	26
1.3	The storage ring of Brookhaven Experiment E821 [24].	29
1.4	The outline of J-PARC Muon $g - 2$ /EDM experiment [29].	31
1.5	The overview of J-PARC Muon $g - 2$ /EDM experiment storage magnet.	33
2.1	The concept of the conventional beam injection into the storage magnet. The beam is injected into the storage magnet by the use of a device called the inflector. The red dotted line shows the injected beam with the help of an inflector, while the green thick lines show the corrected beam orbit after the kick. To avoid the beam hit at the wall of storage magnet within the first turn, a kicker system is needed to correct the injected beam orbit.	36
2.2	The layout of the three-dimensional spiral injection scheme.	37
2.3	Left: Black dashed trajectory shows the beam injection into the storage magnet without the kick. Black thick trajectory shows the case wherein a suitable kick is applied to the beam to stop the beam at the midplane. Right: Black dashed trajectory shows the pitch angle of the beam with respect to the vertical position of the kick; in this case trajectory shows the beam that has not been subjected to a kick, the trajectory represented in black thick indicate that the pitch angle reduced to zero when the kick is applied to the beam.	38
2.4	The radial field component \vec{B}_r and stopping volume for the kick angle 60 mrad as a function of the kicker duration.	40
2.5	The coordinate system and function of weak focusing for the charged particle. The charged particle exhibits simple harmonic motion under the influence of the weak focusing in the horizontal and vertical direction.	41
2.6	Frenet-Serret coordinate system.	44
2.7	The beam phase-space ellipse in the horizontal plane. Twiss parameters $(\beta_x, \alpha_x, \gamma_x)$ describes the shape and orientation of the beam phase-space ellipse.	47
2.8	Gaussian distribution for horizontal beam phase-space. The solid ellipse represents the 1σ of the Gaussian distribution.	49

2.9	Left: Beam injection without phase space matching. The below plots shows the beam cross section at the injection point. The storage magnet coordinates are referred as global coordinates (X_g, Y_g, Z_g). For the convenience, the beam phase-space at the injection point is shown in beam coordinates (X, Y, Z). It is evident that without phase space matching beam drastically blow-up in the vertical direction. Right: Beam injection with phase space matching. When appropriate XY-coupling (phase space matching) was applied to the injected beam, the vertical blow-up reduce sufficiently.	50
3.1	The side view of the 3D model of the three-dimensional Spiral Injection Test Experiment (SITE).	53
3.2	Above: A Photo of SITE setup. Below: A top view photo of the straight beamline, with each component labeled.	54
3.3	Above: Layout of electron gun high voltage (H.V) power supply station. Below: H.V station and electron gun.	55
3.4	Photo of the LaB₆ cathode used in electron gun. The diameter of the cathode is 2 mm	56
3.5	Left: Electric potential contour plots of the electron gun. Right: The electron beam trajectories through electron gun.	57
3.6	Left: The electron gun was operated at 80 keV. H.V of electron gun was recorded as a function of time to check the stability during the operation. Right: Current of electron gun as a function of time.	58
3.7	Left: Cut view of 3-D model of SITE' magnetic lens. Right: Axial magnetic field of magnetic lens.	60
3.8	Schematic of electric chopper system.	61
3.9	Right: Mechanical structure and dimension of chopper system. Left: Potential contours on the electrodes.	62
3.10	Left: H.V electrode attached to the vacuum feed through and its support. Right: Chopper's electrodes in vacuum chamber	62
3.11	Collimator used at SITE's beamline. The diameter of the collimator is 3 mm and depth is 5 mm. The black burn mark is due to the beam hitting on the collimator.	63
3.12	Three rotating quadrupoles and their rotation system.	64
3.13	The field measurement setup for the rotation quadrupole system.	66
3.14	Above: The focusing strength of the quadrupole magnet as a function of the excitation current. The focusing strength increase linearly with respect to the applied current. Below: The focal length of the quadrupole magnet as a function of the excitation current.	67

3.15	The magnetic field measurement of the rotation quadruple magnets system in the longitudinal direction. Above graph shows the axial field measurement at horizontal position $x = \pm 5$, and below plot presents the axial field measurement at vertical position $y = \pm 5$. Color lines dotted lines represents the field measurement and dashed line is showing the CST simulation results.	68
3.16	Transverse magnetic field profile of the quadrupole magnet. Color dots are showing the field measurement results and black line are CST simulation results.	69
3.17	The rectangular dipole magnet three dimensional model.	71
3.18	Left: The rectangular dipole magnet. The diople magnet at the SITE beamline.	71
3.19	Left: The blue solid line shows the CST simulation and red dots are correspond to the field measurement results. Right: The percentage difference between measured values and CST simulation.	72
3.20	The role of second dipole magnet is shown. In order to control the injected beam angle with more freedom a second dipole magnet was added to the injection beam pipe.	73
3.21	Left: The 3-D Model and dimensions of the second dipole magnet. Right: The second dipole magnet.	74
3.22	Left: The field measurement and CST simulation of second bending magnet. Right: The percentage difference between measured values and CST simulation.	74
3.23	Left: Schematic view of storage magnet with reference trajectory and monitors. Right: Storage magnet and vacuum chamber.	76
3.24	Above: The axial field of the storage magnet along with the vertical position of the storage magnet. The black solid lines are the CST-simulation and color points are the experimental field measurement. The current of the main coil was fixed to 8 A and correction coil current was changed from 0-10 A (opposite polarity to the main coil). As the correction coil's current increases the weak focusing potential increases. Below: The radial field of the storage magnet along with the vertical position of the storage magnet.	77
4.1	The energy loss of the electron beam in nitrogen gas. The red point indicates the energy loss for the 80 keV electron beam.	80
4.2	The setup of the GM at the top of the storage magnet. The GM consists of the valve for nitrogen gas inlet and CCD camera. The picture on the right shows the inside view of storage magnet's vacuum chamber and the red dotted line corresponds as expected.	81
4.3	Configuration of the optical system.	82
4.4	Inside view of the storage magnet's vacuum chamber depends upon the characteristics of the lens and camera.	83

4.5	Two copper sheets of height (350 mm) had been joined together to make a copper sheet of height 700 mm. The black sheet of height 700 mm and width 1257 mm was attached to the thin copper sheet by Araldite Rapid Epoxy.	83
4.6	The procedure of cutting copper and black sheets, as well as placing the black sheets inside the vacuum chamber.	84
4.7	Left: Vacuum chamber without the black sheet. The light reflection from the wall of the vacuum chamber can be seen very clearly. Right: Vacuum chamber with the black sheet. The light reflection suppressed considerably after the insertion of the black sheet.	84
4.8	Above: The beam injection into the storage magnet without the black sheet. Reflection from the wall of the vacuum chamber is the major source of background. Below: The beam injection into the storage magnet with the black sheet. The background decrease dramatically with black sheet insertion.	86
4.9	The dimensions of the storage magnet vacuum chamber and position of the wire scanner 1 and 2 with respect to the center of the vacuum chamber. These dimensions were used to calibrate the center of the wire scanners and storage magnet.	88
4.10	The principle and mechanics of the wire scanner.	89
4.11	Above: Wire scanner 1 consists of four segmented horizontal wire to measure the vertical beam profile and one vertical wire to measure the horizontal beam profile. Below: Wire scanner 2 consists of only four segmented horizontal wires to measure the vertical beam profile.	89
4.12	The principle of the horizontal beam size measurement. The black circle shows the beam orbit (diameter = 24 cm). The red circle presents the circular path on which vertical wire traverse to measure the horizontal beam profile (diameter = 35 mm). The vertical wire was placed at 35 mm away from the center of the wire scanner 1 support. In order to extract the horizontal beam size the vertical wire was placed at the fixed vertical position, and wire scanner support bar was rotated at its own axis by the rotary actuator. As vertical wire rotates it provides the information of horizontal beam position and horizontal beam size.	90
4.13	Magnetically-coupled Rotary/Linear Feedthrough (MRLF) for the vertical and rotary movement of the wires. On the left is the 3-D model of the MRLF [66] and to the right shows the MRLF used at the SITE.	92
4.14	Above: The 3-D model of the linear actuator [67]. Below: The linear actuator for the vertical movement of the MRLF.	93
4.15	The 3-D model of the rotary actuator [68]. The rotary actuator used for the rotation of the MRLF for the horizontal beam size measurement.	94

4.16	Above: The velocity of the actuator was set to 1 mm/sec. To check the linearity, data were taken at different points and fitted with a linear function. Below: Actuator set values versus digital scale readout. To check the linearity between the set value and readout, data was taken. The set values and readout values agree well within the uncertainty of the digital readout system ($\pm 50\mu m$).	95
4.17	(a) Schematic of the two-wire scanner setup. (b) Wire scanner system on the top of the storage magnet.	96
4.18	The control system layout for the actuator and wire scanner.	97
4.19	The screenshot of the oscilloscope control program. This program was used for the wire scanner data online plotting and data logging.	98
4.20	The beam current at the wire as a function of the cathode's heater current of the electron gun.	98
5.1	(a) The quadrupole scan setup. The quadrupole scan had been done with all three quadrupoles independently. (b) The cross section of the quadrupole magnet. The bore radius of quadrupole magnet is 25 mm and effective length is 56 mm.	102
5.2	The copper plate used to observe the beam profile (via OTR). The horizontal and vertical lines were drawn on the copper plate in order to determine the conversion factor from the pixels data of the photo to the millimeter.	103
5.3	(a) A raw picture from the CMOS-camera without applying any quadrupole magnet. (b) The above figure converted from RGB to the Grayscale for further analysis. The conversion factor from pixels to mm is 10 Pixels/mm in both transverse planes.	104
5.4	(a) and (b) are the beam profiles in the vertical and horizontal focus respectively. (c) and (d) represents the beam profile data for vertical and horizontal planes.	105
5.5	The change in RMS beam size due to the different level of the background.	106
5.6	The beam position shift due to the quadrupole magnet misalignment error. The black points are weighted average of data points. And red line is the linear fit to the data.	107
5.7	(a), (c) and (e) shows the vertical beam size square as a function of the quadrupole magnet 1, 2 and 3 respectively. Whereas (b), (d) and (f) shows the horizontal beam size square as a function of the quadrupole magnet 1, 2 and 3 respectively. The color points in each picture are correspond to the repeated measurement and black points are the weighted mean of the repeated measurement.	109
5.8	The beam images with different strength of vertical focused quadrupole magnet 1. False colors were added to the pictures for the better visibility.	110
5.9	The beam images with different strength of horizontal focused quadrupole magnet 1. False colors were added to the pictures for the better visibility.	111

5.10	The beam size squared as function of quadrupole strength. (a) and (b) shows the vertical and horizontal scan for the quadrupole 1 respectively. (c) and (d) shows the vertical and horizontal scan for the quadrupole 2. (e) and (f) shows the vertical and horizontal scan for the quadrupole 3.	112
5.11	the comparison of the emittance values between experimental results and CST-PS simulation.	117
5.12	The β_x and β_y at Q1,Q2, Q3 and their transformation to the collimator position.	119
5.13	The α_x and α_y at Q1, Q2, Q3 and their transformation to the collimator position.	120
5.14	The γ_x and γ_y at Q1,Q2, Q3 and their transformation to the collimator position.	121
5.15	The phase space distribution at the collimator. This phase space satisfy the emittance and Twiss parameters given in the Table 5.9.	122
5.16	The layout of the beamline for the 4-D beam matrix reconstruction.	126
5.17	(a) The gray-scale (setting#14) picture. (b) The 3-D histogram of the above picture. The background was estimated as a 2D slope picture data. The red patch shows the background estimation. (c) The green highlighted region indicates the area selected for the RMS beam size measurement after the background estimation.	127
5.18	The beam images with different settings. False colors were added to the pictures for the better visibility.	128
6.1	Left: A horizontal flat beam was assumed inside the storage magnet and reverse track it to find the required beam slopes at the injection point. Right: The beam frame is used to describe the beam shape at the injection point. X and Y represents the horizontal and vertical planes respectively, and Z is the beam motion direction.	130
6.2	The slopes of the beam correlations at the matching point $Y_g = -600$ mm. The beam correlations plots are shown in the beam coordinates. The dots represents the data points obtained from the reverse tracking at the matching point and solid line (red line) are the linear fit to these points.	131
6.3	The input beam phase-space distribution. The the values of emittance and Twiss parameter for these distributions are given in Table 6.2.	136
6.4	The coupled beam phase-space at the matching point. The line (blue) are the required beam slopes at the injection point.	136
6.5	(a) The beam injection into the storage magnet without phase space matching, the phase-space distribution and the emittance and Twiss parameters are given in Fig. 6.3 and Table 6.2 respectively. (b) The beam injection into the storage magnet with phase-space matching, the phase-space distribution and the emittance and Twiss parameters are given in Fig. 6.4 and Table 6.3, 6.4 respectively.	137

6.6	The slopes of the beam phase-space at the matching point. Error of 5%, 10%, 15%, and 20% was introduced to each correlation in order to find their effect on the vertical beam size in the storage magnet.	138
6.7	(a) The beam injection into the storage magnet with 0% error on the a_{xy} slope, while other slopes ($a_{xx'}$, $a_{yy'}$) were kept at the original values. Where (b), (c), and (d) shows the beam injection into the storage magnet with 5%, 10%, 15%, error on slope a_{xy} slope.	140
6.8	The vertical beam size growth at the kick point due to the change in the slope values. The biggest growth in the beam size was observed due to the change in $X - Y$ correlation slope. And the (X, X') correlation has the least effect on the beam growth.	141
6.9	The evolution of the beta function and beam size through the array of six quadrupole magnets.	142
6.10	Left: The 3-D plot of tracking simulation of the beam injection with appropriate coupling as mentioned in the Table 6.3 and 6.4. Right: The histogram of the vertical beam size as a function of the vertical beam position.	142
6.11	(a) The layout of the beamline, beamline composed of three rotatable quadrupole magnets, a rectangular bending magnet and drift space. The rotatable quadrupole magnets were placed in the downstream direction of the collimator. The dimensions and mutual distances among magnets are also shown. (b) The photo of the experimental setup of the matching beamline.	145
6.12	The simulated beam phase-space with the three rotation quadrupole magnets. The solid blue line shows the ideal slopes for the beam phase-space matching. The beamline setting is described in the Table 6.7.	146
6.13	The beam profile of the injected beam. The false colors were added to the picture for better visualization.	147
6.14	Above: The simulation of the beam phase-space distribution without applying quadrupole magnets. Below: The injected beam profile at the beam profile monitor. The false colors were added for the better visual effects.	150
6.15	Above: The gas monitor results of the beam injection into the storage magnet without rotation quadrupole magnets. The false colors were added to the photo for better visualization. It is evident from the gas monitor results that the beam blow-up in vertical direction as it traverses through the storage magnet.	151
6.16	(a) The tracking simulation of the beam injection (CST-PS) into the storage magnet without phase-space matching. The black open circle shows the points at which the beam sizes were measured. (b) The vertical beam size was measured by using a wire scanner. The black points are the wire scanner 1 data. The green histogram is a simulation result of CST-PS. The orange line is a global fit to experimental data.	152

6.17	(a) The tracking simulation of the beam injection (CST-PS) into the storage magnet without phase-space matching. The black open circle shows the points at which the beam sizes were measured. (b) The black points are the wire scanner 2 data. The green histogram is a simulation result of CST-PS. The orange line is the fit to experimental data. The wire scanner 2 is located at 180 Degree away (cyclotron period) from the wire scanner 1 position.	153
6.18	(a) The beam phase-space at the injection point with the Twiss parameters as listed in the Table 6.3 , but coupling parameters were set to zero. (b) Particle Tracking with the beam phase-space as mentioned in the in (a) as the beam traverse through the storage magnet beam blow-up drastically in the vertical direction. It signifies that the xy-coupling to the beam cross section is the most important parameter to controls the vertical beam spread in the solenoidal-type storage magnet.	154
6.19	Above: The gas monitor results of the beam injection into the storage magnet with rotation quadrupole magnets set up as mentioned in Table 6.7. Below: The horizontal projection of the above picture. The three turns can be visualized easily from this data.	157
6.20	(a) The tracking simulation of the beam injection (CST-PS) into the storage magnet without phase-space matching. The black open circle shows the points at which the beam sizes were measured. (b) The vertical beam size is measured by using a wire scanner. The black points are the wire scanner 1 data. The red histogram is a simulation result of CST-PS. The orange line is the global fit to experimental data.	158
6.21	(a) The tracking simulation of the beam injection (CST-PS) into the storage magnet without phase-space matching. The black open circle shows the points at which the beam sizes were measured. (b) The vertical beam size was measured by using a wire scanner. The black points are the wire scanner 2 data. The red histogram is a simulation result of CST-PS. The orange line is the fit to experimental data. The wire scanner 2 is located at 180 Degree away (half cyclotron period) from the wire scanner 1 position.	159
6.22	(a) The 3-D plot of the 2-D projection of the beam profile in the storage magnet. The positive X-axis corresponds to the wire scanner 1 location and negative show the wire scanner 2 location. The black histogram is the CST-PS simulation and grey plot show the experimental data. (b) The zoom up view of the wire scanner 1 location.	160
6.23	The horizontal beam profile at different vertical positions. Average horizontal beam profile form first turn to the second turn was 0.65 mm (1σ)	161

6.24	The comparison of the vertical beam sizes growth in the storage magnet without phase-space matching, with appropriate combination of rotatable quadrupole magnets and simulated perfect matching.	163
6.25	The comparison of the pitch angle between without phase space matching and with appropriate combination of rotatable quadrupole magnets.	164
7.1	(a) The concept of the vertical kicker. The beam enters in the storage magnet at 40 Degree and radial field of the storage magnet reduce the injection to 4-5 Degree as it approaches the boundary of the weak focusing field. At $Y_g = -100$ mm a vertical kick applied to the beam to gradually reduce the pitch angle of the beam to the zero. (b) The pitch angle of the injected beam. And its reduction due to the radial field of the storage magnet and kicker field.	166
7.2	The character of the symmetrical kicker. The orange line shows the reduction in the pitch angle of the beam from the injection point to the kick point. The blue curve shows the kick due to the symmetrical kicker, the pitch angle of the beam reduces smoothly in the of the symmetrical kicker. After applying kick the pitch angle reduces to the zero.	168
7.3	The symmetrical kick and separatrix. The blue curve is the symmetrical kick. The closed circles shows the stable storage orbit. If the particles lands on the closed circle after the kick the will get store. Th red circles shows the storage orbit for $Y_g = \pm 30$ mm.	169
7.4	The character of the localized kicker. The orange line shows the reduction in the pitch angle of the beam from the injection point to the kick point. The black curve shows the kick due to the localized kicker, the pitch angle reduces to zero in 10 steps.	170
7.5	The localized kick and separatrix.	171
7.6	The oscillation of the pitch angle in the weak focusing field.	172
7.7	The oscillation of the beam in the vertical direction in the weak focusing field.	172
7.8	Above: The design of the symmetrical kicker. Below: The radial magnetic field of the symmetrical kicker coils.	174
7.9	Above: The design of the localized kicker. Below: The kicker field of the localized kicker coils.	175
7.10	The vacuum chamber and kicker symmetrical kicker coils.	177
7.11	The average ohmic losses in the wall of the vacuum chamber due to the symmetrical kicker coils.	177
7.12	The vacuum chamber and kicker localized kicker coils.	178
7.13	The average ohmic losses in the wall of the vacuum chamber due to the localized kicker coils.	178

7.14	The power loss in the wall of the vacuum chamber due to the symmetric and localized kicker coils.	179
7.15	The magnetic field reduction in the case of symmetrical kicker due to eddy current flow in the wall of the vacuum chamber.	179
7.16	The magnetic field reduction in the case of localized kicker due to eddy current flow in the wall of the vacuum chamber.	180
7.17	(a) The circuit diagram of the kicker power supply. (b) The current through kicker coils. (d) The voltage across kicker coils.	181
7.18	The beam vertical phase-space at the kick point.(a) The vertical phase space acceptance of the kicker. (b) The vertical phase-space at the kick point with phase-space matching. (c) The same vertical phase-space as mentioned in (b) except flipped it's sign to the focusing. This case has been simulated in order to show the injection efficiency in the ideal beam phase-space at the kick point. (d) The vertical phase-space at the kick point without any phase-space matching. . .	183
7.19	The kicker tracking with the phase-space matching (XY-coupled) to estimate the injection efficiency. Th grey lines shows the separatrix for the field index 1.65×10^{-2} . The closed contours presents the stable region and open hyperbolas shows the un-stable region. The red closed lines are presents the stored beam, whereas, open line shows the lost particles.	184
7.20	The kicker tracking with flipped XY-coupled phase space. The closed blue contours represents the stored beam. In this case 100% beam get stored.	185
7.21	The tracking of the beam in transient field of the kicker with the energy spread of $\Delta E/E = 6 \times 10^{-4}$. In this scenario, the injection efficiency reduce to 67%. . .	187
A.1	The screenshot of the DPO-7104 oscilloscope control program.	195
B.1	The beam phase space with setting others than best run are shown. In (a) and (b) (X, Y) , and (X, X') were matched preferentially while (Y, Y') was ignored.	201
B.2	The wire scanner a and 2 results with beam phase-space setting as shown in Fig.B.1.	202
B.3	The comparison of the vertical beam sizes growth in the storage magnet with the phase space settings as shown in Fig. B.1.	203

List of Tables

3.1	Comparison of Parameters Between E34 and SITE.	52
3.2	Electron gun specifications.	53
3.3	Electric Chopper System Parameters.	61
3.4	Rotating Quadrupole Magnet Parameters.	64
3.5	Dipole Magnet 1 Parameters.	72
3.6	Dipole Magnet 2 Parameters.	73
3.7	Storage Magnet Parameters.	75
4.1	Wire Scanner Parameters	91
5.1	The Quadrupole Magnets Vertical Misalignment.	106
5.2	The Quadrupole Magnets Horizontal Misalignment.	106
5.3	The beam size square (Weighted Mean) and quadrupole magnet strength values for Q1-scan.	113
5.4	The beam size square (Weighted Mean) and quadrupole magnet strength values for Q2-scan.	114
5.5	The beam size square (Weighted Mean) and quadrupole magnet strength values for Q3-scan.	115
5.6	The transverse emittance values form Q1, Q2, and Q3 scans.	116
5.7	The values of Twiss parameters from Q1, Q2, and Q3 scans at the quadrupole magnet location.	116
5.8	Twiss parameters transformation from Q1,Q2 and Q3 to the Collimator	118
5.9	The weighted mean of Emittance and Twiss parameters at the Collimator	118
5.10	The drift spaces of the beamline.	126
5.11	The beamline setting and respective values of $\sigma_{1,11}$, $\sigma_{1,33}$, $\sigma_{1,13}$	126
5.12	The values of the beam matrix elements at the reconstruction point.	128
5.13	The Coupling Strength for the SITE beamline.	128
6.1	The beam slopes at the matching point.	132
6.2	The initial beam phase space parameters.	135
6.3	The beam phase-space parameters at the matching point.	135
6.4	Coupling Parameters for the Matched Beam Phase Space.	135
6.5	Matching beamline quadrupole magnets parameters	143

6.6	The drift spaces for the beamline.	144
6.7	The Three Rotatable Quadrupole Magnets Matching Beamline Parameters. . . .	146
6.8	The Comparison of the Beam Slopes between the Simulation and Measured from the Beam Profile Monitor.	162
6.9	The Vertical Beam Sizes as a function of the Vertical Position of the Storage Magnet	162
6.10	The Pitch Angel as a Function of the Vertical Position of the Storage Magnet . .	164
7.1	The beam position and pitch angle at kick point.	168
7.2	Symmetrical Kicker Coil Parameters.	173
7.3	Localized Kicker Coil Parameters.	173
7.4	Power loss due to the Eddy Current.	176
7.5	Kicker Power supply Parameters.	182
7.6	Injection Efficiency	183

Chapter 1

Introduction

Ever since the discovery of the muon [1], it has been observed to play a vital role in understanding our universe. The anomalous magnetic dipole moment of the muon is one of the intriguing measurements that can extend our knowledge of physics beyond the Standard Model. The most recent measurement of the muon's $g - 2$ at BNL(E821) was achieved with a discrepancy of more than 3.5σ as compared with the equally precise Standard Model prediction. This unresolved discrepancy could be indicative of the establishment of new physics beyond the Standard Model. Therefore, a new J-PARC (Japan Proton Accelerator Research Complex) muon's $g - 2$ /EDM (E34) is under preparation to resolve this fascinating discrepancy. The E34 experiment will employ a completely new approach to measure the muon's $g - 2$. The final goal of the E34 is to measure the muon's $g - 2$ with a precision of 0.1 ppm and the electron dipole moment (EDM) down to the value of 10^{-21} e.cm.

To measure the muon's $g - 2$ a low-emittance (0.5π mm mrad) polarized muon beam will be stored in a precise magnetic field to determine the evolution of the spin precession vector with respect to time. In the E34 experiment, the muon beam with a momentum of $300 \text{ MeV}/c$ will be injected into a 3-T magnetic resonance imaging (MRI)-type solenoid magnet to store the muon beam on a 0.66 m diameter orbit. The MRI-type storage magnet will provide an unprecedented local field uniformity of 0.1 ppm. A new three-dimensional spiral injection scheme has been invented to inject the beam into the MRI-type magnet. This new injection scheme will enhance injection efficiency and overcome technical challenges that are related to the small storage orbit diameters.

The three-dimensional spiral injection scheme is an unprecedented injection idea; therefore, a demonstration experiment to establish the feasibility of this new injection scheme is inevitable. Herein, I describe the demonstration of a novel spiral injection scheme with the electron beam for the E34 experiment.

The Spiral Injection Test Experiment (SITE) consisting of a 2 m long straight beamline with energy of 80 keV and a solenoid storage magnet to store the electron beam has been designed and built. The requirement of the XY-coupled beam for the solenoid-type storage magnet is

confirmed, and the beam monitor for the beam position and profile in the storage magnet to confirm appropriate matching is also discussed. The kicker system to store the electron beam at the midplane of the storage magnet has also been developed. Other important aspects of the spiral injection scheme will also be illustrated in this thesis.

1.1 Structure of this thesis

This thesis is structured into eight chapters. A brief description of each chapter is as follows:

- The following sections of this chapter will briefly describe the physics background of the Muon's $g - 2$ /EDM properties. The principle of the Muon's $g - 2$ /EDM experiments and current status will also be discussed.
- Chapter 2 describes the basic idea and requirements of a spiral injection scheme. The concept of a kicker system to guide the beam to the storage region and the weak focusing system for the beam confinement has been described and discussed along with the phase space requirement for the solenoid-type magnet.
- The description of the SITE with the detail of each component is discussed in Chapter 3.
- Chapter 4 explains the development of the beam monitors for the solenoid-type storage magnet. Two kinds of monitors have been built for beam monitoring in the storage magnet, namely: a non-invasive gas monitor for qualitative monitoring and a wire scanner for quantitative monitoring.
- Chapter 5 presents DC beam commissioning at SITE. The emittance of the beam at the entrance of the matching beamline has been measured by the quadrupole scan is described in detail.
- Chapter 6 explains the experimental results of phase space matching and its effect on vertical beam size reduction.
- To stop the beam at the midplane of the storage magnet, a kicker system is needed. A detailed simulation study of the kicker and its development is described in chapter 7.
- Chapter 8 provides the conclusion and future outlooks.

1.2 Muon's Anomalous Magnetic Dipole Moment

The Muon possesses an intrinsic magnetic field and spin angular momentum. When muons are placed in an external magnetic field, their internal magnet tends to align (rotate) itself with the external magnetic field. The strength of the internal magnet and the rate of the

magnet's gyration determine the muon's gyro-magnetic ratio. For muons, the relation between the magnetic dipole moment and the spin is as follows:

$$\vec{\mu}_\mu = g_\mu \frac{e}{2m_\mu} \vec{s} \quad (1.1)$$

Where, $\vec{\mu}_\mu$ is the magnetic dipole moment (MDM), g is the gyromagnetic ratio, e is the elementary charge on muon, m_μ is the mass of muon, and \vec{s} is the spin of muon. In Dirac's quantum theory the value of g is equal to 2 for all fundamental particles like muons [2].

$$g_\mu = 2(1 + a_\mu), \quad a_\mu = \frac{g_\mu - 2}{2} \quad (1.2)$$

The a_μ is known as an anomaly or anomalous magnetic dipole moment of the muon. In the framework of the Standard Model (SM) of particles of physics, the small finite value of a_μ appears due to the quantum fluctuations or the exchange of virtual particles. The SM value can be shown as a sum of three gauge sectors [3]

$$a_\mu^{SM} = a_\mu^{QED} + a_\mu^{Weak} + a_\mu^{had} \quad (1.3)$$

Figure 1.1 shows the Feynman diagram for the contributions from QED, weak and hadronic sectors [3]. The most recent prediction of QED and weak contributions are: $a_\mu^{QED} = (11658471.90 \pm 0.01) \times 10^{-10}$ [4] and $a_\mu^{Weak} = (15.36 \pm 0.1) \times 10^{-10}$ [5], respectively. The hadronic contribution was recently reported in [6, 7]. The total SM prediction for a_μ^{SM} results in

$$a_\mu^{SM} = (11659181.08 \pm 3.78) \times 10^{-10} \quad (1.4)$$

The Muon $g-2$ experiment (E821) at Brookhaven National Lab (BNL) [8] concluded a_μ^{Exp} as follows:

$$a_\mu^{Exp} = (11659209.10 \pm 6.33) \times 10^{-10} \quad (1.5)$$

The deviation from SM prediction is:

$$\Delta a_\mu = a_\mu^{Exp} - a_\mu^{SM} = (28.02 \pm 7.37) \times 10^{-10} \quad (1.6)$$

This difference leads to the 3.8σ discrepancy between a_μ value from SM prediction and BNL $g-2$ experiment measurement.

Even though the SM is theoretically successful, its inability to include gravity and lack of explanation for dark matter has led many scientists to believe that it is incomplete. The a_μ could be a signal of New Physics (NP) beyond the SM. One of the theoretical schemes for NP would be the supersymmetric (SUSY) expansion of the SM. SUSY implements a symmetric mapping between fermions (spin $\frac{1}{2}$) and bosons (integer spin) by changing the spin by $1/2$ units. The SUSY scenario can be an explanation for the muon anomaly. For a SUSY mass equal to Λ , the contribution to a_μ is given by [9, 10]:

$$a_\mu^{SUSY} \cong \text{sign}(\mu) 130 \times 10^{-11} \tan \beta \left(\frac{100 \text{ GeV}}{\Lambda} \right)^2 \quad (1.7)$$

Where, the factor $\tan \beta$ is the ratio of the vacuum expectation values of the two Higgs fields, the $\text{sign}(\mu)$ is the SUSY μ parameter.

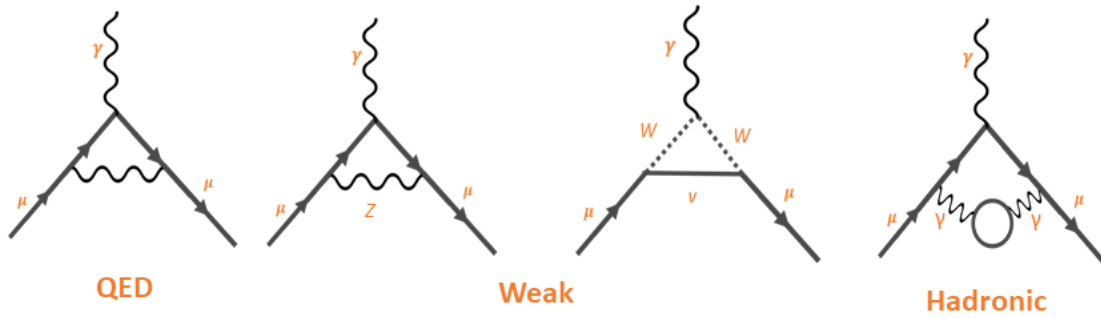


Figure 1.1: Feynman diagrams for a_μ^{SM} . From left to right: first order QED contribution, lowest order weak and hadronic contribution [3].

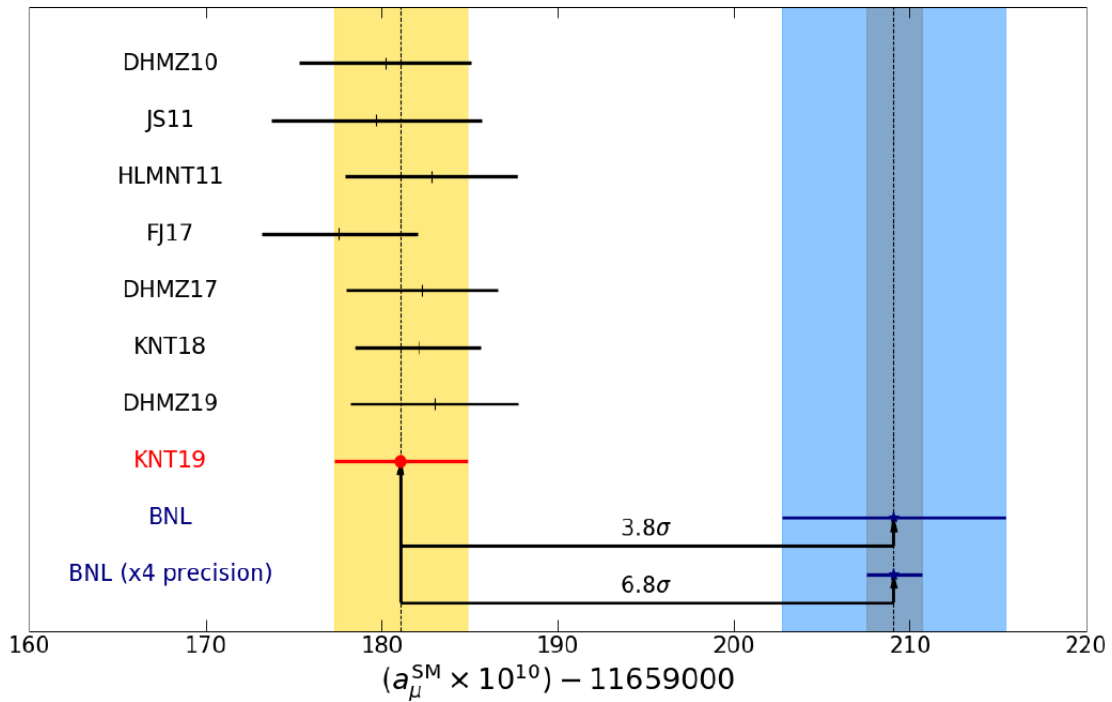


Figure 1.2: The comparison between the SM model prediction value from different groups and the latest value of the muon $g - 2$ measurement from E821 [7].

1.3 Muon's Electric Dipole Moment

The finite value of the permanent EDM of elementary particles violates the parity (P) and time-reversal (T) symmetries under the CPT theorem, where C represents the charge conjugation. According to the SM, the EDMs of elementary particles is far beyond the experimental sensitivity. However, in extensions of the SM, obtaining larger EDMs of elementary particles is possible. Hence, any non-zero value of EDM could be an indicator of new physics [11]. The EDM of the muon can be shown as follows:

$$\vec{d}_\mu = \eta_\mu \frac{e}{2m_\mu c} \vec{s} \quad (1.8)$$

Where, η_μ is the size of the EDM, e and m are the charge and mass of the muon, and \vec{s} is the muon spin. The muon's EDM and a_μ can be derived from similar operators; therefore, a_μ discrepancy from the SM can be an evidence of a non-zero EDM [12]. This is one of the motivation to search for the muon's EDM simultaneously with the a_μ measurement. The E821 provided the most stringent constraint on the EDM value [13]:

$$\vec{d}_\mu \leq 1.8 \times 10^{-19} \text{ e.cm} \quad (1.9)$$

1.4 Historical Glimpse of Muon $g - 2$ Experiments

The first a_μ measurement was performed in 1957 by *Garwin, et al.*, and they reported a final value of $g_\mu = 2(1.00113)$ with the precision of 0.007% [14]. This measurement agrees well with Schwinger's first order QED calculation [15]. After *Garwin, et al.*, there was motivation to test the QED more stringently to observe the failure of QED. Therefore, a new measurement of a_μ with the precision of 5164 ppm was implemented at the CERN [16, 17]. The first CERN experiment concluded on the following a_μ value with the precision of 5164 ppm:

$$a_\mu = (1162 \pm 5) \times 10^{-6} \quad (1.10)$$

The first CERN-I experiment was performed with a non-relativistic muon beam at a rest muon lifetime of 2.2 μ s. Therefore, a measurement period to a few lifetimes was the limitation of the CERN-I experiment.

The next experiment at CERN was conducted with a storage ring whose diameter was 5 m. The magnetic field was 1.711 T, $\vec{P}_\mu = 1.27 \text{ GeV}/c$, and $\gamma_\mu = 12.06$. A weak magnetic focusing was used to confine the beam in the storage magnet [18]. The CERN-II experiment concluded on a a_μ value with a precision of 266 ppm:

$$a_\mu = (11661 \pm 3.1) \times 10^{-7} \quad (1.11)$$

The storage ring of the CERN-II experiment contained a pion production target inside the ring. Therefore, the background from the pion production target installed inside the storage ring deteriorated the performance of the detector, and limited the sensitivity of the CERN-II experiment.

The CERN-III [19] experiment was performed with the following four improvements over the CERN-II experiment:

- Direct injection of a pion beam into the storage ring, which reduces the background for the detector
- Improved injection: Use of a device called an inflector for the beam injection to cancel the fringe field of the storage magnet
- Longer muon lifetime $64.4 \mu\text{s}$ with the use of a magic momentum $\gamma = 29.3$, which results in an increased measurement time
- The more homogeneous magnetic field as compared to CERN-2

The CERN-III concluded on a a_μ value with the precision of 7.3 ppm

$$a_\mu = (1165924 \pm 8.5) \times 10^{-9} \quad (1.12)$$

1.5 The BNL Muon's $g - 2$ Experiment (E821)

To further enhance the precision of a_μ compared to the CERN—III, the muon $g - 2$ experiment at Brookhaven National Laboratory (BNL) (E821) was started in 1984. E821 aimed to measure the muon anomaly up to a precision of 0.54 ppm, where the electroweak contribution becomes measurable. This level of precise measurement of the muon anomaly is also a stringent constraint for new physics.

The BNL $g - 2$ experiment used the same experimental techniques as in CERN-III. However, several ingenious techniques have been introduced to enhance the precision of a_μ . The 24 GeV/c proton beam from the BNL Alternating Gradient Synchrotron (AGS) strikes at the pion production target. This secondary pion traverses through the 80 m long pion-muon-decay channel. The tertiary-polarized muon beam from pion decay is directly injected into the storage ring of 711 cm.

A superconducting inflector [20] was used to inject the beam into the storage magnet. The inflector cancels the fringe field of the storage magnet. The storage ring [21] was a continuous superconducting magnet of field strength 1.45 T. Electric quadrupoles were used to confine the muon beam into the storage magnet. A pulsed kicker system [22] was also placed in the storage ring to prevent the beam from hitting the wall of the inflector within the cyclotron period of 149 s. Figure 1.3 shows the storage ring of the BNL $g - 2$ experiment.

The decay electrons were detected by the calorimeters to measure the precession frequency. The magnetic field was measured with nuclear magnetic resonance probes [23]. The BNL $g - 2$ experiment concluded on a final value of a_μ after the series of measurement with the precision of 0.54 ppm [8]

$$a_\mu = (116592089 \pm 54 \pm 33 \pm 63) \times 10^{-11} \quad (1.13)$$

Where, the first error is statistical, the second is systematic, and the third is the total error.

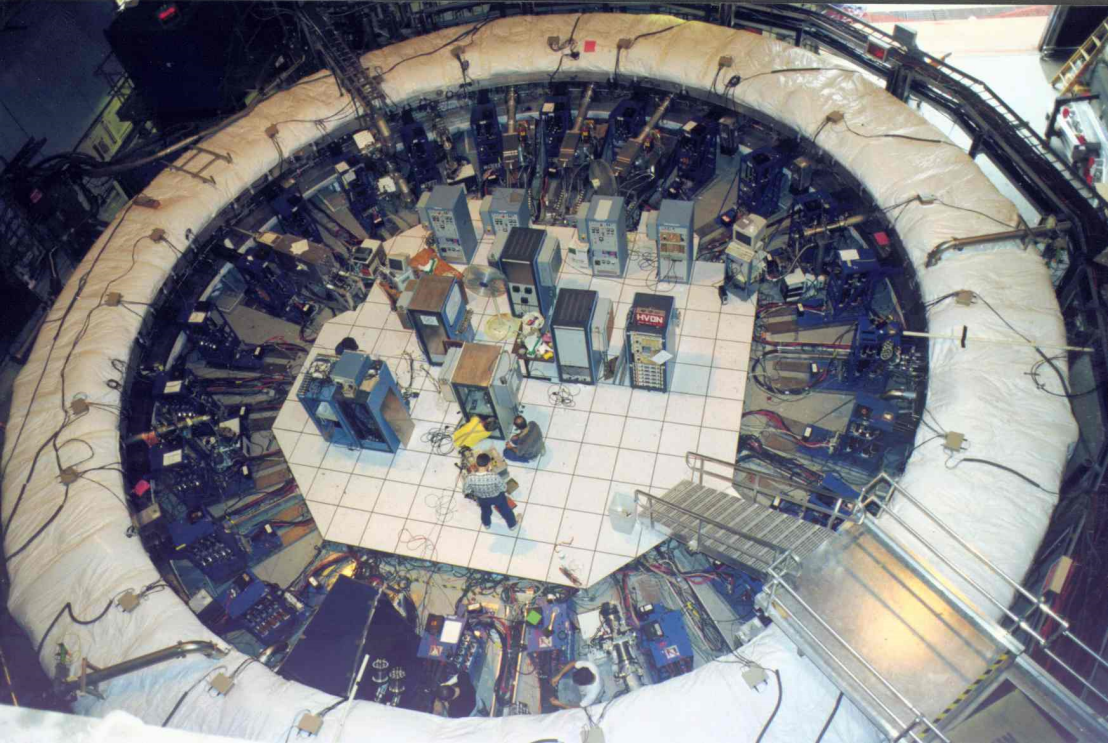


Figure 1.3: The storage ring of Brookhaven Experiment E821 [24].

1.5.1 Principle of Measurement

The measurement principle of the anomalous magnetic moment of muon in the BNL $g - 2$ experiment was the same as in CERN-III. The cyclotron frequency for the muons circulating in the storage ring in the presence of the magnetic and electric field is given by:

$$\vec{\omega}_c = -\frac{e}{m} \left[\frac{\vec{\beta}}{\gamma} - \frac{\gamma}{\gamma^2 - 1} \left(\frac{\vec{B} \times \vec{E}}{c} \right) \right] \quad (1.14)$$

Where, e is the elementary charge, m is the mass of particle, \vec{B} \vec{E} are the magnetic and electric fields, respectively. β and γ are relativistic factors given as:

$$\vec{\beta} = \frac{\vec{v}}{c} \quad , \quad \gamma = \frac{1}{\sqrt{1 - \beta^2}} \quad (1.15)$$

The spin rotation frequency was first derived by the [25]. Here, I will present the version given in [26]

$$\begin{aligned} \vec{\omega}_s = -\frac{e}{m} \left[\left(\frac{g-2}{2} + \frac{1}{\gamma} \right) \vec{B} - \left(\frac{g-2}{2} + \frac{\gamma}{\gamma+1} \right) (\vec{\beta} \cdot \vec{B}) \vec{\beta} - \left(\frac{g-2}{2} + \frac{1}{\gamma+1} \right) \left(\vec{\beta} \times \frac{\vec{E}}{c} \right) \vec{\beta} \right] \\ - \frac{e}{m} \left[\frac{\eta}{2} \left(\frac{\vec{E}}{c} - \frac{\gamma}{\gamma+1} \left(\vec{\beta} \times \frac{\vec{E}}{c} \right) \vec{\beta} + \vec{\beta} \times \vec{B} \right) \right] \end{aligned} \quad (1.16)$$

The upper term in Eq. (1.16) corresponds to the precession frequency due to the g factor, while the lower term correlates with the spin rotation due to the EDM. If we consider the value

of η to be negligibly small, then the lower term will vanish. The difference between spin rotation frequency and cyclotron frequency ($\vec{\omega}_{a_\mu} = \vec{\omega}_s - \vec{\omega}_c$) is called the anomalous spin precession frequency ($\vec{\omega}_{a_\mu}$). Further, by defining $a_\mu \equiv \frac{g-2}{2}$ Eq. (1.16) will become

$$\vec{\omega}_{a_\mu} = -\frac{e}{m} \left[a_\mu \vec{B} - a_\mu \left(\frac{\gamma}{\gamma+1} \right) (\vec{\beta} \cdot \vec{B}) \vec{\beta} - \left(a_\mu - \frac{1}{\gamma^2-1} \right) \frac{\vec{\beta} \times \vec{E}}{c} \right] \quad (1.17)$$

The BNL $g - 2$ experiment selected a so called magic $\gamma_{magic} \approx 29.3$ at γ_{magic} ; consequently, the third term in Eq. (1.17) vanishes along with the second term in Eq. (1.17) if the muon only lies in a plane perpendicular to the magnetic field of the storage magnet. Subsequently, Eq. (1.17) is simplified to the following form:

$$\vec{\omega}_{a_\mu} = -\frac{e}{m} a_\mu \vec{B} \quad (1.18)$$

In experiment, $\vec{\omega}_{a_\mu}$ is measured using the decay positron signals, i.e.,

$$\mu^+ \rightarrow e^+ + \bar{\nu}_\mu + \nu_e \quad (1.19)$$

The magnetic field \vec{B} is measured by observing the Larmor frequency of stationary protons ($\vec{\omega}_p$) with the NMR probes. In BNL $g - 2$ experiment magnetic field was determined with pulsed nuclear magnetic resonance (NMR).

$$\vec{\omega}_p = g_p \left(\frac{e\vec{B}}{2m_p} \right) \quad (1.20)$$

Where, g_p is the gyromagnetic factor of the proton. On rearranging Eq. (1.20), the \vec{B} becomes:

$$\vec{B} = \frac{2m_p \vec{\omega}_p}{eg_p} \quad (1.21)$$

Put the value of \vec{B} from (1.21) into (1.18) and solve for a_μ :

$$a_\mu = \frac{g_p m_\mu \vec{\omega}_a}{2 m_p \vec{\omega}_p} \quad (1.22)$$

Equation (1.22) can also be written as:

$$a_\mu = \frac{g_p m_\mu \vec{\omega}_a}{g_\mu m_p \vec{\omega}_p} (1 + a_\mu) \quad (1.23)$$

Let's define

$$\lambda \equiv \frac{g_\mu m_p}{g_p m_\mu} \quad R \equiv \frac{\vec{\omega}_a}{\vec{\omega}_p} \quad (1.24)$$

Hence a_μ will become:

$$a_\mu = \frac{R}{\lambda - R} \quad (1.25)$$

Here, $\lambda = 3.183345137 \pm 85$ is the muon-to-proton magnetic moment ratio. This value was measured by Muonium (the μ^+e^- atom) hyperfine structure experiment [27]. A new high precision measurement of Muonium hyperfine structure experiment is under preparation at J-PARC [28].

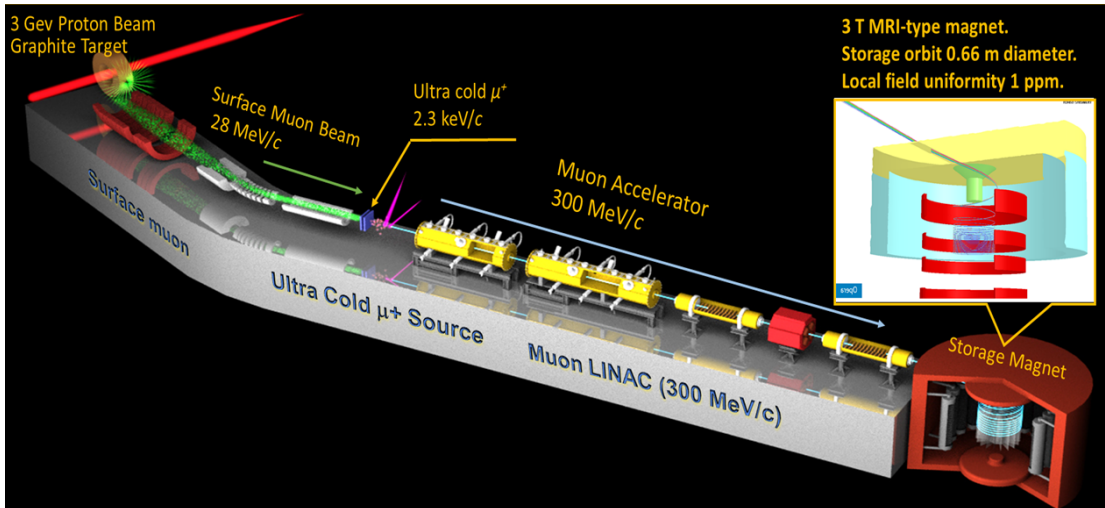


Figure 1.4: The outline of J-PARC Muon $g - 2$ /EDM experiment [29].

1.6 J-PARC Muon's $g - 2$ /EDM Experiment

The J-PARC muon $g - 2$ /EDM experiment (E34) intends to measure a_μ with the statistical uncertainty of 450 ppb and systematic less than 70 ppb. The EDM is probed down to the value of 1.5×10^{-21} e.cm [29]. The overview of E34 is shown in Fig. 1.4.

The E34 will employ many new and novel approaches to reach the goal sensitivity of a_μ and d_μ . The salient features of E34 are as follows:

- Low emittance: In E34, a primary proton beam of energy 3 GeV will hit the graphite target. The proton beam collision at the graphite target will produce π^+ (pions). These pions decay near the surface of the target and produce surface muon beam of momentum 29.8 MeV/c and approximately 100% polarization.

$$\pi^+ \rightarrow \mu^+ + \nu_\mu \quad (1.26)$$

Since the surface muon beam is tertiary, it comprises a very large intrinsic emittance. A surface muon beam transport line has been designed to transfer the muon beam to the cooling station [30]. To reduce the transverse emittance, the surface muon beam will hit on the laser-ablated silica aerogel. The majority of the muons will diffuse from the aerogel target into the vacuum region as the muonium atoms (Mu: μ^+e^-) [31, 32]. Subsequently, Mu will be ionized by the laser to remove the e^+ . Hence, a low emittance or thermal muon beam will be developed in this way.

- Muon reacceleration: The thermal muons will be accelerated by the series of acceleration method, to the momentum of 300 MeV/c. Recently, first stage muon acceleration by RFQ has been successfully demonstrated [33].
- Compact storage magnet: A compact MRI-type solenoid magnet of field strength 3 T will be used as a storage magnet for the E34. The choice of solenoid magnet has an advantage

of an unprecedented local field uniformity of 0.1 ppm at the storage plane. This storage magnet has a small fiducial volume. The diameter of the stored beam will be 0.66 m. Therefore, the conventional injection scheme is not applicable. A novel three-dimensional spiral injection scheme has been invented to inject the beam into the compact storage magnet [34]. Chapter 2 will describe this injection scheme in detail. Due to the injection of the low emittance beam into the storage magnet, a very weak magnetic focusing ($n \sim 10^{-4}$) is sufficient to confine the muon beam within a storage orbit. The storage magnet is shown in Fig 1.5.

As described earlier, a low emittance beam can be injected into the compact storage magnet and a very weak magnetic focusing ($n \sim 10^{-4}$) can confine the muon beam. Therefore, no strong electric focusing is necessary in the storage magnet.

$$\vec{\omega} = \vec{\omega}_a + \vec{\omega}_\eta \quad (1.27)$$

$$\vec{\omega} = -\frac{e}{m} \left[a_\mu \vec{B} - \left(a_\mu - \frac{1}{\gamma^2 - 1} \right) \frac{\vec{\beta} \times \vec{E}}{c} + \frac{\eta}{2} \left(\vec{\beta} \times \vec{B} + \frac{\vec{E}}{c} \right) \right] \quad (1.28)$$

Since in E34 no electric field is present, the second term vanishes, and no magic momentum is needed; this is in contrast to the E821.

$$\vec{\omega} = -\frac{e}{m} \left[a_\mu \vec{B} + \frac{\eta}{2} (\vec{\beta} \times \vec{B}) \right] \quad (1.29)$$

The precession vectors, ω_a and ω_η , are orthogonal to each other. Therefore, E34 is able to measure $g - 2$ and EDM simultaneously. The principle of a_μ extraction is the same as mentioned in Section 1.5.1.

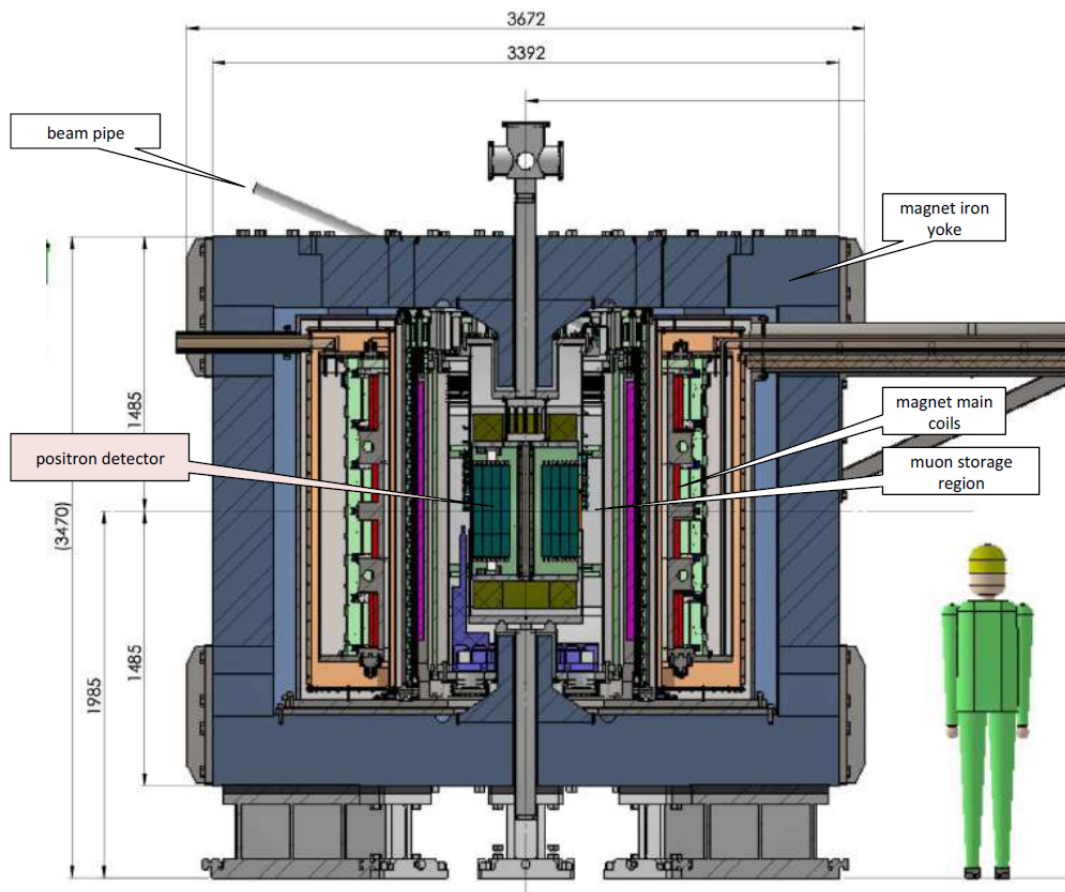


Figure 1.5: The overview of J-PARC Muon $g - 2$ /EDM experiment storage magnet.

Chapter 2

Three–Dimensional Spiral Injection Scheme

In this chapter, the need for the three-dimensional spiral injection scheme will be described. The basic concept of the spiral injection and essential techniques to realize this injection scheme will also be explained.

2.1 Why Three–Dimensional Spiral Injection?

Conventional accelerator injection systems contain an inflector magnet for the beam injection into the storage ring. The inflector magnets are essential components of the injection system to minimize the interference from the storage magnet field to the injected beam bunches. The BNL muon $g - 2$ experiment used the superconducting inflector [20] to cancel the storage magnet of field 1.7 T to avoid interference of the storage magnet field to the injected beam.

After the beam injection into the storage magnet, a kicker magnet is essential to correct the injected beam orbit to avoid the beam hit at the wall of the inflector within one cyclotron period. The cyclotron frequency ($\vec{\omega}_c$) and time-period (T) in the presence of only the magnetic field can be calculated as follows:

$$\vec{\omega}_c = \frac{q\vec{B}}{m_\mu\gamma} \quad , \quad T = \frac{2\pi}{\omega_c} \quad (2.1)$$

Where, \vec{B} is the magnetic field and q , m , γ are charge, mass, and Lorentz factor of the charge particle, respectively. In the case of the BNL $g - 2$ experiment $\gamma = 29.2$, magnetic field of 1.7 T results in $T = 149$ ns. The required kick angle to correct the injected beam can be calculated as follows:

$$\theta = \frac{s}{r} \quad (2.2)$$

Where, θ is the kick angle, s is the required displacement, and r is the radius of the storage ring. In E821 the radius of the stored beam was 7.11 m and the required displacement to avoid the

beam hit at the wall of the inflector was 0.077 m, resulting in the required kick angle of 10 mrad. Hence, in E821 the injected muon beam was kicked by angle 10 mrad within 140 ns [22]. The concept of the conventional injection scheme is shown in Fig. 2.1.

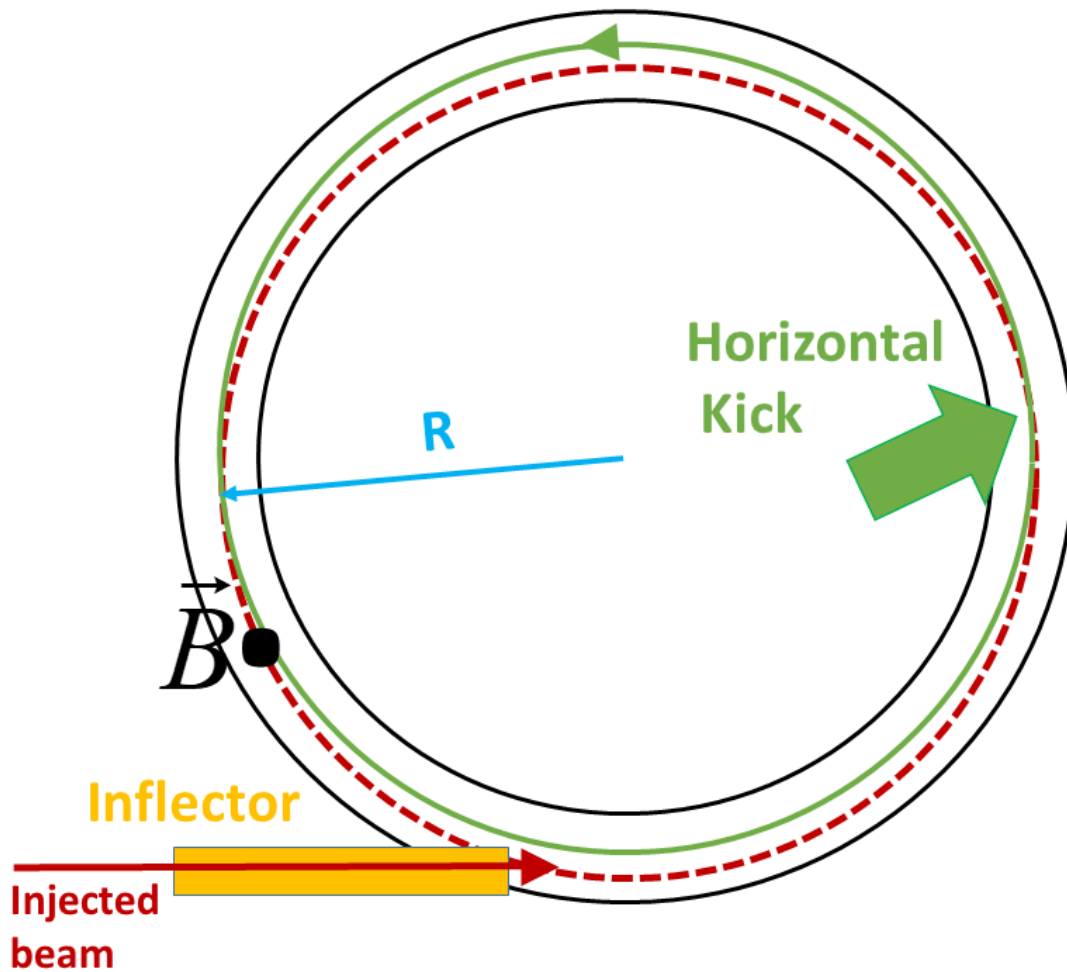


Figure 2.1: The concept of the conventional beam injection into the storage magnet. The beam is injected into the storage magnet by the use of a device called the inflector. The red dotted line shows the injected beam with the help of an inflector, while the green thick lines show the corrected beam orbit after the kick. To avoid the beam hit at the wall of storage magnet within the first turn, a kicker system is needed to correct the injected beam orbit.

As explained in Section 1.5, the J-PARC Muon $g - 2$ /EDM experiment (E34) will use a compact solenoid magnet of strength 3 T. This compact storage magnet will provide the local field uniformity of 0.1 ppm, which is essential to reach the ultimate sensitivity goal of 0.14 ppm for a_μ . The diameter of the storage orbit will be 0.66 m. The 3 T magnetic field is too high to be canceled by the inflector or any other existent technology.

In E34, the value of $\gamma = 3$ and field strength of 3 T results in the cyclotron period of 7.4 ns. In the case of E34, the radius of the stored beam orbit is 0.33 m, and according to Eq. (2.2), the required kick angle to correct the beam orbit will become 233 mrad within 7.4 ns. The 233 mrad kick within 7.4 ns is currently impossible to be achieved using any available technology. Hence,

one can conclude that conventional injection scheme is not applicable in the case of E34 because:

- The 3 T magnetic field cannot be canceled by the inflector
- The 233 mrad kick angle within 7.4 ns rapidly expands to be achieved by current technology

A novel three-dimensional spiral injection scheme has been invented to overcome the earlier stated challenges and to achieve high injection and storage efficiency. The next section will describe the basic concept of the newly invented injection scheme.

2.2 Basic idea of Spiral Injection Scheme

In the three-dimensional spiral injection scheme, the beam will be injected at a vertical angle into the solenoid magnet. The radial magnetic field of the solenoid will reduce the injection angle to a smaller value as it approaches to the midplane. To stop the vertical motion, a kicker will apply a force in the opposite direction of the vertical beam motion, and the beam will completely stop at the midplane of the storage magnet. The duration of the kick could be in several cyclotron periods. To confine the vertical motion of the beam in the storage volume, a very weak magnetic focusing will be applied. Figure 2.2 shows the basic layout of the three-dimensional spiral injection scheme. In Fig 2.2 (X_g, Y_g, Z_g) are the storage magnet coordinates. The detailed basic concept can be found at [34].

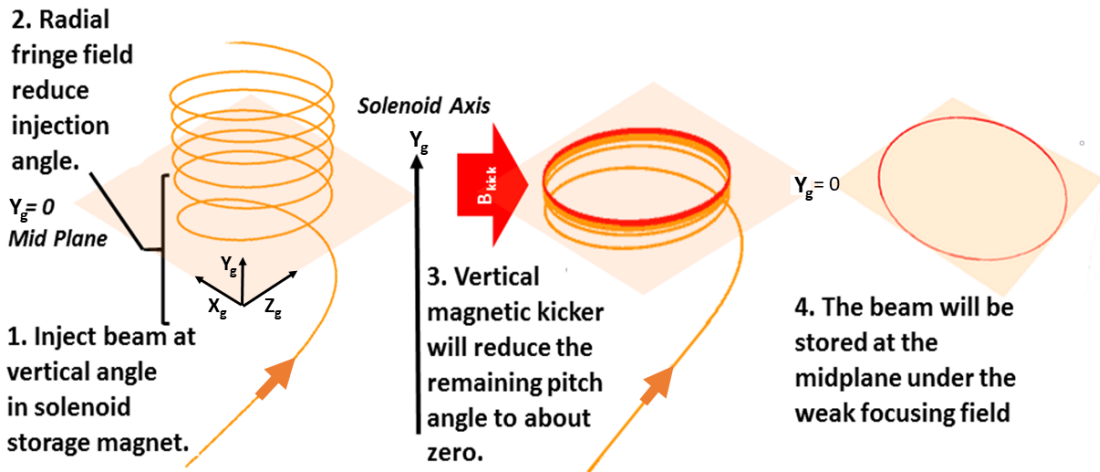


Figure 2.2: The layout of the three-dimensional spiral injection scheme.

2.3 Vertical Kicker System

As explained earlier, the beam is injected into the storage magnet at a vertical angle; therefore, the beam has a component parallel to the axial magnetic field of the solenoid magnet and starts spiraling through the storage magnet. The radial fringe field of the solenoid storage magnet will reduce the injection angle of the beam to some extent.

To store the beam at the center of the storage magnet, the pitch angle of the beam must be reduced to almost zero as it reaches the storage region. A pulsed magnetic kicker will be used to decrease the pitch angle $\psi = \frac{P_y}{|P|}$ of the beam to zero, where P_y is the beam momentum in the vertical direction and $|P|$ is the total momentum of the particle. Figure 2.3 illustrates the character of the magnetic kicker. The black dashed trajectory shows the motion of the beam inside the storage magnet without a kicker; it is observed that the injection angle of the beam reduced due to the radial fringe field but does not decrease to zero. The beam passed through the middle region of the storage magnet without getting stopped. When the appropriate kick is applied to the beam, as shown in the black thick trajectory, the pitch angle is reduced to zero. The curved region in Fig. 2.3 (right) depicts the weak focusing region.

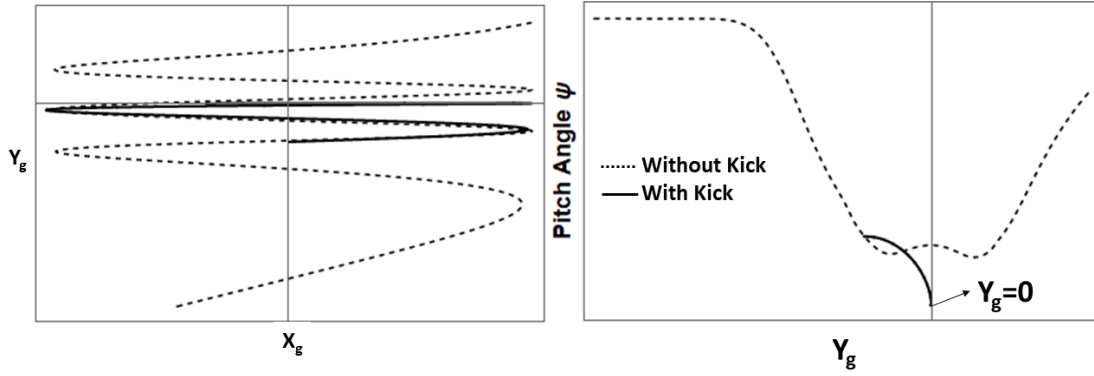


Figure 2.3: Left: Black dashed trajectory shows the beam injection into the storage magnet without the kick. Black thick trajectory shows the case wherein a suitable kick is applied to the beam to stop the beam at the midplane. Right: Black dashed trajectory shows the pitch angle of the beam with respect to the vertical position of the kick; in this case trajectory shows the beam that has not been subjected to a kick, the trajectory represented in black thick indicate that the pitch angle reduced to zero when the kick is applied to the beam.

The pulsed magnetic kicker has to produce the radial field, which will be perpendicular to the vertical component of the momentum of the beam. The required radial magnetic field and a stopping volume [35] (region needed to stop the beam) may be calculated as follows:

$$\vec{F} = q\vec{v} \times \vec{B}, \quad \vec{F} = m\vec{a}, \quad \Rightarrow \quad m\vec{a} = q\vec{v} \times \vec{B} \quad (2.3)$$

$$\begin{pmatrix} a_x \\ a_y \\ a_z \end{pmatrix} = \frac{q}{m} \begin{pmatrix} B_z v_y - B_y v_z \\ B_x v_z - B_z v_x \\ B_y v_x - B_x v_y \end{pmatrix} \quad (2.4)$$

$$a_y = \frac{q}{m} v_L B_R(R, y) \sin(\omega t) \quad (2.5)$$

Where, $v_L = \sqrt{v_x^2 + v_z^2}$, integrating Eq. (2.5) with respect to time gives:

$$v_y = v_{y_0} + \frac{q}{m} \int_0^t v_L B_R(R, y) \sin(\omega t) dt \quad (2.6)$$

In order to simplify above equation let's assume small angle approximation in that case v_L will remain constant and can be taken out of integral in Eq. (2.6)

$$v_y = v_{y_0} + \frac{q}{m} v_L \int_0^t B_R(R, y) \sin(\omega t) dt \quad (2.7)$$

For half sine shape $t = \frac{T}{2} = \frac{\pi}{\omega}$. Solving Eq. (2.6) for $B_R(R, y)$ gives:

$$B_R(R, y) = -\frac{m v_{y_0} \omega}{2 q v_L} \quad (2.8)$$

If we consider $\theta_{kick} = v_{y_0}/v_L$ and $\omega = \frac{2\pi}{T}$, where T is the time period, then Eq. (2.8) will become:

$$B_R(R, y) = -\frac{\pi m \theta_{kick}}{q T} \quad (2.9)$$

The total kicker field for the half sine shape can written as follows:

$$B_{kick} = B_R \cdot \sin\left(\frac{2\pi t}{T_{kick}}\right) \quad (2.10)$$

Where, T_{kick} is the kick duration. Integrating Eq. (2.6) can give the volume to stop the beam as follows:

$$y_0 = -\int_{t_0}^{t_0 + \frac{\pi}{\omega}} v_y(t) dt = \frac{c}{m\gamma} \frac{T}{4} P_{y_0} \quad (2.11)$$

Where P_{y_0} is the vertical momentum, m , γ and c are the mass, Lorentz factor and speed of light. Figure 2.4 shows the behavior of Eq. (2.9) and (2.11) for the 60 mrad kick angle. As the time period increases, the required strength of kick field decreases and stopping volume increases. These analytical formulas represent only rough estimation. To calculate the realistic field for the kick system and determine the behavior of charge particle through the kicker field, a numerical simulation is necessary. The kicker coil has been designed in the CST [36], and a custom Runge-Kutta 4th Order Method (*RK-4*) program in *Mathematica* [37] has also been developed to track charged particles in the transient field of the kicker. In Chapter 7, the detailed kicker study for SITE will be described.

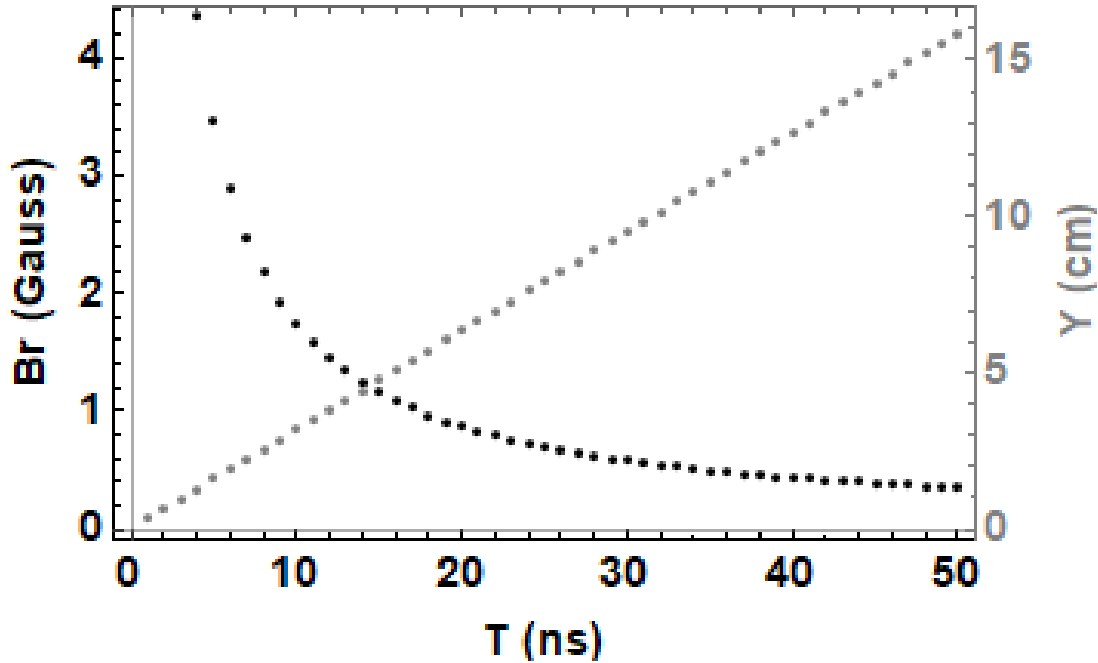


Figure 2.4: The radial field component \vec{B}_r and stopping volume for the kick angle 60 mrad as a function of the kicker duration.

2.4 Weak Focusing System

The kicked beam will be stopped at the midplane of storage magnet. To confine the stored beam orbit into the required vertical and horizontal amplitudes, a weak magnetic focusing will be applied [38, 39]. In this section, we will derive the equation of motion for the charged particle under the weak focusing field. Figure 2.5 shows the coordinate system and the function of the weak focusing field. Under the weak focusing field, the charged particle exhibits simple harmonic motion. The first complete framework of weak focusing was developed by *D. W. Kerst et al.* [40]. In this text the version given in [41] will be used.

Let us consider a local coordinate system $(\hat{x}, \hat{y}, \hat{s})$, that moves along the ideal particle. The restoring force for the orbit other than the ideal orbit can be shown as Lorentz force and centripetal force, i.e.,

$$F_y = q\beta c B_x - \gamma m \ddot{y} \quad (2.12)$$

$$F_x = -q\beta c B_y + \gamma m \ddot{x} \quad (2.13)$$

Where, F_x , F_y and B_x , B_y are the components of the force and magnetic field vectors in the horizontal and vertical directions, respectively. β and γ are relativistic factors, m is the rest mass of particle and \ddot{x} , \ddot{y} are the accelerations in the horizontal and vertical directions, and c is the speed of light. Then, the position vector is:

$$\vec{r} = R\hat{x} + y\hat{y} \quad (2.14)$$

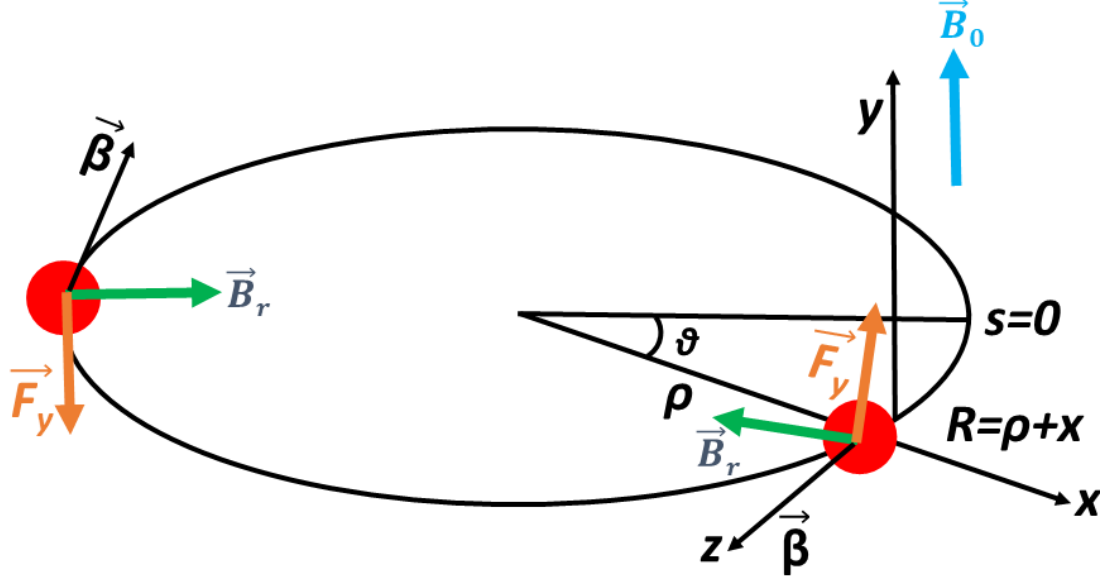


Figure 2.5: The coordinate system and function of weak focusing for the charged particle. The charged particle exhibits simple harmonic motion under the influence of the weak focusing in the horizontal and vertical direction.

While the corresponding velocity and acceleration is given by:

$$\vec{v} = \dot{\vec{r}} = \dot{R}\hat{x} + R\dot{\hat{x}} + \dot{y}\hat{y} = \dot{R}\hat{x} + R\dot{\theta}\hat{s} + \dot{y}\hat{y} \quad (2.15)$$

$$\vec{a} = \dot{\vec{v}} = \ddot{R}\hat{x} + (2\dot{R}\dot{\theta} + R\ddot{\theta})\hat{s} + R\dot{\theta}\dot{\hat{s}} + \ddot{y}\hat{y} \quad (2.16)$$

If $\dot{\hat{s}} = -\dot{\theta}\hat{x} = -\frac{\dot{v}}{R}\hat{x}$ and inserting it in Eq. (2.16) gives:

$$\vec{a} = \left(\ddot{x} - \frac{v^2}{R} \right) \hat{x} + \frac{2\dot{x}v}{R} \hat{s} + \ddot{y}\hat{y} \quad (2.17)$$

Furthermore, on inserting \ddot{y} and \ddot{x} in Eq. (2.12) and (2.13) and solving for \ddot{y} and \ddot{x} gives:

$$\ddot{y} - \frac{q\beta c B_x}{\gamma m} = 0 \quad (2.18)$$

$$\ddot{x} - \frac{v^2}{R} + \frac{q\beta c B_x}{\gamma m} = 0 \quad (2.19)$$

Changing the derivative from time to θ gives:

$$t = \frac{R}{\beta c} \theta \quad \rightarrow \quad \frac{d}{dt} = \frac{\beta c}{R} \frac{d}{d\theta} \quad (2.20)$$

If $p = \gamma m \beta c$, and writing Eq. (2.18) and (2.19) in terms of θ gives:

$$\frac{d^2 y}{d\theta^2} - \frac{q B_x}{p} R^2 = 0 \quad (2.21)$$

$$\frac{d^2 x}{d\theta^2} + \left(\frac{q B_y}{p} R - 1 \right) R = 0 \quad (2.22)$$

Since we know that magnetic rigidity is $p = qB_0\rho$, and from Fig. 2.5 $R = \rho\left(1 + \frac{x}{\rho}\right)$, then Eq. (2.22) will become:

$$\frac{d^2x}{d\theta^2} + \left[\frac{B_y}{B_0}\left(1 + \frac{x}{\rho}\right) - 1\right]R = 0 \quad (2.23)$$

The magnetic guide field for the off-orbits will become:

$$B_y = B_0\left(1 + \frac{1}{B_0}\frac{\partial B_y}{\partial x}x + \dots\right) \quad (2.24)$$

Ignoring the second order and higher terms in Eq. (2.24) and define a quantity “ n ”

$$n = \frac{\rho}{B_0}\frac{\partial B_y}{\partial x} \quad (2.25)$$

where, “ n ” is known as the field index, and insert Eq. (2.24) with the definition of field index in Eq. (2.23):

$$\frac{d^2x}{d\theta^2} + (1 - n)x = 0 \quad (2.26)$$

A similar procedure for Eq. (2.18) will result in:

$$\frac{d^2y}{d\theta^2} + ny = 0 \quad (2.27)$$

Equation (2.26) and (2.27) describe the weak focusing. To have stable motion in the vertical and horizontal planes, the stability criterion is as follows:

$$0 < n < 1 \quad (2.28)$$

Where, $n < 1$ is for the horizontal stability and $n > 0$ corresponds to the vertical stability. These equations are in the form of a simple harmonic oscillator, and their solutions are well known.

$$x(\theta) = A\cos(\theta\sqrt{1-n}) + B\sin(\theta\sqrt{1-n}) \quad (2.29)$$

$$y(\theta) = C\cos(\theta n) + D\sin(\theta n) \quad (2.30)$$

and derivative

$$\dot{x}(\theta) = \sqrt{1-n}[-A\sin(\theta\sqrt{1-n}) + B\cos(\theta\sqrt{1-n})] \quad (2.31)$$

$$\dot{y}(\theta) = n[-C\sin(\theta n) + D\cos(\theta n)] \quad (2.32)$$

To find constants A and B , consider the following initial condition.

$$x_0 = x(\theta = 0) = A, \quad \dot{x}_0 = \frac{\sqrt{1-n}}{\rho}\dot{x} \quad (2.33)$$

$$A = x_0, \quad B = \frac{\rho}{\sqrt{1-n}}\dot{x}_0 \quad (2.34)$$

Similarly, for the vertical direction, the results will be:

$$C = y_0, \quad D = \frac{\rho}{\sqrt{n}}\dot{y}_0 \quad (2.35)$$

Insert Eq. (2.34) and (2.35) into $x(\theta)$, $\dot{x}(\theta)$, $y(\theta)$, $\dot{y}(\theta)$

$$x(\theta) = x_0 \cos(\theta\sqrt{1-n}) + \frac{\rho}{\sqrt{1-n}} \dot{x}_0 \sin(\theta\sqrt{1-n}) \quad (2.36)$$

$$\dot{x}(\theta) = -\frac{\sqrt{1-n}}{\rho} x_0 \sin(\theta\sqrt{1-n}) + \dot{x}_0 \cos(\theta\sqrt{1-n}) \quad (2.37)$$

$$y(\theta) = y_0 \cos(\theta n) + \frac{\rho}{\sqrt{n}} \dot{y}_0 \sin(\theta n) \quad (2.38)$$

$$\dot{y}(\theta) = -\frac{\sqrt{n}}{\rho} x_0 \sin(\theta n) + \dot{y}_0 \cos(\theta n) \quad (2.39)$$

Taking $\theta = \frac{s}{\rho}$, ρ is the ideal beam orbit, and defining betatron phases:

$$\phi_x(s) \equiv \frac{s}{\rho} \sqrt{1-n}, \quad \phi_y(s) \equiv \frac{s}{\rho} \sqrt{n} \quad (2.40)$$

Then, the solutions can be written in matrix form as follows:

$$M_H = \begin{pmatrix} \cos(\phi_x(s)) & \frac{\rho}{\sqrt{1-n}} \sin(\phi_x(s)) \\ -\frac{\sqrt{1-n}}{\rho} \sin(\phi_x(s)) & \cos(\phi_x(s)) \end{pmatrix} \quad (2.41)$$

$$M_V = \begin{pmatrix} \cos(\phi_y(s)) & \frac{\rho}{n} \sin(\phi_y(s)) \\ -\frac{n}{\rho} \sin(\phi_y(s)) & \cos(\phi_y(s)) \end{pmatrix} \quad (2.42)$$

The transformation for horizontal and vertical directions will be as follows:

$$X = M_H X_0 \quad (2.43)$$

$$Y = M_V Y_0 \quad (2.44)$$

The number of oscillation performed by a charged particle in horizontal or vertical plane is known as a 'tune'. The horizontal and vertical tunes can be calculated as follows:

$$\nu_x = \sqrt{1-n}, \quad \nu_y = \sqrt{n} \quad (2.45)$$

The realistic design of coils to obtain the required weak focusing field will be discussed in the next chapter. For the J-PARC $g-2$ experiment, the field index is set at $n = 1.5 \times 10^{-4}$. This small value of “ n ” was chosen to avoid the contribution to a_μ precession from the weak magnetic focusing. In the case of SITE, we set the field index value to 1.65×10^{-2} . The purpose of SITE is to prove the feasibility of this new idea, not to obtain any physics results. Therefore, this large value of “ n ” was chosen for the ease of the experiment.

2.5 Beam Phase Space Requirements

In this section, the basic concepts in transverse beam dynamics and related parameters will be described briefly. For a detailed review on beam dynamics see [42], [43], [44], and [45]. In the later part of this section, the beam phase-space requirements for the 3-D spiral injection will be described.

2.5.1 Concepts in beam dynamics

In accelerator physics, the motion of each particle is described by using the coordinates along the design trajectory s of a reference particle. This coordinate system is known as Frenet-Serret, as shown in Fig 2.6. The 6-dimensional phase space vector in Frenet-Serret coordinate system is given by:

$$X(s) = \begin{pmatrix} x \\ x' \\ y \\ y' \\ z \\ \delta \end{pmatrix}, \quad (2.46)$$

where x and y are the transverse displacements from the design trajectory s , z is longitudinal displacement from the reference particle. The coordinates $x' = \frac{dx}{ds}$, $y' = \frac{dy}{ds}$ represent the horizontal and vertical slopes with respect to the reference trajectory, $\delta = \frac{\Delta p}{p_s}$ is the momentum deviation from the reference momentum. In some instances it is more convenient to use the transverse momenta p_x , p_y instead of slopes. The relationship between them can be described as following: $x' = \frac{p_x}{p_s}$, $y' = \frac{p_y}{p_s}$, where p_s denotes the particle momentum along the reference trajectory. The later convention is used in this thesis.

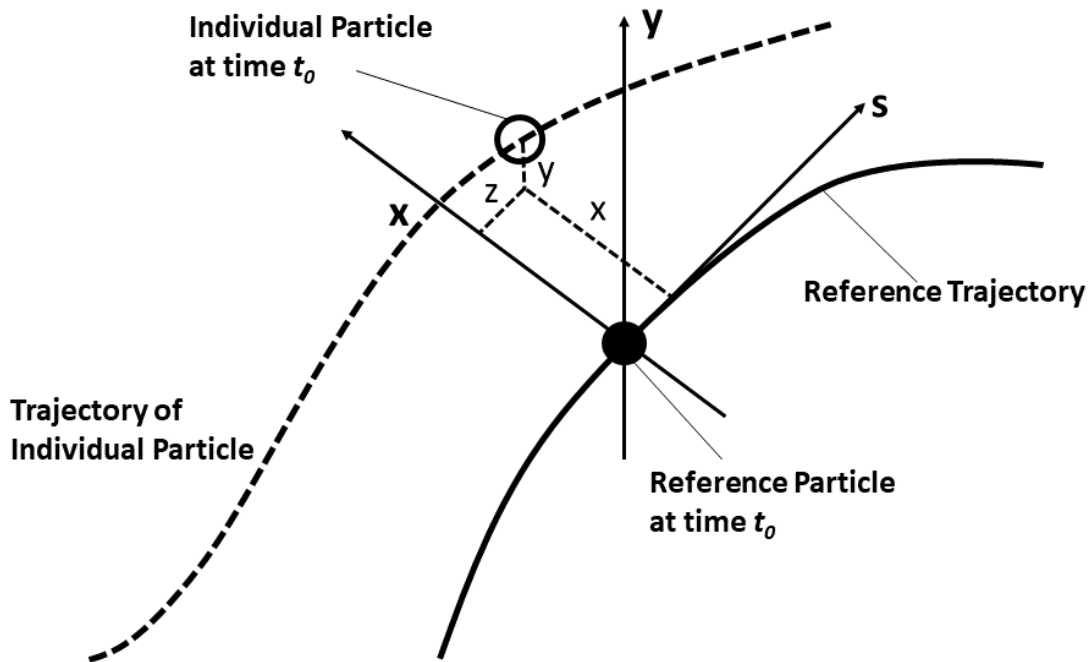


Figure 2.6: Frenet-Serret coordinate system.

The motion of charged particles through an electromagnetic field (beamline), is govern by the Lorentz force:

$$\vec{F} = q(\vec{E} + \vec{v} \times \vec{B}), \quad (2.47)$$

where q is the charge of the particle, \vec{v} its velocity, and \vec{E} and \vec{B} are the electric and magnetic field vectors respectively. Electric fields are used to accelerate the particles, while magnetic fields are used to deflect and to focus the beam. In this text, we will concentrate only on the effect of magnetic fields on the particle motion.

If the beamline consists only of drift spaces, dipole, (skew) quadrupole magnets, the magnetic fields depend linearly on the deviation of the particle from the reference path. If we ignore the momentum deviation ($\delta = 0$) and longitudinal motion, then the equations of horizontal and vertical motion can be written as:

$$x''(s) + k_x \cdot x(s) = 0, \quad y''(s) + k_y \cdot y(s) = 0, \quad (2.48)$$

where k_x and k_y are

$$k_x = \frac{1}{\rho^2} - \frac{1}{B \cdot \rho} \frac{dB}{dx}, \quad k_y = \frac{1}{B \cdot \rho} \frac{dB}{dx} \quad (2.49)$$

The parameter ρ is the bending radius of the reference trajectory at the position s and $\frac{1}{B \cdot \rho} \frac{dB}{dx}$ shows focusing strength of the quadrupole magnet. Eq. (2.48) is known as Mathieu-Hill equations. The detailed derivation of Eq. (2.48) can be found at [42].

The differential equation of the motion of a particle through the individual components (drift space, quadrupole, and bending magnets, etc.) can be established explicitly. Therefore, the solutions of the equations of motion with linear approximation can be shown as:

$$X(s) = M \cdot X(s_0), \quad (2.50)$$

$$\begin{pmatrix} x \\ x' \\ y \\ y' \end{pmatrix} = \begin{pmatrix} m_{11} & m_{12} & m_{13} & m_{14} \\ m_{21} & m_{22} & m_{23} & m_{24} \\ m_{31} & m_{32} & m_{33} & m_{34} \\ m_{41} & m_{42} & m_{43} & m_{44} \end{pmatrix} \begin{pmatrix} x_0 \\ x'_0 \\ y_0 \\ y'_0 \end{pmatrix} \quad (2.51)$$

The 4×4 matrix M shows the transfer matrix that describes the transportation of the particle phase-space from the entrance to the exit of a beamline. When a particle passes through a beamline composed of different components, the final phase space can be shown as the product of the individual transfer matrices:

$$X(s) = M_n \cdot M_{n-1} \cdot \dots \cdot R_1 \cdot X(s_0), \quad (2.52)$$

where $X(s)$ and $X(s_0)$ are phase space vectors at the initial and final position respectively, and M_1, M_2, \dots, M_n represents the transfer matrix of individual components of the beamline from

s_0 to s . In the case of completely decoupled motion, the off-diagonal elements in Eq. (2.51) will become zero. The transformation matrices of each beamline component (drift spaces, bending magnet, quadrupole magnet) will be described in the forthcoming Chapter.

2.5.2 Emittance and Twiss parameters

The Mathieu-Hill equation (Eq. (2.48)) is similar to the simple harmonic oscillator, therefore, the general solution to Eq. (2.48) and its derivatives can be written as [42]

$$q(s) = \sqrt{\epsilon_q \beta_q(s)} \cdot \cos(\phi_q(s) + \phi_{q0}) \quad (2.53)$$

$$q'(s) = \frac{\sqrt{\epsilon}}{\beta} (\alpha_q(s) \cdot \cos(\phi_q(s) + \phi_{q0}) + \sin(\phi_q(s) + \phi_{q0})) \quad (2.54)$$

where q stands for the one of the transverse coordinate x or y and ϵ , ϕ_{q0} are constants. The phase function $\phi_q(s)$ is given by

$$\phi_q(s) = \int_{s_0}^s \frac{d\bar{s}}{\beta_q(\bar{s})} + \phi_{q0} \quad (2.55)$$

Eq. (2.53) and (2.54) can be a solution of Eq. (2.48), if the following relation satisfied:

$$\frac{1}{2}\beta_q(s)\beta_q''(s) - \frac{1}{4}\beta_q'^2 + K_q(s)\beta_q^2(s) = 1 \quad (2.56)$$

Combined Eq. (2.53) and (2.54) in terms of invariant of motion ϵ

$$\gamma(s)q(s)^2 + 2\alpha(s)q(s)q'(s) + \beta(s)q'(s)^2 = \epsilon \quad (2.57)$$

where $\alpha(s) = -\frac{1}{2}\beta'(s)$ and $\gamma = \frac{(1+\alpha(s)^2)}{\beta(s)}$. Eq. (2.57) is the equation of an ellipse. The ellipse parameters β , α and γ , are called Twiss parameters.

The single particle, whose motion is governed by Eq. (2.48), traverse along the contour of an ellipse given by Eq. (2.57). The shape and orientation of an ellipse change as it moves through the accelerator, but its area remains constant.

So far, the motion of a single particle within phase space was described. Now let's consider ensemble of particles, whose trajectories fill a certain area in the horizontal phase space (x , x_0). As shown above, an ensemble of particles always remains inside of a phase space ellipse, while moving along the accelerator. Only the shape and orientation of this ellipse changes while its area remains constant. The area A of this ellipse, enclosing a certain fraction of particles in phase space, divided by π , is called horizontal emittance ϵ_x

$$\epsilon_x = \frac{A}{\pi} \quad (2.58)$$

Figure 2.7 denotes the horizontal phase space ellipse and also shows the elaborate the relationship between the ellipse and Twiss parameters. And horizontal phase-space ellipse equation can be shown as below:

$$\gamma_x x^2 + 2\alpha_x x x' + \beta_x(s) x'^2 = \epsilon \quad (2.59)$$

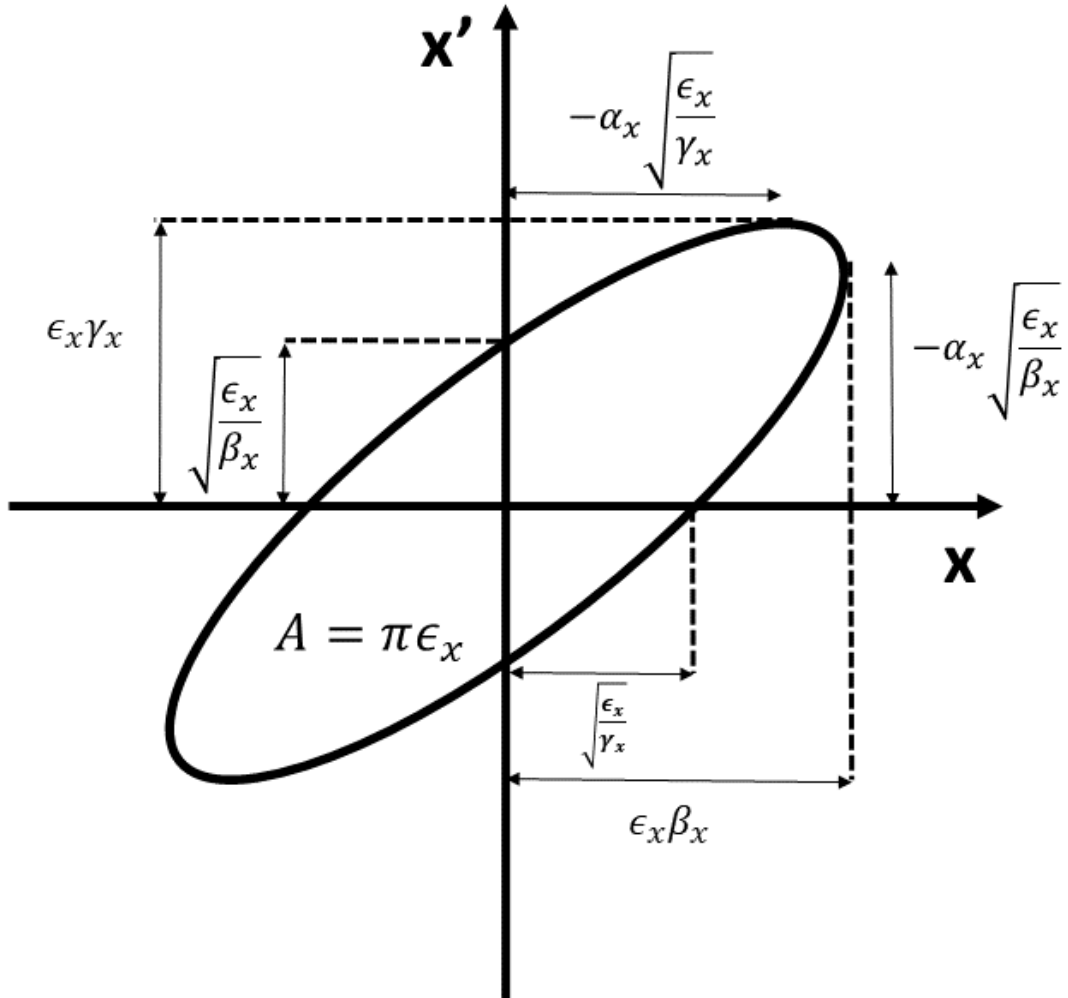


Figure 2.7: The beam phase-space ellipse in the horizontal plane. Twiss parameters $(\beta_x, \alpha_x, \gamma_x)$ describes the shape and orientation of the beam phase-space ellipse.

2.5.3 Beam matrix

Let's write the equation of the horizontal phase space ellipse by introducing the symmetric two-dimensional beam matrix:

$$\begin{pmatrix} x & x' \end{pmatrix} \begin{pmatrix} \sigma_{11} & \sigma_{12} \\ \sigma_{21} & \sigma_{22} \end{pmatrix}^{-1} \begin{pmatrix} x \\ x' \end{pmatrix} = 1 \quad (2.60)$$

Since, $\sigma_{21} = \sigma_{12}$, this can be written as

$$\sigma_{22}x^2 + 2\sigma_{12}xx' + \sigma_{11}x'^2 = \det\sigma, \quad (2.61)$$

Comparing Eq. (2.59) and Eq. (2.61) will results in the Twiss parameters, the emittance, and the beam matrix:

$$\sigma = \begin{pmatrix} \sigma_{11} & \sigma_{12} \\ \sigma_{21} & \sigma_{22} \end{pmatrix} = \epsilon_x \begin{pmatrix} \beta_x & -\alpha_x \\ -\alpha_x & \gamma_x \end{pmatrix} \quad (2.62)$$

$$\epsilon_x = \sqrt{\det\sigma} = \sqrt{\sigma_{11}\sigma_{22} - \sigma_{12}^2}. \quad (2.63)$$

This analogy can be generalized to n -dimensional phase space. The emittance expresses the area (or volume) of the phase space ellipse consist of all or a certain portion of particles of the beams. The 4×4 beam matrix can be written as below:

$$\sigma = \begin{pmatrix} \langle xx \rangle & \langle xx' \rangle & \langle xy \rangle & \langle xy' \rangle \\ \langle x'x \rangle & \langle x'x' \rangle & \langle x'y \rangle & \langle x'y' \rangle \\ \langle yx \rangle & \langle yx' \rangle & \langle yy \rangle & \langle yy' \rangle \\ \langle y'x \rangle & \langle y'x' \rangle & \langle y'y \rangle & \langle y'y' \rangle \end{pmatrix} = \begin{pmatrix} \sigma_{xx} & \sigma_{xy} \\ \sigma_{xy}^T & \sigma_{yy} \end{pmatrix}. \quad (2.64)$$

Where, $\langle xx \rangle, \langle yy \rangle$ are RMS beam sizes. The most common choice to describe the distribution of particles is Gaussian distribution. If we consider a two-dimensional Gaussian phase-space distribution in the horizontal plane and only consider the 2-D emittance defined in Eq. (2.63), the ellipse calculated by the second moments include about 1σ of the particles in the beam. Figure 2.8 represents the Gaussian distribution for horizontal phase-space. The solid ellipse denotes the 1σ of the Gaussian distribution.

In Chapter 5, a technique known as a quadrupole scan will be introduced in detail to measure the emittance of the beam.

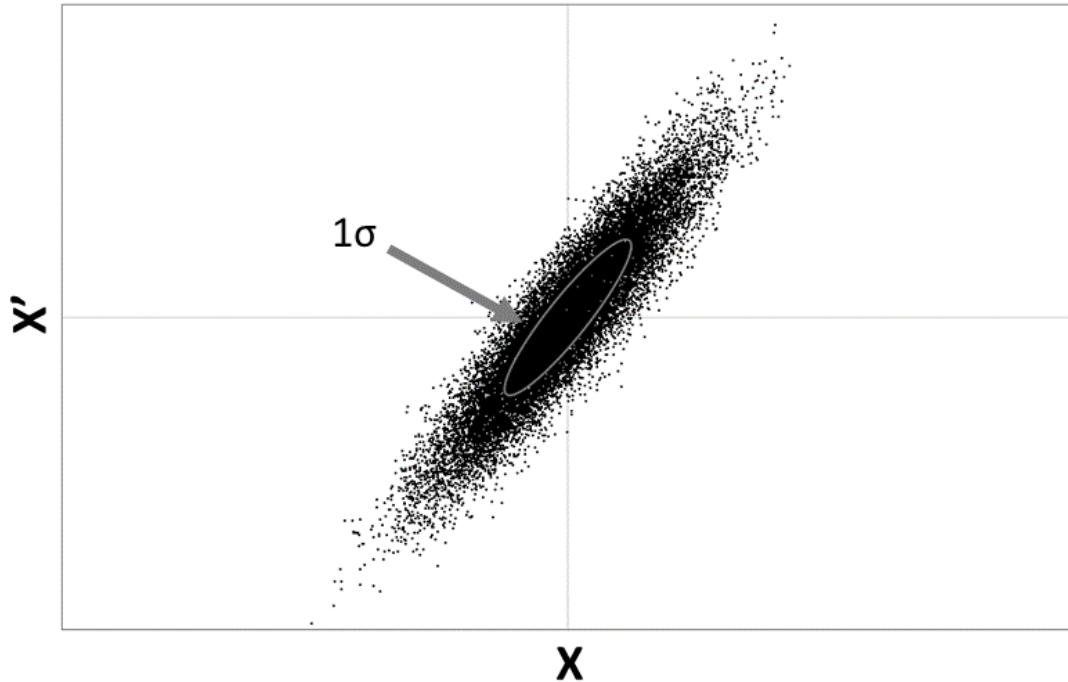


Figure 2.8: Gaussian distribution for horizontal beam phase-space. The solid ellipse represents the 1σ of the Gaussian distribution.

2.5.4 Beam Phase Space Requirements for 3-D Spiral Injection

Due to the axial symmetric field of the solenoid magnet a strongly XY -coupled beam is needed for the successful 3-D spiral injection scheme. Moreover, the radial fringe field of the solenoid magnet causes the vertical blow-up of the injected beam, as the beam moves through the storage magnet. The particles at different vertical positions sense different radial field and eventually takes different vertical paths. Therefore, the beam phase-space matching is indispensable for 3-D spiral injection.

In order to overcome the vertical blow-up of the beam, a matched beam (or appropriate XY -coupled) at the injection point is required. Here, XY -Coupling is referred to the rotation of the principle axes between horizontal (X , X') and vertical (Y , Y') planes. The detailed description/calculations and results of the beam phase-space matching will be discussed in Chapter 6.

Figure 2.9 (left) represents the beam injection without phase space matching and the below plot shows the beam cross-section at the injection point. In Fig. 2.9 the storage magnet coordinates will be referred as global coordinates (X_g , Y_g , Z_g). For the convenience, the beam phase-space at the injection point is shown in beam coordinates (X , Y , Z). It is evident that without phase space matching beam drastically blow-up in the vertical direction. Figure 2.9 (right) shows the beam injection with appropriate phase space matching. When appropriate XY -coupling (phase space matching) was applied to the injected beam, the vertical blow-up reduced sufficiently.

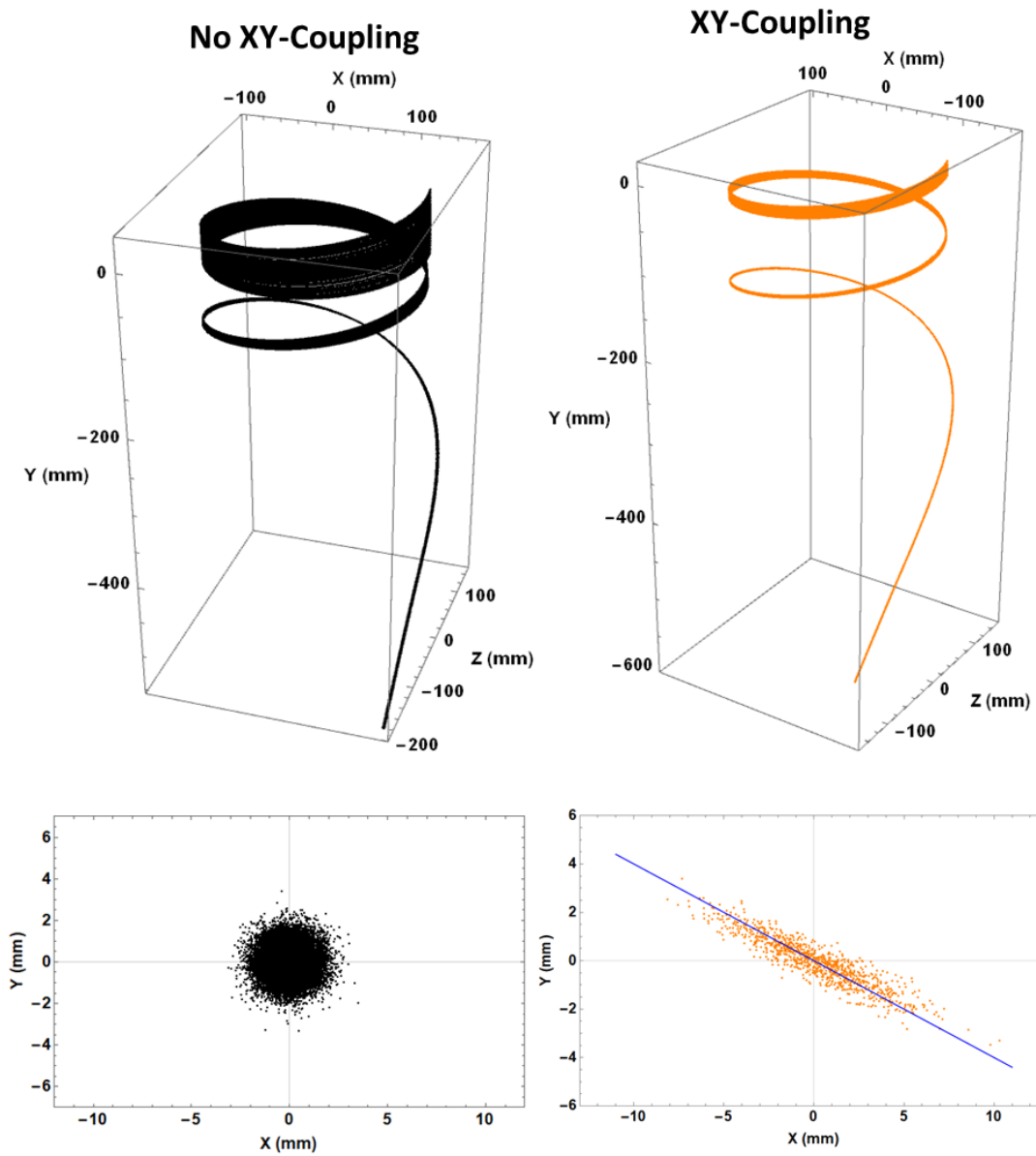


Figure 2.9: Left: Beam injection without phase space matching. The below plots shows the beam cross section at the injection point. The storage magnet coordinates are referred as global coordinates (X_g, Y_g, Z_g) . For the convenience, the beam phase-space at the injection point is shown in beam coordinates (X, Y, Z) . It is evident that without phase space matching beam drastically blow-up in the vertical direction. Right: Beam injection with phase space matching. When appropriate XY-coupling (phase space matching) was applied to the injected beam, the vertical blow-up reduce sufficiently.

Chapter 3

Spiral Injection Test Experiment (SITE) with Electron Beam

The three-dimensional spiral injection scheme is an unproven idea, and no real precedent exists for this new injection scheme. Therefore, a demonstration experiment to prove the feasibility of this unprecedented injection scheme is inevitable. A scale down Spiral Injection Test Experiment (SITE) via the use of an electron beam was developed at the KEK Tsukuba campus. The following are the salient features of SITE:

- SITE used a scale-down solenoid storage magnet. The weak focusing and magnetic kicker are included.
- SITE provides the freedom to experiment with the electron beam without any stringent time/cost constraint of the muon beam time availability.
- SITE provided an opportunity to develop the beam monitors for the solenoid storage magnet.
- The beam phase space matching for the solenoid-type storage magnet is challenging and is also tested at SITE.

In this chapter, the SITE experimental setup will be described in detail.

3.1 Experimental Setup of SITE

The SITE setup consists of a 2 m long beamline and a solenoid storage magnet to store the electron beam. The beamline consists of following components:

- Electron Gun: A triode-type thermionic electron gun with a **LaB₆** cathode was used to generate the DC electron beam. In Section 3.2, the electron gun details will be discussed.

- **Magnetic Lens:** After the electron gun, a magnetic lens is placed to focus the low energy beam. A pair of steering coils is also placed to control the transverse position of the beam. The brief detail of the magnetic lens is shown in Section 3.3.
- **Electric Chopper:** An electric chopper system is placed after the magnetic lens to generate the pulsed beam. In Section 3.4, the electric chopper system will be discussed.
- **Collimator:** A collimator was placed after the electric chopper. The collimator served as the beam dump for the chopper system and was also used to create the differential vacuum pumping system for the gas monitor in the storage magnet. The collimator is described in 3.5.
- **Rotating quadrupole magnets:** Three rotating quadrupole magnets have been placed after the collimator. These magnets are used to produce the required phase space for the storage magnet. The design and field measurement is discussed in Section 3.6.
- **Dipole Magnet:** A bending magnet (BM1) was placed on the straight beamline to deflect the beam at 40 Degree toward the storage magnet. A second bending magnet (BM2) was also placed near the injection point to control the injection angle slightly. In Section 3.7 dipole magnets will be discussed in detail.
- **Storage Magnet:** The dipole magnet will guide the beam to the normal conducting solenoid magnet. The storage magnet has been designed to store the electron beam into the orbit of 0.24 m diameter. Details of the storage magnets are discussed in 3.8.

A pulsed magnetic kicker was also developed to store the beam at the center of the storage magnet. The kicker system for the SITE will be discussed in chapter 7 of this thesis. The layout of the SITE experimental setup with each component is shown in Fig. 3.1. A comparison of parameters between SITE and E34 is given in Table 3.1. Some progress reports of SITE can be found at [46, 47, 35]. The SITE experimental setup photo is shown in Fig. 3.2.

Table 3.1: Comparison of Parameters Between E34 and SITE.

Parameters	E34	SITE
Particle Specie	μ^+	e^-
Magnetic field strength	3 T	82.5 Gauss
Momentum	300 MeV/c	297 keV/c
Cyclotron Period	7.4 ns	5 ns
Storage orbit diameter	0.66 m	0.24 m
XY-Coupling	Yes	Yes

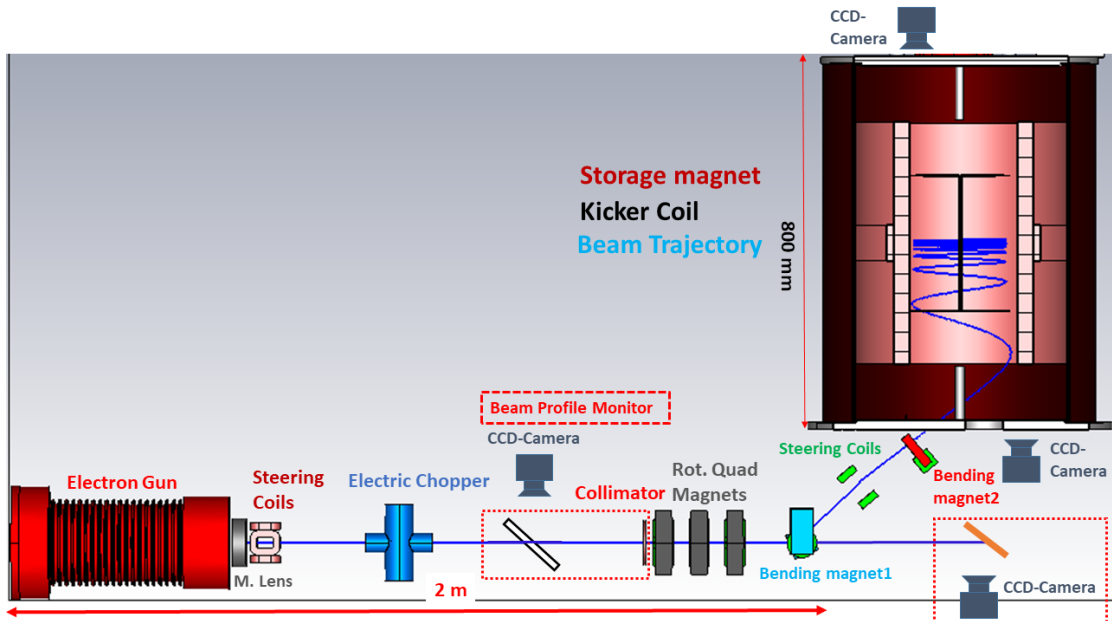


Figure 3.1: The side view of the 3D model of the three-dimensional Spiral Injection Test Experiment (SITE).

3.2 Electron Gun

A thermionic electron gun with a LaB_6 cathode of 2 mm diameter was used to produce the electron beam. This electron gun was previously used for the production high brightness X-ray experiment [48] at KEK. The electron gun was operated at 80 keV and the maximum achievable beam current was 100 mA. From a radiation and thermal safety point of view, the electron gun was operated at 0.5 mA. An isolation transformer of a maximum capacity of 200 kV was used to transfer electrical power from the AC source to a high-voltage power supply electron gun. The specifications of the electron gun are given in Table 3.2. The experimental layout of the electron gun high voltage (H.V) station is shown 5.1.

Table 3.2: Electron gun specifications.

Parameters	Values
Extraction Voltage	80 kV
Maximum current	100 mA
Grid type	Aperture
Cathode material	LaB_6
Cathode Diameter	2.0 mm
Cathode Grid Voltage	2 keV

The electron gun consists of a LaB_6 cathode of diameter 2.0 mm. The LaB_6 cathode was chosen due to its low work function (2.70 eV), modest vacuum requirement, and a 50-fold greater service life than that of tungsten cathode. Figure 3.4 shows the photo of the LaB_6 cathode. After

3.2. ELECTRON GUN

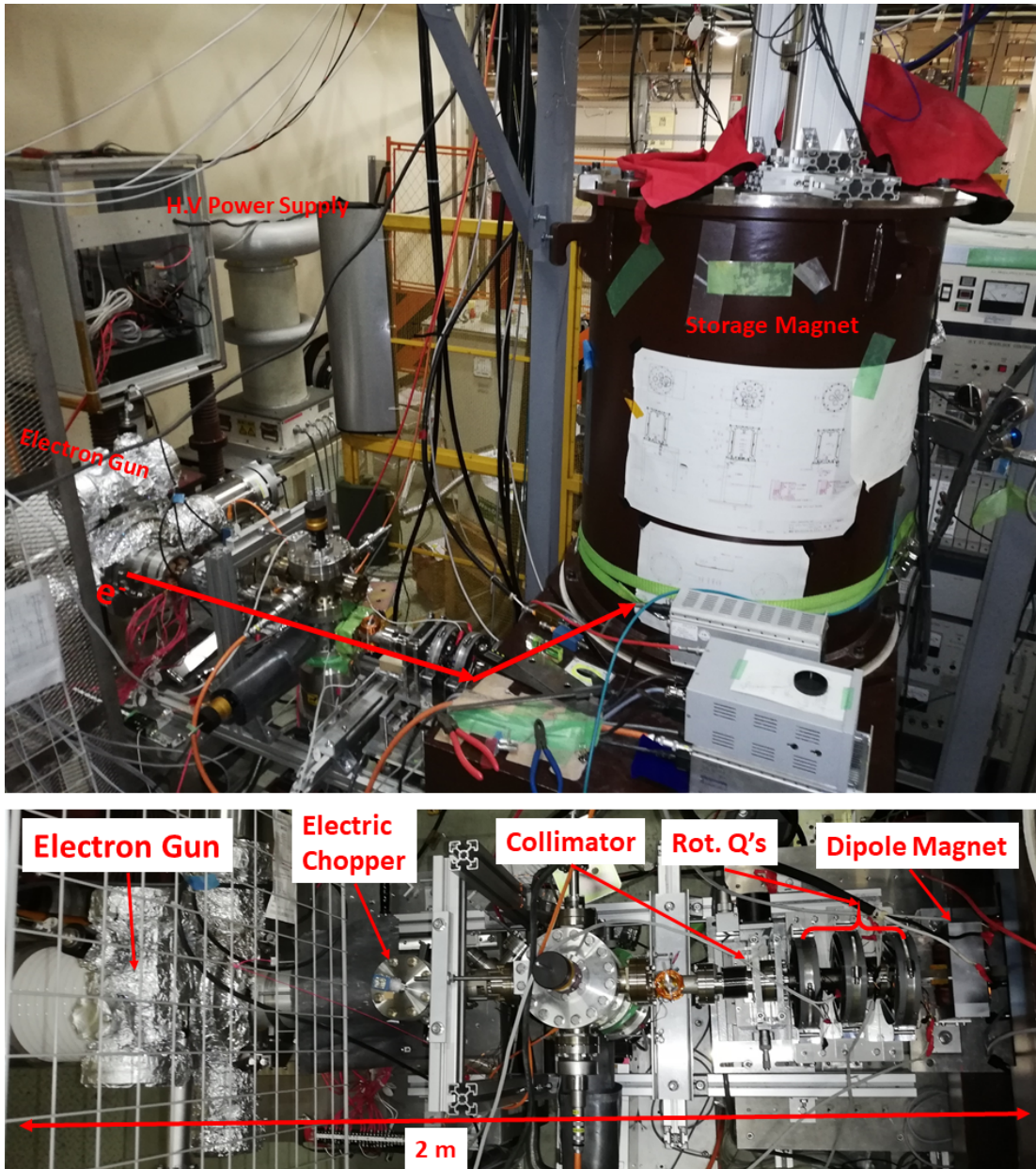


Figure 3.2: Above: A Photo of SITE setup. Below: A top view photo of the straight beamline, with each component labeled.

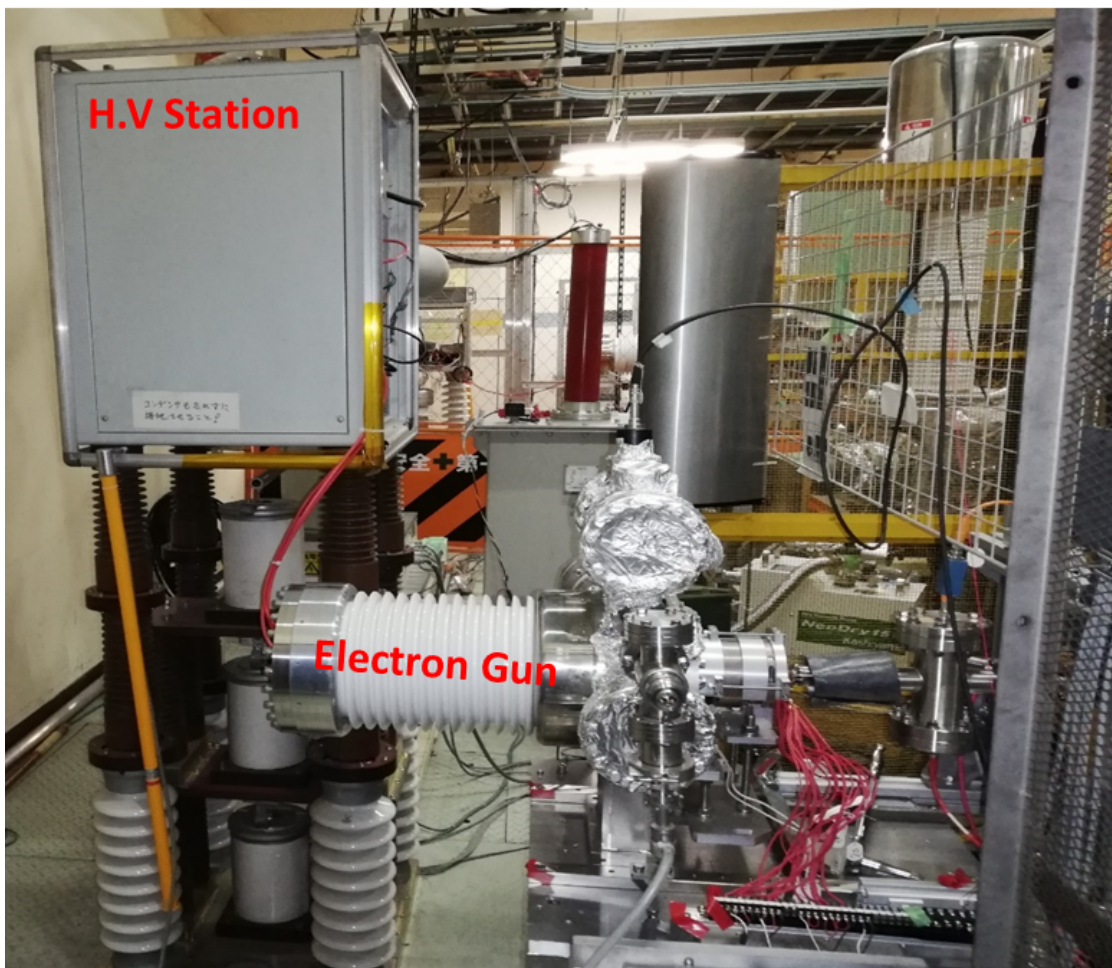
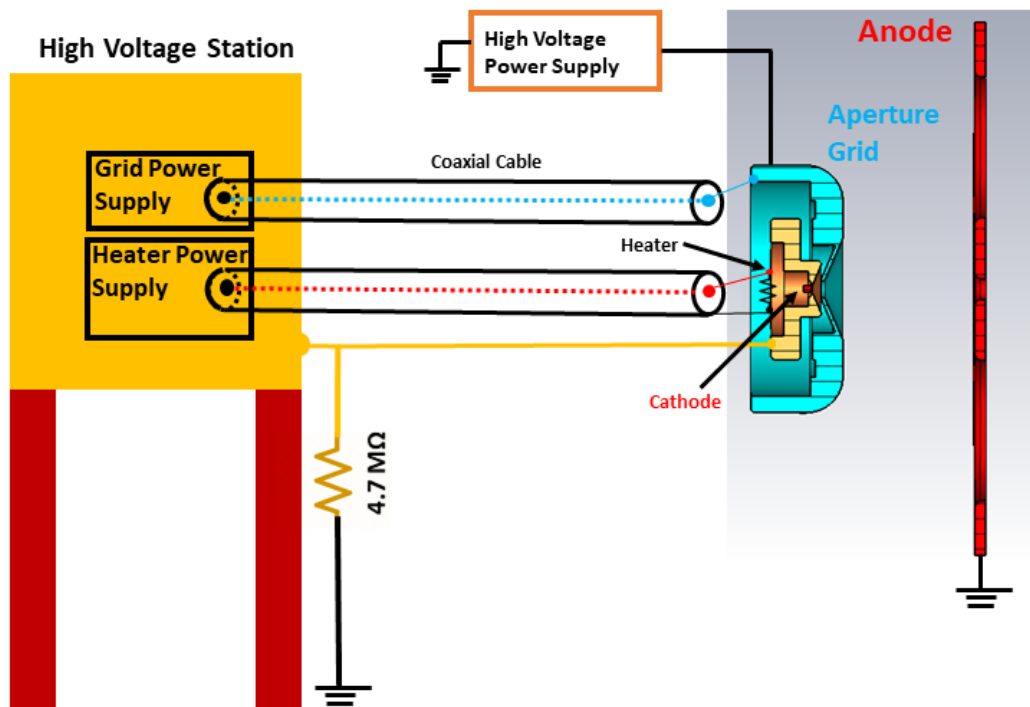


Figure 3.3: Above: Layout of electron gun high voltage (H.V) power supply station. Below: H.V station and electron gun.

the cathode, a Wehnelt electrode was placed to focus the emitted electrons. An aperture grid was placed after the Wehnelt to control the beam current from the electron gun. Afterward, the aperture grid anode was placed to extract the emitted electrons. The 3-D simulation of electron gun has been done in the CST-PS [36]. The potential contours and electron beam trajectories are shown in Fig. 3.5. The emittance of the beam at the exit of the electron gun (Anode) in CST-PS [36] simulation was 1.45 mm mrad in both transverse planes.

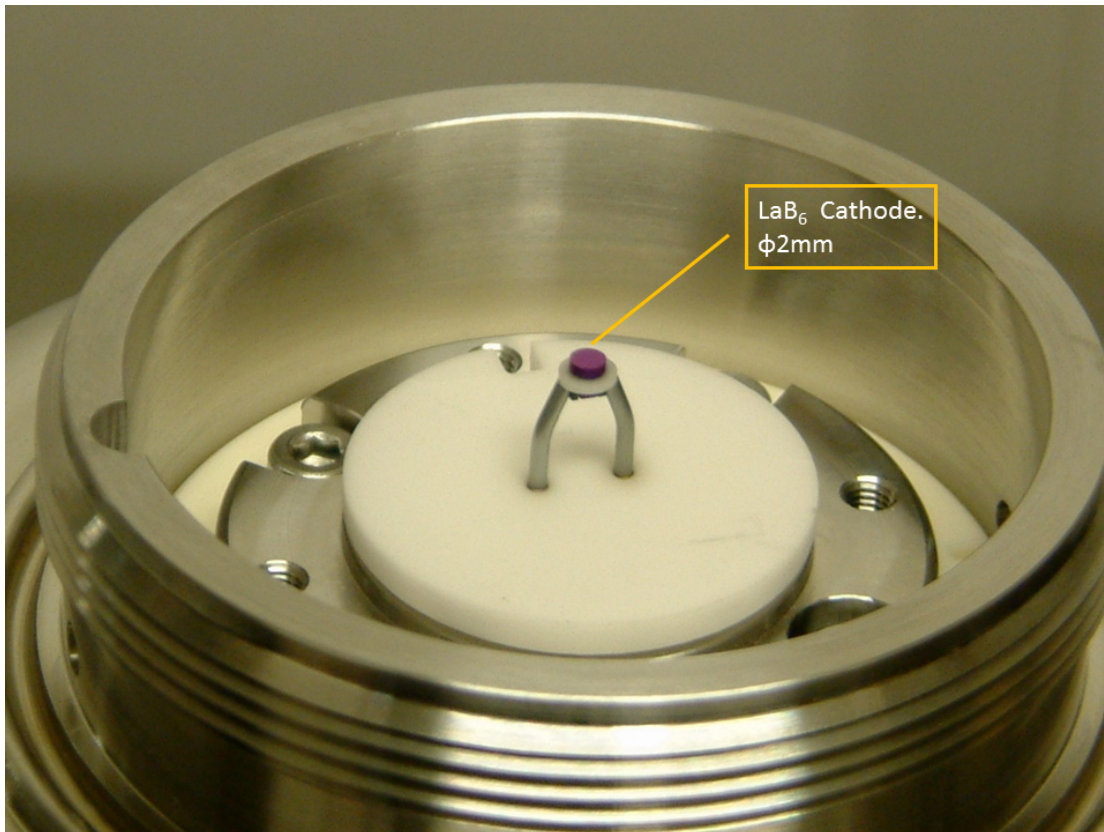


Figure 3.4: Photo of the **LaB₆** cathode used in electron gun. The diameter of the cathode is 2 mm

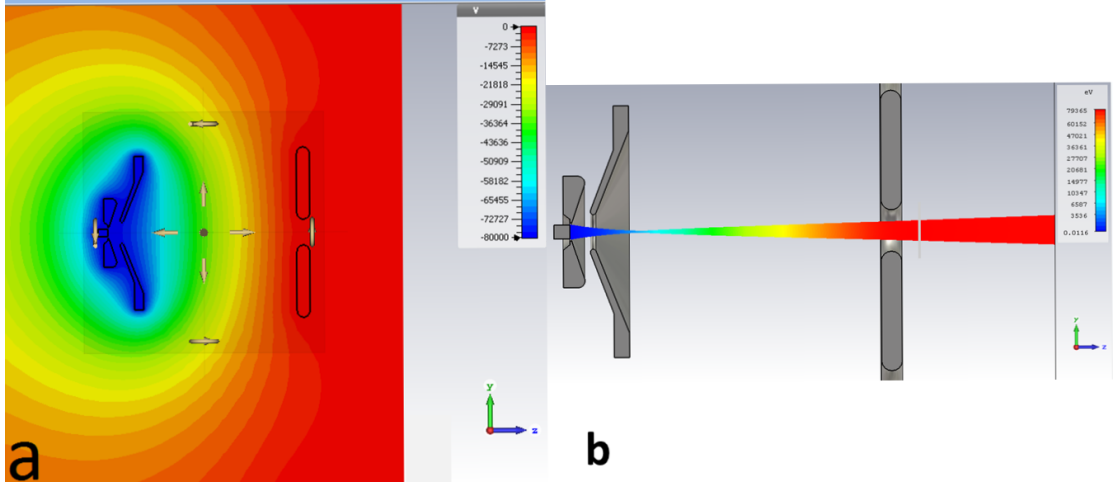


Figure 3.5: Left: Electric potential contour plots of the electron gun. Right: The electron beam trajectories through electron gun.

3.2.1 Emission Process

In the thermionic emission process, a piece of metal or appropriate conducting material (cathode: in our case LaB_6) is heated to a high temperature. If the applied temperature is high enough, a part of electrons get kinetic energy equal or greater than the work function (ϕ) of the cathode material, then electrons will escape through the surface of the cathode.

In thermionic emission, the maximum number of emitted particles depends on the temperature of the surface. There are two regimes for the thermionic emission.

- In the temperature-limited model, the emission current depends on temperature of the cathode, while in the case of the temperature-limited regime, Richardson's law [49] gives the current density of emitted electrons.

$$J(x) = A_R T^2 \exp\left(\frac{-\phi}{kT}\right) \quad (3.1)$$

Where, A_R is Richardson's constant with a value $1.2 \times 10^6 \frac{\text{A}}{\text{m}^2 \text{k}^2}$, ϕ is the work function of the metal, T is the applied temperature, and k is the Boltzmann constant.

- In the case of the space-charge regime, the cathode temperature is set at its maximum, and the emission of particles depends on the extraction voltage only. The current density in the case of space-charge limited regime is given by Childs-Langmuir law [50]

$$J(x) = \left(\frac{4\epsilon_0}{9} \sqrt{\frac{2e}{m}}\right) \frac{V_A^{\frac{3}{2}}}{b^2} \quad (3.2)$$

Where, $J(x)$ is the current density, V_A is the applied voltage, ϵ_0 is the permittivity of free space, b is the distance from emitting surface, m and e are the mass and charge of the electron.

During beam time of SITE, the electron gun was operated in a temperature-limited regime, providing the freedom to control the beam current at a fixed applied voltage.

3.2.2 Electron Gun Stability

During the beam operation of the electron gun H.V and current in H.V circuit, were saved on logger [51], to check the stability of the electron gun. The beam current of the electron gun can be estimated by subtracting the current in the H.V circuit while the heater of cathode is OFF from the total current flows in the H.V circuit while heater of the cathode is ON

$$I_{beam} = I_t - I_{bg} \quad (3.3)$$

Where, I_{beam} is the beam current, I_t is the total current flows in the H.V circuit while heater is On. And I_{bg} is the current in the H.V circuit while heater was off. Figure 3.6 shows the recorded H.V and current data. The current on the right in Fig. 3.6 decreases rapidly after the electron gun is turned on, one of the possibility of this rapid decrease is due to the spoiled vacuum caused by the out-gassing of the cathode. After the operation of 30 minutes the vacuum becomes stable and current also settles down. The electron gun was operated at 80 keV, voltage stability was 0.008% (80000 ± 5.29 V). The beam current stability was 0.94% (1.2 ± 0.01 mA). This voltage and current stability is enough small to not cause any significant beam instability and acceptable for the SITE.

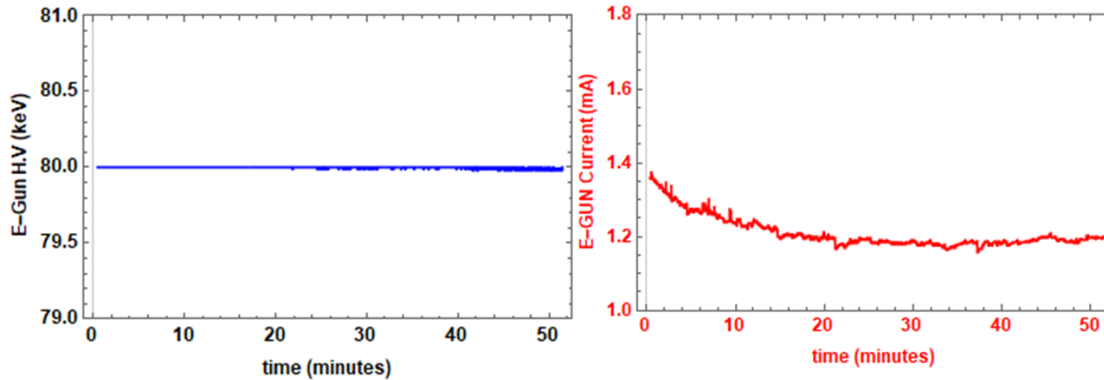


Figure 3.6: Left: The electron gun was operated at 80 keV. H.V of electron gun was recorded as a function of time to check the stability during the operation. Right: Current of electron gun as a function of time.

3.3 Magnetic Lens

A magnetic lens is a beam optics manipulation component that is used to focus the beam in both transverse directions. In SITE, a magnetic lens was placed after the electron gun. Magnetic lens consists of a coil of copper wires inside the iron pole pieces. A current through the coils produces a magnetic field in the bore of the pole pieces. The rotationally symmetric magnetic field is inhomogeneous in such a way that it is weak in the center of the gap and becomes stronger close to the bore. Electrons close to the center are less strongly deflected than those passing the lens far from the axis. The overall effect is that the beam is focused on a spot. The transfer matrix of a magnetic lens can be written as a product of rotation matrix in and focusing matrix in both transverse directions:

$$M_{solenoid} = M_{rotation} \cdot M_{focusing} \quad (3.4)$$

$$M_{rotation} = \begin{pmatrix} \cos(kL) & 0 & \sin(kL) & 0 \\ 0 & -\cos(kL) & 0 & \sin(kL) \\ -\sin(kL) & 0 & \cos(kL) & 0 \\ 0 & -\sin(kL) & 0 & \cos(kL) \end{pmatrix} \quad (3.5)$$

$$M_{focusing} = \begin{pmatrix} \cos(kL) & \frac{\sin(kL)}{k} & 0 & 0 \\ -\sin(kL) & \cos(kL) & 0 & 0 \\ 0 & 0 & \cos(kL) & \frac{\sin(kL)}{k} \\ 0 & 0 & -\sin(kL) & \cos(kL) \end{pmatrix} \quad (3.6)$$

Where, k is a focusing strength ($k = \frac{B}{2B\rho}$) and L is a length of magnetic lens. Hence, magnetic lens focus provides the focusing in both transverse planes simultaneously [52, 53] with a rotation of transverse planes by an angle of kL . Figure 3.7 (left) shows the cut view of 3-D model of SITE magnetic lens, while the axial field of the magnetic lens is shown on the right.

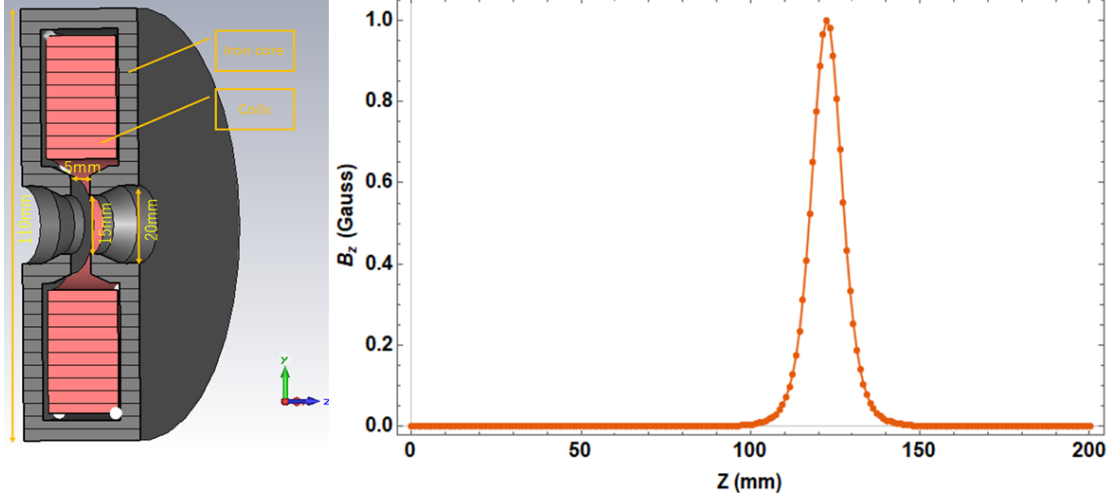


Figure 3.7: Left: Cut view of 3-D model of SITE's magnetic lens. Right: Axial magnetic field of magnetic lens.

3.4 Electric Chopper

An electric chopper system has been developed to generate the pulsed electron beam for the SITE. Fast response, simple structure, and low cost make the electric chopper system the best choice for the generation of pulse beam for the low energy beam.

The electric chopper system consists of a pair of the electrode and a beam dump. One of the electrodes is attached to the positive DC H.V power supply, which permanently deflects the electron beam to beam dump location (in our case collimator: section 3.5). The other electrode was connected to the pulse power supply, during the active time of the pulse power supply the beam passes through the collimator and otherwise remain deflected and stopped at the collimator. Figure 3.8 shows the schematic and principle of the electric chopper system.

The required voltage for the electric chopper system depends on the electron beam energy, electrode spacing, length of the electrodes, and distance to the beam dump location with respect to the position of the electrode. The required deflection angle θ can be calculated as following:

$$\theta = \frac{qV_d l}{(\gamma m c^2 \beta^2) d} \quad (3.7)$$

Where, q is charge of elementary particle, l is the length of electrodes, V_d is the required deflection voltage, d is the gap between the electrodes, m is the rest mass of electron, c is the speed of light, γ and β are the relativistic factor of the beam.

$$y = \frac{(\gamma - 1)V_d l}{(\gamma \beta^2) d V_{acc}} \left(D + \frac{l}{2} \right), \quad (3.8)$$

where, y is a distance on which the beam deflects, V_{acc} is the accelerating voltage of the beam, D is a distance of beam dump (collimator) from the electrodes end, and l is the length of electrodes.

The parameters of the SITE electric chopper system are given in the Table 3.3. A simulation of the chopper system had been carried in CST-ES [36]. Figure 3.9 (left) shows the 3-D model

of the chopper system and the picture on the right depicts the potential contours of the chopper system in CST simulation. Figure 3.9 (left) presents the support structure and feed through connection to the H.V plate, while on the right is the cross section of the electrodes assembly in the vacuum chamber. The ceramic feedthrough is a standard 5 kV single-ended coaxial MHV connector.

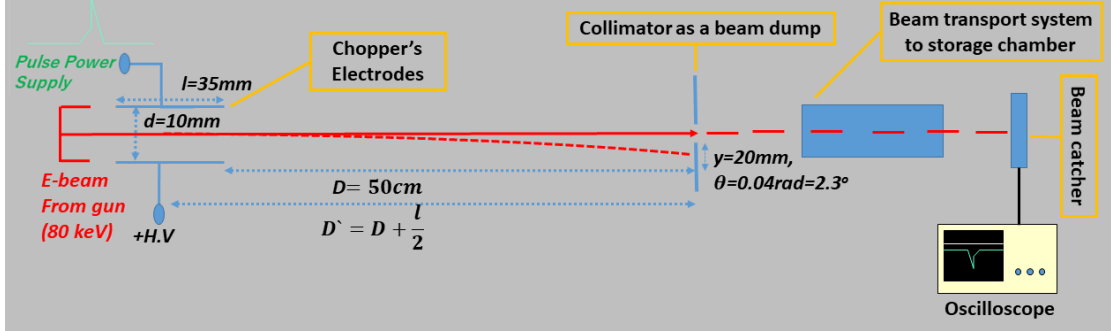


Figure 3.8: Schematic of electric chopper system.

Table 3.3: Electric Chopper System Parameters.

Parameter	Value
Chopper Deflecting Voltage	1.6 kV
Electrode Length	35 mm
Aperture (Width \times Height)	20 mm \times 10 mm
Deflection Angle	0.04 rad
Pulse Width	2 ns
Frequency	50 Hz
Capacitance	50 pF

3.4. ELECTRIC CHOPPER

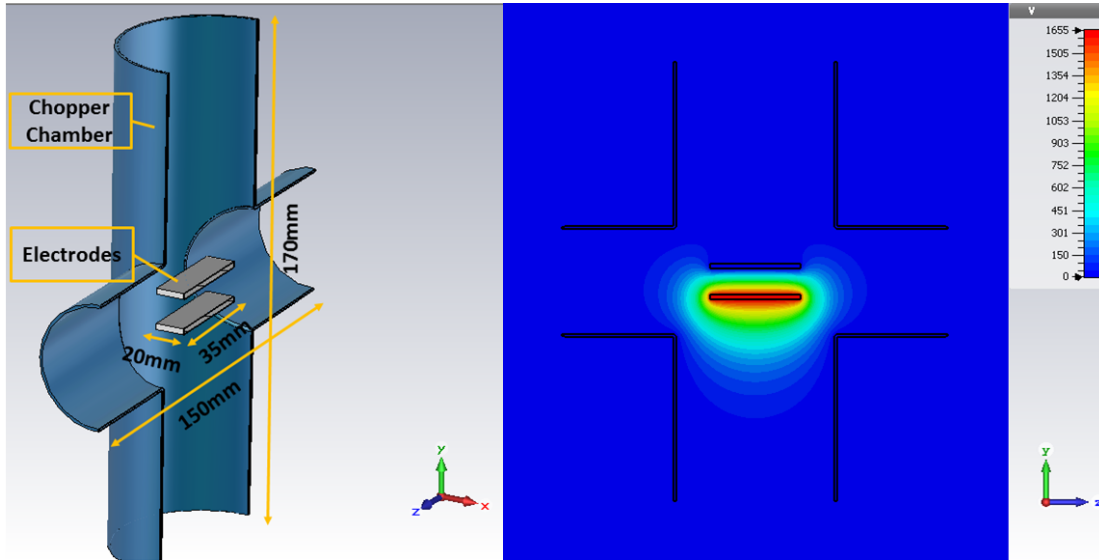


Figure 3.9: Right: Mechanical structure and dimension of chopper system. Left: Potential contours on the electrodes.

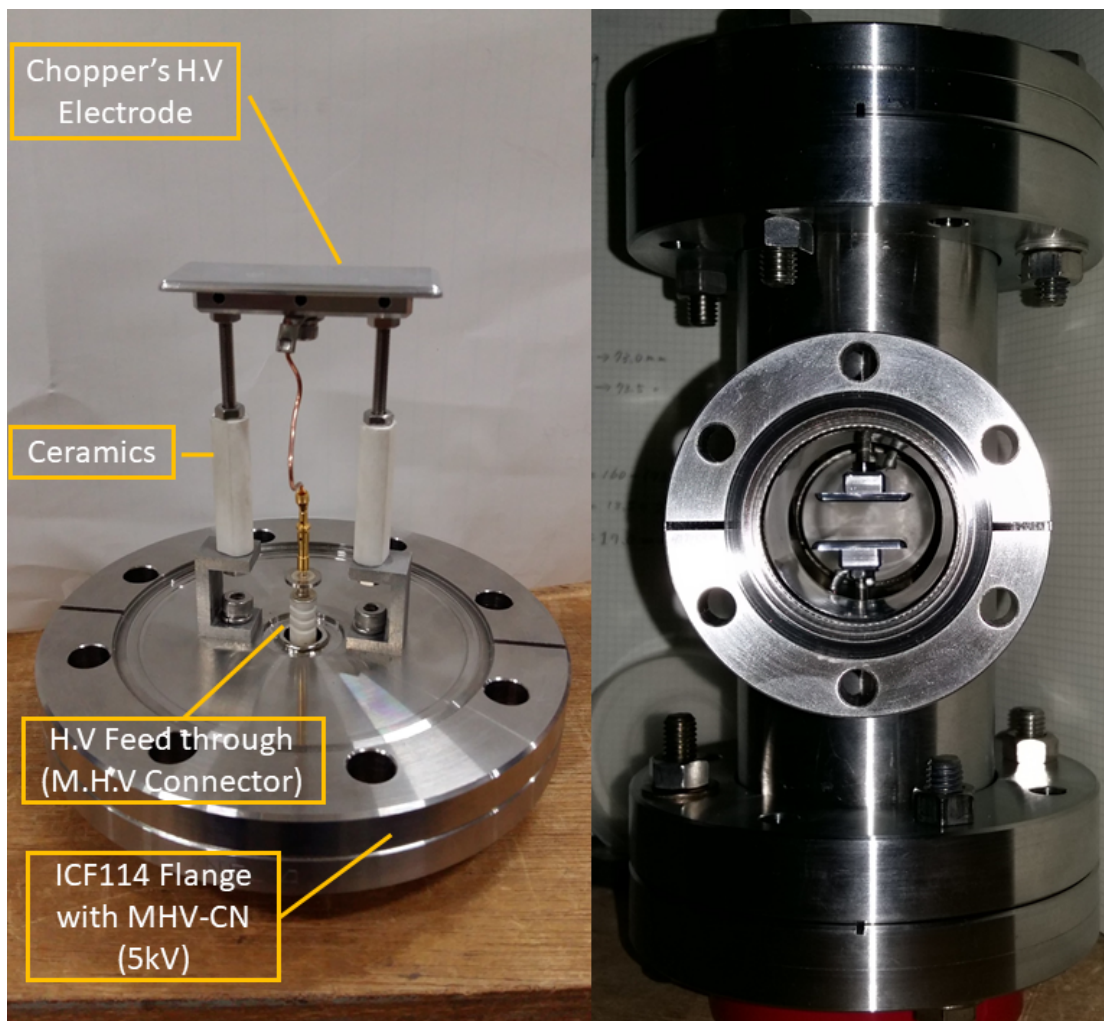


Figure 3.10: Left: H.V electrode attached to the vacuum feed through and its support. Right: Chopper's electrodes in vacuum chamber

3.5 Collimator

A collimator of diameter 3 mm and depth of 5 mm was placed after the electric chopper system. The following are the functions of the collimator:

- It serves as beam dump for the electric chopper system
- It was also used to create the differential vacuum pumping system for the gas monitor of the storage magnet. The differential pumping is a method wherein the large pressure difference is maintained between different regions of a single vacuum system. The pressure difference is maintained by a collimator and extra pumping on the high vacuum region part. In the straight section of the beamline, a high vacuum was the requirement of the electron gun operation (1.5×10^{-6} mbar), the medium vacuum (1.5×10^{-3} mbar) with the insertion of N_2 gas was maintained in the storage magnet.
- The collimator also served to remove the beam halo from the electron gun.

Figure 3.11 shows the collimator used at SITE. The black burn mark is due to the beam hitting the collimator.

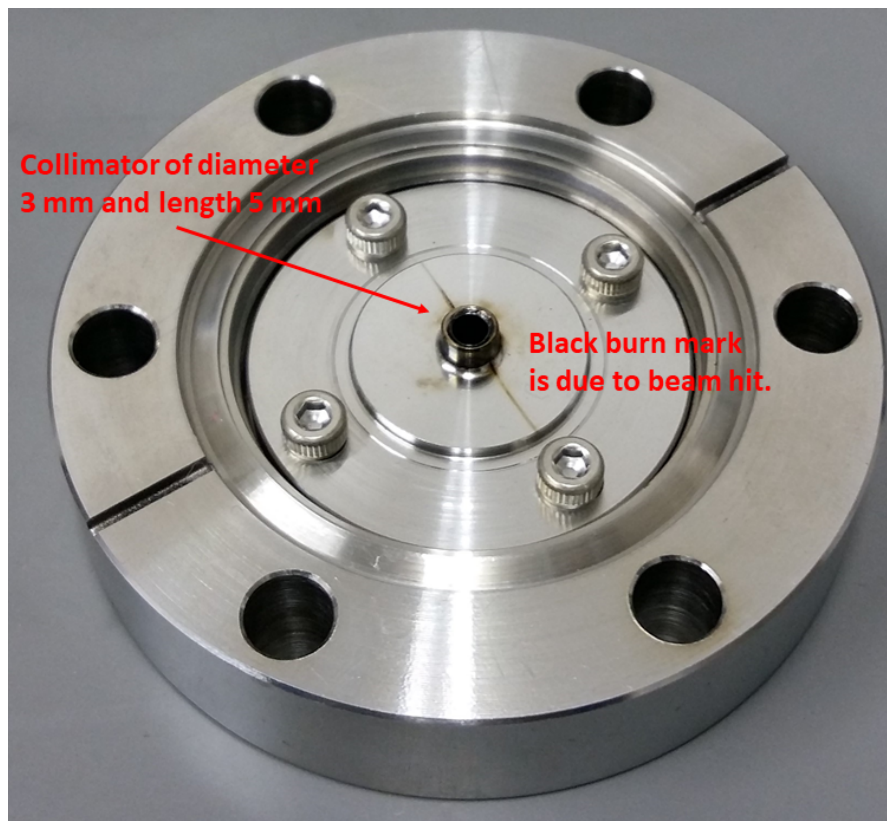


Figure 3.11: Collimator used at SITE's beamline. The diameter of the collimator is 3 mm and depth is 5 mm. The black burn mark is due to the beam hitting on the collimator.

3.6 Rotatable Quadrupole Magnets

As described in Chapter 2 an XY -coupled beam is key to the successful spiral injection. To produce the required XY -coupled beam for the phase space matching, quadrupole magnets with arbitrary rotation angles are required. For SITE, three rotating quadrupole magnets have been designed and manufactured. These rotating quadrupole magnets can rotate ± 45 Degree around the axial field direction. The rotating quadrupole magnets system consists of a base plate to support the quadrupole and rotation system. The quadrupole magnets were enclosed in a circular ring, and the ring was placed in a support system such that we can rotate it about ± 45 Degree manually. Figure 3.12 shows the rotating quadrupole magnets and support system for the rotation. Table 3.4 summarizes the rotating quadrupole magnet parameters.

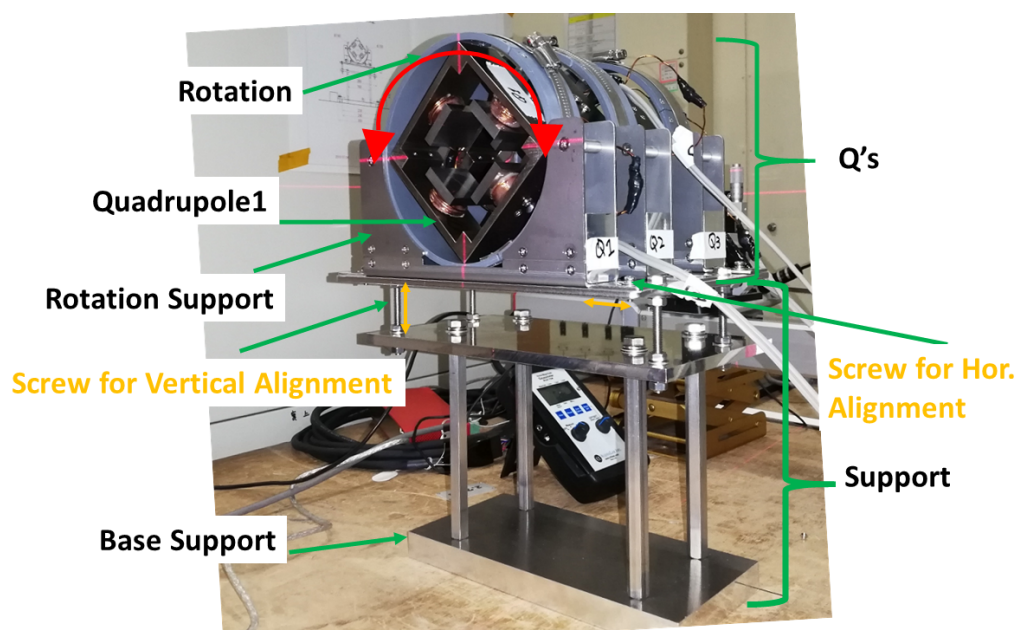


Figure 3.12: Three rotating quadrupoles and their rotation system.

Table 3.4: Rotating Quadrupole Magnet Parameters.

Parameter	Value
Rotation Angle	± 45 Degree
Number of Quads	3
Ampere-Turns per pole (NI)	50 A t
Number of Turns	25
Field Gradient at 2 A	0.19 T/m
Bore Radius	25 mm
Pole Length	35 mm
Effective Length	56 mm

The motion of particle through arbitrary angle quadrupole magnet can be found by the following transfer matrix:

$$M_{Rot.Quad} = R(\alpha)^{-1} \cdot M_{Quarupole} \cdot R(\alpha) \quad (3.9)$$

Where, $M_{Rot.Quad}$ is the rotation quadrupole magnet transfer matrix, $R(\alpha)$ is rotation matrix with angle α , and $M_{Quarupole}$ is the normal quadrupole magnet transfer matrix. For vertical and horizontal direction, quadrupole magnets can be written as follows:

$$M_{QV} = \begin{pmatrix} \cosh(kl_q) & \frac{\sinh(\sqrt{k}l_q)}{\sqrt{k}} & 0 & 0 \\ \sqrt{k} \sinh(\sqrt{k}l_q) & \cosh(\sqrt{k}l_q) & 0 & 0 \\ 0 & 0 & \cos(\sqrt{k}l_q) & \frac{\sin(\sqrt{k}l_q)}{\sqrt{k}} \\ 0 & 0 & -\sqrt{k} \sin(\sqrt{k}l_q) & \cos(\sqrt{k}l_q) \end{pmatrix} \quad (3.10)$$

$$M_{QH} = \begin{pmatrix} \cos(\sqrt{k}l_q) & \frac{\sin(\sqrt{k}l_q)}{\sqrt{k}} & 0 & 0 \\ -\sqrt{k} \sin(\sqrt{k}l_q) & \cos(\sqrt{k}l_q) & 0 & 0 \\ 0 & 0 & \cosh(\sqrt{k}l_q) & \frac{\sinh(\sqrt{k}l_q)}{\sqrt{k}} \\ 0 & 0 & \sqrt{k} \sinh(\sqrt{k}l_q) & \cosh(\sqrt{k}l_q) \end{pmatrix} \quad (3.11)$$

Where, M_{QV} and M_{QH} are the transfer matrix of the quadrupole magnet in the vertical and horizontal direction. Where, $k[\text{m}^{-2}]$ is the focusing strength of the quadrupole, magnet which depends on the field gradient $g[\text{T/m}]$,

$$k[\text{m}^{-2}] = 0.3 \frac{g[\text{T/m}]}{P[\text{GeV}/c]}, \quad g[\text{T/m}] = \frac{2\mu_0 n I}{R^2}, \quad f = \frac{1}{kl_q} \quad (3.12)$$

where, $P(\text{GeV}/c)$ is the momentum, μ_0 is the permeability of free space and it's value is $4\pi \times 10^{-7}$ H/m, n is number of turns, I is the excitation current, R is the bore radius of the quadrupole magnet, f is the focal length of the quadrupole magnet, l_q is the effective length of the quadrupole magnet and given as follows:

$$l_q = \frac{\int_{-\infty}^{+\infty} \vec{g}(z) dz}{g_0}, \quad l_q \approx l + R \quad (3.13)$$

The rotation matrix can be written as:

$$R = \begin{pmatrix} \cos(\alpha) & 0 & \sin(\alpha) & 0 \\ 0 & \cos(\alpha) & 0 & \sin(\alpha) \\ -\sin(\alpha) & 0 & \cos(\alpha) & 0 \\ 0 & -\sin(\alpha) & 0 & \cos(\alpha) \end{pmatrix} \quad (3.14)$$

3.6.1 Field Measurement

The field measurement setup for the rotation quadrupole magnet is shown in Fig. 3.13. The field measurement setup consists of the following components

- Hall probe
- An XYZ stage to adjust the position of hall probe
- A linear actuator to sweep hall probe

In order to measure the magnetic field, the hall probe [54] had been attached to the aluminum bar and mounted on the XYZ stage. The hall probe [54] and XYZ -stage setup were mounted on the linear guide to sweep hall probe in the desired direction.

Figure 3.14 is showing the focusing strength of the quadrupole magnet as a function of the excitation current. The focusing strength increases linearly with respect to the applied current. Below: The focal length of the quadrupole magnet as a function of the excitation current.

Figure 3.15 presents the magnetic field measurement of the rotation quadrupole magnets system in the longitudinal direction. The above graph shows the axial field measurement at a horizontal position $x = \pm 5$, and the below plot presents the axial field measurement at a vertical position of $y = \pm 5$. The colored dotted lines present the field measurement and the solid black line is showing the CST simulation results.

Figure 3.16 shows the transverse magnetic field profile of the quadrupole magnet. The color dots are showing the field measurement results and the black line are CST simulation results. The simulation and experimental results are in good agreement with each other.

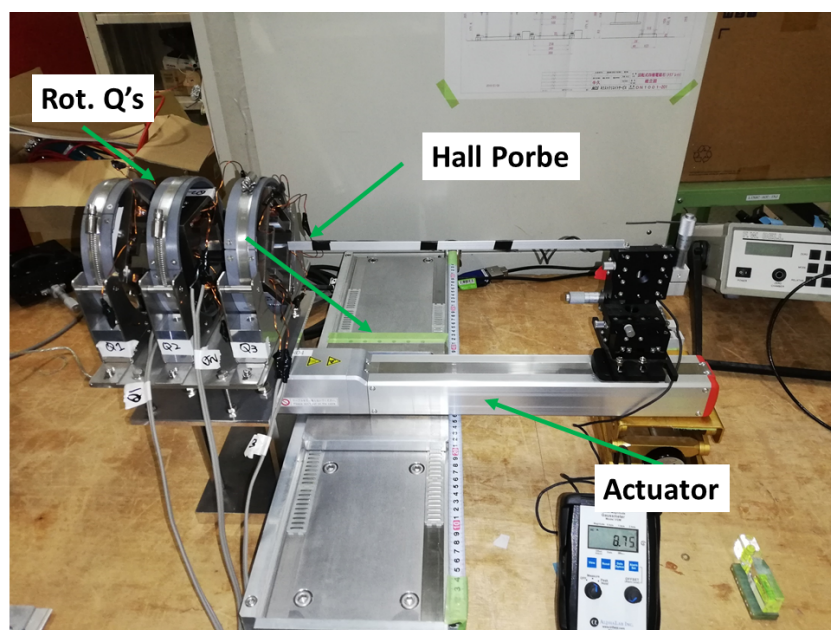


Figure 3.13: The field measurement setup for the rotation quadrupole system.

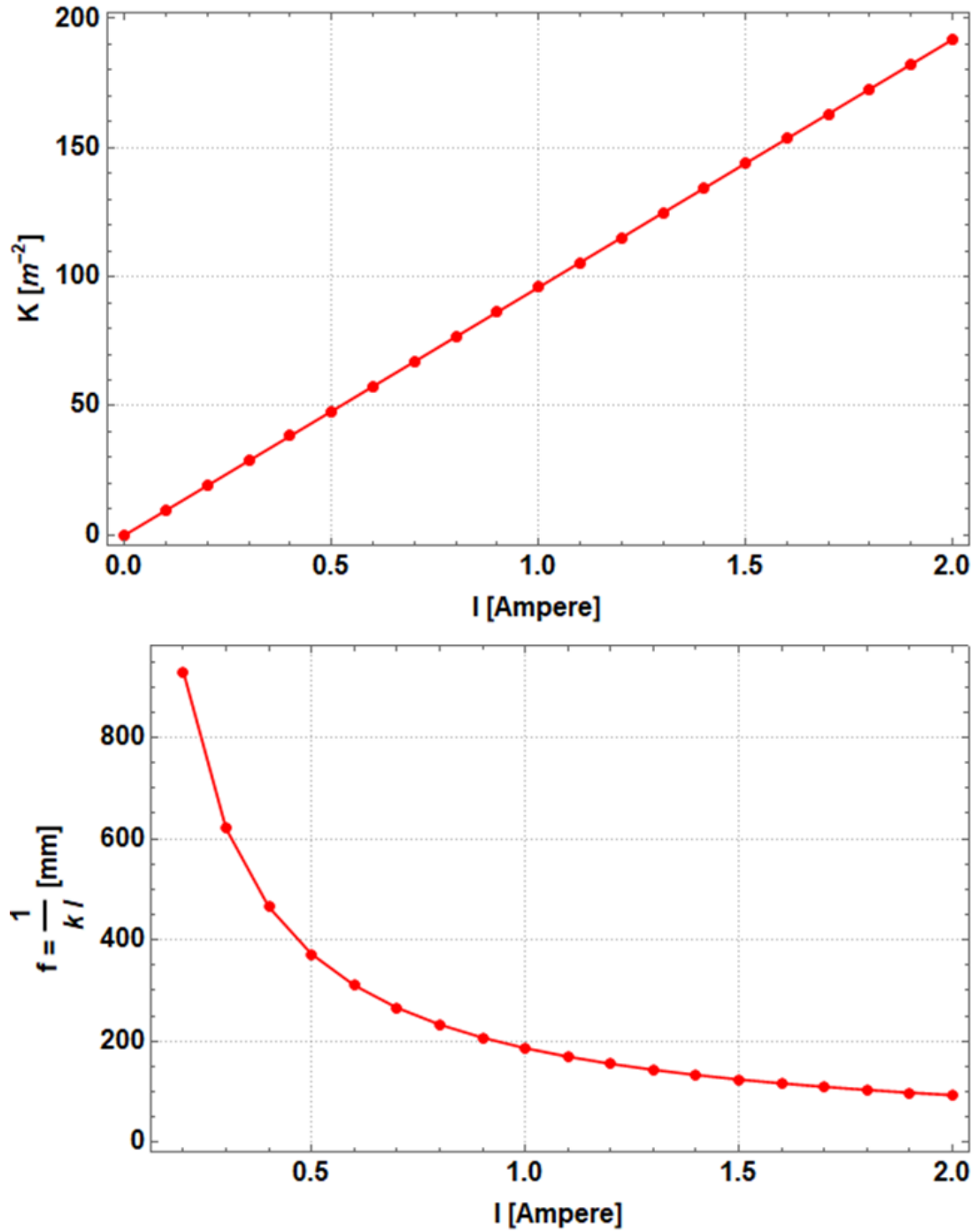


Figure 3.14: Above: The focusing strength of the quadrupole magnet as a function of the excitation current. The focusing strength increase linearly with respect to the applied current. Below: The focal length of the quadrupole magnet as a function of the excitation current.

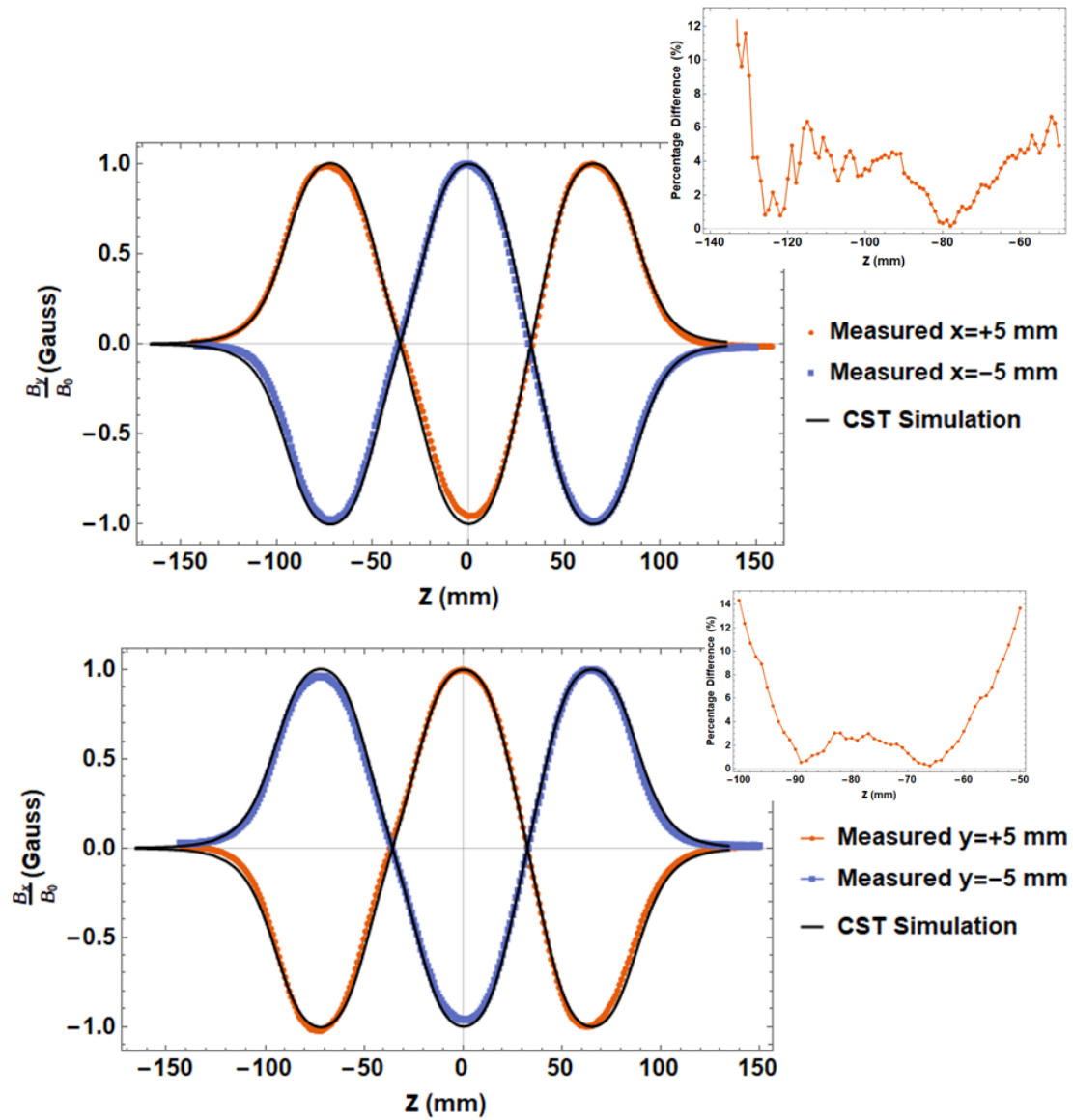


Figure 3.15: The magnetic field measurement of the rotation quadrupole magnets system in the longitudinal direction. Above graph shows the axial field measurement at horizontal position $x = \pm 5$, and below plot presents the axial field measurement at vertical position $y = \pm 5$. Color lines dotted lines represents the field measurement and dashed line is showing the CST simulation results.

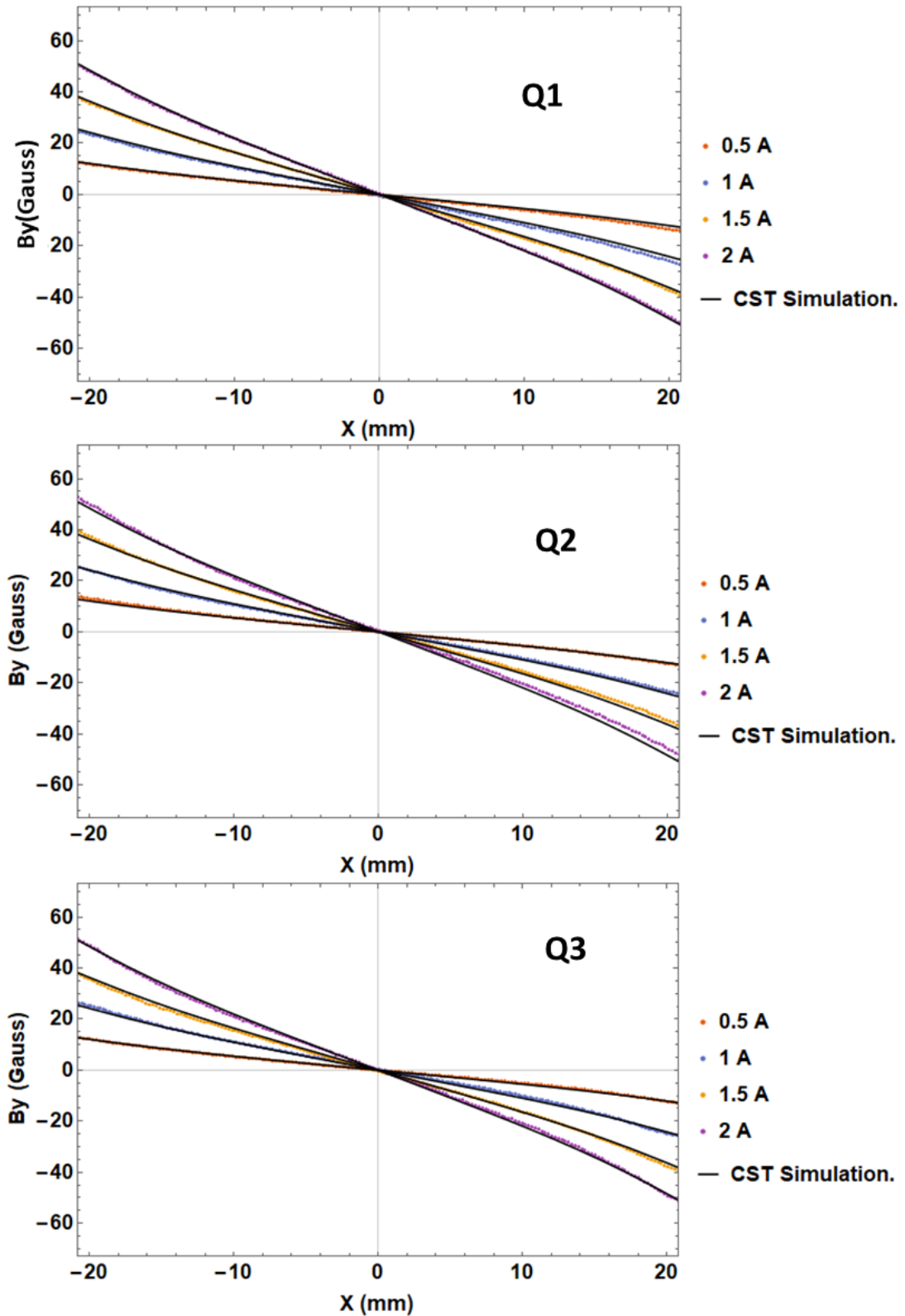


Figure 3.16: Transverse magnetic field profile of the quadrupole magnet. Color dots are showing the field measurement results and black line are CST simulation results.

3.7 Dipole Magnet

In order to inject the electron beam into the storage magnet, a rectangular dipole magnet has been built. A second dipole magnet also has been mounted on the injection pipe to slightly control the injection angle of the beam. The forthcoming sections will describe the details of the dipole magnet.

3.7.1 Dipole Magnet 1

A rectangular pole dipole magnet was designed for the SITE. The rectangular dipole magnet simply deflects the beam in the bending direction, whereas in the non-deflecting plane it has a focusing effect. The transfer matrix of the rectangular dipole magnet [42] is given as follows:

$$M_{rectangular} = M_{edge} \cdot M_{dipole} \cdot M_{edge} \quad (3.15)$$

For a deflection angle θ , $\alpha = \frac{\theta}{2}$. The transformation matrix in deflecting plane is given as:

$$M_H = \begin{pmatrix} 1 & 0 \\ -\frac{\tan(\alpha)}{\rho} & 1 \end{pmatrix} \begin{pmatrix} \cos(\theta) & \rho \sin(\theta) \\ -\frac{\sin(\theta)}{\rho} & \cos(\theta) \end{pmatrix} \begin{pmatrix} 1 & 0 \\ -\frac{\tan(\alpha)}{\rho} & 1 \end{pmatrix} \quad (3.16)$$

$$M_H = \begin{pmatrix} 1 & \rho \sin(\theta) \\ 0 & 1 \end{pmatrix} \quad (3.17)$$

Whereas transformation matrix of rectangular bending magnet in the non deflecting plane is given as:

$$M_V = \begin{pmatrix} 1 & 0 \\ -\frac{\tan(\alpha)}{\rho} & 1 \end{pmatrix} \begin{pmatrix} 1 & \rho\theta \\ 0 & 0 \end{pmatrix} \begin{pmatrix} 1 & 0 \\ -\frac{\tan(\alpha)}{\rho} & 1 \end{pmatrix} \quad (3.18)$$

$$M_V = \begin{pmatrix} 1 - \theta \tan(\frac{\theta}{2}) & \rho\theta \\ -\frac{1}{\rho} \tan(\frac{\theta}{2})(2 - \theta \tan(\frac{\theta}{2})) & 1 - \theta \tan(\frac{\theta}{2}) \end{pmatrix} \quad (3.19)$$

Where, ρ is the bending curvature. The bending curvature can be calculated from magnetic rigidity formula

$$B\rho = \frac{10P(\text{GeV}/c)}{2.9979} \quad (3.20)$$

The NI (Ampere-Turns per pole) and deflection angle are given as follows:

$$NI = \frac{Bg}{\mu_0}, \quad \theta = \frac{B_0 l_{effective}}{B\rho} \quad (3.21)$$

where $l_{effective}$ is effective length and can be calculated as follow

$$l_{effective} = \frac{\int_{-\infty}^{+\infty} B(z) dz}{B_0}, \quad l_{effective} \approx l + gap \quad (3.22)$$

The magnet design and geometry result on pole length of 46 mm, with a gap of 18 mm and yoke size of 103 mm \times 140 mm. The dipole magnet consists of two coils with 30 windings

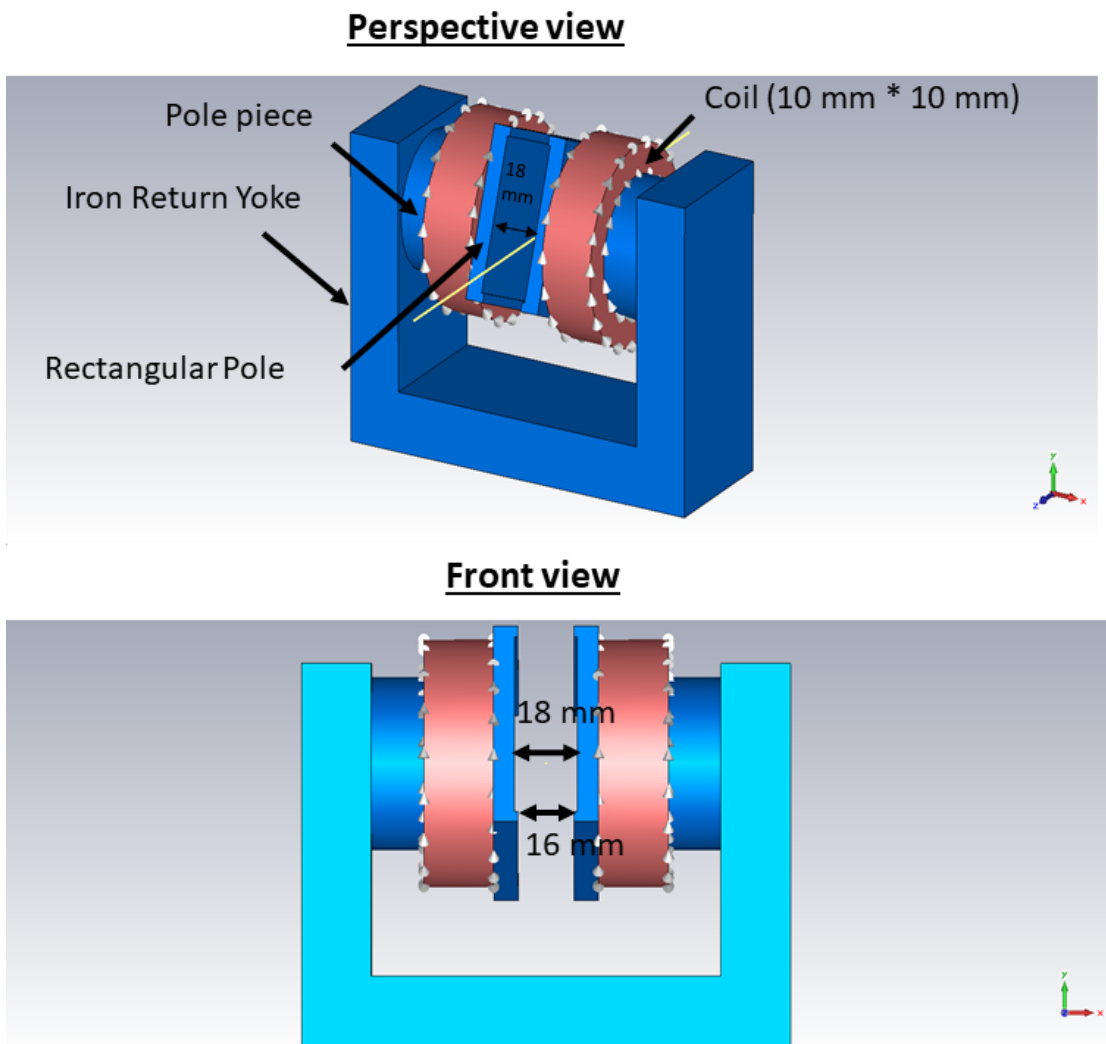


Figure 3.17: The rectangular dipole magnet three dimensional model.

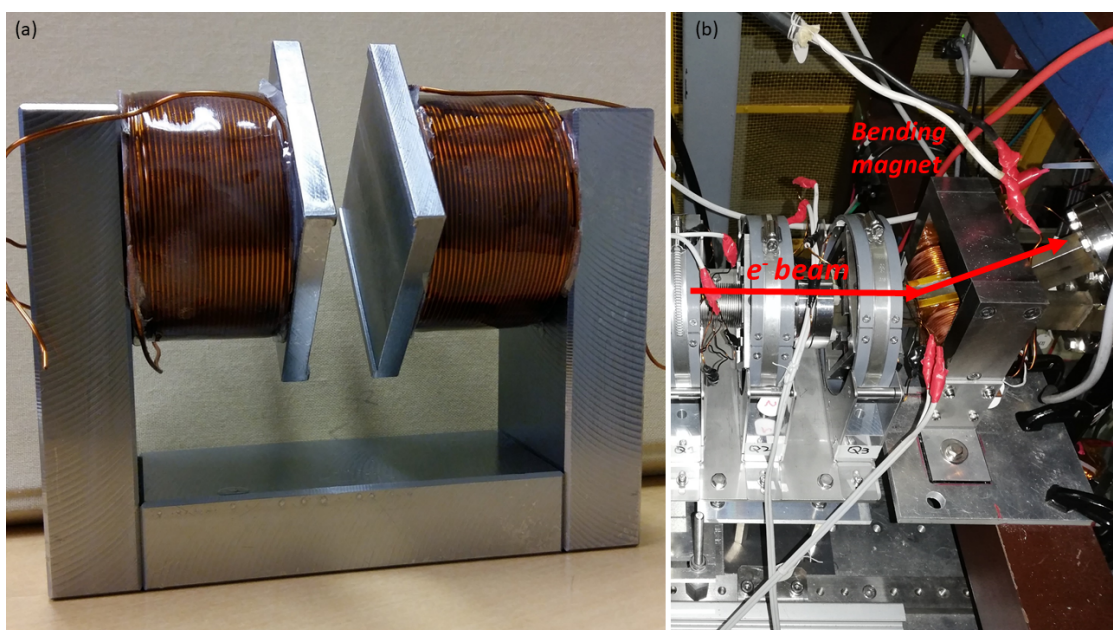


Figure 3.18: Left: The rectangular dipole magnet. The diople magnet at the SITE beamline.

Table 3.5: Dipole Magnet 1 Parameters.

Parameter	Value
Ampere-Turns per pole	90 A t
Number of Turns	30
Pole Gap	18 mm
Pole Length	56 mm
Effective Length	78 mm
Pole Shape	Rectangular
$B\rho$	9.90×10^{-4} T.m

each. Figure 3.17 shows the different views of the 3-D model of the dipole magnet. Table 3.7 summarize the parameters of the dipole magnet.

The magnetic field of the dipole magnet has been measured by the hall probe [54]. Figure 3.19 left shows the magnetic field measurement and CST simulation. Figure 3.19 right is a percentage difference between the simulation and the experiment. The difference in good field region is less than 0.4%, but at the edges, the difference becomes 15% due to hall probe alignment error. Hall probe was aligned with bubble gauge which has error of 10%. The simulation and experimental results are in agreement within the uncertainty.

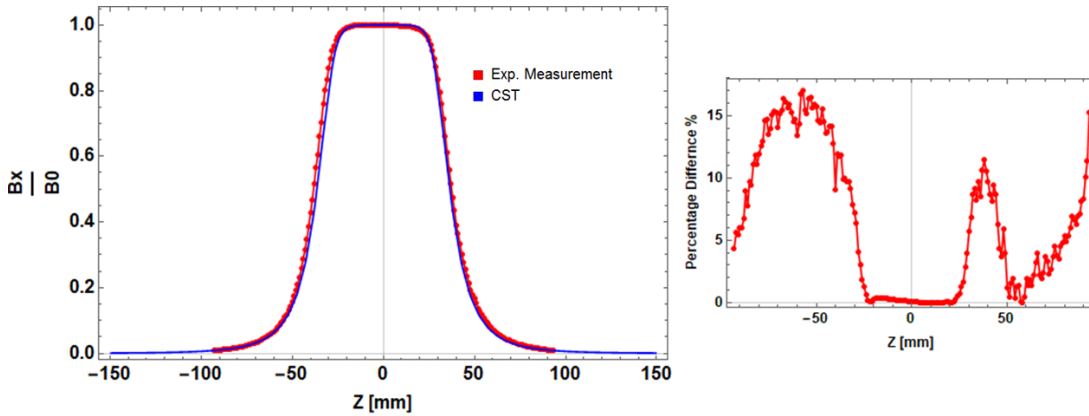


Figure 3.19: Left: The blue solid line shows the CST simulation and red dots are correspond to the field measurement results. Right: The percentage difference between measured values and CST simulation.

3.7.2 Dipole Magnet 2

A second dipole magnet has been placed at the injection pipe. The second dipole magnet increase injection angle acceptance into the storage magnet. Figure 3.20 shows the function of second dipole magnet. Figure 3.21 presents the 3-D model and dimensions of the second dipole magnet. Parameters of the second dipole magnet are shown in the Table 3.6. Field measurement results with CST-EM simulation comparison are shown in the Fig. 3.22.

Table 3.6: Dipole Magnet 2 Parameters.

Parameter	Value
Ampere-Turns	100 A t
Number of Turns	100
Pole Gap	49.5 mm
Pole Length	18 mm
Effective Length	78.5 mm
$B\rho$	9.90×10^{-4} T.m

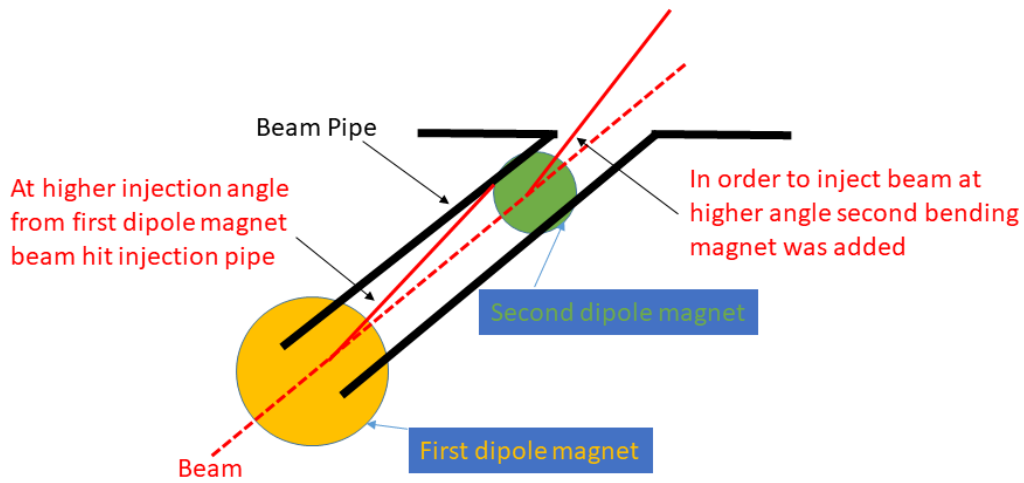


Figure 3.20: The role of second dipole magnet is shown. In order to control the injected beam angle with more freedom a second dipole magnet was added to the injection beam pipe.

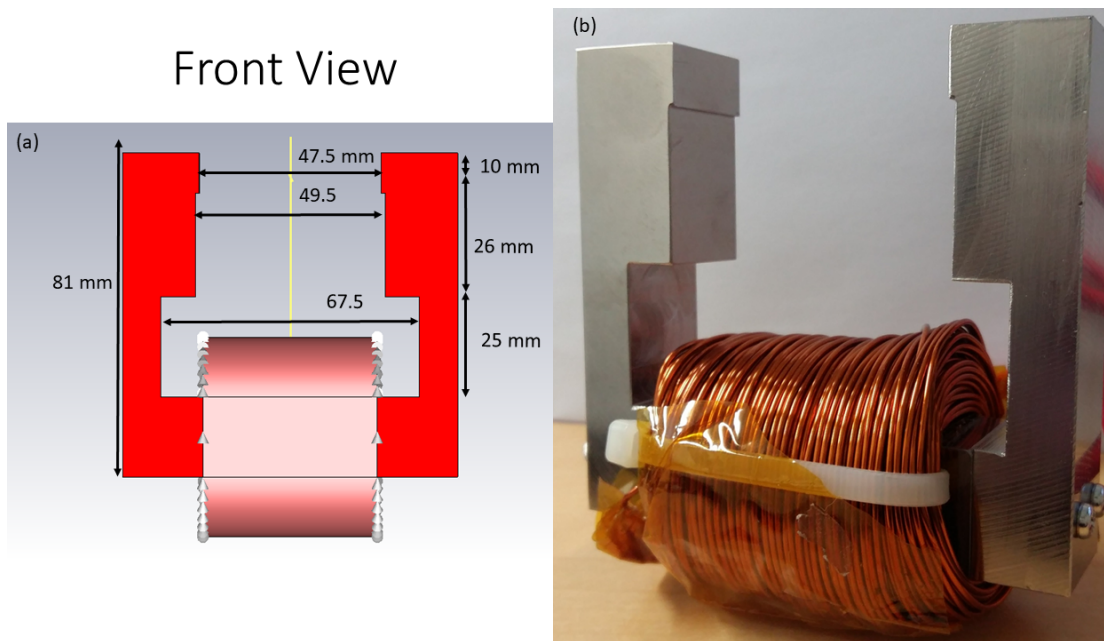


Figure 3.21: Left: The 3-D Model and dimensions of the second dipole magnet. Right: The second dipole magnet.

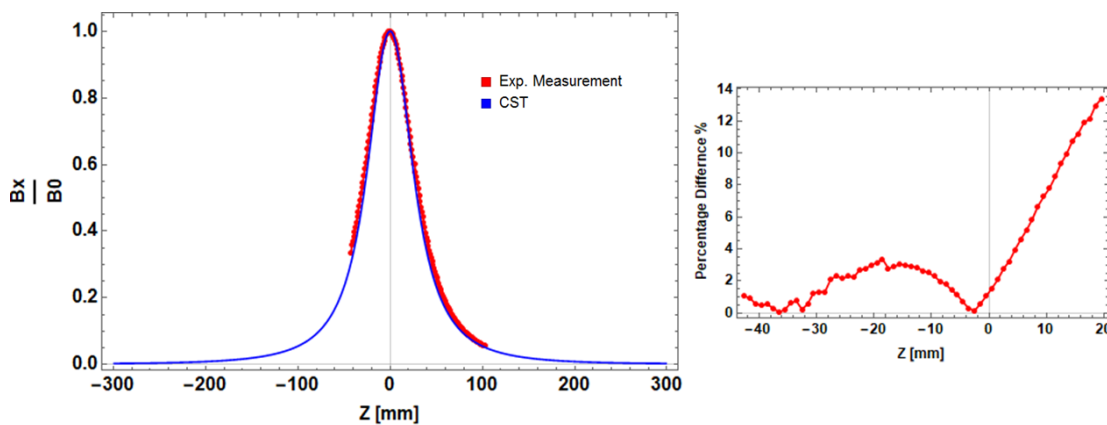


Figure 3.22: Left: The field measurement and CST simulation of second bending magnet. Right: The percentage difference between measured values and CST simulation.

3.8 Storage Magnet

The storage magnet is a solenoid electromagnet placed inside a cylindrical iron yoke of height 800 mm and a diameter of 600 mm, the thickness of iron yoke is 5 mm. The top and bottom sides of the iron yoke are closed by a 20 mm thick iron plate to avoid field leakage from the storage magnet. The iron poles of 120 mm height and thickness 20 mm are placed at the center of the top and bottom iron plates. Both upper and lower iron plates have four viewing windows. Upper windows are used to install CCD-cameras and feed-throughs for wire scanner. The holes on lower iron yoke were used for gas valve, CCD-camera and also to inject the electron beam. The main coil of the storage magnet has 540 turns. A correction coil of 80 turns has been placed at the center of the main coils to produce weak focusing potential. Figure 3.23 left shows the schematic of the storage magnet, and right is a solenoid magnet and vacuum chamber.

Table 3.7: Storage Magnet Parameters.

Parameter	Value
Iron Yoke Height	800 mm
Main Coil Turns	540
Correction Coil Turns	80
Field Strength	82.5 Gauss
Field Index (n)	1.65×10^{-2}

3.8.1 Field Measurement

The magnetic field of the storage magnet has been measured by the *ALPHA LAB INC.* [54] hall probe, with an accuracy of 1%. Figure 3.24 above shows the axial field of the storage magnet along with the vertical position of the storage magnet and below is the radial field of the storage magnet along with the vertical position of the storage magnet. Above: The axial field of the storage magnet along with the vertical position of the storage magnet. The black solid lines are the CST-simulation and color points are the experimental field measurement. The current of the main coil was fixed to 8 A and correction coil current was changed from 0-10 A (opposite polarity to the main coil). As the correction coil's current increases the weak focusing potential increases. Below: The radial field of the storage magnet along with the vertical position of the storage magnet.

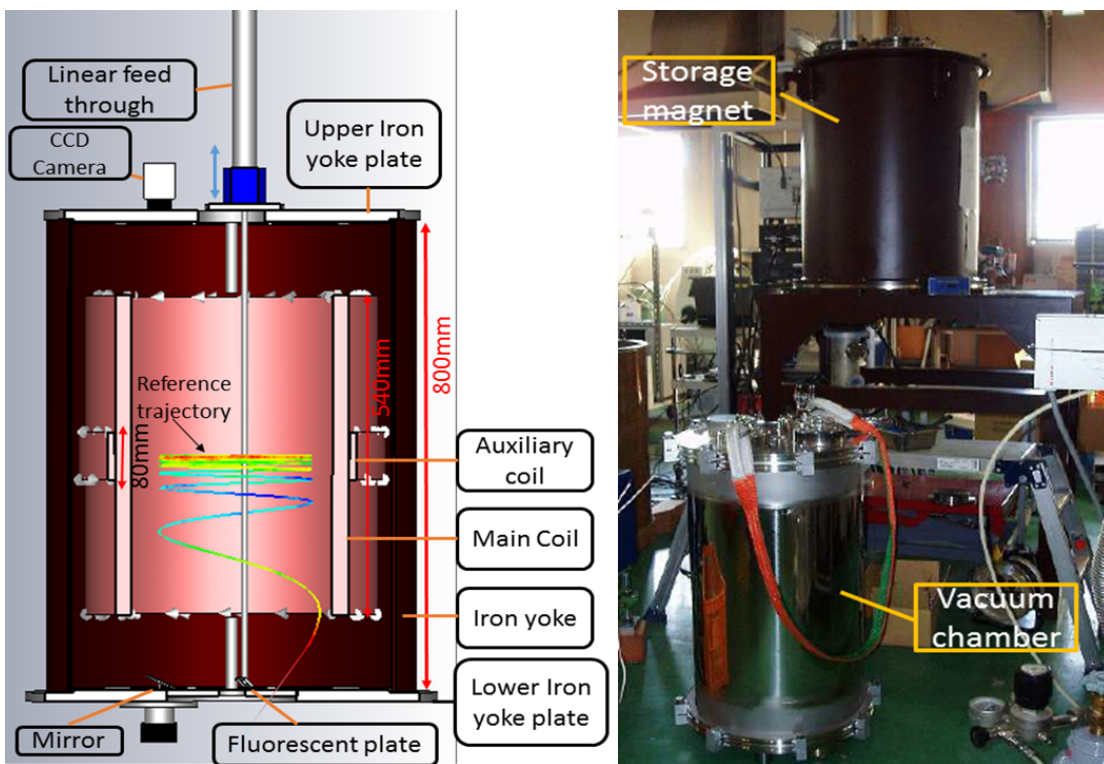


Figure 3.23: Left: Schematic view of storage magnet with reference trajectory and monitors. Right: Storage magnet and vacuum chamber.

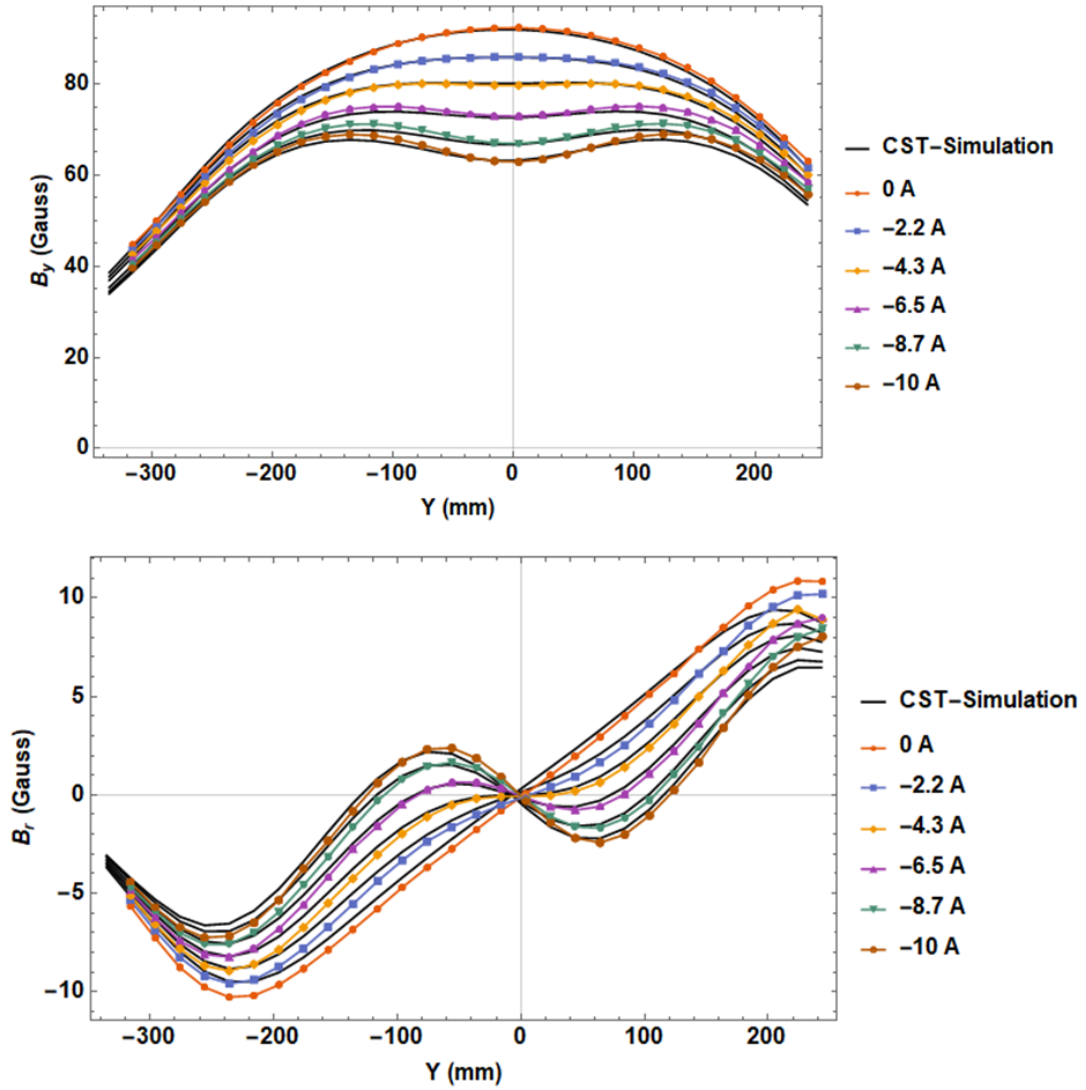


Figure 3.24: Above: The axial field of the storage magnet along with the vertical position of the storage magnet. The black solid lines are the CST-simulation and color points are the experimental field measurement. The current of the main coil was fixed to 8 A and correction coil current was changed from 0-10 A (opposite polarity to the main coil). As the correction coil's current increases the weak focusing potential increases. Below: The radial field of the storage magnet along with the vertical position of the storage magnet.

Chapter 4

Development of Beam Monitors for SITE's Storage Magnet

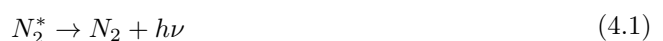
Beam monitoring inside the solenoid-type storage magnet is very challenging due to the mechanical constraints of the solenoid magnet. Two kinds of beam monitors have developed and tested at the SITE

- Gas Monitor: A Gas Monitor (GM) for non-invasive beam monitoring inside the storage magnet is developed. The GM is a robust approach to qualitatively monitor beams inside the storage magnet. It provides information about the beam orbit position, the number of turns, and so on.
- Wire Scanner: The GM is a quick way to monitor the beam inside the storage magnet but it lacks the important quantitative information about the beam position and profile inside the storage magnet. Therefore, a unique wire scanner system has been designed for qualitative beam monitoring inside the solenoid storage magnet.

In this chapter, the detailed principle and development of the beam monitor for the SITE storage magnet will be described.

4.1 Gas Monitor

When the electron beam passes through nitrogen gas, it excites the nitrogen gas molecules. Nitrogen gas de-excitation results in a light emission in the blue wavelength range $390 \text{ nm} < \lambda < 470 \text{ nm}$ [55]. This kind of non-invasive monitor in literature is known as beam-induced fluorescence, gas monitor, or fluorescence Monitor [56, 57]. In this text, we will call it Gas Monitor (GM). The light emission process from the excited nitrogen gas molecule can be written as below:



Where, N_2^* shows the excited nitrogen gas molecule, and N_2 presents the de-excited nitrogen gas molecule after emitting a photon. The photons yield emitted from the gas and beam interaction is given as:

$$Y_\gamma = N_e \frac{dE}{dx} \times \Delta x \times \rho \times \Omega \quad (4.2)$$

Where, N_e is the number of electrons (corresponding to the beam current), $\frac{dE}{dx}$ is the deposit energy in the material[58, 59], Δx is the beam travel distance in the gas, ρ is density of gas, and Ω depends on the optical system. The $\frac{dE}{dx}$, which is the energy loss by ionization [3] can be calculated from the Bathe-Bloch formula as given below:

$$\frac{dE}{dx} = Kz^2 \frac{Z}{A} \frac{1}{\beta^2} \left[\frac{1}{2} \ln \frac{2m_e c^2 \beta^2 \gamma^2 T_{max}}{I^2} - \beta^2 - \frac{\delta(\beta\gamma)}{2} \right] \quad (4.3)$$

The energy loss for the 80 keV electron beam in nitrogen gas is equal to $4.23 \text{ MeV cm}^2/\text{g}$. Fig. 4.1 shows the energy loss of the electron beam in the nitrogen gas. The $\rho = 0.011P$ ($\rho = \frac{1}{R_{spe.T}}$). A beam current of $100 \mu\text{A}$, $\Omega = 8.33 \times 10^{-5}$, and a gas pressure of 0.015 Pa ($1.5 \times 10^{-4} \text{ mbar}$) are assumed. By inserting these values in Eq. (4.2), the number of photons will be:

$$Y_\gamma = 2.90 \times 10^6 \quad (4.4)$$

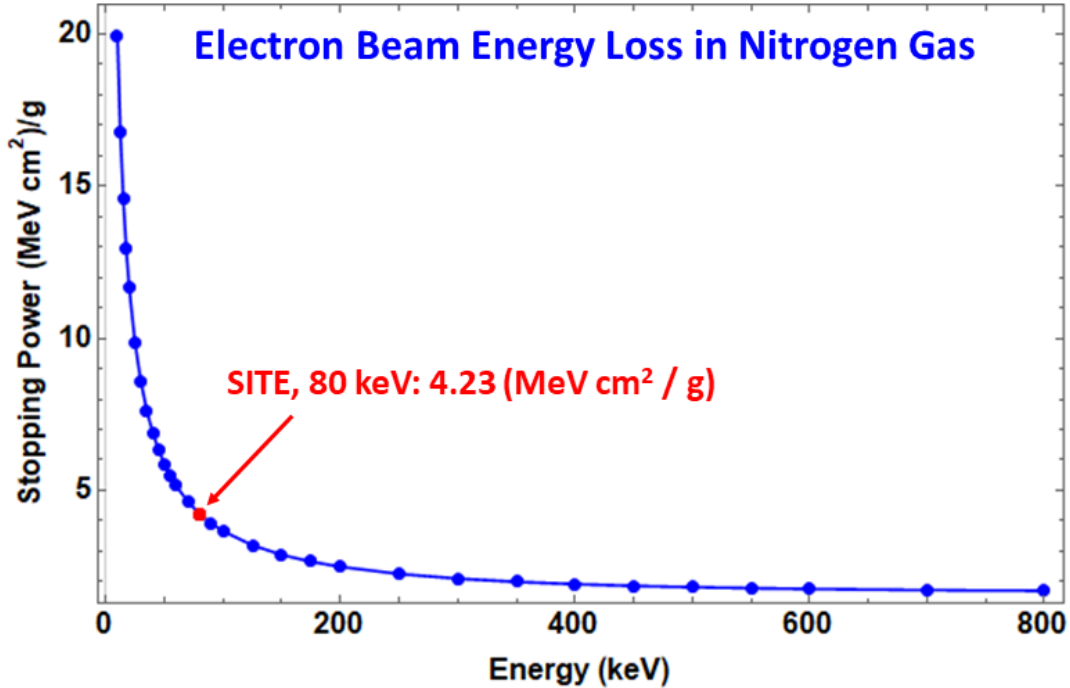


Figure 4.1: The energy loss of the electron beam in nitrogen gas. The red point indicates the energy loss for the 80 keV electron beam.

4.1.1 Gas Monitor Setup

The electron beam leaves the high vacuum region of a pressure of 1.5×10^{-6} mbar through a 3 mm diameter and 5 mm thick stainless steel collimator, into a nitrogen gas dominated medium vacuum region of a pressure of 1.5×10^{-3} mbar. This medium vacuum region consists of a bending section and a storage magnet. This technique of maintaining two different vacuums by a small diameter collimator is known as the differential vacuum pumping. The GM setup comprises a valve for the nitrogen gas inlet [60], a CCD camera to capture photons from the viewing port of nitrogen gas volume along the electron beam path. Figure 4.2 shows the setup of a GM for the SITE.

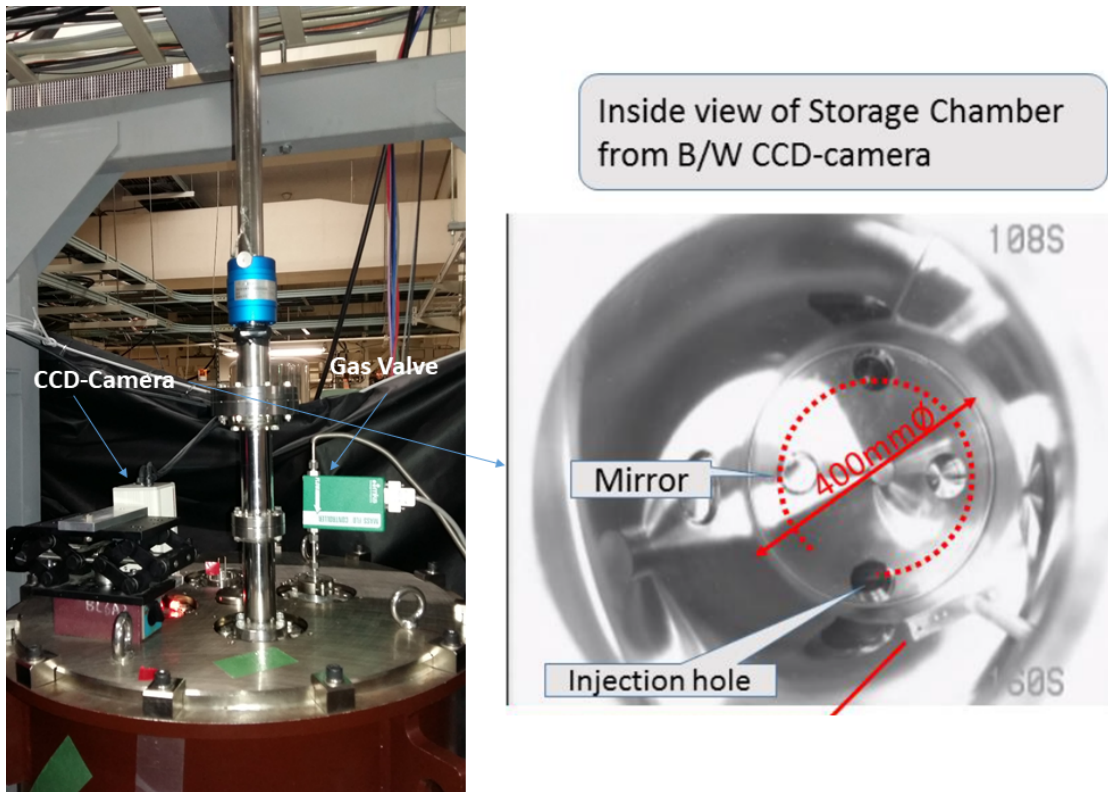


Figure 4.2: The setup of the GM at the top of the storage magnet. The GM consists of the valve for nitrogen gas inlet and CCD camera. The picture on the right shows the inside view of storage magnet's vacuum chamber and the red dotted line corresponds as expected.

4.1.2 Optical System

The light from the nitrogen gas de-excitation was collected by a Hamamatsu 5985 B/W Chilled CCD camera [61]. The lens of F-number 1.8 and focal length 4.8 mm was used [62]. Figure 4.3 shows the configuration of the optical system. The optical system depends on the characteristic of the lens and camera. In Fig. 4.3 G is the object size, which is the diameter of the vacuum chamber, i.e., 400 mm in our case. The g is the minimum object distance and it is the characteristic of the lens, which in case our lens has a value is 0.3 m. B is the image size on

the camera lens. In the case of the Hamamatsu C5985 CCD camera, the sensor size is $1/2''$ (6.4 mm). f' is the focal length of the lens, which can be calculated by the following formula:

$$f' = \frac{g}{\frac{G}{B} + 1} \quad (4.5)$$

The focal length of a lens for a given system depends upon three factors

- Sensor size of the camera
- Minimum object distance
- Object size

The depth of the storage magnet's vacuum chamber is 600 mm. The lens of focal length 4.8 mm and camera specification restrict the view up to 400 mm from the bottom of the vacuum chamber. The possible inside view of the storage magnet vacuum chamber is shown in Fig. 4.4. The gray and blue areas in Fig. 4.4 represent the area of storage magnet, which can be captured by the use optical system.

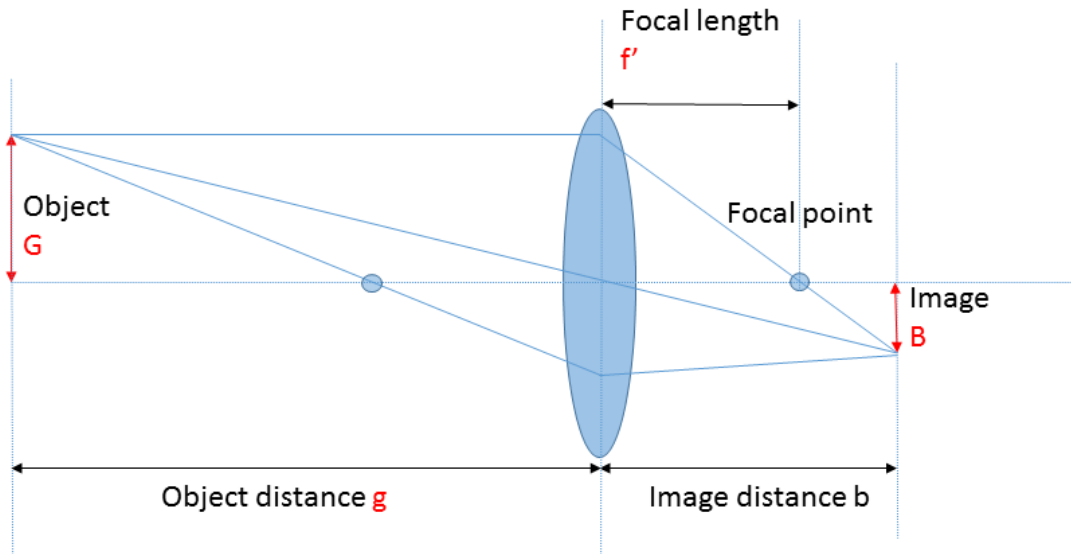


Figure 4.3: Configuration of the optical system.

4.1.3 Light Reflection Suppression

The light reflection from the vacuum chamber's wall and the bottom plate is a big source of background light in the CCD-camera data. The wall of the vacuum chamber was covered with a black sheet to avoid light reflection from the chamber wall. A Light Exclusion Super Black Sheet from SHIBUYA OPTICAL CO., LTD [63] was used to blacken the walls and the bottom plate of the vacuum chamber. As a precaution, the black sheet was not attached directly to the wall of the storage magnet. First, we pasted it on the thin copper sheet (0.5 mm) by Araldite Rapid epoxy [64] and then inserted it inside the storage magnet.

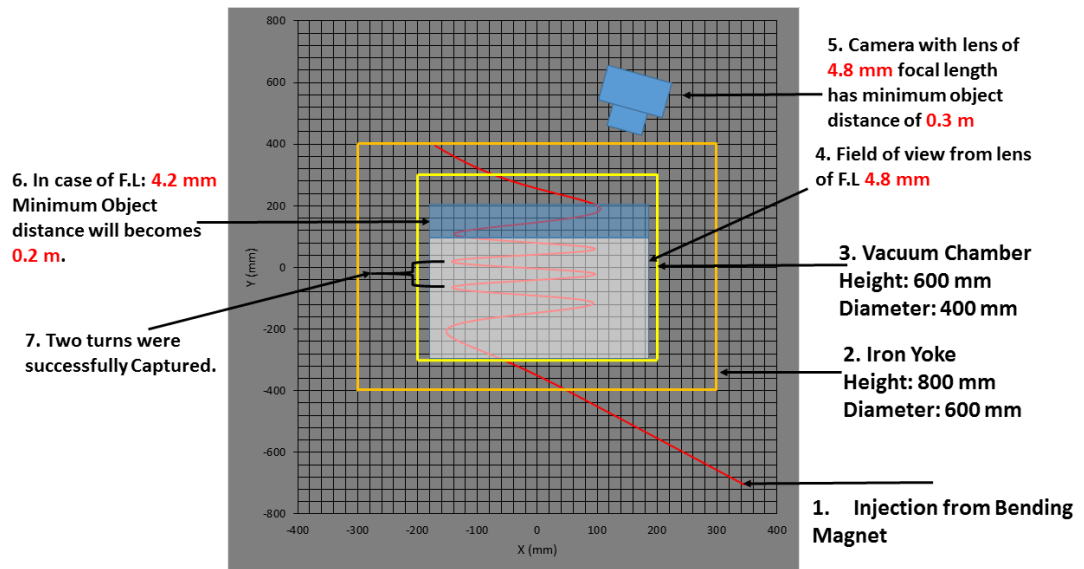


Figure 4.4: Inside view of the storage magnet's vacuum chamber depends upon the characteristics of the lens and camera.

Figure 4.5 shows the black sheet pasted on to thin copper sheet using Araldite Rapid epoxy. Figure 4.6 shows the process of cutting the copper and black sheets and inserting them into the vacuum chamber.



Figure 4.5: Two copper sheets of height (350 mm) had been joined together to make a copper sheet of height 700 mm. The black sheet of height 700 mm and width 1257 mm was attached to the thin copper sheet by Araldite Rapid Epoxy.

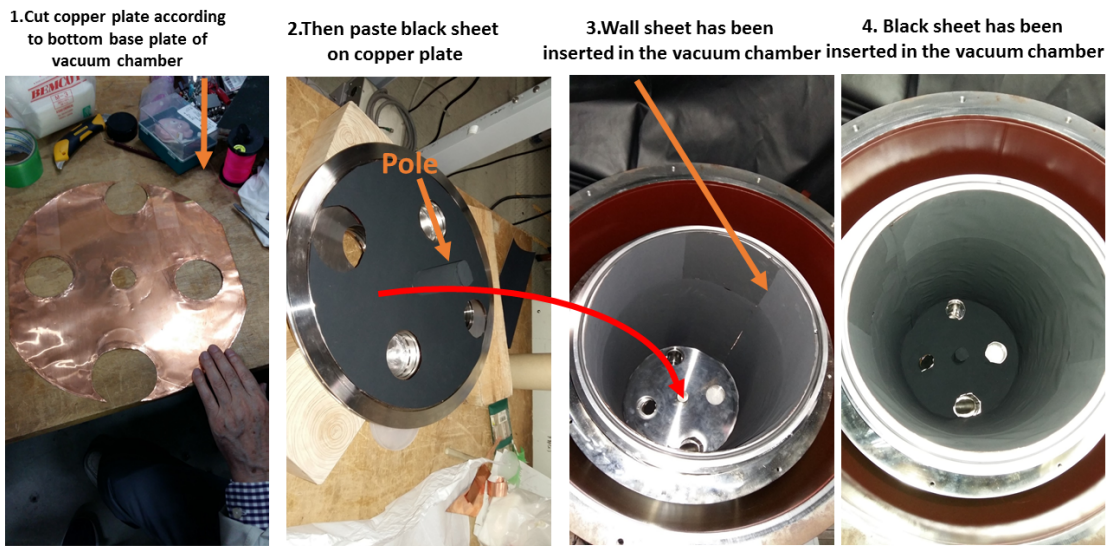


Figure 4.6: The procedure of cutting copper and black sheets, as well as placing the black sheets inside the vacuum chamber.



Figure 4.7: Left: Vacuum chamber without the black sheet. The light reflection from the wall of the vacuum chamber can be seen very clearly. Right: Vacuum chamber with the black sheet. The light reflection suppressed considerably after the insertion of the black sheet.

4.1.4 Performance of the Gas Monitor

The major concern after inserting the black sheet was maintaining the vacuum level of the vacuum chamber. After the black sheet insertion. It was found that, the black sheet did not cause any significant out-gassing in the vacuum chamber. And the vacuum pressure reached the desired value of the vacuum 7.2×10^{-5} mbar within 2 hours.

Figure 4.8 shows the difference between the beam injection with and without the black sheet. In Fig. 4.8 (above) the electron beam enter through the injection hole and takes a spiral path into the storage magnet, the light reflection at the bottom plate of the storage magnet's vacuum chamber can be seen very clearly. This light reflection seems to suppress the original beam signal from the Gas monitor. Figure 4.8 (below) shows the instance of the electron beam injection into the storage magnet with the black sheet insertion at walls of the vacuum chamber. The background light from the reflective surface of the vacuum chamber completely vanishes with the insertion of the black sheet.

Without Black Sheet



With Black Sheet

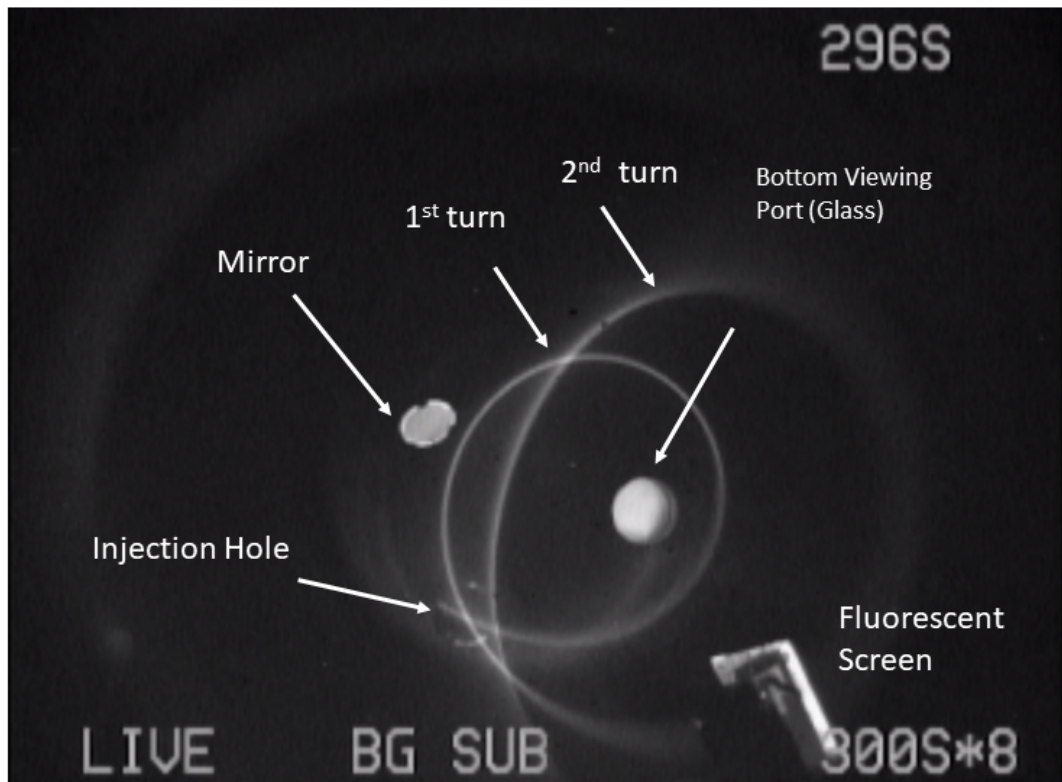


Figure 4.8: Above: The beam injection into the storage magnet without the black sheet. Reflection from the wall of the vacuum chamber is the major source of background. Below: The beam injection into the storage magnet with the black sheet. The background decrease dramatically with black sheet insertion.

4.2 Wire Scanner

The information of the beam vertical and horizontal profiles inside the storage magnet is crucial to confirm the appropriate phase space matching. Therefore, quantitative beam monitoring inside the storage magnet is one of the keys to the successful three-dimensional spiral injection scheme.

The wire scanners are extensively used in the accelerator complex for the transverse beam profile measurement; however, it is the first instance of using such a kind of monitor for the solenoid storage magnet. The mechanical constraints of the solenoid magnet make beam monitoring very challenging. Two-wire scanners of a stroke length of 500 mm were designed and developed to measure the beam profile, position, and evolution in the storage magnet [65]. The forthcoming sections will describe the details of the wire scanner.

4.2.1 Basic Principle and Design of Wire Scanner

In the wire scanner-type monitors, the beam hits the wire and deposits energy into the wire and charges converted to a corresponding current. The voltage across a resistor is proportional to the instantaneous current absorbed in the wire. To measure the transverse beam profile, wires were moved perpendicularly with respect to the beam position, and the beam current was measured at each position.

Two-wire scanners were designed and built for the SITE. Herein, I will refer to them as “wire scanner 1” and “wire scanner 2”. The wire scanner 1 was installed at 2 cm away from the injection point and wire scanner 2 was placed at 180 Degrees (half cyclotron period) away from wire scanner 1 for the beam profile measurement at the half cyclotron period. Wire scanner 1 consists of four horizontal wires and one vertical wire. The horizontal wire was divided into four segments to measure the radial offset of the beam. The horizontal wires were moved vertically to measure the vertical beam profile. One vertical wire is also installed on the wire scanner 1 to measure the horizontal beam profile. To measure the horizontal beam profile, the vertical wire was rotated around the axis of the supporting bar of wire scanner 1. The support bar of the wire scanner was placed at the 12 cm away from the center of the storage magnet.

Figure 4.9 shows the dimensions of the storage magnet vacuum chamber and position of the wire scanner 1 and 2 with respect to the center of the vacuum chamber. These dimensions were used to calibrate the center of the wire scanners and storage magnet. In the case of the SITE, a copper wire of 1 mm diameter was used to measure the horizontal and vertical beam profile. Figure 4.10 presents the concept and mechanics of the wire scanner. Figure 4.11 shows the 3-D model and the actual build of the wire scanner.

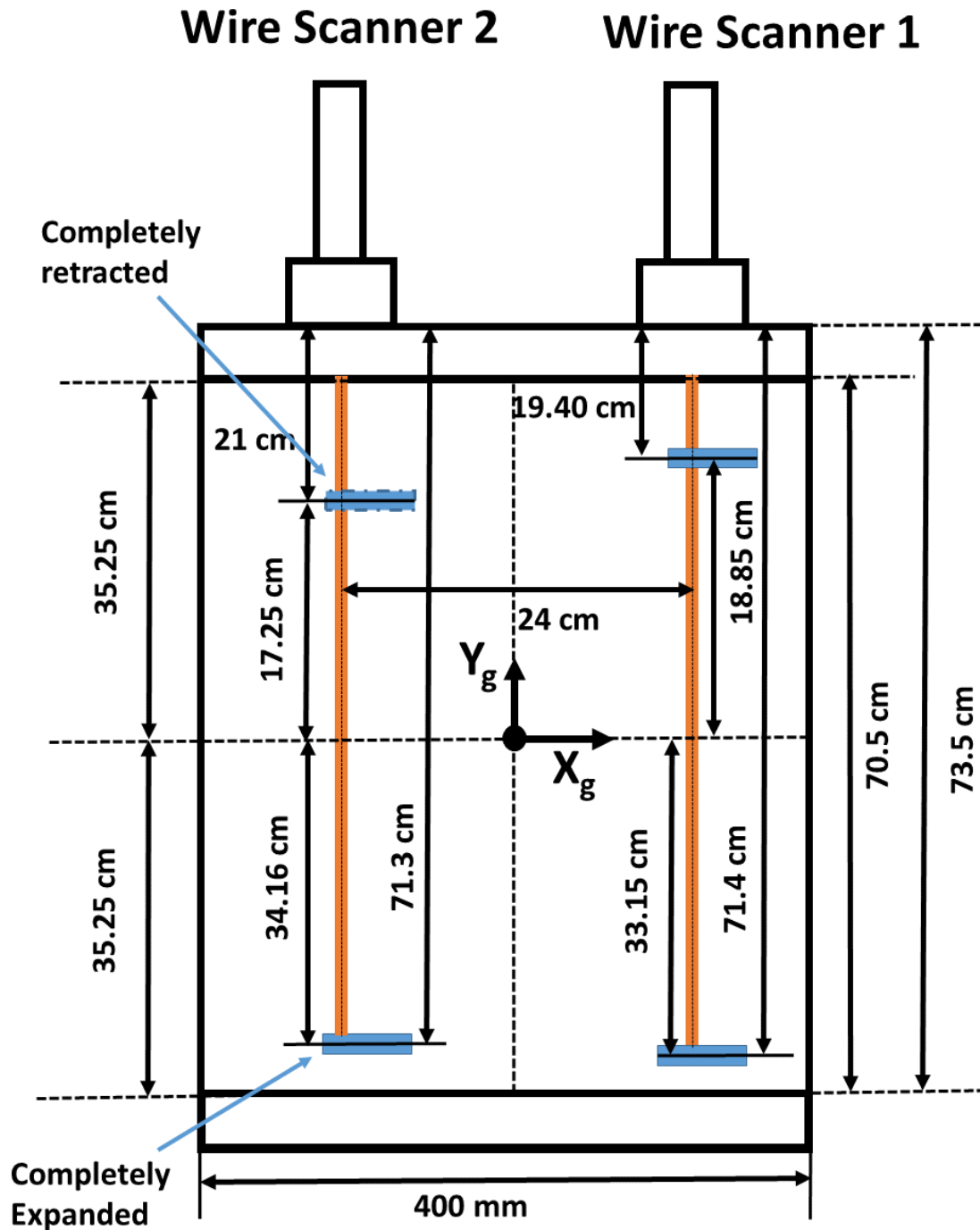


Figure 4.9: The dimensions of the storage magnet vacuum chamber and position of the wire scanner 1 and 2 with respect to the center of the vacuum chamber. These dimensions were used to calibrate the center of the wire scanners and storage magnet.

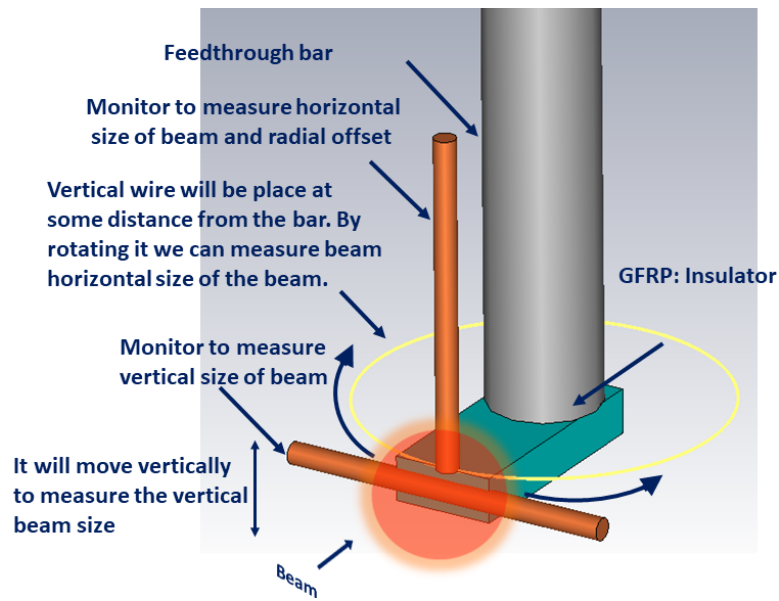
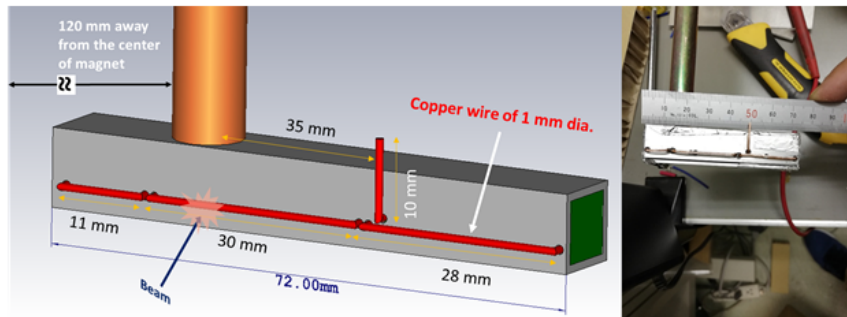


Figure 4.10: The principle and mechanics of the wire scanner.

Wire Scanner 1



Wire Scanner 2

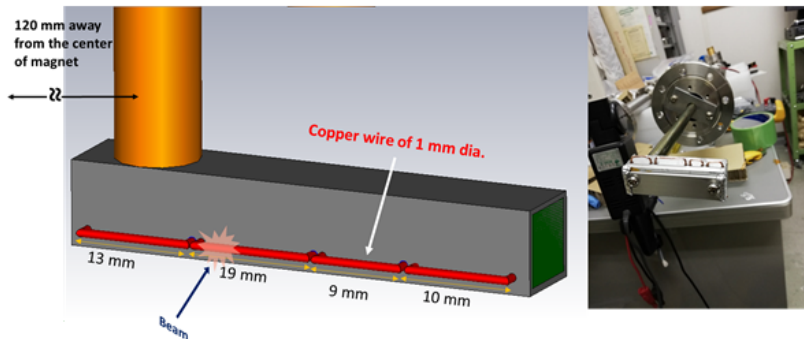


Figure 4.11: Above: Wire scanner 1 consists of four segmented horizontal wire to measure the vertical beam profile and one vertical wire to measure the horizontal beam profile. Below: Wire scanner 2 consists of only four segmented horizontal wires to measure the vertical beam profile.

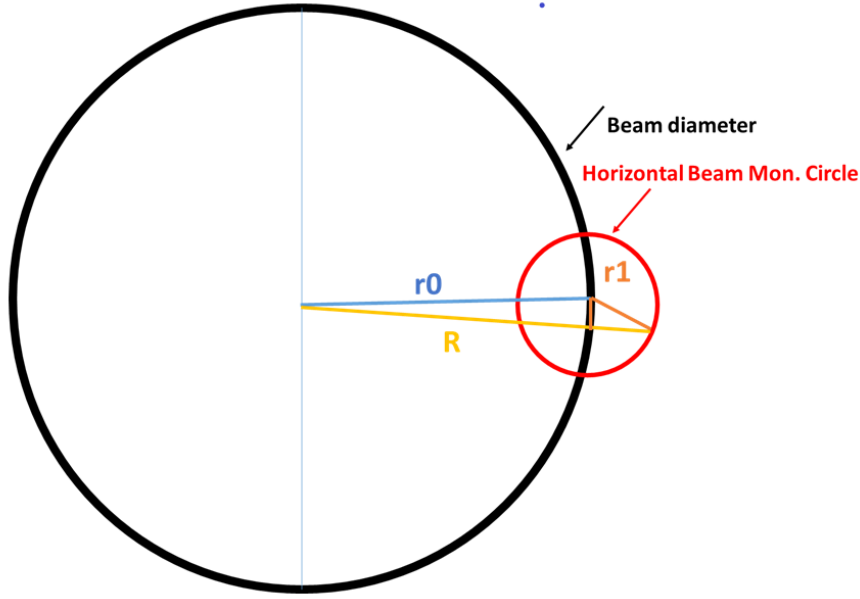


Figure 4.12: The principle of the horizontal beam size measurement. The black circle shows the beam orbit (diameter = 24 cm). The red circle presents the circular path on which vertical wire traverse to measure the horizontal beam profile (diameter = 35 mm). The vertical wire was placed at 35 mm away from the center of the wire scanner 1 support. In order to extract the horizontal beam size the vertical wire was placed at the fixed vertical position, and wire scanner support bar was rotated at its own axis by the rotary actuator. As vertical wire rotates it provides the information of horizontal beam position and horizontal beam size.

The detailed principle of the horizontal beam profile measurement is shown in the Fig. 4.12. The black circle shows the beam orbit (diameter = 24 cm). The red circle presents the circular path on which vertical wire traverse to measure the horizontal beam profile (diameter = 35 mm). The vertical wire was placed at 35 mm away from the center of the wire scanner 1 support. In order to extract the horizontal beam size the vertical wire was placed at the fixed vertical position, and wire scanner support bar was rotated at its own axis by the rotary actuator. As vertical wire rotates it provides the information of horizontal beam position and horizontal beam size. The radial position R of the vertical wire can be computed as follows:

$$\begin{aligned}
 R^2 &= (r_0 + r_1 \cos(\theta))^2 + r_1^2 \sin^2(\theta) \\
 R^2 &= r_0^2 + 2r_0r_1 \cos(\theta) + r_1^2 \\
 R &= r_0 + r_1 \cos(\theta)
 \end{aligned} \tag{4.6}$$

where r_0 is the beam orbit radius and equal to 120 mm, r_1 is a distance of the vertical wire from the beam orbit and equal to the 35 mm. The θ is the angular distance and given as follows:

$$\theta = \sum_{i=1}^n \omega t_i \tag{4.7}$$

Where, ω is the angular velocity of the rotary actuator and equal to the 0.5 Degree/sec. The

summation is over the required range of distance, and t_i is the position of the i th step.

4.2.2 Mechanical Design

The mechanical design of the wires scanners composed of following items:

- Magnetically-coupled Rotary/Linear Vacuum Feedthrough (MRLF) [66]
- A linear actuator for the vertical motion [67]
- A rotary actuator for the rotation of feedthrough [68]
- T-slot aluminum frame
- Electric feedthrough to obtain the current signal of the wire out of the storage magnet

The copper wires of 1 mm diameter were supported by the holes of the GFRP (Glass Fiber Reinforced Epoxy). The wires through the GFRP holes go to the electric feedthrough. The GFRP support for the copper wires was used to keep the copper wires isolated from the rest of the system (to prevent current leakage). The outside of the GFRP was enclosed with metal to prevent charge up due to the beam hit.

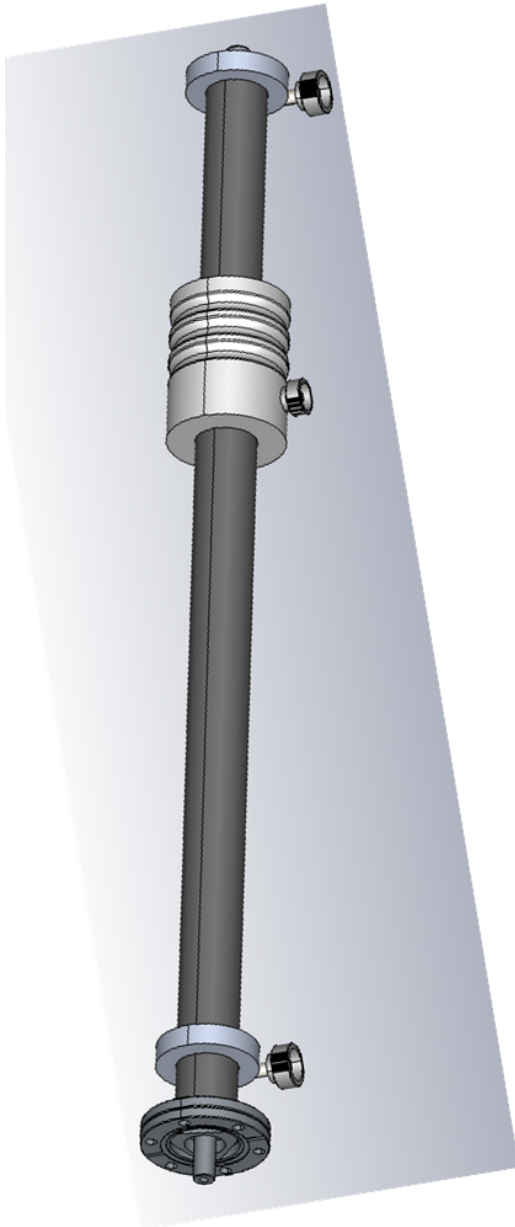
The copper wire and its support box were attached to the hollow copper pipe. The hollow support bar (made of copper) was used to connect copper wires with the electric feedthrough. The support bar was attached to the magnetically-coupled rotary/linear vacuum feedthrough (MRLF) [66] to move wires in the desired directions. Figure 4.13 shows the MRLF used at SITE. The MRLF was attached to a driving system to move the MRLF precisely and remotely during the beamtime.

The deriving system was composed of a linear actuator [67] for the vertical beam profile measurement and a rotary actuator for the horizontal beam profile measurement [68]. Figure 4.14 and 4.15 show the linear and rotary actuator used for the SITE's wire scanner. The schematic view of the wire scanner system is shown in Fig. 4.17. Table 4.1 shows the parameters of the wire scanner. Figure 4.16 shows the linearity between actuator set values and digital scale readout. We confirmed the linearity within the uncertainty of the digital scale readout $\pm 0.5\mu m$.

Table 4.1: Wire Scanner Parameters

Parameter	Value
Number of wire scanners	2
Stroke Length	500 mm
Position Repeatability	0.05 mm
Resolution	1 mm
Wire Diameter	1 mm
Beam Intensity	20-100 μA

Linear feedthrough 3D-model



Linear feedthrough used at SITE

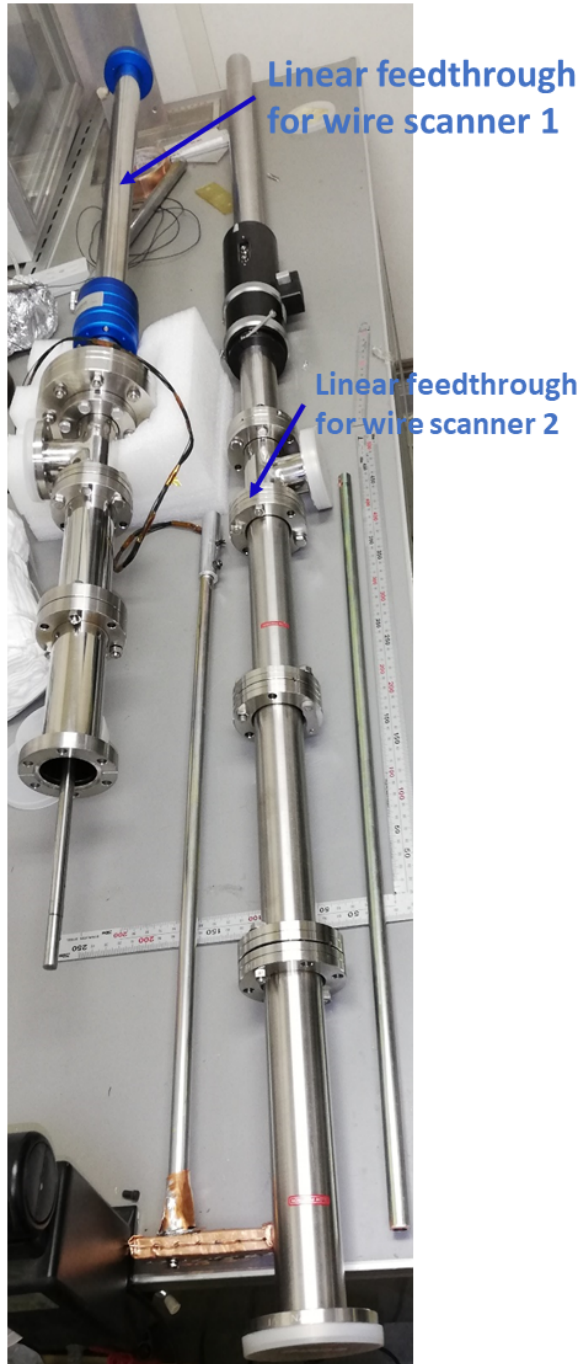


Figure 4.13: Magnetically-coupled Rotary/Linear Feedthrough (MRLF) for the vertical and rotary movement of the wires. On the left is the 3-D model of the MLRF [66] and to the right shows the MRLF used at the SITE.

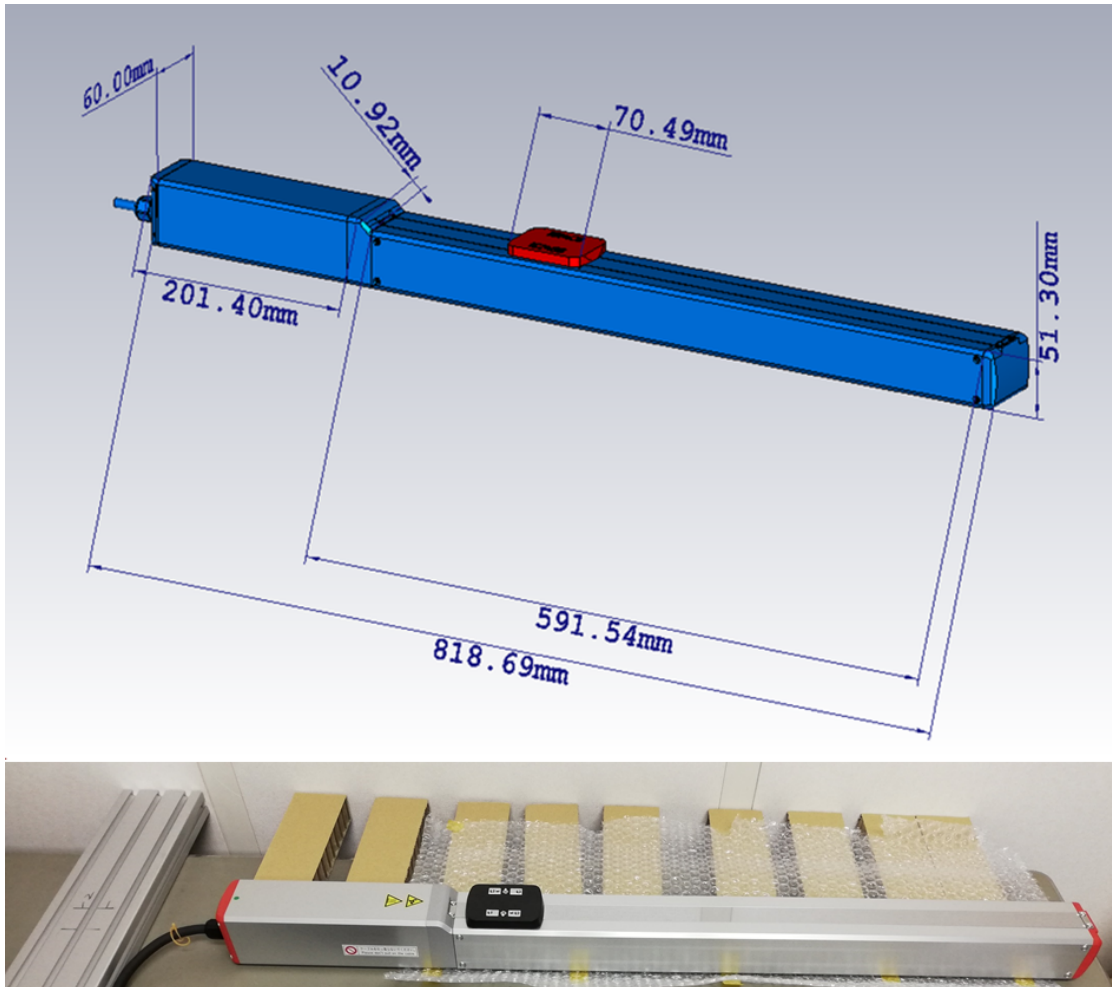


Figure 4.14: Above: The 3-D model of the linear actuator [67]. Below: The linear actuator for the vertical movement of the MRLF.

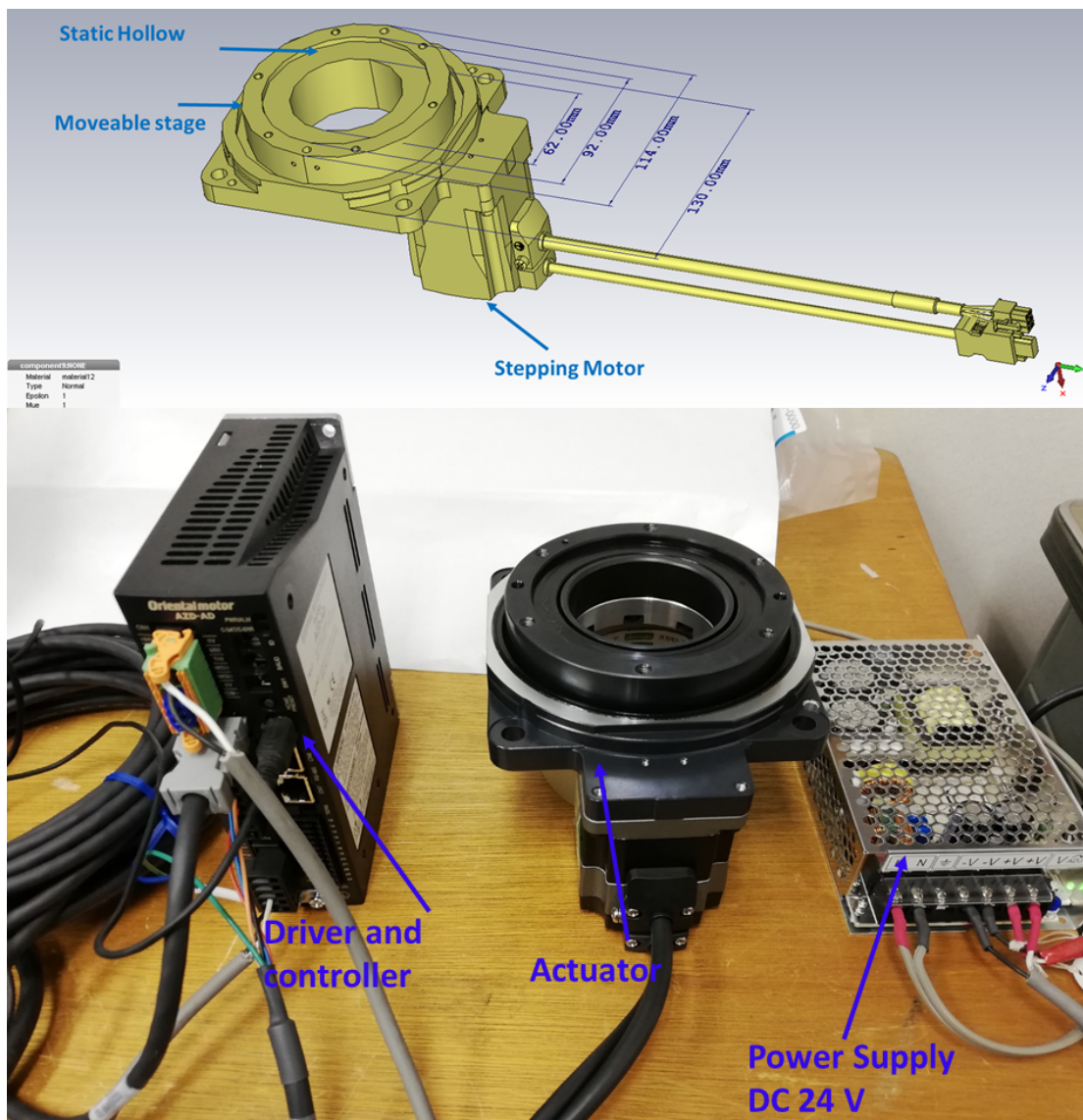


Figure 4.15: The 3-D model of the rotary actuator [68]. The rotary actuator used for the rotation of the MRLF for the horizontal beam size measurement.

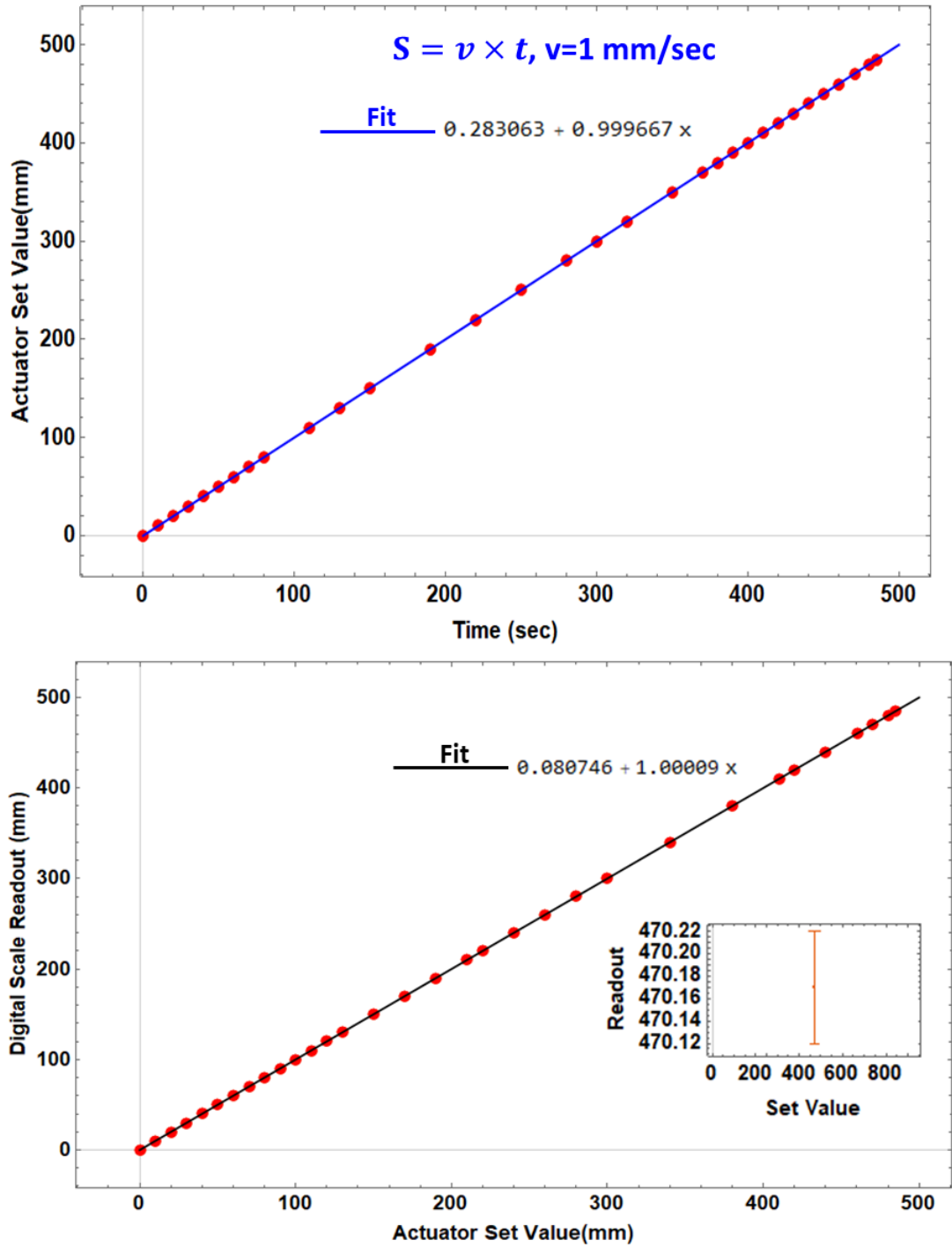


Figure 4.16: Above: The velocity of the actuator was set to 1 mm/sec. To check the linearity, data were taken at different points and fitted with a linear function. Below: Actuator set values versus digital scale readout. To check the linearity between the set value and readout, data was taken. The set values and readout values agree well within the uncertainty of the digital readout system ($\pm 50 \mu\text{m}$).

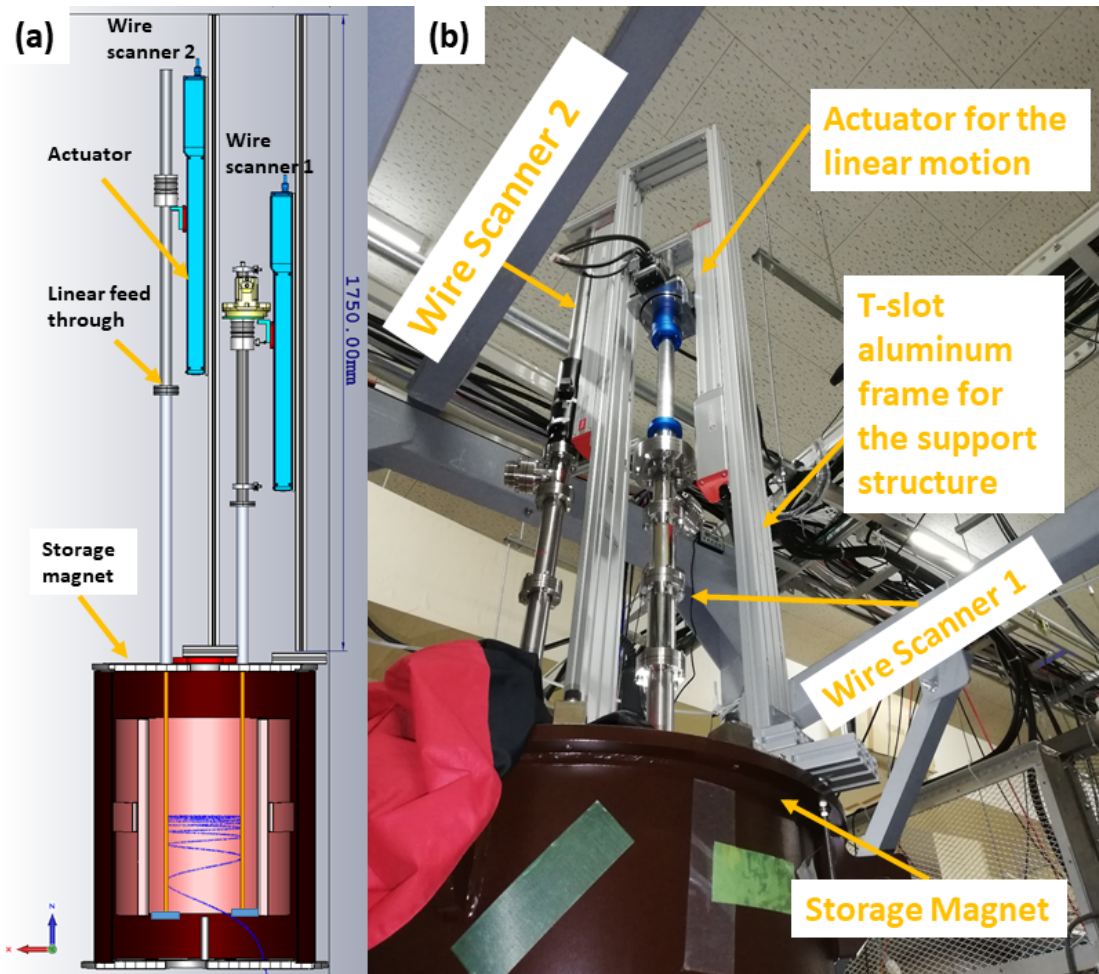


Figure 4.17: (a) Schematic of the two-wire scanner setup. (b) Wire scanner system on the top of the storage magnet.

4.2.3 Data Acquisition System

The signal from the wires was taken out of the vacuum chamber via vacuum feedthroughs and terminated into the 1 M Ω terminal of an oscilloscope. The Tektronix DPO 7104 (1 GHz) oscilloscope was used [69]. A GUI¹ C# program was developed in Microsoft Visual Studio [70] to log the data from the wire scanner. The vertical and rotary actuators were controlled by their respective programs provided by the vendor. This program also features online plotting during the beam test. The control system layout of the for the actuator and oscilloscope is shown in Fig. 4.18. Figure 4.19 is the screenshot of the oscilloscope control program. Figure 4.20 presents the beam current at the wire as a function of the cathode's heater current of the electron gun. During the beam operation electron gun was operated in temperature limited regime, therefore the beam current increase as a function of the cathode's heater current. The electron gun was operated at the cathode's heater current in the range 0.72-0.80 A due to radiation and thermal safety point of view. Under this region a good linearity between cathode's heater current and the beam current at the wire can be seen from the Fig. 4.20.

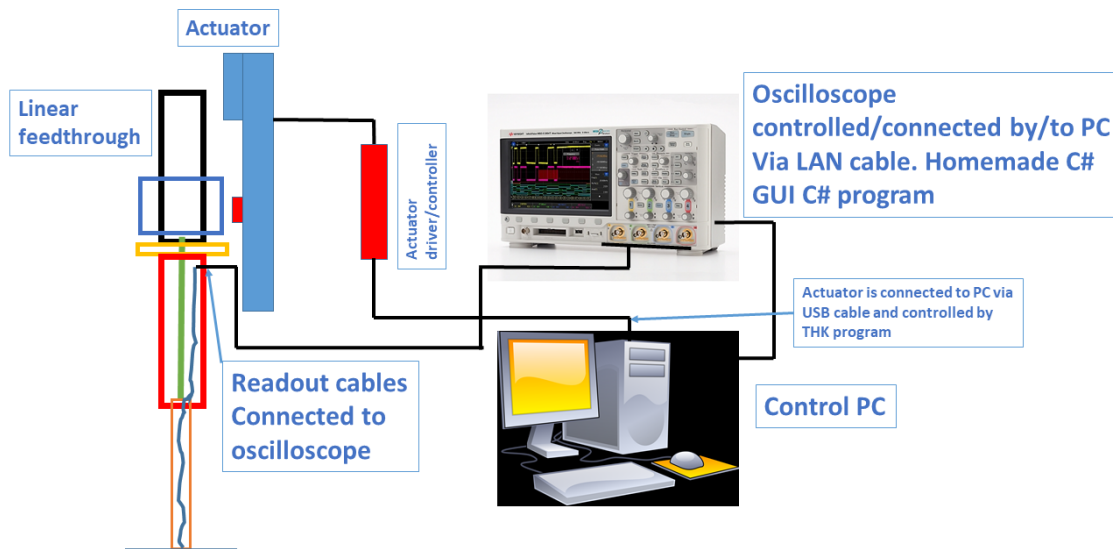


Figure 4.18: The control system layout for the actuator and wire scanner.

¹Graphical User Interface

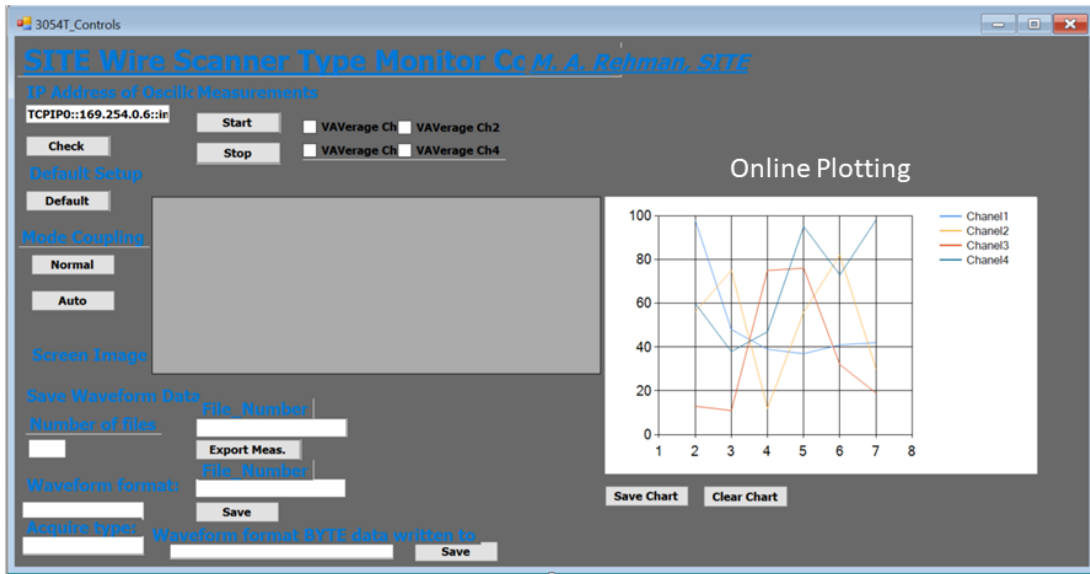


Figure 4.19: The screenshot of the oscilloscope control program. This program was used for the wire scanner data online plotting and data logging.

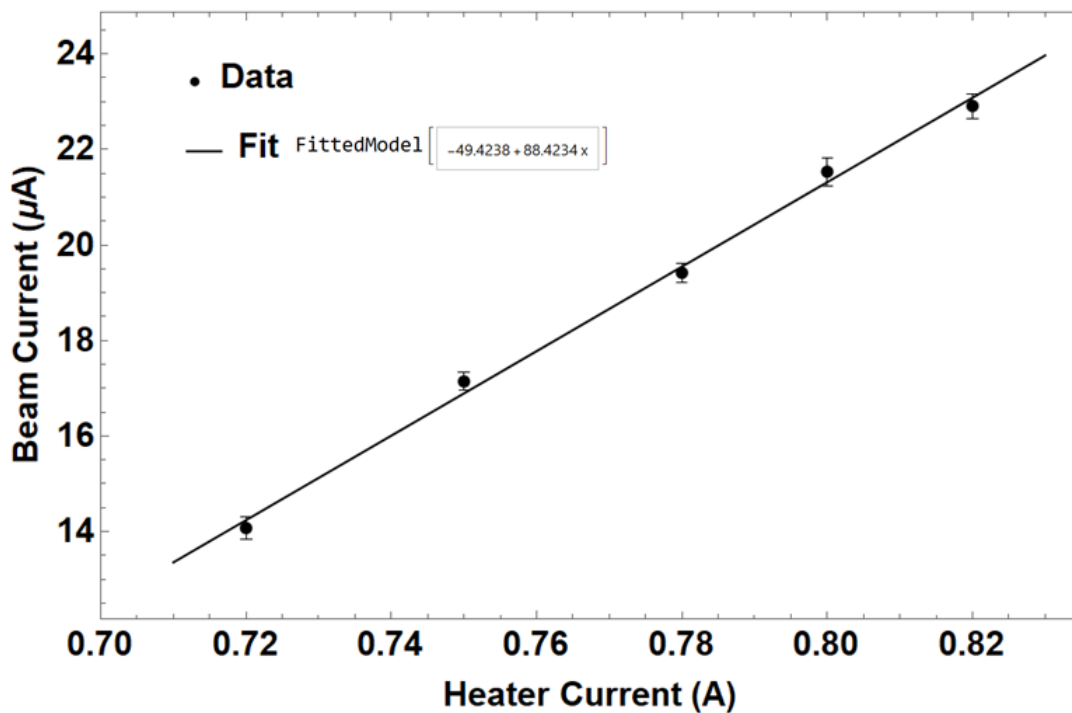


Figure 4.20: The beam current at the wire as a function of the cathode's heater current of the electron gun.

Chapter 5

Beam Commissioning with DC Beam

This chapter will describe the basic beam studies conducted at SITE.

5.1 Emittance Measurement By Quadrupole Scan

The charged particle emittance is a measure of beam size and beam divergence angle. Hence, it is necessary to measure this figure of merit to describe charged particle beam quality. In this Chapter, a well-known quadrupole scan technique will be described to measure the emittance of the beam.

In the quadrupole scan technique, the beam size is changed by varying the strength of the quadrupole magnet [71]. To determine beam emittance at the point P_0 , a beamline with one quadrupole magnet and a one screen monitor ¹ at the location P_1 is needed. The transformation of sigma matrix is as follows:

$$\sigma_1 = M\sigma_0M^T \quad (5.1)$$

Where, σ_0 is the beam matrix at the location P_0 and σ_1 corresponds to the location P_1 and M is a transport line matrix from point P_0 to P_1 . The full 4×4 beam matrix (σ) is given as:

$$\sigma = \begin{pmatrix} \sigma_{11} & \sigma_{12} & \sigma_{13} & \sigma_{14} \\ \sigma_{21} & \sigma_{22} & \sigma_{23} & \sigma_{24} \\ \sigma_{31} & \sigma_{32} & \sigma_{33} & \sigma_{34} \\ \sigma_{41} & \sigma_{42} & \sigma_{43} & \sigma_{44} \end{pmatrix} = \begin{pmatrix} \sigma_{xx} & \sigma_{xy} \\ \sigma_{xy}^T & \sigma_{yy} \end{pmatrix} \quad (5.2)$$

The terms σ_{xy} and σ_{xy}^T represents the inter plane coupling. In Section 5.4 inter plane terms will be treated in detail. In this section, I will treat horizontal and vertical planes completely

¹In the case of SITE, OTR (Optical Transition Radiation) from a 0.1 mm thick sheet of copper was used to observe the transverse beam size.

independent. Therefore, σ_{xy} and σ_{xy}^T will vanish. Hence, the horizontal and vertical terms in Eq. (5.1) can be written independently as follows:

$$\sigma_{xx} = \begin{pmatrix} \langle x^2 \rangle & \langle xx' \rangle \\ \langle x'x \rangle & \langle x'^2 \rangle \end{pmatrix}, \quad \sigma_{yy} = \begin{pmatrix} \langle y^2 \rangle & \langle yy' \rangle \\ \langle y'y \rangle & \langle y'^2 \rangle \end{pmatrix} \quad (5.3)$$

In Eq. (5.1), M is the transport line matrix and M^T is the transpose of M . In the case of one quadrupole and drift space, M will be:

$$M = D.Q_F \quad (5.4)$$

Where, Q_F is the transfer matrix of the quadrupole in the focusing direction and D is the drift space transfer matrix.

$$Q_F = \begin{pmatrix} \cos(\sqrt{k}l_q) & \frac{\sin(\sqrt{k}l_q)}{\sqrt{k}} \\ -\sqrt{k}\sin(\sqrt{k}l_q) & \cos(\sqrt{k}l_q) \end{pmatrix}, D = \begin{pmatrix} 1 & d \\ 0 & 1 \end{pmatrix} \quad (5.5)$$

The M will become:

$$M = \begin{pmatrix} m_{11} & m_{12} \\ m_{21} & m_{22} \end{pmatrix} = \begin{pmatrix} \cos(\sqrt{k}l_q) - d\sqrt{k}\sin(\sqrt{k}l_q) & d\cos(\sqrt{k}l_q) + \frac{\sin(\sqrt{k}l_q)}{\sqrt{k}} \\ -\sqrt{k}\sin(\sqrt{k}l_q) & \cos(\sqrt{k}l_q) \end{pmatrix} \quad (5.6)$$

Where, $k[m^{-2}]$ is the strength of Q_F , $l_q[m]$ is the effective length of Q_F and d is a distance from Q_F to the screen monitor. Then substituting Eq. (5.6) and (5.2) in Eq. (5.1) will results $\sigma_{1,11}$ as follows:

$$\sigma_{1,11} = m_{11}^2\sigma_{0,11} + 2m_{12}m_{11}\sigma_{0,12} + m_{12}^2\sigma_{0,22} \quad (5.7)$$

Where, m_{11} and m_{12} are the matrix elements, as shown in Eq. (5.6). Rewriting Eq. (5.7) in terms of the matrix elements m_{11} and m_{12} gives:

$$\sigma_{1,11} = \left(\cos(\sqrt{k}l_q) - d\sqrt{k}\sin(\sqrt{k}l_q) \right)^2 \sigma_{0,11} + 2 \left(\cos(\sqrt{k}l_q) - d\sqrt{k}\sin(\sqrt{k}l_q) \right) \left(d\cos(\sqrt{k}l_q) + \frac{\sin(\sqrt{k}l_q)}{\sqrt{k}} \right) \sigma_{0,12} + \left(d\cos(\sqrt{k}l_q) + \frac{\sin(\sqrt{k}l_q)}{\sqrt{k}} \right)^2 \sigma_{0,22} \quad (5.8)$$

The emittance and Twiss parameters can be measured at the location P_0 by measuring the beam size at P_1 ($\sigma_{1,11}$: Beam size squared) as a function of the quadrupole magnet strength and then fitting it with Eq. (5.8). The $\sigma_{0,11}$, $\sigma_{0,12}$, and $\sigma_{0,22}$ will be extracted from the fitting function and then the corresponding emittance (ϵ_0) and Twiss ($\beta_0, \alpha_0, \gamma_0$) parameters at the location P_0 can be computed as follows:

$$\epsilon_0 = \sqrt{\sigma_{0,11}\sigma_{0,22} - \sigma_{0,12}^2} \quad (5.9)$$

$$\beta_0 = \frac{\sigma_{0,11}}{\epsilon_0} \quad (5.10)$$

$$\alpha_0 = -\frac{\sigma_{0,12}}{\epsilon_0} \quad (5.11)$$

$$\gamma_0 = \frac{\sigma_{0,22}}{\epsilon_0} \quad (5.12)$$

The error propagation for emittance is as follows:

$$\delta\epsilon = \pm \frac{1}{2} \sqrt{\frac{4 |\delta\sigma_{12}\sigma_{12}|^2 - \delta\sigma_{22}^2\sigma_{11}^2 + \delta\sigma_{11}^2\sigma_{22}^2}{\sigma_{11}\sigma_{22} - \sigma_{12}^2}} \quad (5.13)$$

Where, $\delta\epsilon$ is the emittance error. $\delta\sigma_{11}$, $\delta\sigma_{12}$, and $\delta\sigma_{22}$ represent the errors on the beam matrix element.

5.2 Emittance Measurement at SITE Beamline

Three quadrupole magnets had been placed after the collimator for the phase space matching. These quadrupole magnets also have been used to measure the emittance of the beam after the collimator. The beam profile monitor consists of a copper plate and CMOS-camera. When the electron beam hits the copper plate placed at 45 Degree with respect to the beam, optical transition radiation (OTR) arises at the surface of the copper plate due to the motion of a charged particle beam from the vacuum to the metal. The OTR from the copper was observed by the CMOS-camera [72]. The beam profile monitor setup is shown in Fig. 5.1 (a). The distance of the quadrupole magnets from the beam profile monitor are also shown in Fig. 5.1 (a). Figure 5.1 (b) represents the cross section of the quadrupole magnet. The bore radius of quadrupole magnets is 25 mm and effective length is 56 mm.

5.2.1 Image Analysis

The beam images from the CMOS-camera as a function of the quadrupole strength were saved on PC. A Mathematica [37] program has been developed to extract the beam size information from the picture data. The following steps have been done to analyze the beam profile from the images:

- Convert RGB data to Grayscale
- Measure beam profiles across vertical or horizontal pixels
- Remove background from beam profile data
- Measure RMS size

Figure 5.3 (a) shows a raw picture of beam profile from copper plate taken by the CMOS-camera without applying any quadrupole magnet. Figure 5.3 (b) is the conversion of Fig. 5.3 (a) RGB to the Grayscale for further analysis. Figure 5.2 shows the copper plate used to observe the beam profile (via OTR). The horizontal and vertical lines were drawn on

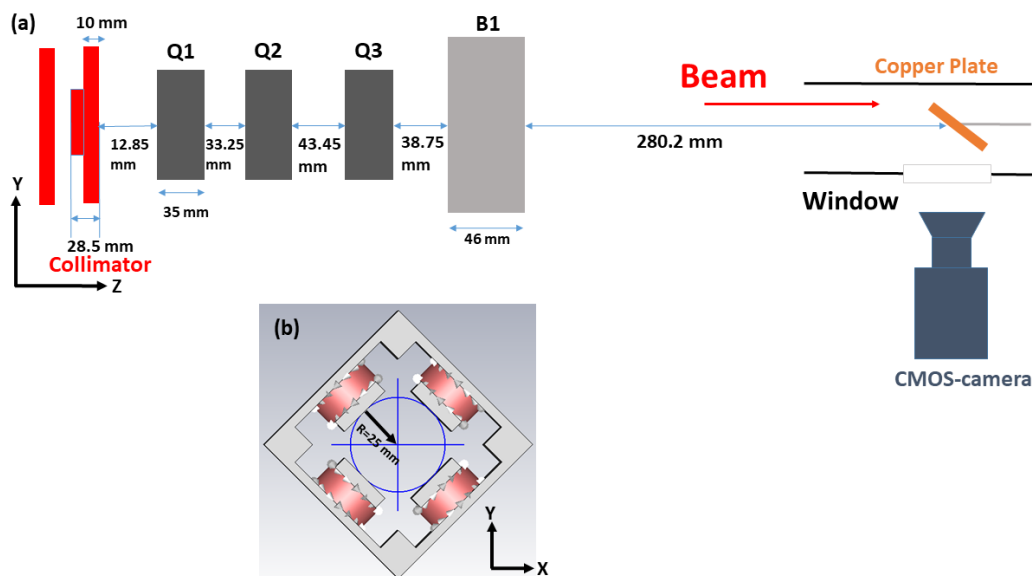


Figure 5.1: (a) The quadrupole scan setup. The quadrupole scan had been done with all three quadrupoles independently. (b) The cross section of the quadrupole magnet. The bore radius of quadrupole magnet is 25 mm and effective length is 56 mm.

the copper plate in order to determine the conversion factor from the pixels data of the photo to the millimeter. The conversion factor from pixels to mm can be obtained by dividing the number of pixels into horizontal and vertical directions to the known distance in millimeters. The conversion factor from pixels to mm was 10 ± 0.2 Pixels/mm in both transverse planes.

Figure 5.4 is an illustration of the analysis process. Figure 5.4 (a) and (b) represents the beam images with vertical and horizontal focus respectively. And Fig. 5.4 (c) and (d) are the slice (contains 10 pixels) of horizontal and vertical projections to obtain a transverse beam profile. The apparent tilted beam profile in Fig. 5.4 (d) is due to the rotation of (± 5) Degree of screen monitor itself. For coupling measurement (section 5.4) we corrected the screen monitor tilt to ± 1 Degree.

It is necessary to remove the background from the beam profile data in order to measure the RMS beam size. The background was estimated from the slope fit. The green highlighted curve in Fig. 5.4 (c) and (d) indicated the area selected for the RMS beam size measurement. Figure 5.5 shows the change in RMS beam size due to the different level of the background. This kind of change will cause ± 0.004 [mm] and ± 0.005 [mm] of systematic error to vertical and horizontal beam sizes respectively.

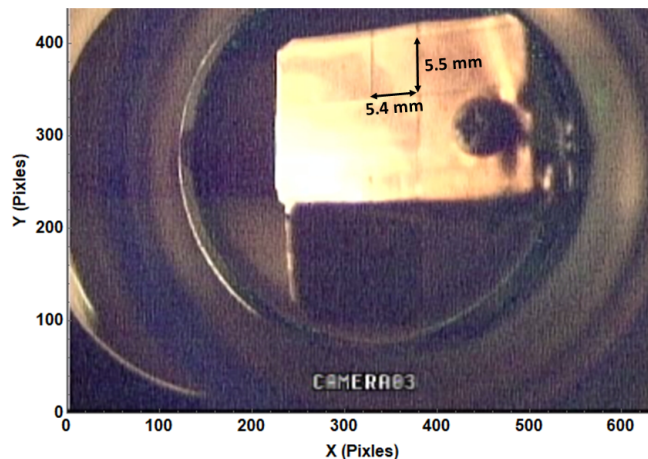


Figure 5.2: The copper plate used to observe the beam profile (via OTR). The horizontal and vertical lines were drawn on the copper plate in order to determine the conversion factor from the pixels data of the photo to the millimeter.

5.2.2 Misalignment of Quadrupole Magnets

The quadrupole magnet had been aligned on the beamline by Laser Survey meter. In order to know the misalignment of the quadrupole magnets precisely with the beam, a so-called beam-based alignment method can be used. In the beam based alignment of the quadrupole magnet method, the position shift of the transverse beam profile as a function of the quadrupole magnets strength was obtained from the beam profile monitor. And the misalignment of the quadrupole magnets can be estimated from the information of the beam shift on the screen monitor as a function of the quadrupole magnet strength.

Due to the quadrupole magnet misalignment an error dipole field produced. The angular kick to the beam due to the quadrupole magnet misalignment of distance Δd is given as [73]:

$$\theta = \frac{gl}{B\rho} \Delta d = \frac{\Delta d}{f} \quad (5.14)$$

Where, g is the quadrupole magnet field gradient, $B\rho$ is the magnetic rigidity, f is focal length and l is effective length of the quadrupole magnet. If one knows the effective angular kick due to the misalignment then the Eq. (5.14) can be written as:

$$\Delta d = \frac{\theta B\rho}{gl} = \theta f \quad (5.15)$$

Figure 5.6 shows the beam position shift due to the quadrupole magnet misalignment error. Each measurement was repeated 10 times. The black points represent the weighted average of data points. And the red line is the linear fit to the data. Table 5.1 and 5.2 are showing the effective kick and misalignment of Q1-Q3 in vertical and horizontal direction respectively.

From this study we found that quadrupole magnet are miss aligned within ± 1 mm. And this small misalignment does not cause any significant effect on beam. Furthermore, horizontal and

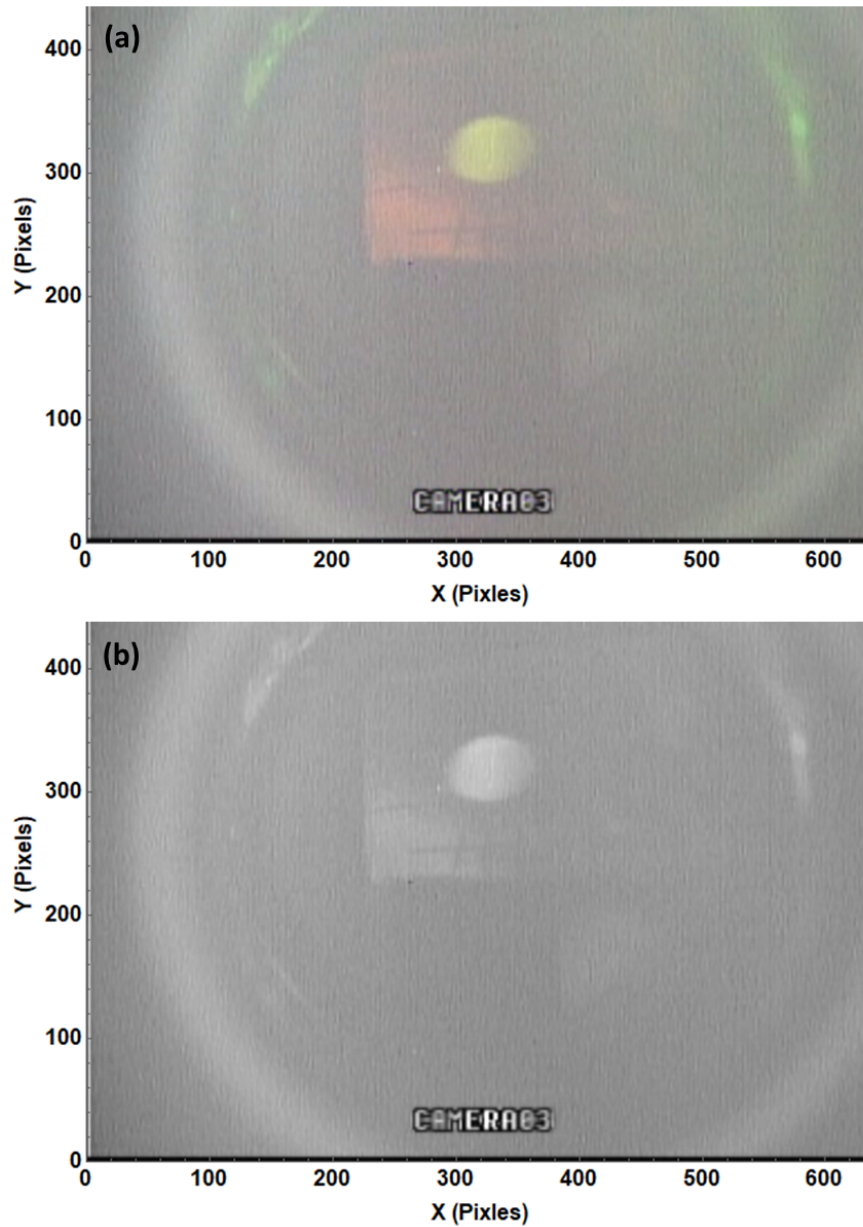


Figure 5.3: (a) A raw picture from the CMOS-camera without applying any quadrupole magnet. (b) The above figure converted from RGB to the Grayscale for further analysis. The conversion factor from pixels to mm is 10 Pixels/mm in both transverse planes.

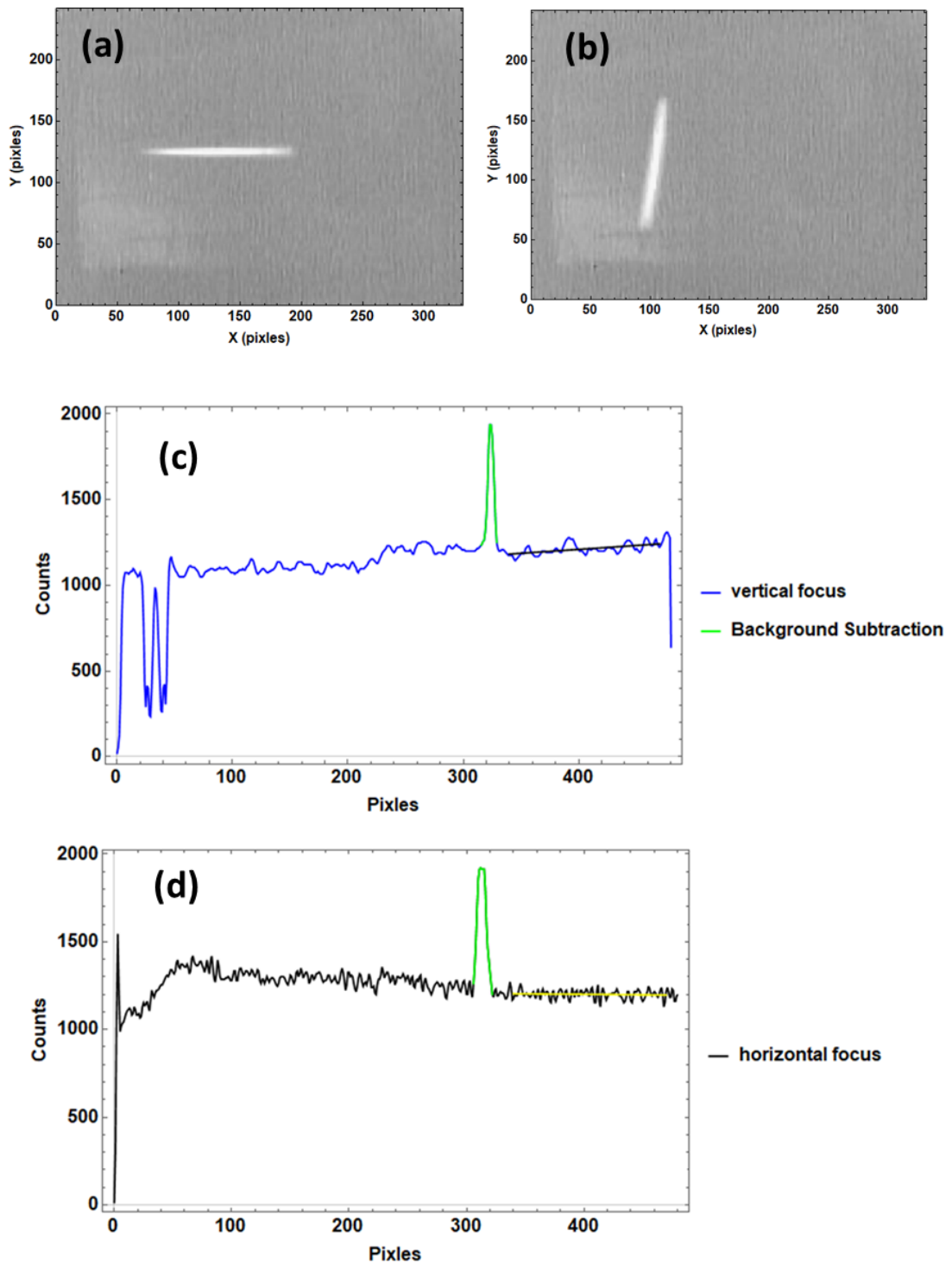


Figure 5.4: (a) and (b) are the beam profiles in the vertical and horizontal focus respectively. (c) and (d) represents the beam profile data for vertical and horizontal planes.

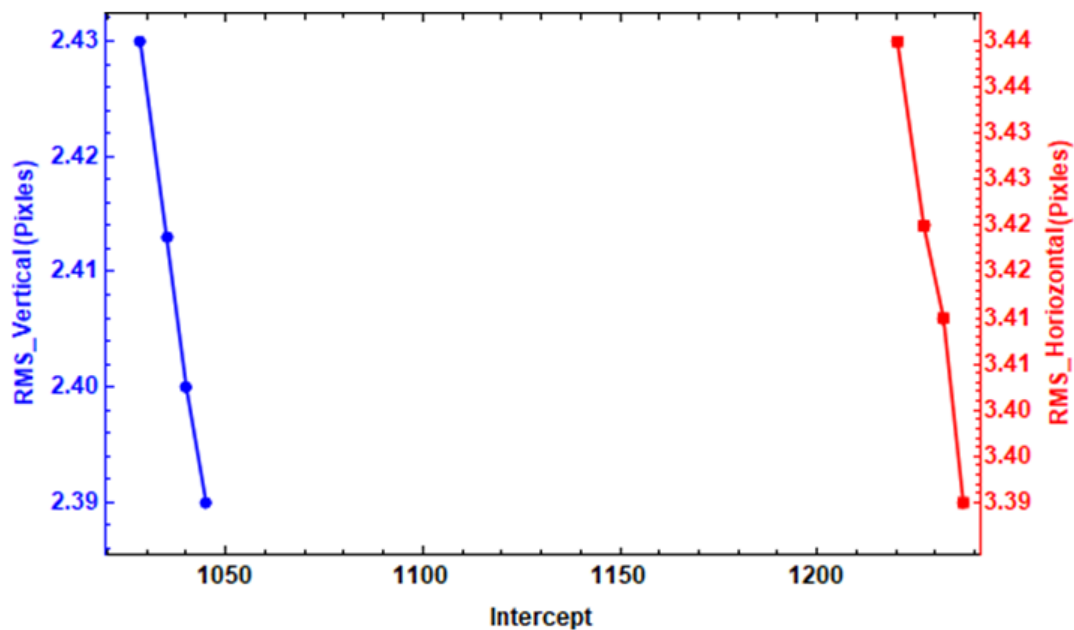


Figure 5.5: The change in RMS beam size due to the different level of the background.

vertical steering coils had been placed after the quadrupole magnets to compensate the effect of the quadrupole magnets misalignment.

Table 5.1: The Quadrupole Magnets Vertical Misalignment.

Quadrupole Magnet	θ [mrad]	Δd [mm]
Q1	2.25	0.38
Q2	5.86	0.94
Q3	5.13	0.78

Table 5.2: The Quadrupole Magnets Horizontal Misalignment.

Quadrupole Magnet	θ [mrad]	Δd [mm]
Q1	4.74	0.80
Q2	0.11	0.018
Q3	3.67	0.56

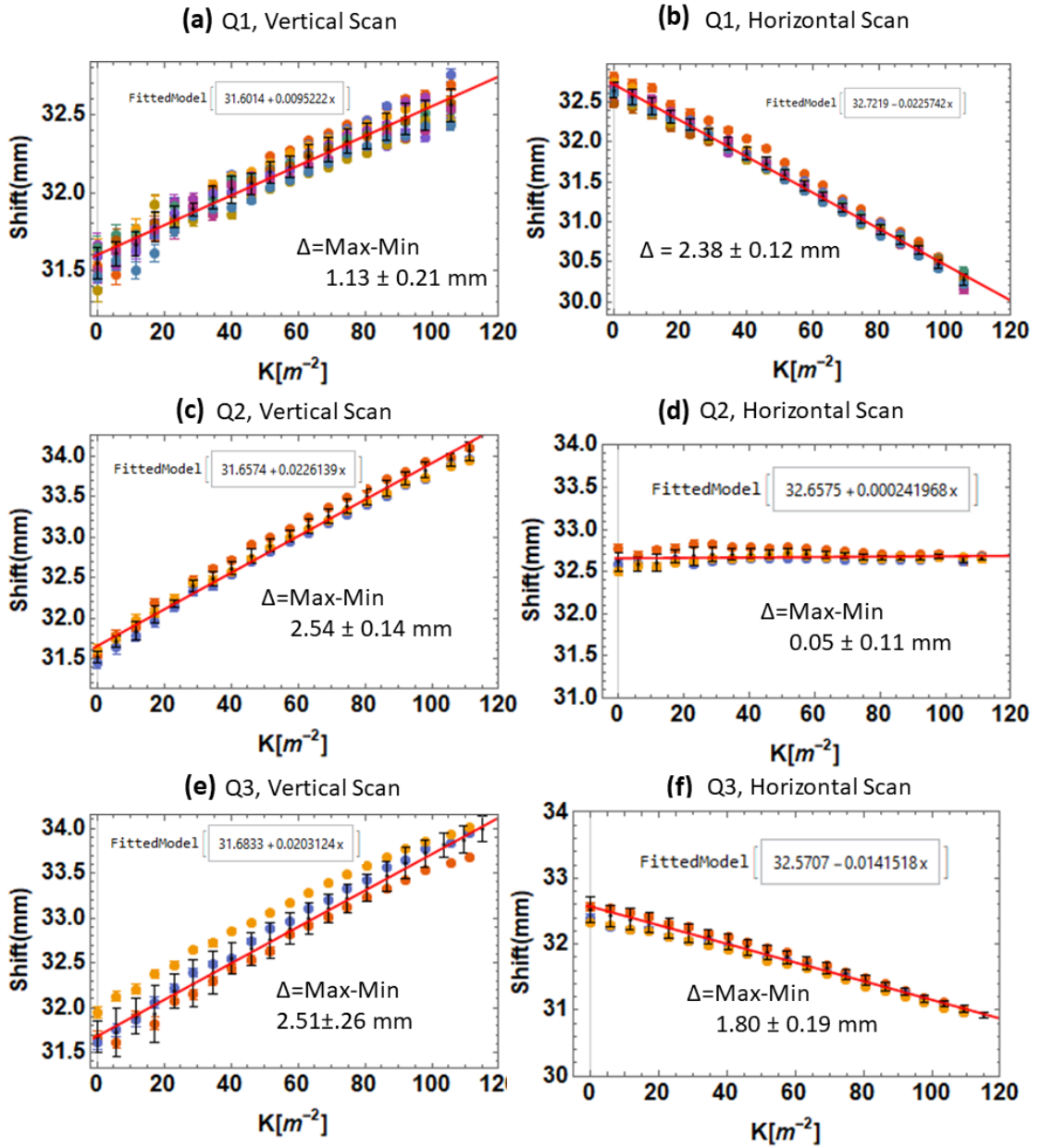


Figure 5.6: The beam position shift due to the quadrupole magnet misalignment error. The black points are weighted average of data points. And red line is the linear fit to the data.

5.3 Results

The emittance measurement at SITE was performed by all three quadrupoles magnets. Figure 5.7 (a), (c) and (e) shows the vertical beam size square as a function of the quadrupole magnet 1, 2 and 3 respectively. Whereas, (b), (d) and (f) shows the horizontal beam size square as a function of the quadrupole magnet 1, 2 and 3 respectively. The color points in each picture are correspond to the repeated measurement and black points are the weighted mean of the repeated measurement. Figure 5.8 and 5.9 shows the beam images with different strengths of vertical and horizontal focused quadrupole magnet 1 respectively. The quadrupole magnet strength corresponding to the each picture is given in Table 5.3.

The errors in Fig. 5.7 are statistical errors calculated from the errors of the rms beam size measurements. The transverse beam sizes were measured 12 times for Q1 (both transverse planes) and 6 time for the Q2 and Q3 scans. The weighted mean of each beam size can be calculated as follows:

$$\langle \hat{x} \rangle = \sum_{i=1}^{i=n} \frac{x_i / \sigma_i^2}{1 / \sigma_i^2} \quad (5.16)$$

Where, (x_1, x_2, \dots, x_n) are correspond to the beam sizes and $\langle \hat{x} \rangle$ is the weighted mean and σ_i is the error of each value. The error of the weighted mean (σ) is given as follows:

$$\sigma = \sqrt{\frac{1}{\sum_{i=1}^{i=n} 1 / \sigma_i^2}} \quad (5.17)$$

Figure 5.10 shows the weighted mean of beam size squared as function of quadrupole strength. Figure 5.10 (a) and (b) shows the vertical and horizontal scan for the quadupole 1 respectively. (c) and (d) shows the vertical and horizontal scan for the quadupole 2. Figure 5.10 (e) and (f) shows the vertical and horizontal scan for the quadupole 3. The data were fitted with the Eq. (5.8). Table 5.3, 5.4 and 5.5 shows the quadrupole magnets strength and beam size square (weighted mean) for Q1, Q2 and Q3 scans respectively.

Matrices (5.18), (5.19) and (5.20) represents the sigma matrices at Q1, Q2 and Q3 respectively. Table 5.6 shows the measured emittance values, calculated by using Eq.(5.9) for Q1, Q2 and Q3, and the comparison between the thick lens and thin lens approximation also presented. Table 5.7 shows the Twiss parameters, calculated by using Eq.(5.10), (5.11) (5.12) for thick lens results. The emittacne calculated from the CST simulation was 0.5 mm mrad in both transverse planes. The apparent difference in measured value (Q-scan) of emittance from the simulation is due to the the cathode degradation overtime. Figure 5.11 details the comparison of the emittance values between experimantal results and CST-PS simulation.

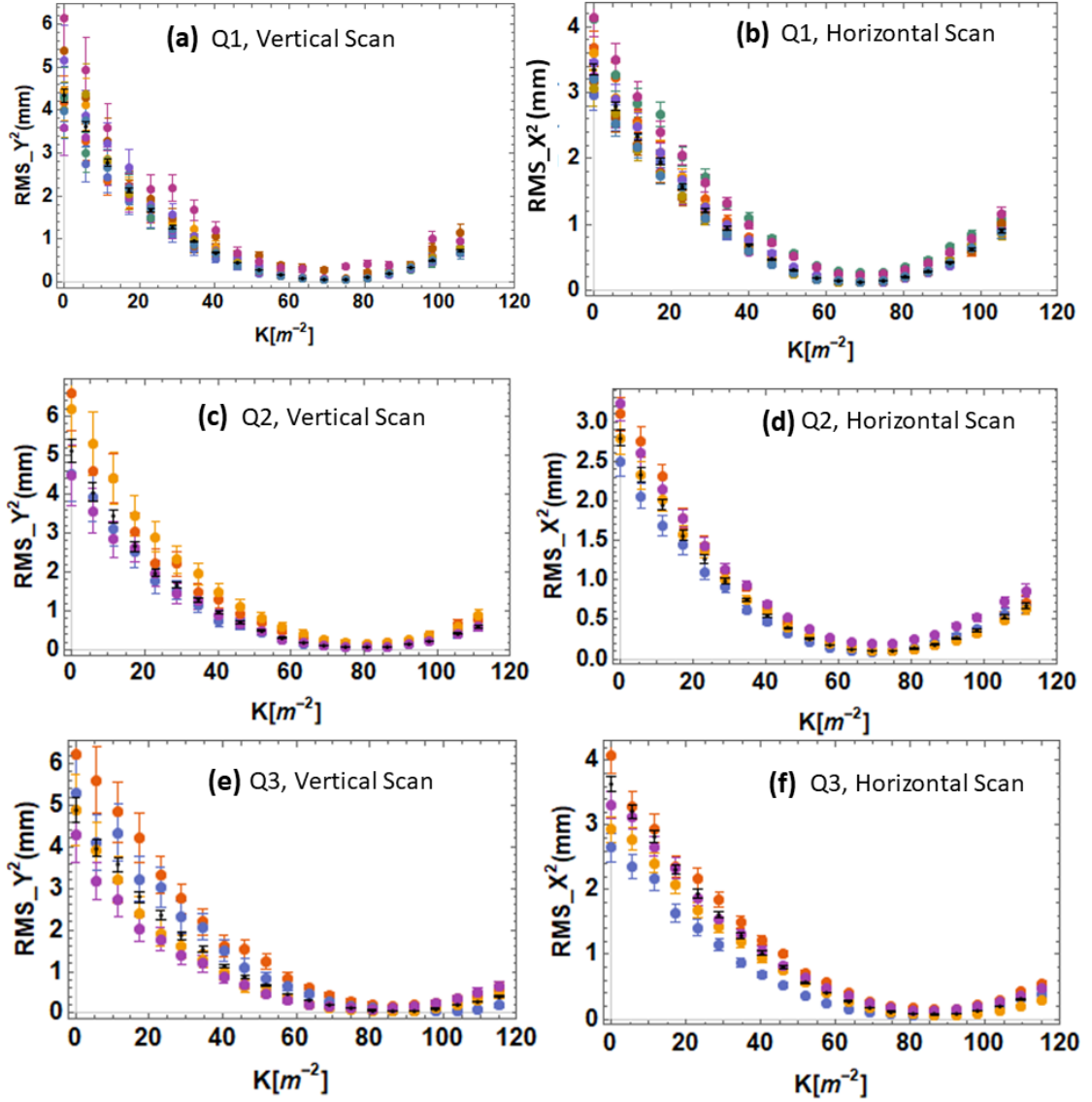


Figure 5.7: (a), (c) and (e) shows the vertical beam size square as a function of the quadrupole magnet 1, 2 and 3 respectively. Whereas (b), (d) and (f) shows the horizontal beam size square as a function of the quadrupole magnet 1, 2 and 3 respectively. The color points in each picture are correspond to the repeated measurement and black points are the weighted mean of the repeated measurement.

5.3. RESULTS

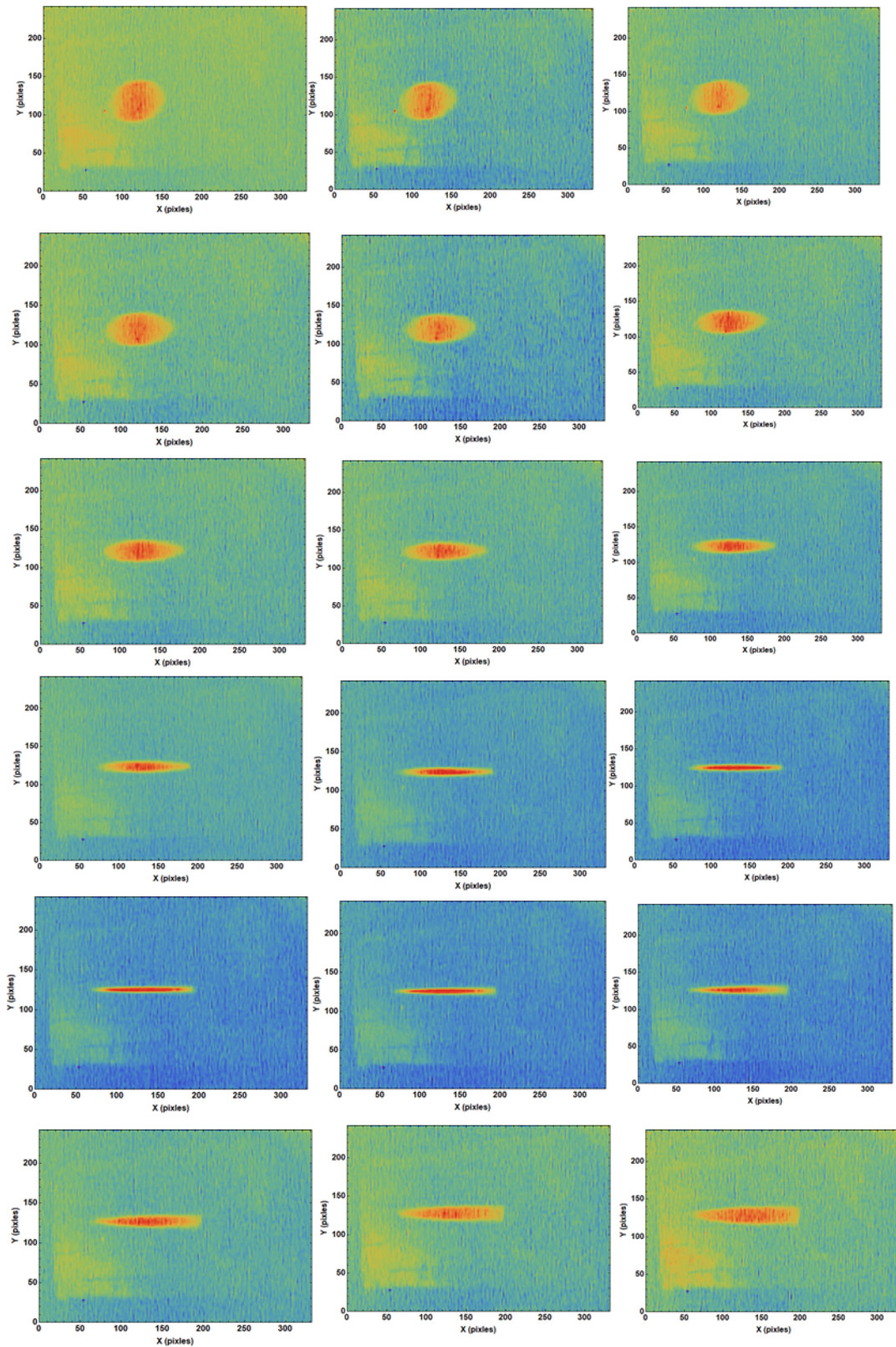


Figure 5.8: The beam images with different strength of vertical focused quadrupole magnet 1. False colors were added to the pictures for the better visibility.

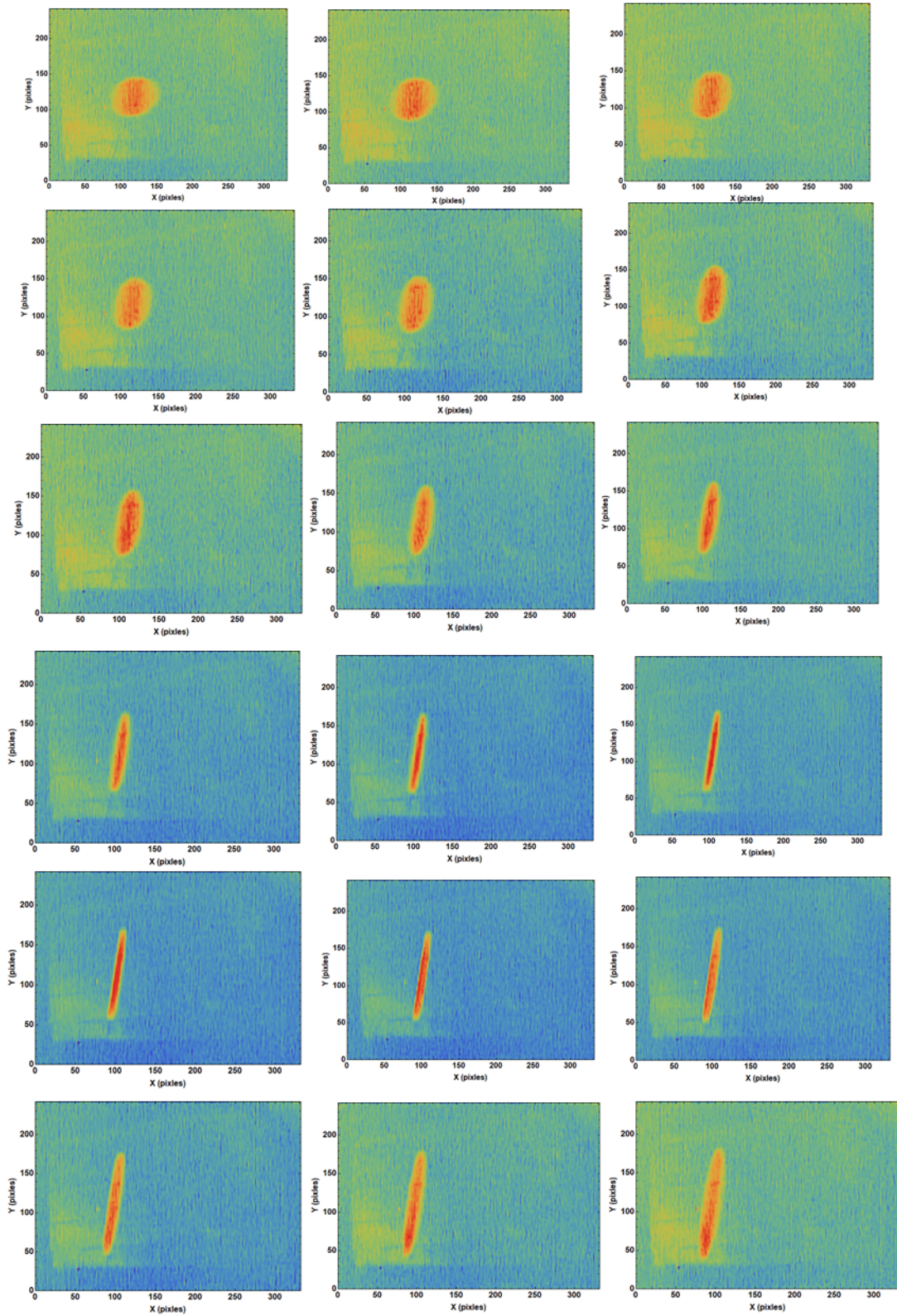


Figure 5.9: The beam images with different strength of horizontal focused quadrupole magnet
1. False colors were added to the pictures for the better visibility.

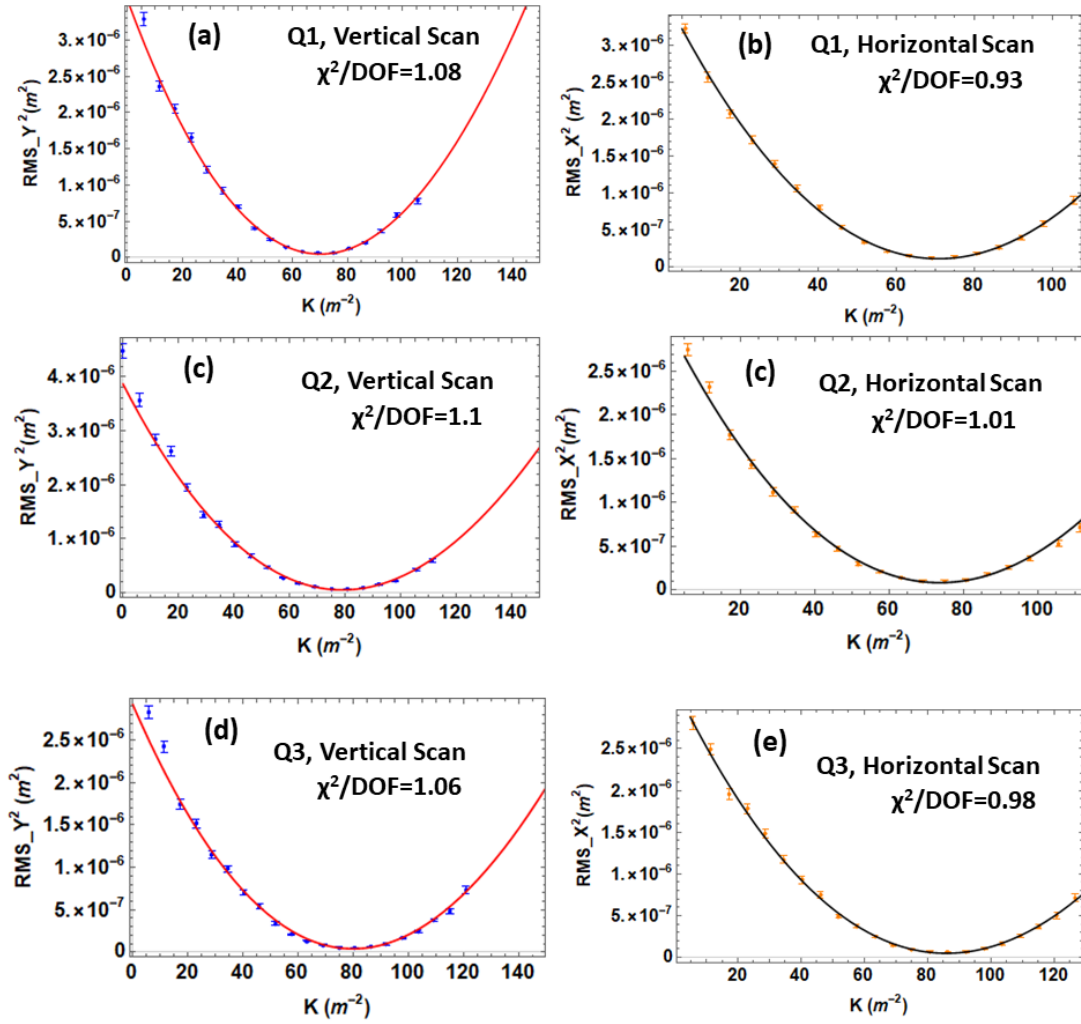


Figure 5.10: The beam size squared as function of quadrupole strength. (a) and (b) shows the vertical and horizontal scan for the quadrupole 1 respectively. (c) and (d) shows the vertical and horizontal scan for the quadrupole 2. (e) and (f) shows the vertical and horizontal scan for the quadrupole 3.

Table 5.3: The beam size square (Weighted Mean) and quadrupole magnet strength values for Q1-scan.

k (m^{-2})	Vertical (mm^2)	Horizontal (mm^2)
5.75	3.29 ± 0.10	3.24 ± 0.10
11.51	2.36 ± 0.07	2.57 ± 0.07
17.27	2.04 ± 0.06	2.08 ± 0.06
23.03	1.65 ± 0.06	1.72 ± 0.05
28.78	1.21 ± 0.04	1.39 ± 0.05
34.54	0.92 ± 0.04	1.06 ± 0.05
40.30	0.697 ± 0.027	0.80 ± 0.04
46.06	0.398 ± 0.018	0.536 ± 0.025
51.81	0.250 ± 0.014	0.333 ± 0.017
57.57	0.145 ± 0.009	0.209 ± 0.016
63.33	0.082 ± 0.006	0.151 ± 0.011
69.09	0.059 ± 0.006	0.119 ± 0.011
74.84	0.064 ± 0.008	0.130 ± 0.016
80.60	0.120 ± 0.008	0.180 ± 0.017
86.36	0.199 ± 0.014	0.262 ± 0.021
92.12	0.366 ± 0.023	0.391 ± 0.026
97.87	0.589 ± 0.033	0.59 ± 0.04
105.55	0.78 ± 0.04	0.90 ± 0.05

5.3. RESULTS

Table 5.4: The beam size square (Weighted Mean) and quadrupole magnet strength values for Q2-scan.

k (m^{-2})	Vertical (mm^2)	Horizontal (mm^2)
5.75	2.75 ± 0.07	3.26 ± 0.12
11.51	2.32 ± 0.06	2.52 ± 0.10
17.27	1.77 ± 0.06	2.32 ± 0.09
23.03	1.43 ± 0.05	1.73 ± 0.06
28.78	1.12 ± 0.04	1.27 ± 0.05
34.54	0.91 ± 0.04	1.12 ± 0.05
40.30	0.631 ± 0.030	0.78 ± 0.04
46.06	0.464 ± 0.024	0.60 ± 0.04
51.81	0.295 ± 0.021	0.417 ± 0.025
57.57	0.208 ± 0.015	0.244 ± 0.016
63.33	0.131 ± 0.012	0.151 ± 0.011
69.09	0.098 ± 0.011	0.091 ± 0.009
74.84	0.095 ± 0.012	0.055 ± 0.007
80.60	0.115 ± 0.013	0.054 ± 0.004
86.36	0.178 ± 0.020	0.075 ± 0.007
92.12	0.257 ± 0.024	0.131 ± 0.011
97.87	0.352 ± 0.024	0.193 ± 0.015
105.55	0.53 ± 0.04	0.372 ± 0.026
111.22	0.71 ± 0.05	0.53 ± 0.04

Table 5.5: The beam size square (Weighted Mean) and quadrupole magnet strength values for Q3-scan.

k (m^{-2})	Vertical (mm^2)	Horizontal (mm^2)
5.75	2.30 ± 0.08	2.92 ± 0.08
11.51	1.96 ± 0.07	2.59 ± 0.07
17.27	1.41 ± 0.06	2.03 ± 0.06
23.03	1.23 ± 0.05	1.85 ± 0.05
28.78	0.93 ± 0.04	1.54 ± 0.05
34.54	0.79 ± 0.04	1.22 ± 0.05
40.30	0.569 ± 0.028	0.96 ± 0.04
46.06	0.436 ± 0.024	0.96 ± 0.04
51.81	0.274 ± 0.020	0.512 ± 0.024
57.57	0.168 ± 0.012	0.385 ± 0.020
63.33	0.105 ± 0.009	0.260 ± 0.016
69.09	0.067 ± 0.007	0.156 ± 0.012
74.84	0.045 ± 0.005	0.102 ± 0.010
80.60	0.039 ± 0.004	0.074 ± 0.009
86.36	0.051 ± 0.005	0.064 ± 0.010
92.12	0.077 ± 0.009	0.068 ± 0.010
97.87	0.134 ± 0.010	0.108 ± 0.011
103.53	0.200 ± 0.017	0.171 ± 0.015
109.39	0.306 ± 0.021	0.268 ± 0.023
115.15	0.390 ± 0.03	0.379 ± 0.028
120.90	0.59 ± 0.04	0.52 ± 0.04

$$\sigma_{Q1} = \begin{pmatrix} 0.79 & 1.61 & 0 & 0 \\ 1.61 & 3.71 & 0 & 0 \\ 0 & 0 & 0.78 & 1.55 \\ 0 & 0 & 1.55 & 3.3 \end{pmatrix} \quad (5.18)$$

$$\sigma_{Q2} = \begin{pmatrix} 0.96 & 1.65 & 0 & 0 \\ 1.65 & 3.19 & 0 & 0 \\ 0 & 0 & 1.19 & 1.85 \\ 0 & 0 & 1.85 & 3.03 \end{pmatrix} \quad (5.19)$$

$$\sigma_{Q3} = \begin{pmatrix} 1.17 & 1.98 & 0 & 0 \\ 1.98 & 3.69 & 0 & 0 \\ 0 & 0 & 1.21 & 1.98 \\ 0 & 0 & 1.98 & 3.4 \end{pmatrix} \quad (5.20)$$

Table 5.6: The transverse emittance values from Q1, Q2, and Q3 scans.

	ϵ_x [mm mrad]	ϵ_y [mm mrad]
Q1	0.59 ± 0.07	0.39 ± 0.06
Q2	0.58 ± 0.09	0.43 ± 0.07
Q3	0.62 ± 0.09	0.44 ± 0.08

Table 5.7: The values of Twiss parameters from Q1, Q2, and Q3 scans at the quadrupole magnet location.

	β_x [m]	β_y [m]	α_x	α_y	γ_x [m rad]	γ_y [m rad]
Q1	1.35 ± 0.15	2.0 ± 0.18	-2.73 ± 0.30	-4.0 ± 0.6	6.3 ± 0.7	8.5 ± 0.35
Q2	1.65 ± 0.22	2.60 ± 0.18	-2.85 ± 0.40	-4.3 ± 0.7	5.6 ± 0.9	9.0 ± 1.4
Q3	1.89 ± 0.25	2.75 ± 0.16	-3.2 ± 0.25	-4.5 ± 0.9	6.5 ± 1.2	8.10 ± 1.21

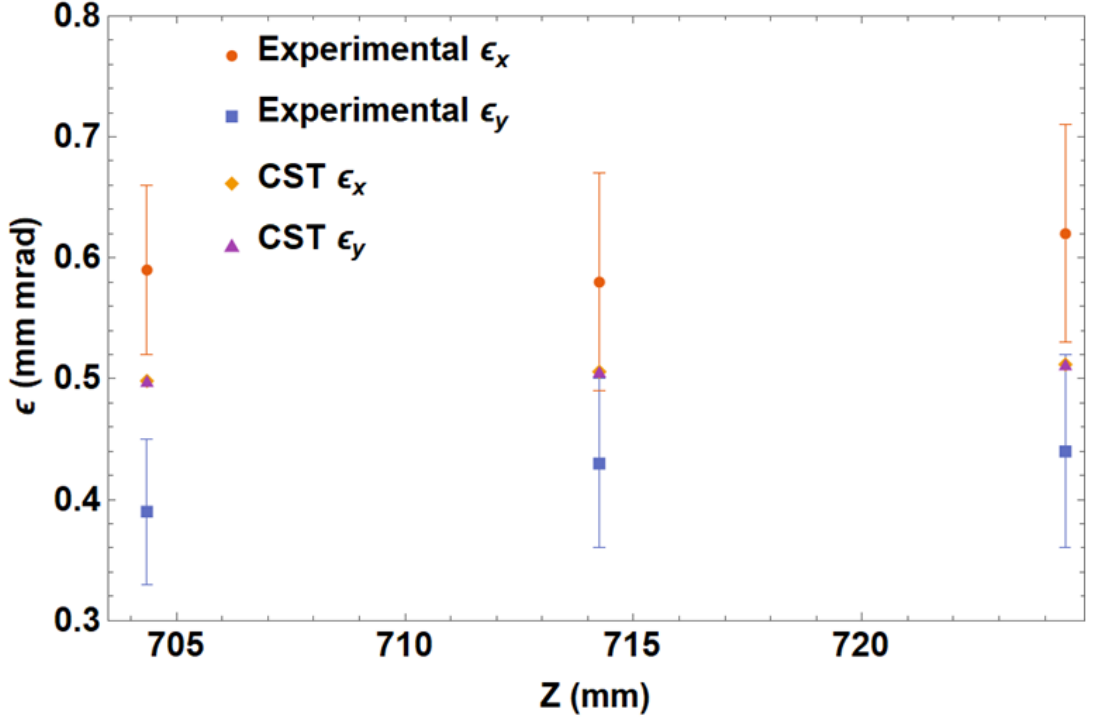


Figure 5.11: the comparison of the emittance values between experimental results and CST-PS simulation.

5.3.1 Beam Phase Space at the Collimator

The quadrupole scan gives the Twiss parameters and emittance at the quadrupole location. In the transport line design, we start from the collimator position. Therefore, it is necessary to find the beam phase space shape (Twiss parameters) and emittance at the collimator location. The beam matrix transform like

$$\sigma_1 = M\sigma_0M^T \quad (5.21)$$

where M is the transport line matrix and M^T is its transpose. In our case, the beam matrix is known at the quadrupole location and in order to find the beam matrix at the collimator location, we have to take the inverse of the above equation.

$$\sigma_0 = M^{-1}\sigma_1(M^T)^{-1} \quad (5.22)$$

If the elements of sigma matrix are known at the collimator then the Twiss parameters can be calculated by the Eq. (5.22). In the case of linear beam dynamics the beam emittance remains constant but Twiss parameters transform along the beamline. Another relation to transform Twiss parameter through drift [71] is as following

$$\begin{pmatrix} \beta(l) \\ \alpha(l) \\ \gamma(l) \end{pmatrix} = \begin{pmatrix} 1 & -2l & l^2 \\ 0 & 1 & -l \\ 0 & 0 & 1 \end{pmatrix} \begin{pmatrix} \beta_0 \\ \alpha_0 \\ \gamma_0 \end{pmatrix} \quad (5.23)$$

above relation gives the Twiss parameters at forward location in. In order to find Twiss parameters at the collimator location, we have to take inverse of the above relation

$$\begin{pmatrix} \beta_0(l) \\ \alpha_0(l) \\ \gamma_0(l) \end{pmatrix} = \begin{pmatrix} 1 & 2l & l^2 \\ 0 & 1 & l \\ 0 & 0 & 1 \end{pmatrix} \begin{pmatrix} \beta \\ \alpha \\ \gamma \end{pmatrix} \quad (5.24)$$

The β and α represent beam size and tilt respectively. And $\gamma = \frac{1+\alpha^2}{\beta}$ depends upon β and α and remain constant in linear beam transport line.

The Twiss parameters from the quadrupole magnet 1 to 3 scan had been transformed to the collimator location by using Eq. (5.24). Table 5.8 shows the transformed Twiss parameters at the collimator. Figure 5.12, 5.13 and 5.14 shows the transformation of β , α and γ from quadrupole magnet location to the collimator. The trend of transformation follows the Eq. (5.24).

Table 5.9 shows the weighted mean of emittance and Twiss parameter values at the collimator position.

Figure 5.15 shows the phase space distribution at the collimator point. Based on Fig. 5.3, Gaussian distribution was used to define the beam phase-space at the collimator location. (6.11).

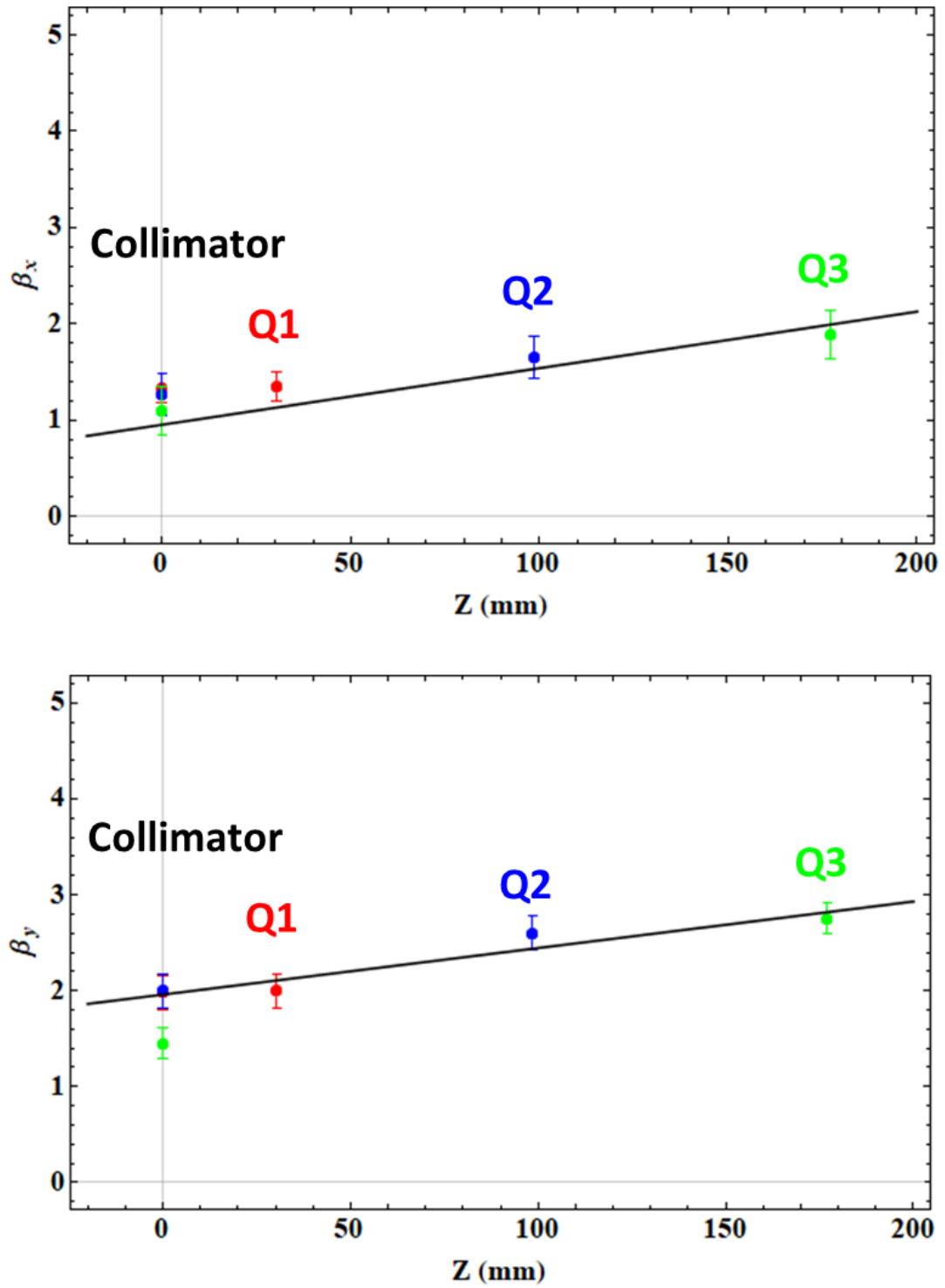
Table 5.8: Twiss parameters transformation from Q1,Q2 and Q3 to the Collimator

	β_x [m]	β_y [m]	α_x	α_y	γ_x [mrad]	γ_y [mrad]
Q1-Colli.	1.33 ± 0.15	1.98 ± 0.18	-2.70 ± 0.31	-3.9 ± 0.6	6.3 ± 0.7	8.50 ± 1.35
Q2-Colli	1.27 ± 0.19	2.00 ± 0.18	-2.41 ± 0.41	-3.6 ± 0.7	5.6 ± 1.1	9.0 ± 1.4
Q3-Colli	1.10 ± 0.25	1.45 ± 0.16	-2.01 ± 0.25	-3.5 ± 0.9	4.99 ± 0.9	8.10 ± 1.21

Table 5.9: The weighted mean of Emittance and Twiss parameters at the Collimator

Parameters	Horizontal	Vertical
ϵ [mm mrad]	0.61 ± 0.05	0.41 ± 0.04
β [m]	1.26 ± 0.10	1.78 ± 0.09
α	-2.30 ± 0.17	-3.69 ± 0.38
γ [mrad]	5.01 ± 0.49	8.4 ± 0.75

$$\sigma_{Initial} = \begin{pmatrix} 0.7687 & 1.4057 & 0 & 0 \\ 1.4057 & 3.0474 & 0 & 0 \\ 0 & 0 & 0.7322 & 1.5177 \\ 0 & 0 & 1.5177 & 3.3738 \end{pmatrix} \quad (5.25)$$

Figure 5.12: The β_x and β_y at Q1,Q2, Q3 and their transformation to the collimator position.

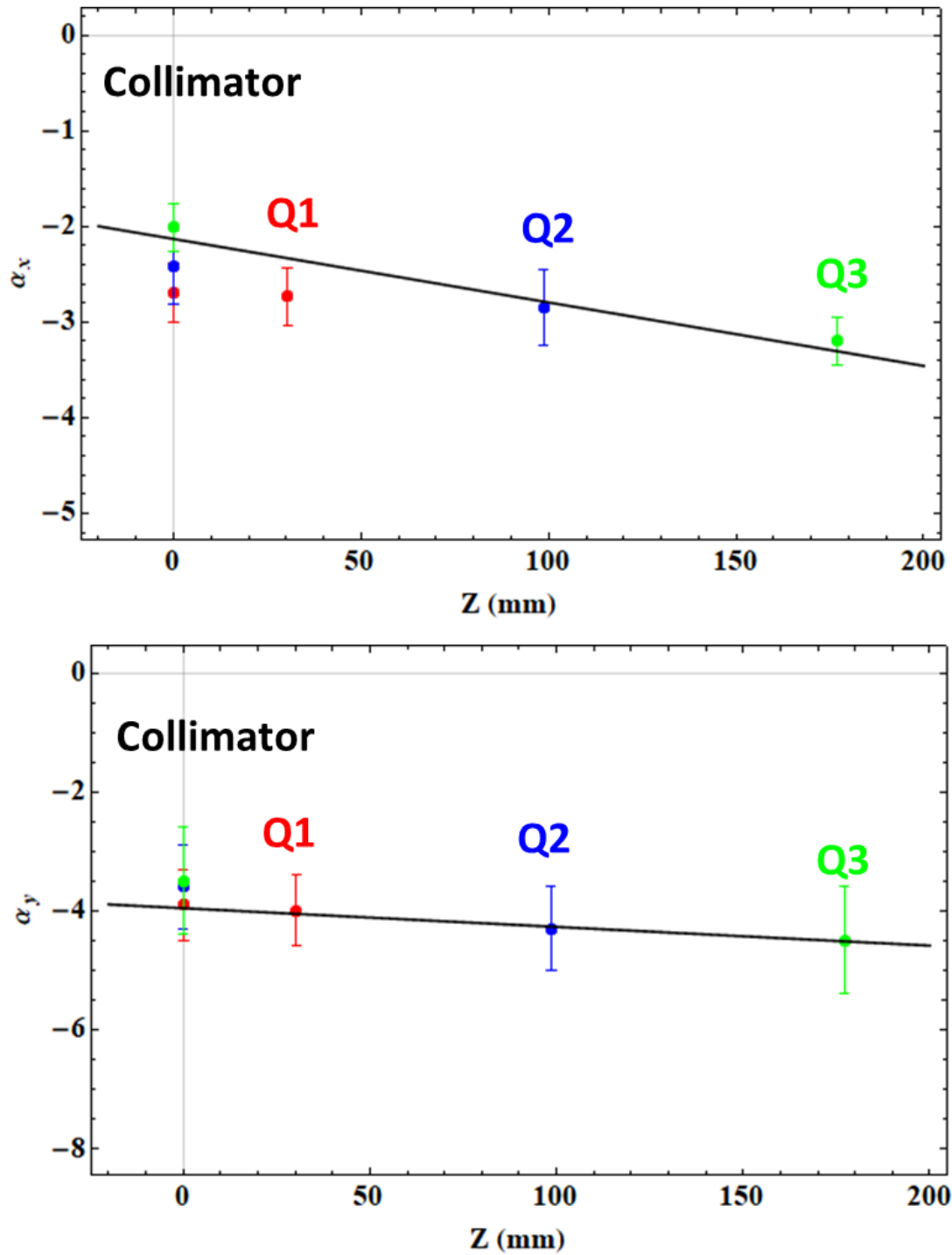
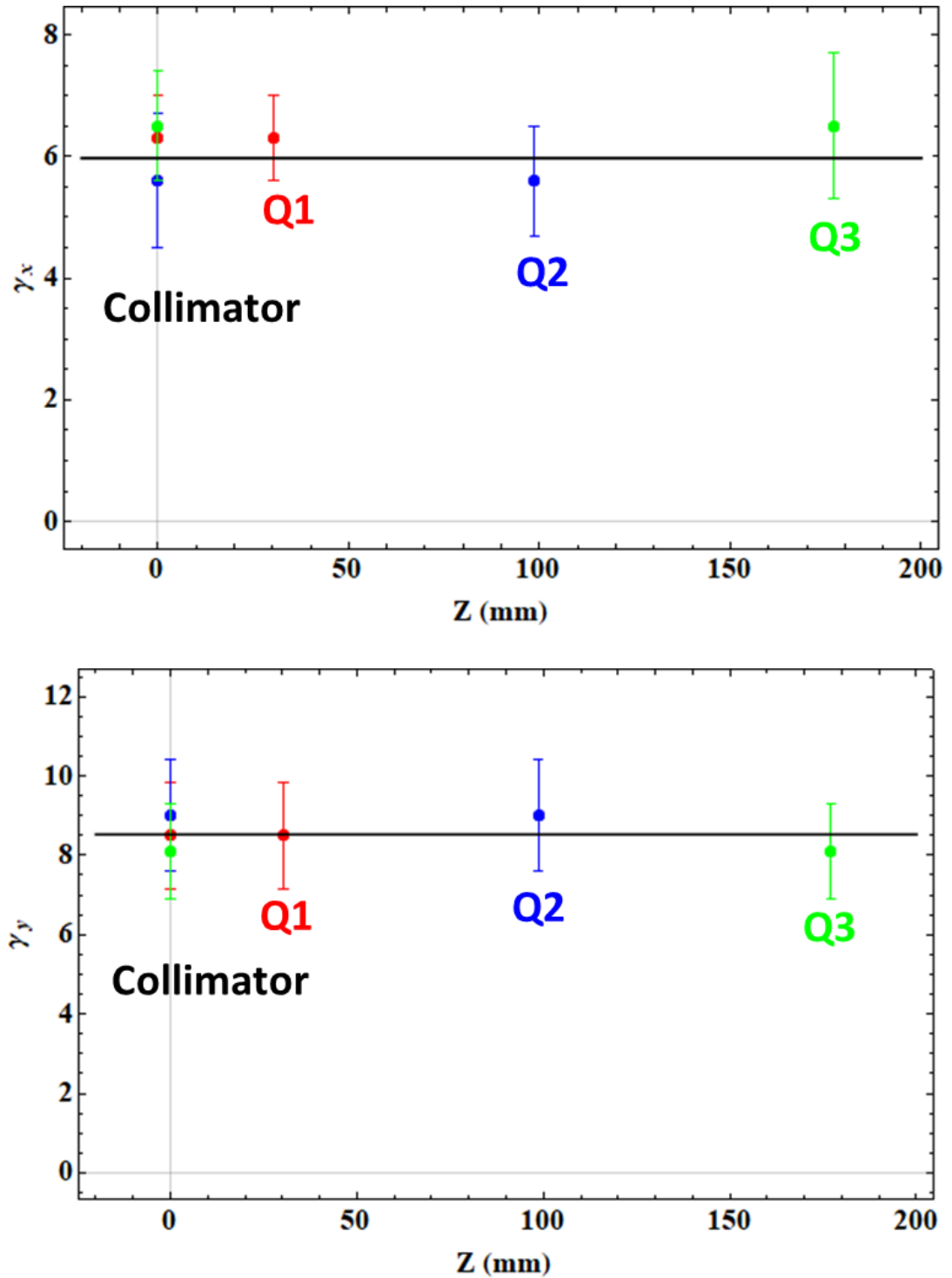


Figure 5.13: The α_x and α_y at Q1, Q2, Q3 and their transformation to the collimator position.

Figure 5.14: The γ_x and γ_y at Q1,Q2, Q3 and their transformation to the collimator position.

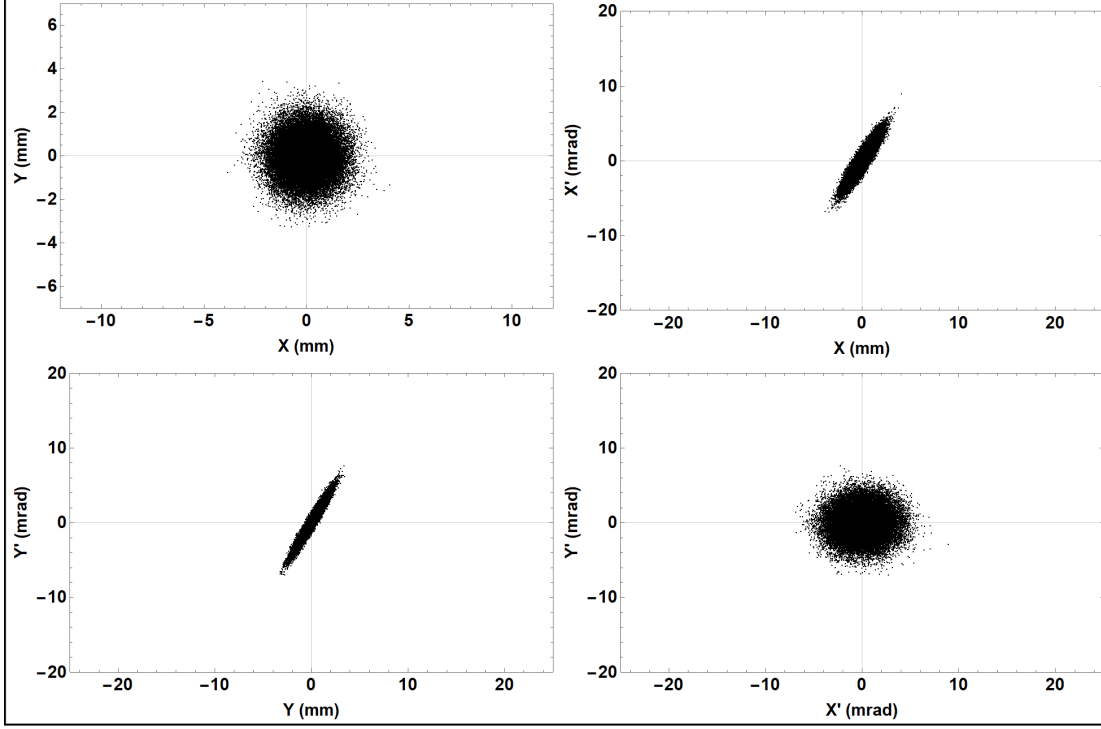


Figure 5.15: The phase space distribution at the collimator. This phase space satisfy the emittance and Twiss parameters given in the Table 5.9.

5.4 Coupling Measurement

If one knows the full beam matrix, then the beam coupling can be estimated. At the SITE beamline a weak magnetic lens (solenoid) was placed after the electron gun to focus the electron beam to the collimator. The magnetic lens is a coupled linear optics element. Therefore, it is necessary to estimate the beam coupling caused by this weak magnetic lens. If one does not assume a zero coupling term in the beam matrix. Then, the transformation of the beam matrix from point p_0 (σ_0) to p_1 (σ_1) will be as follows:

$$\sigma_1 = M\sigma_0M^T, \quad \sigma_0 = \begin{pmatrix} \langle xx \rangle & \langle xx' \rangle & \langle xy \rangle & \langle xy' \rangle \\ \langle x'x \rangle & \langle x'x' \rangle & \langle x'y \rangle & \langle x'y' \rangle \\ \langle yx \rangle & \langle yx' \rangle & \langle yy \rangle & \langle yy' \rangle \\ \langle y'x \rangle & \langle y'x' \rangle & \langle y'y \rangle & \langle y'y' \rangle \end{pmatrix}, \quad \sigma_0 = \begin{pmatrix} \sigma_{0,XX} & \sigma_{0,XY} \\ \sigma_{0,XY}^T & \sigma_{0,YY} \end{pmatrix} \quad (5.26)$$

Where, M is transport line matrix:

$$M = \begin{pmatrix} m_{11} & m_{12} & m_{13} & m_{14} \\ m_{21} & m_{22} & m_{23} & m_{24} \\ m_{31} & m_{32} & m_{33} & m_{34} \\ m_{41} & m_{42} & m_{43} & m_{44} \end{pmatrix} \quad (5.27)$$

If we set the beamline between p_0 and p_1 without transverse coupling (only normal quadrupole

magnets) element, the off-diagonal terms become zero. And Eq.(5.27) will become:

$$M = \begin{pmatrix} m_{11} & m_{12} & 0 & 0 \\ m_{21} & m_{22} & 0 & 0 \\ 0 & 0 & m_{33} & m_{34} \\ 0 & 0 & m_{43} & m_{44} \end{pmatrix} \quad (5.28)$$

The beam transverse sizes and $x - y$ terms will become:

$$\langle x^2 \rangle = \sigma_{1,11} = m_{11}^2 \sigma_{0,11} + 2m_{11}m_{12}\sigma_{0,12} + m_{12}^2 \sigma_{0,22} \quad (5.29)$$

$$\langle y^2 \rangle = \sigma_{1,33} = m_{33}^2 \sigma_{0,33} + 2m_{33}m_{34}\sigma_{0,34} + m_{34}^2 \sigma_{0,44} \quad (5.30)$$

$$\langle xy \rangle = \sigma_{1,13} = m_{11}m_{33}\sigma_{0,13} + m_{12}m_{33}\sigma_{0,14} + m_{11}m_{34}\sigma_{0,23} + m_{12}m_{34}\sigma_{0,24} \quad (5.31)$$

The $\langle xy \rangle$ term can be calculated as a covariance between x and y as follows:

$$\langle xy \rangle = \sigma_{1,13} = \frac{1}{n} \sum_{i=1}^n \langle x_i y_i \rangle \quad (5.32)$$

If the beam is decoupled then the projected rms emittances are the square root of the determinant σ_{xx} and σ_{yy} , and can be shown as ϵ_x and ϵ_y for horizontal and vertical planes respectively.

$$\epsilon_\mu = \sqrt{\langle \mu\mu \rangle \langle \mu' \mu' \rangle - \langle \mu\mu' \rangle^2} \quad (5.33)$$

Where, μ refers to either x or y . If inter plane coupling is non-zero then the eigen emittances ϵ_1 and ϵ_2 can be defined as follows [74, 75, 76]:

$$\epsilon_1 = \frac{1}{2} \sqrt{-\text{tr}[(\sigma_0 J)^2] + \sqrt{\text{tr}^2[(\sigma_0 J)^2] - 16 |\sigma_0|}} \quad (5.34)$$

$$\epsilon_2 = \frac{1}{2} \sqrt{-\text{tr}[(\sigma_0 J)^2] - \sqrt{\text{tr}^2[(\sigma_0 J)^2] - 16 |\sigma_0|}} \quad (5.35)$$

Where, J is four dimensional skew-symmetric matrix given as follows:

$$J = \begin{pmatrix} 0 & 1 & 0 & 0 \\ -1 & 0 & 0 & 0 \\ 0 & 0 & 0 & 1 \\ 0 & 0 & -1 & 1 \end{pmatrix} \quad (5.36)$$

The product of the eigen emittances cannot be greater than the product of the project rms emittances and four-dimensional beam rms emittance can be computed as follows:

$$\epsilon_1 \epsilon_2 = \sqrt{|\sigma_0|} \leq \epsilon_x \epsilon_y \quad (5.37)$$

Where, σ_0 is beam matrix at the desired reconstruction point. In order to measure inter plane coupling a parameter 't' can be defined as follows:

$$t \equiv \frac{\epsilon_x \epsilon_y}{\epsilon_1 \epsilon_2} - 1 \geq 0, \quad (5.38)$$

t equal to zero correspond to the no interplane correlation and $t > 0$ represents the transversely coupled beam.

5.4.1 Results

In the case of SITE, three quadrupole magnets were used to measure the coupling of the beam. Figure 5.16 shows the beamline layout for the coupling measurement. The following beamline transfer matrices were assumed for the coupling measurement:

$$M = L_4 \cdot Q_{3V} \cdot L_3 \cdot Q_{2H} \cdot L_2 \cdot Q_{1V} \cdot L_1 \quad (5.39)$$

$$M = L_4 \cdot Q_{3H} \cdot L_3 \cdot Q_{2V} \cdot L_2 \cdot Q_{1H} \cdot L_1 \quad (5.40)$$

Where, Q_{2V} and Q_{1H} are vertical and horizontal focus normal quadrupole magnets respectively. The $L_1 - L_4$ are drift space as given in Table 5.10. At least four measurements (i.e., 12 equations) are necessary for this evaluation. Although, more measurements will confine the problem more tightly. Therefore, the beam profile measurement with 20 different beamline settings was carried out. First 10 beam profile measurements were carried out with beamline setting as mentioned in (5.39) and later 10 were taken with (5.40).

Figure 5.18 shows the beam profiles with the 10 different beamline settings correspond to the (5.40). False colors were added to the Fig. 5.18 for better visibility. Table 5.11 shows the transverse beam profile and coupling term at the profile monitor for 20 different settings. In Table 5.11, k_1 , k_2 and k_3 represents the focusing strength of Q_{1H} , Q_{2V} and Q_{3H} respectively.

The RMS values of the beam transverse size and X-Y term were used for this measurement. Figure 5.17 (a) shows the gray-scale (setting#4) picture. Figure 5.17 (b) is 3-D histogram of the above picture. It is necessary to remove the background from the beam profile data in order to measure the RMS beam size. The background was estimated (BE) as a 2-D slope of the picture data by using the following function:

$$BE = c + m_1 x + m_2 y \quad (5.41)$$

Where, c is a constant and m_1 and m_2 are slopes in the horizontal and vertical directions. The red inclined plane in Fig 5.17 (b) shows the background estimation. The green highlighted region in Fig. 5.17 (c) indicates the area selected for the RMS beam size measurement after the background subtraction. The conversion factor from pixels to mm is 10 Pixels/mm in both transverse planes.

The aim is to find the coefficients (beam matrix element) of Eq. (5.29), (5.30) and (5.31) in a least-squares sense which best fits all the measured data. For 20 measurement, consider a system of $n = 20$ equations with 3 variables for horizontal plane:

$$\begin{pmatrix} \sigma_{1,11}^1 \\ \sigma_{1,11}^2 \\ \sigma_{1,11}^3 \\ \vdots \\ \sigma_{1,11}^{20} \end{pmatrix} = \begin{pmatrix} m_{11}^1 m_{11}^1 & 2m_{11}^1 m_{12}^1 & m_{12}^1 m_{12}^1 \\ m_{11}^2 m_{11}^2 & 2m_{11}^2 m_{12}^2 & m_{12}^2 m_{12}^2 \\ m_{11}^3 m_{11}^3 & 2m_{11}^3 m_{12}^3 & m_{12}^3 m_{12}^3 \\ \vdots & \vdots & \vdots \\ m_{11}^{20} m_{11}^{20} & 2m_{11}^{20} m_{12}^{20} & m_{12}^{20} m_{12}^{20} \end{pmatrix} \begin{pmatrix} \sigma_{0,11} \\ \sigma_{0,12} \\ \sigma_{0,22} \end{pmatrix} \quad (5.42)$$

The method of least squares was used to find the solution of over determined set of equations Eq. (5.42). Let's say transformation matrix A , beam size matrix at the screen monitor Σ_{1x} and coefficient matrix Σ_{0x} , then the Eq. (5.42) can be written as follows:

$$\Sigma_{1x} = A\Sigma_{0x} \quad (5.43)$$

$$\Sigma_{0,x} = (A^T A)^{-1} A^T \Sigma_{1,x}, \quad (5.44)$$

similarly for vertical plane

$$\Sigma_{0,y} = (A^T A)^{-1} A^T \Sigma_{1,y}. \quad (5.45)$$

For interplane correlations terms the system of $n = 20$ equations with 4 unknowns can be written as follows:

$$\begin{pmatrix} \sigma_{1,13}^1 \\ \sigma_{1,13}^2 \\ \sigma_{1,13}^3 \\ \vdots \\ \sigma_{1,13}^{20} \end{pmatrix} = \begin{pmatrix} m_{11}^1 m_{33}^1 & m_{12}^1 m_{33}^1 & m_{11}^1 m_{34}^1 & m_{12}^1 m_{34}^1 \\ m_{11}^2 m_{33}^2 & m_{12}^2 m_{33}^2 & m_{11}^2 m_{34}^2 & m_{12}^2 m_{34}^2 \\ m_{11}^3 m_{33}^3 & m_{12}^3 m_{33}^3 & m_{11}^3 m_{34}^3 & m_{12}^3 m_{34}^3 \\ \vdots & \vdots & \vdots & \vdots \\ m_{11}^{20} m_{33}^{20} & m_{12}^{20} m_{33}^{20} & m_{11}^{20} m_{34}^{20} & m_{12}^{20} m_{34}^{20} \end{pmatrix} \begin{pmatrix} \sigma_{0,13} \\ \sigma_{0,14} \\ \sigma_{0,23} \\ \sigma_{0,24} \end{pmatrix} \quad (5.46)$$

And similarly Eq. (5.44) and (5.47) the solution of (5.46) can be written as follows:

$$\Sigma_{0,xy} = (A^T A)^{-1} A^T \Sigma_{1,xy}. \quad (5.47)$$

A *Mathematica* program has been developed to solve these system of equation. Table 5.12 shows values of the elements of σ_0 matrix at reconstruction point. The coupling strength for the SITE beamline is shown in Table 5.13. The value of $\epsilon_1 \epsilon_2 = 0.64$ was obtained. And $\epsilon_x \epsilon_y$ results in 0.75. Which corresponds to a coupling strength of $t = 0.17$. In the case of the strongly coupled beam (skew quadrupole magnet) the value of t will be in the range of 2.8. Moreover, in the case of SITE, the required coupling strength (forth coming Chapter) at the matching point is 6.24. Thus, the coupling strength of $t = 0.17$ represents the insignificant beam coupling at the collimator location. Hence, the emittance and Twiss parameters measured from the Quad-scan will be used for the further studies.

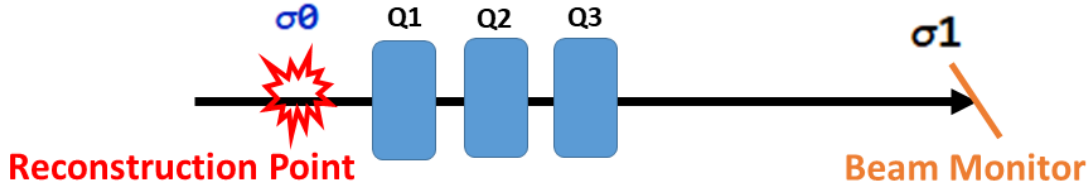


Figure 5.16: The layout of the beamline for the 4-D beam matrix reconstruction.

Table 5.10: The drift spaces of the beamline.

Parameters	Length [mm]
L_1	2.35
L_2	12.25
L_3	22.45
L_4	354.45

 Table 5.11: The beamline setting and respective values of $\sigma_{1,11}$, $\sigma_{1,33}$, $\sigma_{1,13}$.

Setting	k_1 (m^{-2})	k_2 (m^{-2})	k_3 (m^{-2})	$\sigma_{1,11}$ (mm^2)	$\sigma_{1,33}$ (mm^2)	$\sigma_{1,13}$ (mm^2)
1	-38.57	23.10	-21.26	5.95 ± 0.08	1.180 ± 0.016	0.00035 ± 0.00028
2	-63.70	44.37	-21.26	6.31 ± 0.08	0.681 ± 0.009	0.0014 ± 0.0006
3	-63.70	21.17	-23.20	11.60 ± 0.15	0.1936 ± 0.0018	0.0656 ± 0.0032
4	-82.94	55.97	-32.86	9.74 ± 0.11	0.2136 ± 0.0021	0.0346 ± 0.0024
5	-0.00	52.10	-32.86	1.138 ± 0.014	5.76 ± 0.11	0.081 ± 0.005
6	-25.03	69.50	-9.57	0.686 ± 0.008	6.63 ± 0.14	0.067 ± 0.005
7	-25.03	84.97	-9.57	0.2477 ± 0.0032	7.77 ± 0.20	0.206 ± 0.008
8	-25.03	102.37	-9.57	0.156 ± 0.006	21.1 ± 1.0	0.749 ± 0.009
9	-55.97	102.37	-40.6	1.405 ± 0.014	2.738 ± 0.027	0.041 ± 0.002
10	-55.97	102.37	-67.66	3.40 ± 0.05	1.546 ± 0.020	0.0315 ± 0.0025
11	19.23	-36.63	1.83	4.36 ± 0.06	2.642 ± 0.035	0.0100 ± 0.0012
12	19.23	-18.27	20.3	6.60 ± 0.08	0.617 ± 0.007	0.0008 ± 0.0004
13	19.23	-98.50	13.43	10.52 ± 0.13	0.0935 ± 0.0009	0.110 ± 0.004
14	19.23	-158.43	139.2	1.285 ± 0.014	0.453 ± 0.005	0.108 ± 0.004
15	0.096	-158.43	139.2	2.021 ± 0.023	0.22662 ± 0.0026	0.313 ± 0.006
16	40.50	-156.50	116.96	1.424 ± 0.014	0.874 ± 0.009	0.014 ± 0.0015
17	30.83	-162.30	172.06	0.0922 ± 0.0012	2.196 ± 0.033	0.063 ± 0.005
18	48.23	-65.63	34.70	1.559 ± 0.018	5.98 ± 0.11	0.0255 ± 0.0025
19	81.10	-79.17	73.46	0.0655 ± 0.0005	12.22 ± 0.10	0.307 ± 0.004
20	81.10	-189.37	73.46	3.69 ± 0.04	0.1132 ± 0.0011	0.112 ± 0.004

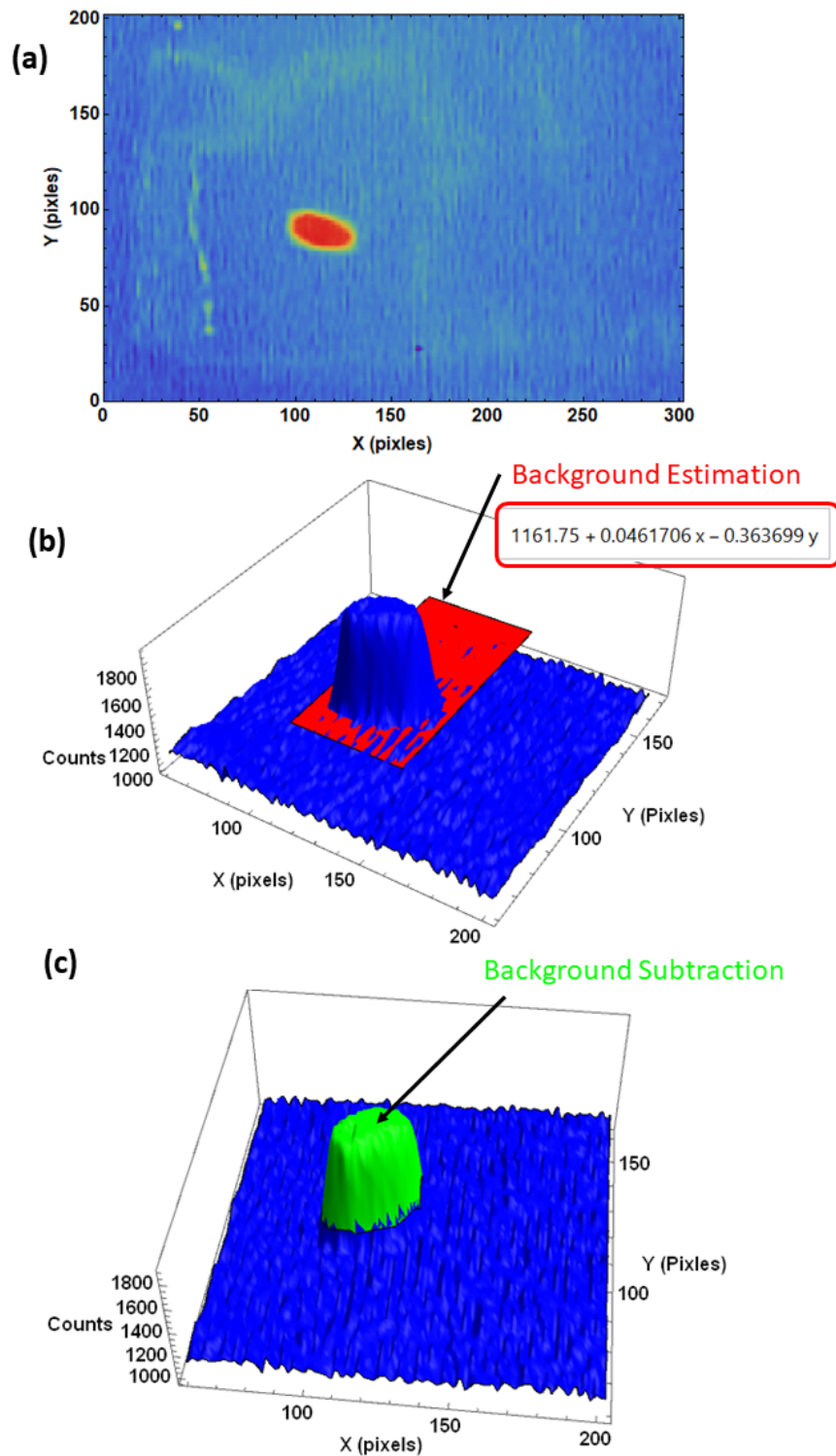


Figure 5.17: (a) The gray-scale (setting#14) picture. (b) The 3-D histogram of the above picture. The background was estimated as a 2D slope picture data. The red patch shows the background estimation. (c) The green highlighted region indicates the area selected for the RMS beam size measurement after the background estimation.

5.4. COUPLING MEASUREMENT

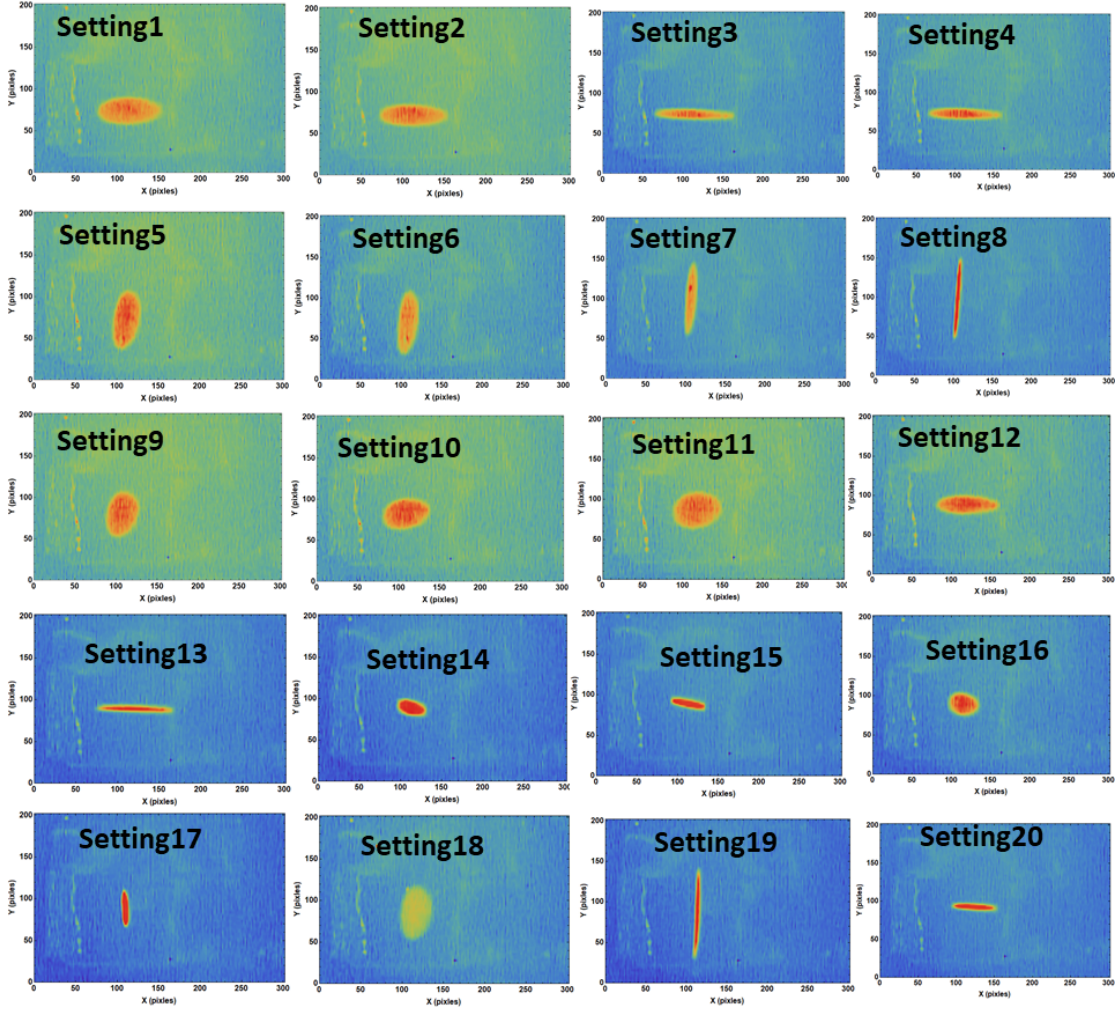


Figure 5.18: The beam images with different settings. False colors were added to the pictures for the better visibility.

Table 5.12: The values of the beam matrix elements at the reconstruction point.

Parameters	Values	Parameters	Values
$\sigma_{0,11}$ [mm ²]	0.444 ± 0.016	$\sigma_{0,22}$ [mrad ²]	5.36 ± 0.05
$\sigma_{0,33}$ [mm ²]	0.764 ± 0.023	$\sigma_{0,44}$ [mrad ²]	0.408 ± 0.06
$\sigma_{0,12}$ [mm mrad]	1.246 ± 0.022	$\sigma_{0,34}$ [mm mrad]	1.560 ± 0.035
$\sigma_{0,13}$ [mm ²]	-0.1011 ± 0.0011	$\sigma_{0,14}$ [mm mrad]	-0.0290 ± 0.0029
$\sigma_{0,23}$ [mm mrad]	-0.2228 ± 0.0028	$\sigma_{0,24}$ [mrad ²]	0.570 ± 0.008

Table 5.13: The Coupling Strength for the SITE beamline.

Parameters	Values
$\epsilon_x \epsilon_y$ [(mm mrad) ²]	0.75 ± 0.1
$\epsilon_1 \epsilon_2 = \sqrt{ \sigma_0 }$ [(mm mrad) ²]	0.64 ± 0.3
t	0.17 ± 0.6

Chapter 6

Experimental Results of Phase Space Matching

One of the most important aspects of the 3-D spiral injection scheme is to produce the required beam phase-space for the injection and confirm its effects on the reductions of vertical beam size. In this chapter, the details of the beam phase-space matching requirements, beamline, and experimental results of the beam phase-space matching on the vertical beam size in the storage magnet will be described and discussed.

6.1 Beam Phase-Space Requirements

6.1.1 Coordinates System

Here, we will distinguish between the global and local coordinates system. The beam injection and 3-D spiral plots will be shown in the storage magnet or global coordinate system. Whereas, the beam phase-space at the injection point will be described in the beam coordinate system for the sake of convenience. In Fig. 6.1 (X_g, Y_g, Z_g) denotes the global (solenoid) coordinate system and (X, Y, Z) is the beam coordinate (beam frame), that is used to describe the 4-D beam phase-space at the matching point. In Fig. 6.1 X and Y represents the horizontal and vertical planes respectively, and Z is the beam motion direction. The X' and Y' are defined as follows:

$$X' = \frac{P_X}{P}, \quad Y' = \frac{P_Y}{P}, \quad P = \sqrt{P_X^2 + P_Y^2 + P_Z^2} \quad (6.1)$$

where, P_X, P_Y represents the horizontal and vertical momentum components respectively, and P is total momentum.

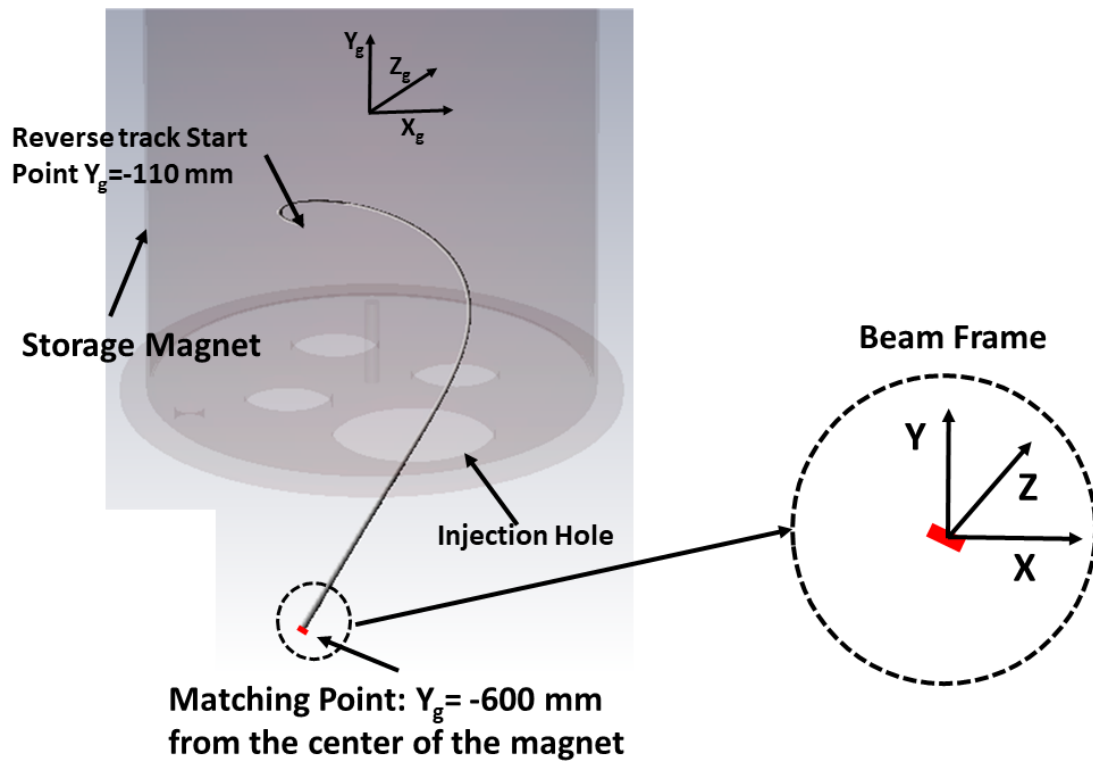


Figure 6.1: Left: A horizontal flat beam was assumed inside the storage magnet and reverse track it to find the required beam slopes at the injection point. Right: The beam frame is used to describe the beam shape at the injection point. X and Y represents the horizontal and vertical planes respectively, and Z is the beam motion direction.

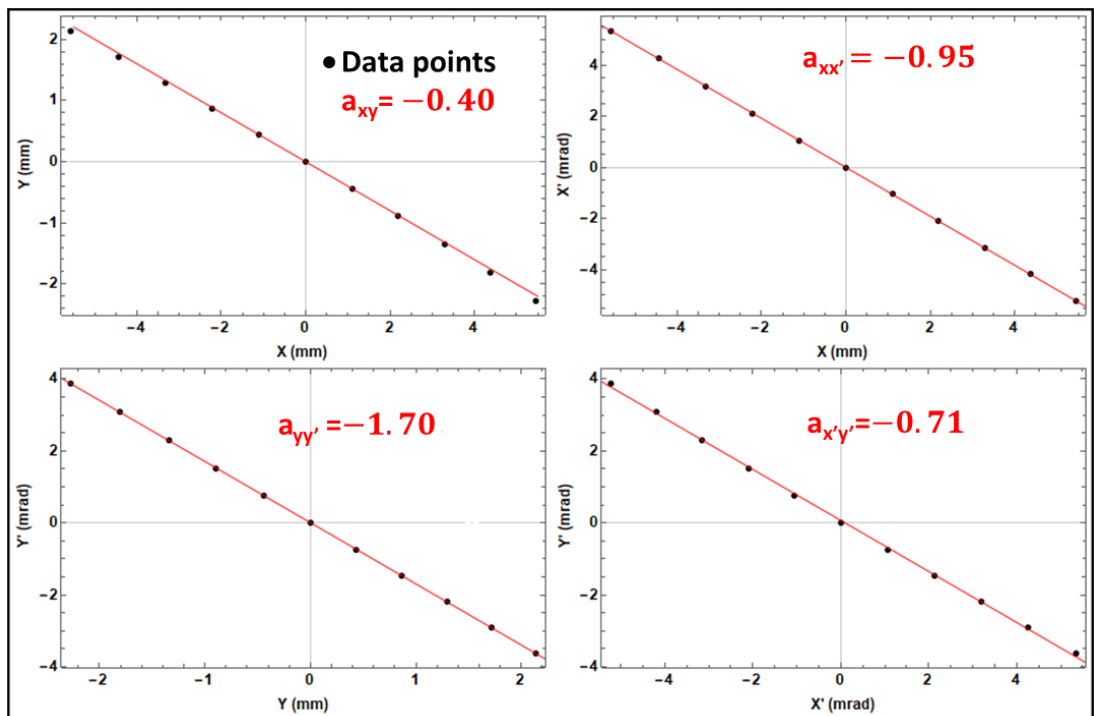


Figure 6.2: The slopes of the beam correlations at the matching point $Y_g = -600$ mm. The beam correlations plots are shown in the beam coordinates. The dots represents the data points obtained from the reverse tracking at the matching point and solid line (red line) are the linear fit to these points.

6.1.2 A Method to Calculate the Beam Phase-Space Requirements at the Matching Point

Due to the axial symmetric field of the solenoid magnet a strongly XY -coupled beam is needed for the successful 3-D spiral injection scheme. Here, XY -coupled will be referred to the rotation of the principal axes of horizontal (X, X') and vertical (Y, Y') planes.

In order to find the required beam phase-space at the injection point, we assumed a horizontal particle distribution at the boundary of weak focusing field ($Y_g = -110$ mm) from the center of the storage magnet, and reverse track it to the matching point (outside of the storage magnet ($Y_g = -600$ mm)). The matching point was chosen outside of the storage magnet as shown in Fig. 6.1, because the beam optics elements (rotatable quadrupole magnets) for the beam phase-space matching cannot be placed inside of the storage magnet.

At the matching point ($Y_g = -600$ mm), the beam phase-space from the reverse tracking in beam coordinate system was calculated. Figure 6.2 presents the beam phase-space at the matching point. The solid dots (black points) in Fig. 6.2 are the data points obtained from the reverse tracking and solid line (red line) is the linear fit to these points. The a_{xy} , $a_{xx'}$, $a_{yy'}$, and $a_{x'y'}$ are slopes of the (X, Y), (X, X'), (Y, Y'), and (X', Y') correlations respectively. The values of these slopes are shown in Table 6.1. The beam phase-space at the matching point shows the strong coupling between horizontal and vertical planes.

Table 6.1: The beam slopes at the matching point.

Correlation	Slope	Value
X, Y	a_{xy}	-0.40
X, X'	$a_{xx'}$ [mm/mrad]	-0.95
Y, Y'	$a_{yy'}$ [mm/mrad]	-1.70
X', Y'	$a_{x'y'}$	-0.71

After finding the required beam phase-space slopes at the matching point as shown in Fig. 6.2, the next target is to find the Twiss and coupling parameters for the distribution of particles at the matching point.

Here, we will describe a transfer matrix method to compute the coupling of the beam at the matching point. Let's assume a matrix M which consists of rotation and Twiss parameters matrix [44, 45, 77]:

$$M = U_{out}^{-1} \cdot D \cdot U_{in}, \quad (6.2)$$

where, U_{in} and U_{out} are input (initial) and output (matching point) rotation matrix, which

satisfy the symplectic ¹ condition. In the case of, uncoupled input beam phase-space U_{in} will be equal to identity matrix. In the case of SITE, the input beam phase-space has no coupling, therefore, Eq. (6.2) can be written as follow:

$$M = U^{-1} \cdot D \quad (6.4)$$

The 4×4 U matrix is given as follow:

$$U_{out} = \begin{pmatrix} \mu & 0 & -R_4 & R_2 \\ 0 & \mu & R_3 & -R_1 \\ R_1 & R_2 & \mu & 0 \\ R_3 & R_4 & 0 & \mu \end{pmatrix} \quad (6.5)$$

where, R_1 , R_2 , R_3 , R_4 are known as coupling parameters (unit less) and non-zero value of these parameters shows the strength of the coupling. The quantity μ is given as $\mu = \sqrt{1 - (R_1 R_4 - R_2 R_3)}$. The matrix D is a diagonal matrix consist of beam input and output Twiss parameters. The matrix D can be written as following:

$$D = \begin{pmatrix} D_X & 0 \\ 0 & D_Y \end{pmatrix} \quad (6.6)$$

Where, D_X in Eq. (6.6) is given as follow:

$$D_X = \begin{pmatrix} \frac{1}{\sqrt{\beta_x^{out}}} & 0 \\ \frac{\alpha_x^{out}}{\sqrt{\beta_x^{out}}} & \sqrt{\beta_x^{out}} \end{pmatrix}^{-1} \phi_X \begin{pmatrix} \frac{1}{\sqrt{\beta_x^{in}}} & 0 \\ \frac{\alpha_x^{in}}{\sqrt{\beta_x^{in}}} & \sqrt{\beta_x^{in}} \end{pmatrix} \quad (6.7)$$

$$\phi_X = \begin{pmatrix} \cos(\phi_x) & \sin(\phi_x) \\ \sin(\phi_x) & \cos(\phi_x) \end{pmatrix} \quad (6.8)$$

Where, ϕ_X is phase advance and correspond to identity in our case. Similarly for D_y . The full form of 4×4 D matrix can be written as follows:

$$D = \begin{pmatrix} \sqrt{\frac{\beta_x^{out}}{\beta_x^{in}}} & 0 & 0 & 0 \\ \frac{\alpha_x^{in}}{\sqrt{\beta_x^{in}} \sqrt{\beta_x^{out}}} - \frac{\alpha_x^{out}}{\sqrt{\beta_x^{in}} \sqrt{\beta_x^{out}}} & \sqrt{\frac{\beta_x^{in}}{\beta_x^{out}}} & 0 & 0 \\ 0 & 0 & \sqrt{\frac{\beta_y^{out}}{\beta_y^{in}}} & 0 \\ 0 & 0 & \frac{\alpha_y^{in}}{\sqrt{\beta_y^{in}} \sqrt{\beta_y^{out}}} - \frac{\alpha_y^{out}}{\sqrt{\beta_y^{in}} \sqrt{\beta_y^{out}}} & \sqrt{\frac{\beta_y^{in}}{\beta_y^{out}}} \end{pmatrix} \quad (6.9)$$

An iterative procedure has been adopted to calculate the coupling parameters.

¹A matrix U is symplectic if it satisfy the following condition [78]:

$$U^T \Omega U = \Omega, \quad \Omega = \begin{pmatrix} 0 & 1 & 0 & 0 \\ -1 & 0 & 0 & 0 \\ 0 & 0 & 0 & 1 \\ 0 & 0 & -1 & 0 \end{pmatrix} \quad (6.3)$$

By changing the $R_1 - R_4$ values, we can change the rotation matrix U and the slope of the input beam. We employed an iterative procedure to control (change: $R_1 - R_4$) the correlation slopes of (X, Y) , (X, X') , (Y, Y') and (X', Y') until the slope of the input distributions coincide with the a_{xy} , $a_{xx'}$, $a_{yy'}$, and $a_{x'y'}$ respectively. In beginning of the iteration procedure the following Twiss parameters were assumed as a starting point:

$$\begin{aligned}\beta_x^{out} &= \beta_x^{in} & \alpha_x^{out} &= a_{xx'} \times \beta_x^{out} \\ \beta_y^{out} &= \beta_y^{in} & \alpha_y^{out} &= a_{yy'} \times \beta_y^{out}\end{aligned}\tag{6.10}$$

These Twiss parameters also has been adjusted to match the slopes of input beam phase-space distribution with the required slope values.

The input beam phase-space distribution as shown in Fig. 6.3 was defined with the emittance and Twiss parameters values, measured by the Q-scan, as described in the Section 5.3.1 of Chapter 5. The output beam phase-space after getting the required Twiss and coupling parameters is shown in Fig. 6.4, the blue lines in Fig. 6.4 are the slopes of the correlation $((X, Y), (X, X'), (Y, Y'), (X', Y'))$ as shown in Table 6.1 and Fig. 6.2.

The input beam matrix (collimator location) of phase space distribution as shown in Fig. 6.3 can be written as σ_{input} :

$$\sigma_{input} = \begin{pmatrix} 0.7687 & 1.4057 & 0 & 0 \\ 1.4057 & 3.0474 & 0 & 0 \\ 0 & 0 & 0.7322 & 1.5177 \\ 0 & 0 & 1.5177 & 3.3738 \end{pmatrix}\tag{6.11}$$

The beam matrix at the matching point σ_{output} after applying iterative procedure will become as following ($\sigma_{output} = M \cdot \sigma_{input} \cdot M^T$, where M is as mentioned in Eq. (6.4) after the iteration procedure):

$$\sigma_{output} = \begin{pmatrix} 7.5984 & -6.8671 & -2.8854 & 4.5811 \\ -6.8671 & 6.4397 & 2.6629 & -3.7417 \\ -2.8854 & 2.6629 & 1.3850 & -2.0953 \\ 4.5811 & -3.7417 & -2.0953 & 4.2997 \end{pmatrix}\tag{6.12}$$

Note, that in the case of the coupled beam off-diagonal terms appear. And coupling strength parameter t (Eq.(5.38)) is equal to 6.24, which signify a strongly XY -coupled beam.

Table 6.2 shows the beam emittance and Twiss parameters for the input beam phase-space distribution and Table 6.3 presents the Twiss parameters of the matched beam. Table 6.4 details the values of the coupling parameters (R_1, R_2, R_3, R_4) for the matched beam. Figure 6.5 (a) shows the beam injection into the storage magnet without phase space matching, the phase-space distribution and the emittance and Twiss parameters are given in Fig. 6.3 and Table 6.2 respectively. Whereas, Fig. 6.5 (b) presents the beam injection into the storage magnet with phase-space matching, the phase-space distribution and the emittance and Twiss parameters

are given in Fig. 6.4 and Table 6.3, 6.4 respectively. It can be seen clearly that the beam vertical blow-up reduce dramatically with appropriate matched beam.

Table 6.2: The initial beam phase space parameters.

Parameters	Horizontal	Vertical
ϵ [mm mrad]	0.61 ± 0.05	0.41 ± 0.04
β_{in} [m]	1.26 ± 0.10	1.78 ± 0.09
α_{in}	-2.30 ± 0.17	-3.69 ± 0.38
γ_{in} [m rad]	5.02 ± 0.49	8.4 ± 0.75
R_1, R_2, R_3, R_4		0
$\sqrt{ \sigma_{input} }$		0.25

Table 6.3: The beam phase-space parameters at the matching point.

Parameters	Horizontal	Vertical
β_{out} [m]	3	3
α_{out}	3	5.2
$\sqrt{ \sigma_{output} }$		0.25
t		6.24

Table 6.4: Coupling Parameters for the Matched Beam Phase Space.

Parameters	Values
R_1	-0.50
R_2 [m]	-0.60
R_3 [1/m]	-0.99
R_4	-1.09

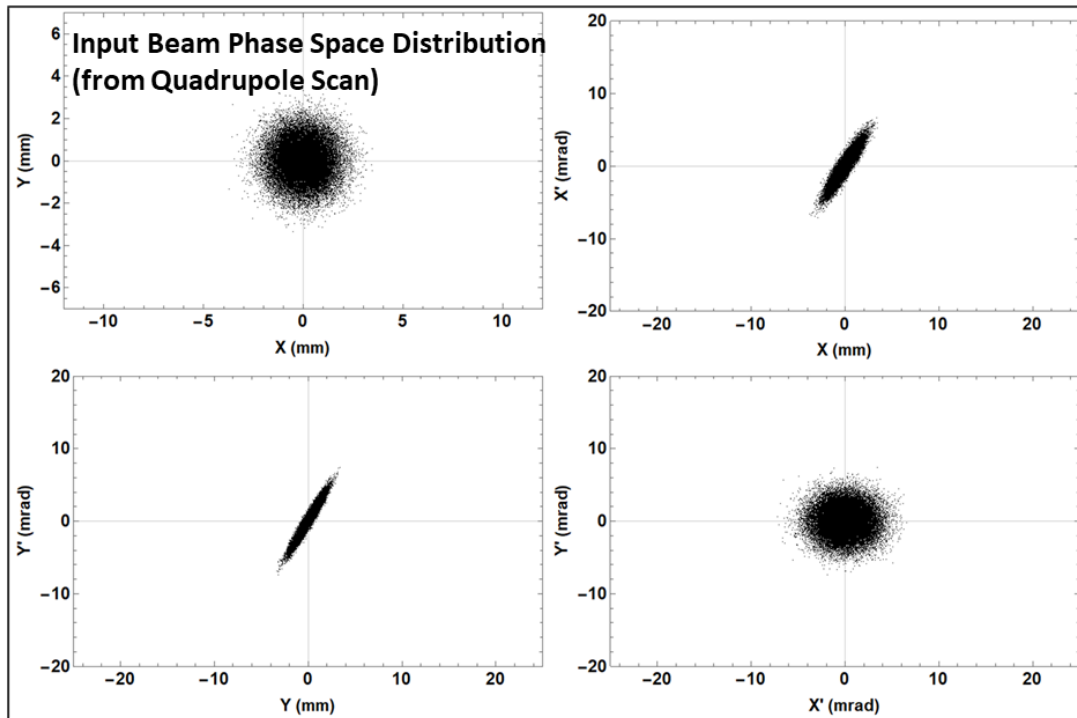


Figure 6.3: The input beam phase-space distribution. The the values of emittance and Twiss parameter for these distributions are given in Table 6.2.

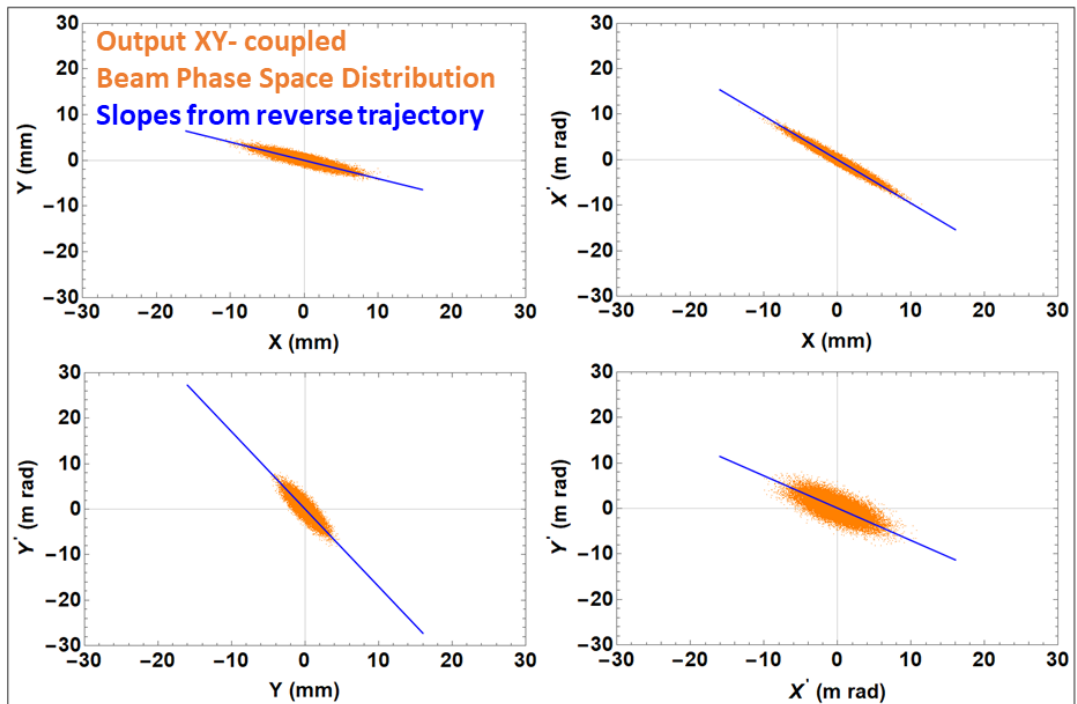


Figure 6.4: The coupled beam phase-space at the matching point. The line (blue) are the required beam slopes at the injection point.

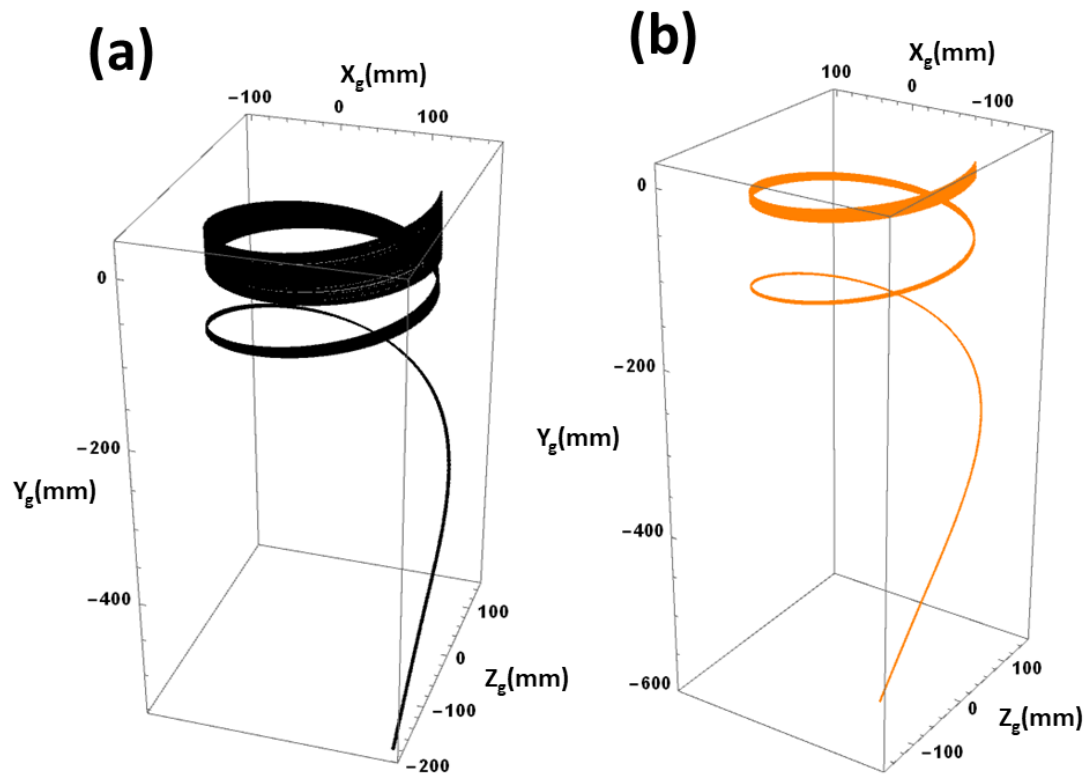


Figure 6.5: (a) The beam injection into the storage magnet without phase space matching, the phase-space distribution and the emittance and Twiss parameters are given in Fig. 6.3 and Table 6.2 respectively. (b) The beam injection into the storage magnet with phase-space matching, the phase-space distribution and the emittance and Twiss parameters are given in Fig. 6.4 and Table 6.3, 6.4 respectively.

6.1.3 Errors on the Beam Phase-Space Slopes

In this section, the effect of errors on the slopes of beam phase-space correlation will be described. A pseudo error was introduced to each slope (a_{xy} , $a_{xx'}$, $a_{yy'}$, $a_{x'y'}$) independently and its effect on the vertical beam size growth was checked by tracking simulation. From this study, we found that which beam phase-space correlation is most and least sensitive to the beam vertical blow-up.

Figure 6.6 shows the slopes of the beam phase-space at the matching point. The blue lines in Fig. 6.6 shows the slopes without any error while the other colors represent 5% (black), 10% (red), 15% (green), and 20% (orange) errors to the original slope value. In order to reveal the effect of each correlation on the vertical beam size growth in the storage magnet, error to each slope of correlation was applied independently, while other slopes were kept at their original values.

Figure 6.7 shows the tracking simulation of the beam injection into the storage magnet with the error on (X, Y) correlation, while the other slopes were kept at their original value. Figure 6.7 (a) shows the tracking with 0% error on the a_{xy} slope, whereas (b), (c), and (d) shows the beam injection into the storage magnet with 5%, 10%, 15%, error on slope of a_{xy} . The vertical beam size growth as a function of the error on a_{xy} slope can be seen very clearly.

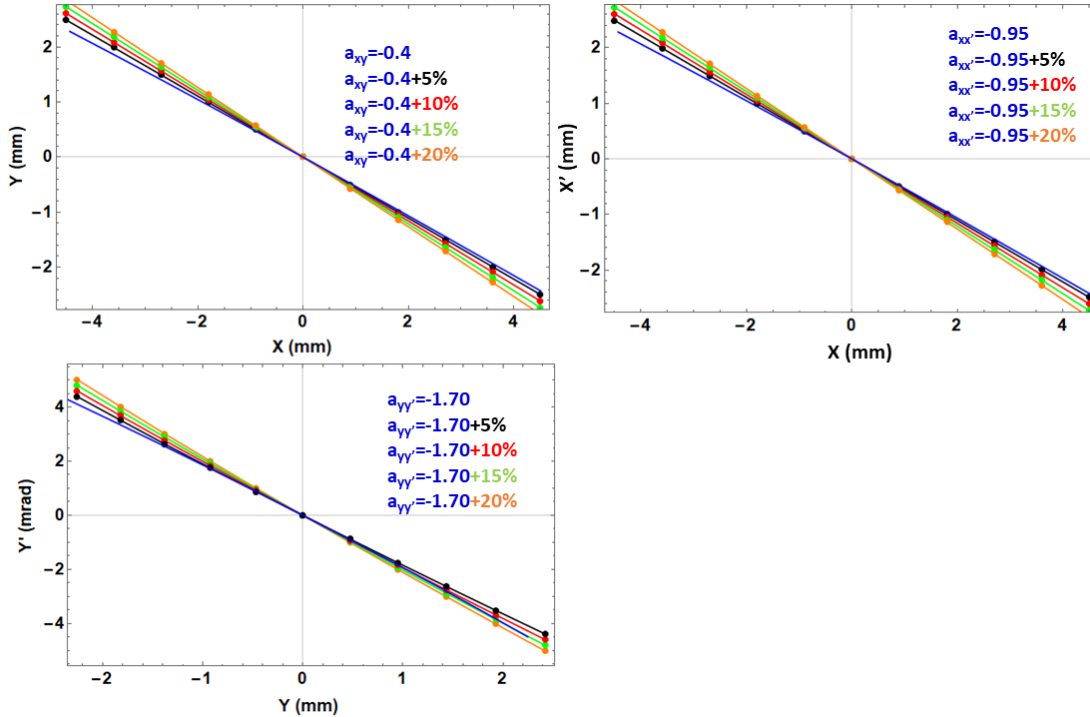


Figure 6.6: The slopes of the beam phase-space at the matching point. Error of 5%, 10%, 15%, and 20% was introduced to each correlation in order to find their effect on the vertical beam size in the storage magnet.

Figure 6.8 present the summary of the vertical beam size growth at the kick point due to the change in the slopes of a_{xy} , $a_{xx'}$ and $a_{yy'}$. The biggest growth in the beam size was observed due to the change in (X, Y) correlation slope (a_{xy}). In the case of 20% change in a_{xy} slope beam size grows to the 5.06 mm, whereas, it grows to the 3.20 mm and 2.15 mm in the case of 20% change in $a_{yy'}$, and $a_{xx'}$ respectively.

The radial fringe field of the solenoid magnet causes the vertical blow-up of the injected beam. As the beam moves through the storage magnet, the particles at different vertical positions sense different radial field and eventually takes different vertical paths. Therefore, the (X, Y) correlation slope (a_{xy}) is most sensitive to the vertical blow-up of the beam. In the injection region of the storage magnet, there is no vertical focusing force is present, therefore, the error on $a_{yy'}$ slope also have effect on vertical blow-up. Whereas, in the horizontal direction solenoid magnet has intrinsic focusing, therefore, the error on $a_{xx'}$ slope does not impose any significant effect on the vertical beam size growth.

For the field index value of 1.65×10^{-2} the vertical beam size should be around 8 mm in order to have sufficient injection efficiency (forth coming section). This study shows that, If we control the slope of a_{xy} with the 10% error and $a_{yy'}$ and $a_{xx'}$ with slopes error of 20% than goal of 8 mm beam size can be achieved.

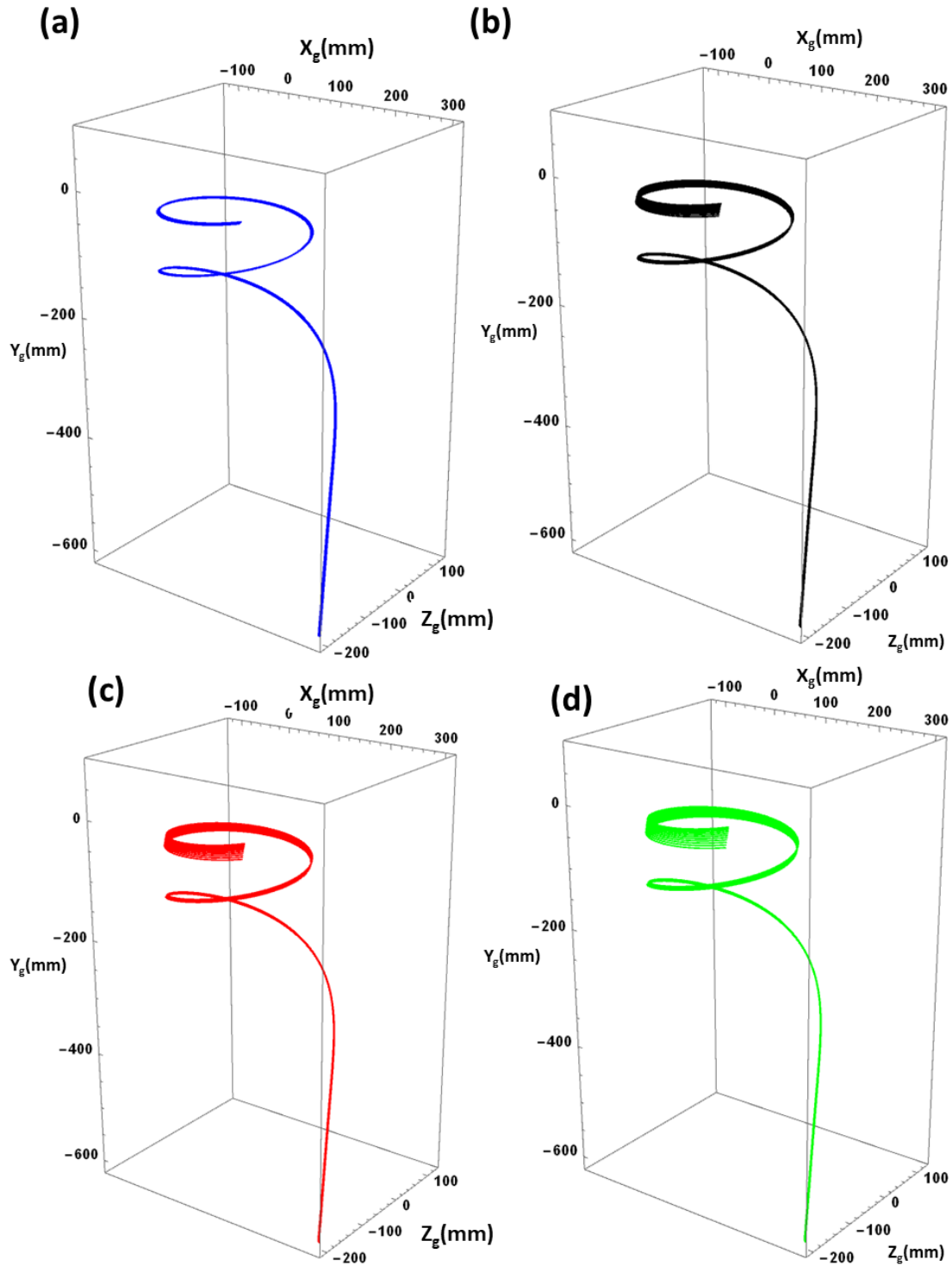


Figure 6.7: (a) The beam injection into the storage magnet with 0% error on the a_{xy} slope, while other slopes ($a_{xx'}$, $a_{yy'}$) were kept at the original values. Where (b), (c), and (d) shows the beam injection into the storage magnet with 5%, 10%, 15%, error on slope a_{xy} slope.

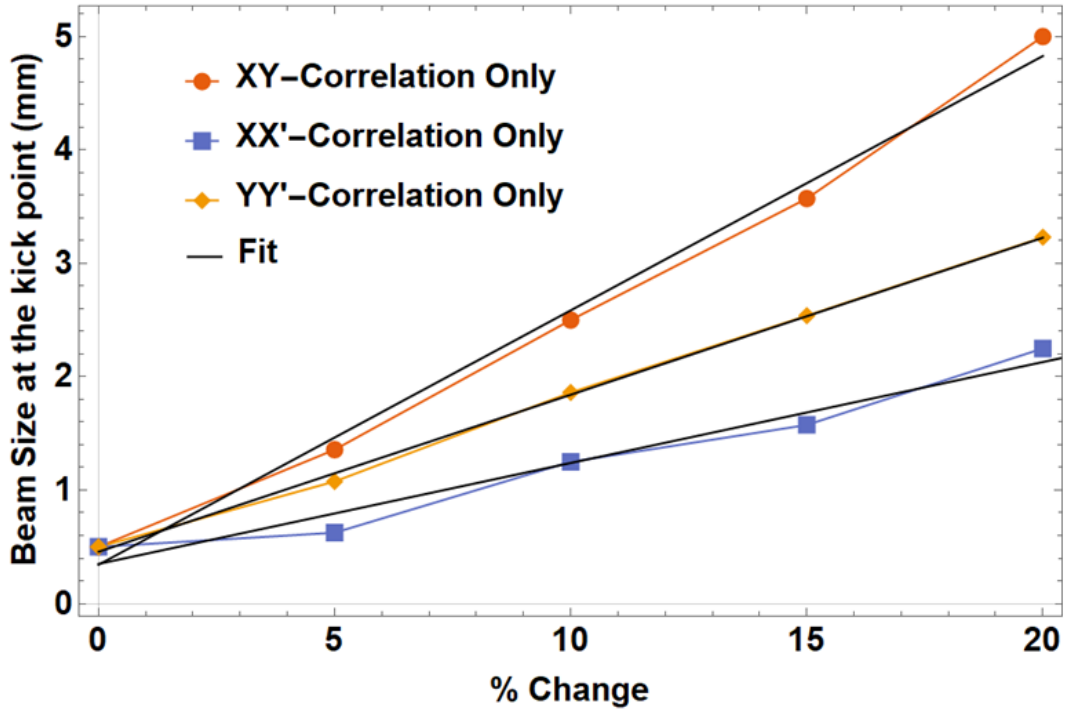


Figure 6.8: The vertical beam size growth at the kick point due to the change in the slope values. The biggest growth in the beam size was observed due to the change in $X - Y$ correlation slope. And the (X, X') correlation has the least effect on the beam growth.

6.2 The Matching Beamline

The SAD ² [79] program was utilized to calculate the beamline optics for the phase space matching. Ideally, four rotatable quadrupole magnets are enough to generate the required beam phase-space. In the case of four rotatable quadrupole magnets, one will have 8 free parameters, to control the 8 parameters of the beam optics ($\alpha_{x,y}, \beta_{x,y}$ and R_1, R_2, R_3, R_4). In the case of four quadrupole magnets required strength for the rotatable quadrupole magnets and drift space becomes stringent. Therefore, at least six quadrupole magnets are required to generate phase-space matching with the realistic parameters of the beamline. Figure. 6.9 show the evolution of the beta function and beam size through the optics element. Table 6.5 represents the required rotation angles and the strength of the beamline quadrupole magnets. The positive values of the k (quadrupole magnet strength) is corresponds to the horizontal focus and negative shows the vertical focus. Figure 6.10 (left) 3-D plot of tracking simulation of the beam injection with appropriate coupling as mentioned in the Table 6.3 and 6.4. Figure 6.10 (right) represents the histogram of the vertical beam size as a function of the vertical beam position. In the case, of the perfect matching vertical beam size still grows to the 5.3 mm at kick point due to the finite size of beam phase-space area at the injection point.

²Strategic Accelerator Design program developed at the KEK.

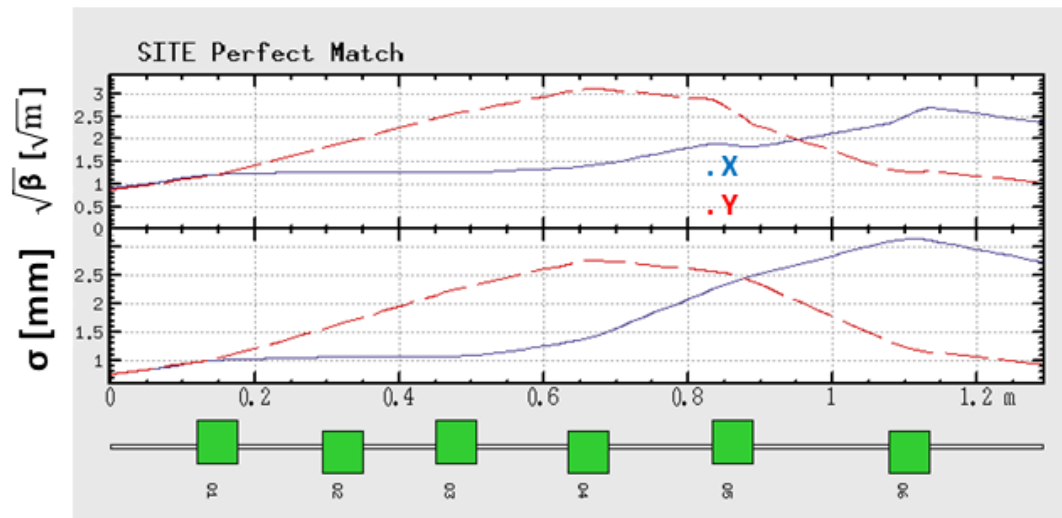


Figure 6.9: The evolution of the beta function and beam size through the array of six quadrupole magnets.

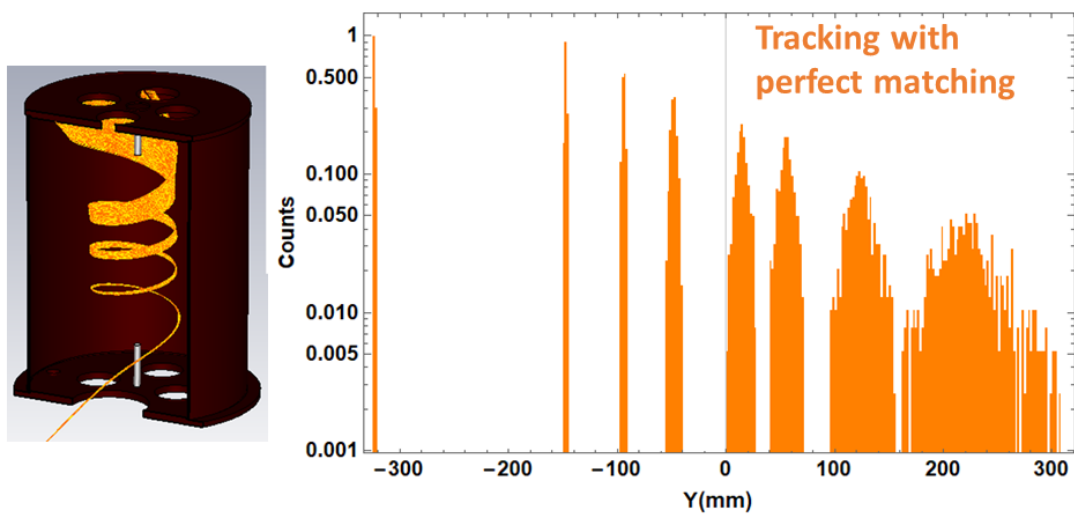


Figure 6.10: Left: The 3-D plot of tracking simulation of the beam injection with appropriate coupling as mentioned in the Table 6.3 and 6.4. Right: The histogram of the vertical beam size as a function of the vertical beam position.

Table 6.5: Matching beamline quadrupole magnets parameters

Parameters	Rotation Angle (Radian)	$K[\text{m}^{-2}]$
Q_1	0.2260	2.58
Q_2	0.4758	-2.10
Q_3	1.6587	1.10
Q_4	-0.3314	-0.83
Q_5	0.7494	0.86
Q_6	1.8395	1.83

6.3 Three Rotatable Quadrupole Magnets Solution

As mentioned in the previous section six quadrupole magnets are needed to perfectly match the initial uncoupled beam to the 3-D spiral injection requirement. Due to the limited space at the SITE beamline, it was not possible to construct a beamline consist of six rotation quadrupole magnets for phase-space matching.

In the case of SITE, the value of the field index is $n = 1.65 \times 10^{-2}$ which provides weak focusing in the region of $Y_g = \pm 50$ mm. From the kicker simulation³ it was determined that if the vertical beam size becomes 8 mm at kick point, then nearly 80% of the beam can be stored. The field index value of $n = 1.65 \times 10^{-2}$ provides a big region to store the beam, hence it relaxes the beam phase-space matching requirement.

From the tracking simulation, it was found that the appropriate combination of three rotatable quadrupole magnets can reduce the vertical beam size up to the 8.06 mm at the kick point. Therefore, three rotation quadrupole magnets were designed and manufactured for the SITE.

6.3.1 Beamline

The matching beamline consists of three rotatable quadrupole magnets, a bending magnet, and drift spaces. Figure 6.11 (a) shows the dimensions of the matching beamline and (b) presents the photo of the experimental setup. These three rotatable quadrupole magnets can be rotated at an arbitrary angle around the beam. The transfer matrix of the beam transport line can be written as follow:

$$M = L_5 \cdot B_{vf} \cdot L_4 \cdot Q_3 \cdot L_3 \cdot Q_2 \cdot L_2 \cdot Q_1 \cdot L_1 \quad (6.13)$$

where, M is a transport line matrix, D represents the drift space, Q_1 , Q_2 , and Q_3 denotes the quadrupole magnets. In the SITE beamline, a rectangular pole dipole magnet was utilized to inject the beam into the storage magnet. The rectangular bending magnet acts as a drift space

³The electron beam tracking in the transient field of the kicker coil. In the forthcoming Chapter, it will be discussed in detail.

in the deflection plane, in the non-deflecting plane it has a finite focusing effect. In the case of 40 Degree injection angle the SITE's bending magnet has focusing strength of $k_b[\text{m}^{-2}] = 21.88$ in the non-deflecting plane. This effect was also included in the transport line program.

A simple beamline program had been developed to set the slopes of the input beam phase-space distribution to the required slopes by changing the focusing strength and rotation angle of the quadrupole magnets. The slope of (X, Y) slope was preferentially adjusted to the required slope and $a_{yy'}$ partially adjusted to the required slope value. And we neglected the $a_{xx'}$ slope as mention in the section 6.1.3.

Table 6.6 lists beamline drift spaces and Table 6.7 shows the experimental set values of quadrupole magnet strengths and rotation angles. The positive value of k shows the horizontal focus while negative values correspond to the vertical focus. These beamline settings were obtained from the program as described above.

As explained in Section 6.1.3, when the beam traverse through the storage magnet, the particles at different vertical positions sense different radial field and eventually takes different vertical paths. Therefore, the (X, Y) correlation slope (a_{xy}) is most sensitive to the vertical blow-up of the beam. In the injection region of the storage magnet, there is no vertical focusing force is present, therefore, the error on $a_{yy'}$ slope also have a considerable effect on vertical blow-up. Whereas in the horizontal direction solenoid magnet has intrinsic focusing, therefore, the error on $a_{xx'}$ slope does not impose any significant effect on the vertical beam growth.

The simulated beam phase-space with the three rotation quadrupole magnets settings as mentioned in the Table 6.7 are shown in the Fig. 6.12. Figure 6.13 shows the beam profile of the injected beam. False colors were added to the picture for better visualization. The white line in Fig. 6.13 is the fitted slope to the beam profile. For the reasons explained above the slopes of (X, Y) and (Y, Y') correlations were preferentially matched with the ideal slopes.

Table 6.6: The drift spaces for the beamline.

Parameters	Length [mm]
L_1	2.35
L_2	12.25
L_3	22.45
L_4	28.25
L_5	210.3

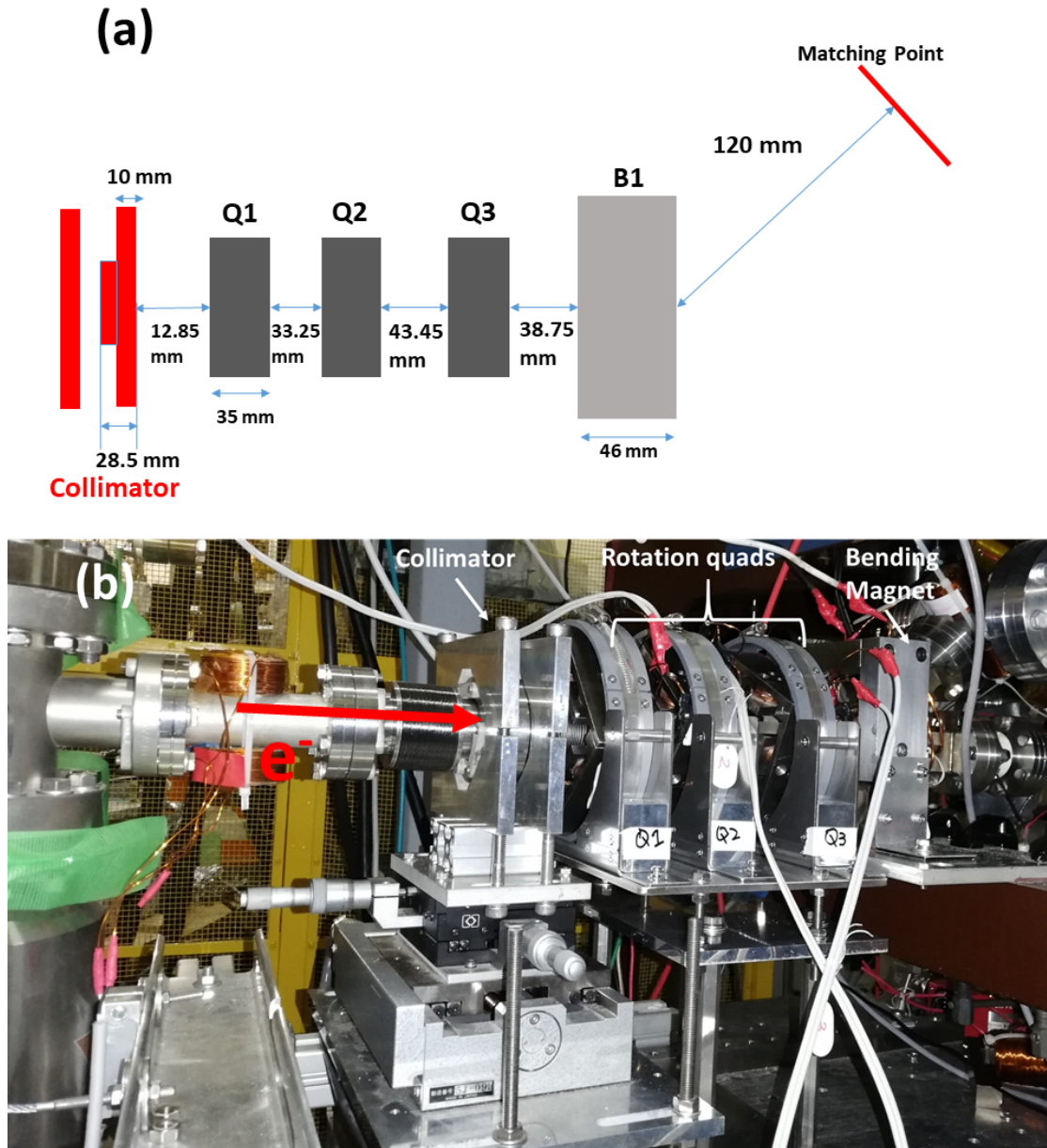


Figure 6.11: (a) The layout of the beamline, beamline composed of three rotatable quadrupole magnets, a rectangular bending magnet and drift space. The rotatable quadrupole magnets were placed in the downstream direction of the collimator. The dimensions and mutual distances among magnets are also shown. (b) The photo of the experimental setup of the matching beamline.

Table 6.7: The Three Rotatable Quadrupole Magnets Matching Beamline Parameters.

Focusing	Quadrupole	Rotation Angle (Degree)	$k[\text{m}^{-2}]$
H	Q_1	20.0	53.17
V	Q_2	26.0	-67.76
V	Q_3	0.0	-24.14

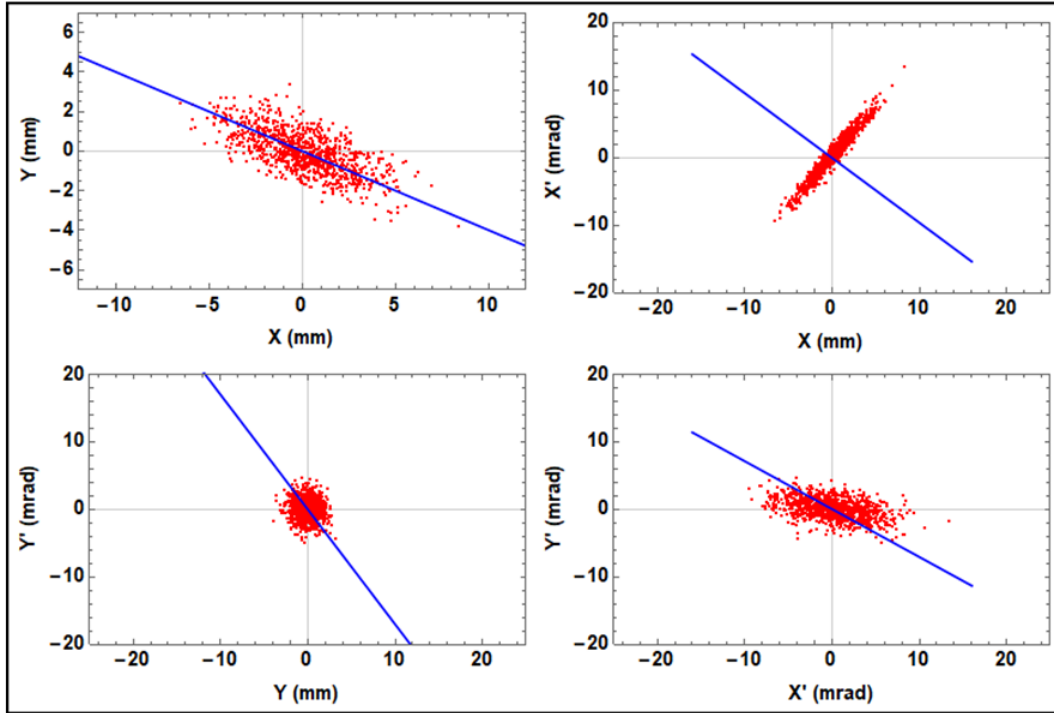


Figure 6.12: The simulated beam phase-space with the three rotation quadrupole magnets. The solid blue line shows the ideal slopes for the beam phase-space matching. The beamline setting is described in the Table 6.7.

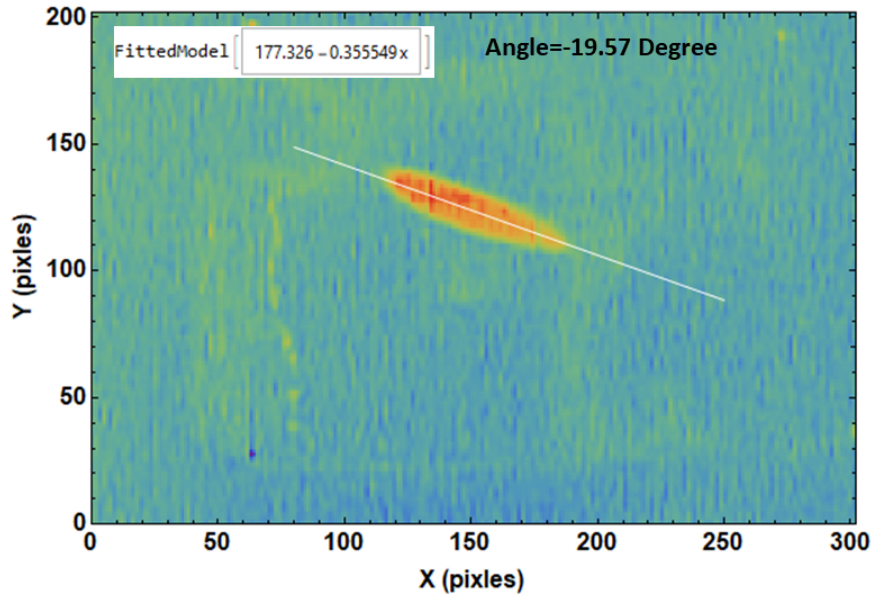


Figure 6.13: The beam profile of the injected beam. The false colors were added to the picture for better visualization.

6.4 Results

In this section, firstly the beam injection into the storage magnet without rotation quadrupole magnets will be described and in the later part, the beam injection with rotatable quadrupole magnets will be described. The results of the gas monitor and wire scanner with different injection are presented and discussed to examine the effect of the beam phase-space matching on the vertical beam size growth. Here, only the results of the beam injection into the storage magnet without any phase space matching and with the best setting that was achieved with the three rotation quadrupole magnets are presented. The wire scanner results with some other settings of the three rotation quadrupole magnets can be seen in Appendix B.

6.4.1 Injection without Rotatable Quadrupole Magnets

In the first step, the beam was injected into the storage magnet while rotatable quadrupole magnets were off. This experiment was performed, in order to reveal the effect of a complete beam mismatch on the vertical beam size growth. Figure 6.14 (above) shows a simulation of the beam phase-space distribution without applying rotatable quadrupole magnets and Fig. 6.14 (below) is the injected beam profile at the beam profile monitor.

Gas Monitor Results

As reported in Chapter 4, in gas monitor the electron beam passes through nitrogen gas, it excites the nitrogen gas molecules. Nitrogen gas de-excitation results in a light emission in the blue wavelength range $390 \text{ nm} < \lambda < 470 \text{ nm}$ [55]. The light from the nitrogen gas de-excitation

was collected by a CCD camera [61]. Figure 6.15 (above) is the gas monitor results of the beam injection into the storage magnet without rotatable quadrupole magnets. The false colors were added to the photo for better visualization. Figure 6.15 (below) shows the horizontal projection of the above picture. As expected, the beam blow-up in the vertical direction as it traverses through the storage magnet without phase-space matching, this effect can be easily visualized qualitatively from the gas monitor result as shown in Fig. 6.15. The gas monitor provides a quick and efficient way of beam monitoring inside the storage magnet, but the lack the quantitative information of the beam size inside the storage magnet. Therefore, a wire scanner was utilized to extract the qualitative information of the beam position and size in the storage magnet.

Wire Scanner Results

In order to measure the beam profile and position information inside the storage magnet, a new type of wire scanner was employed. Please refer to Section 4.2 of Chapter 4, for the detailed principle and structure of the wire scanner system.

The signal from the wires was taken out of the vacuum chamber via electrical vacuum feedthroughs and terminated into the 1 M Ω terminal of an oscilloscope [69]. The data (voltages) were collected using a custom made GUI C# program. Please refer to Appendix A for detail of C# code. The beam current can be calculated by using Ohm's law: $V = IR$, where V is the voltage collected from the oscilloscope, R is the resistance, and equal to 1 M Ω , I is the beam current. During the beam test, the beam current at the Faraday cup was 40 μ A.

Figure. 6.16 (a) shows the CST-PS [36] tracking simulation of the beam injection into the storage magnet with the beam phase-space as given in Fig. 6.14 (No phase-space matching). The beam current was set 40 μ A for the CST-PS simulation. The black open circles show the points at which the beam sizes were measured by using the wire scanner 1. For the convenience, the wire scanner results and simulation are shown in global coordinates (X_g, Y_g, Z_g). Here, Y_g shows the storage magnet (solenoid) axis.

Figure 6.16 (b) details the data of wire scanner 1. The horizontal axis (Y_g) in Fig. 6.16 (b) shows the vertical position of the wire scanner in the storage magnet, and the vertical axis presents the beam current measured along the storage magnet axis. The peaks position in Fig. 6.16 (b) illustrate the beam signal at the different vertical position, and the width of the peak shows the vertical beam size along the storage magnet axis. The distance between these peaks shows the spacing between electron beam orbits, here we refer it as *pitch distance*. The curves in wire scanner data seem to follow the Gaussian distribution. Therefore, we fit the experimental data with the Gaussian function. The multi-peak Gaussian function used to fit the experimental data globally can be written as follows:

$$f(x) = w + \sum_{i=1}^n \frac{1}{\sqrt{2\pi\sigma_i^2}} e^{-\frac{(x_i - \mu_i)^2}{2\sigma_i^2}}, \quad (6.14)$$

where w is the estimation of the baseline and n corresponds to the number of peaks. The

black points in Fig. 6.16 (b) are the wire scanner 1 data, the green histogram illustrates the simulation results of vertical beam size. The orange line is a global fit to the experimental data. The dashed blue line corresponds to the local peak fitting.

Figure 6.17 reports the wire scanner 2 data. The wire scanner 2 was located at 180 Degree away (half cyclotron period) from the wire scanner 1 position. Figure 6.17 (a) shows the simulation and the black open circle illustrates the points at which vertical beam size was measured. Figure 6.17 (b) presents the wire scanner 2 data, black points illustrate wire scanner data and the green histogram presents the simulation results of vertical beam size, and orange and blue curves are global and local fitting to the data. The simulation and experimental data are in good agreement with each other. And no significant discrepancy was found

The vertical beam size at the injection point ($Y_g = -345.46$ mm) was 1.4 ± 0.02 mm. When the beam reaches near to the kick point ($Y_g = -59.57$ mm), the vertical beam size increase up to 31.25 ± 0.21 mm. This large value of vertical beam size at the kick point will greatly reduce the injection efficiency. This drastic beam blow-up in the storage magnet occurred due to beam phase-space miss-matching at the injection point. These results of the wire scanner indicate the need for the beam phase-space matching, to avoid the beam blow-up in the vertical direction.

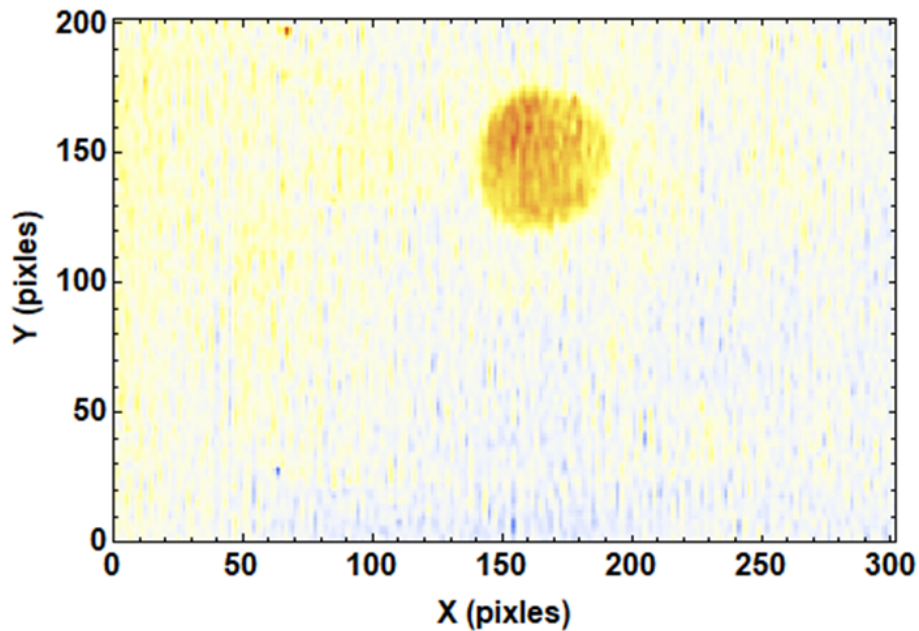
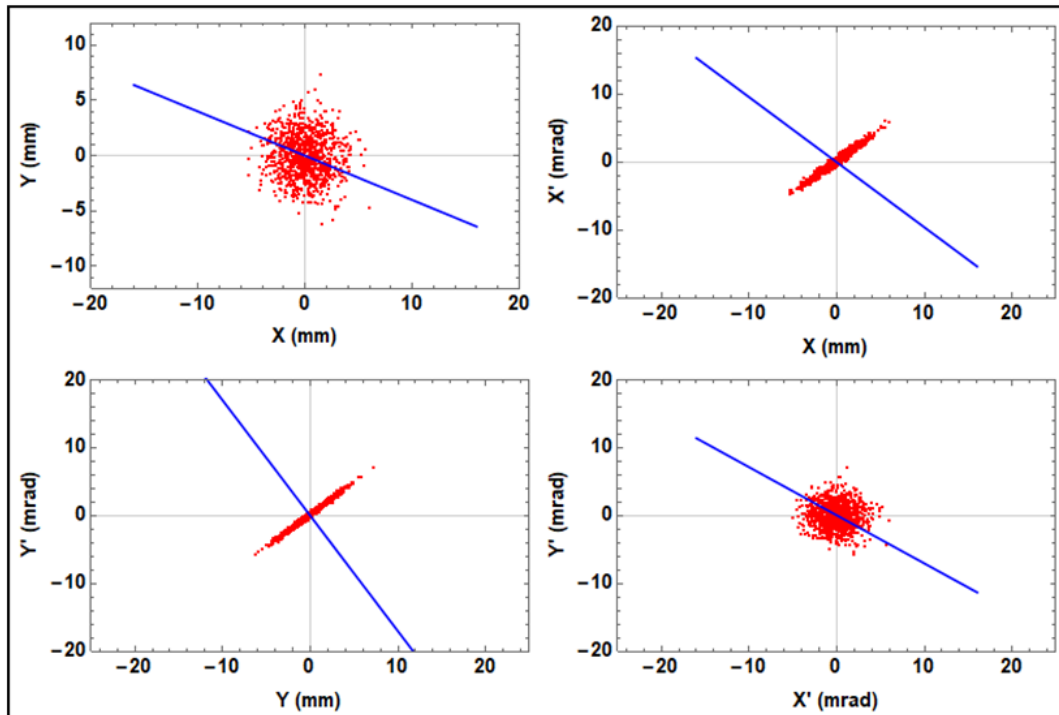


Figure 6.14: Above: The simulation of the beam phase-space distribution without applying quadrupole magnets. Below: The injected beam profile at the beam profile monitor. The false colors were added for the better visual effects.

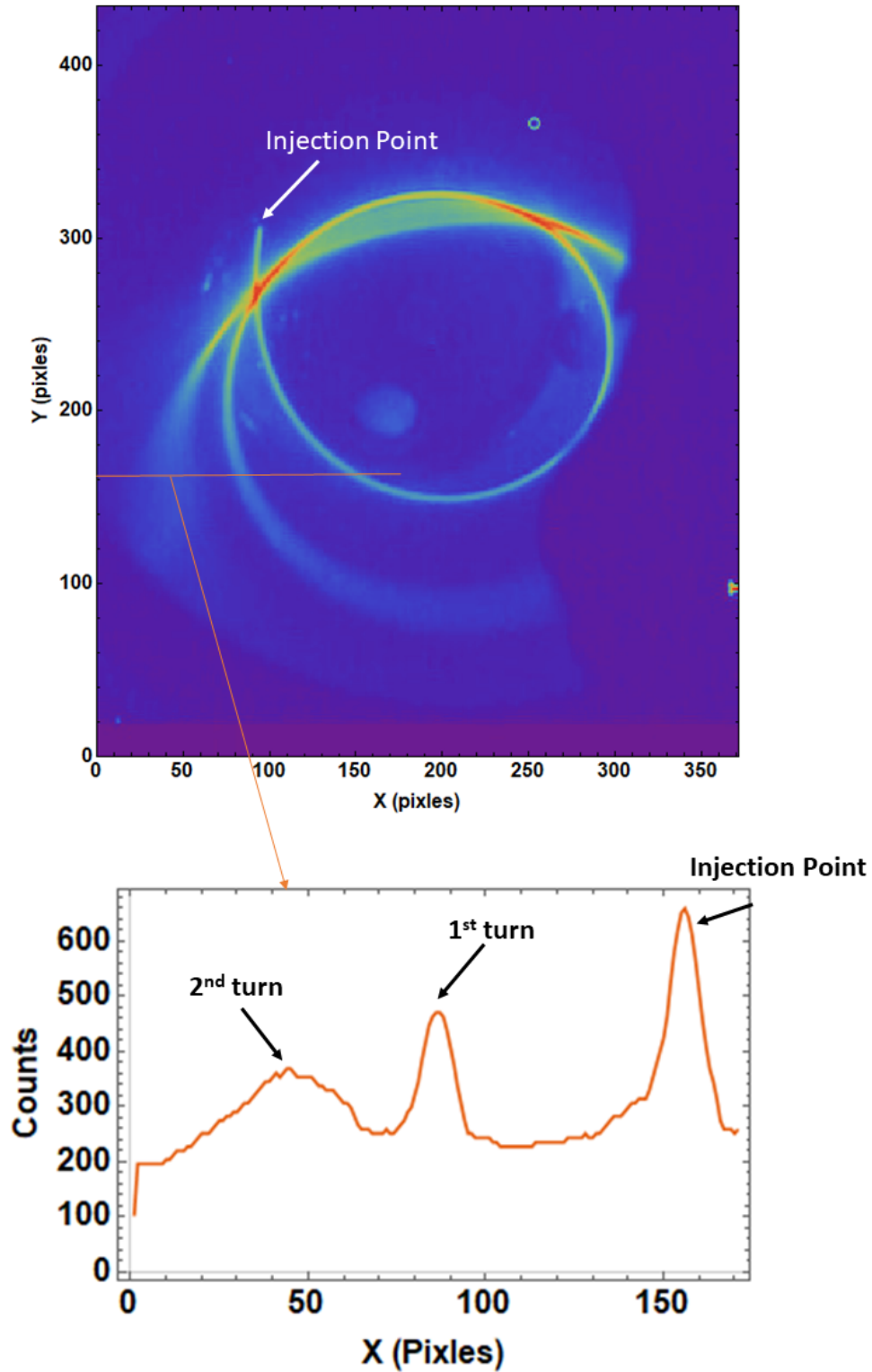


Figure 6.15: Above: The gas monitor results of the beam injection into the storage magnet without rotation quadrupole magnets. The false colors were added to the photo for better visualization. It is evident from the gas monitor results that the beam blow-up in vertical direction as it traverses through the storage magnet.

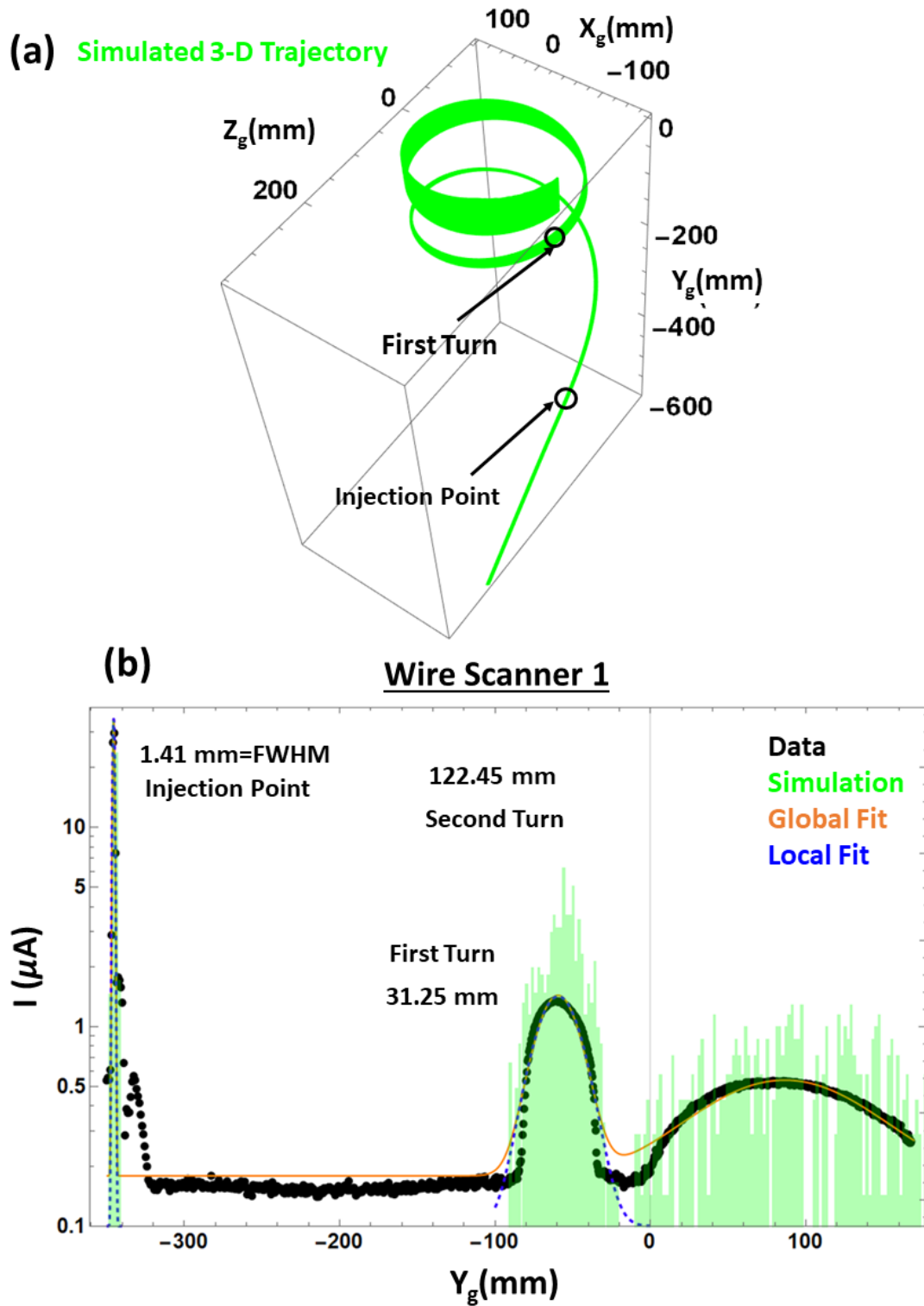


Figure 6.16: (a) The tracking simulation of the beam injection (CST-PS) into the storage magnet without phase-space matching. The black open circle shows the points at which the beam sizes were measured. (b) The vertical beam size was measured by using a wire scanner. The black points are the wire scanner 1 data. The green histogram is a simulation result of CST-PS. The orange line is a global fit to experimental data.

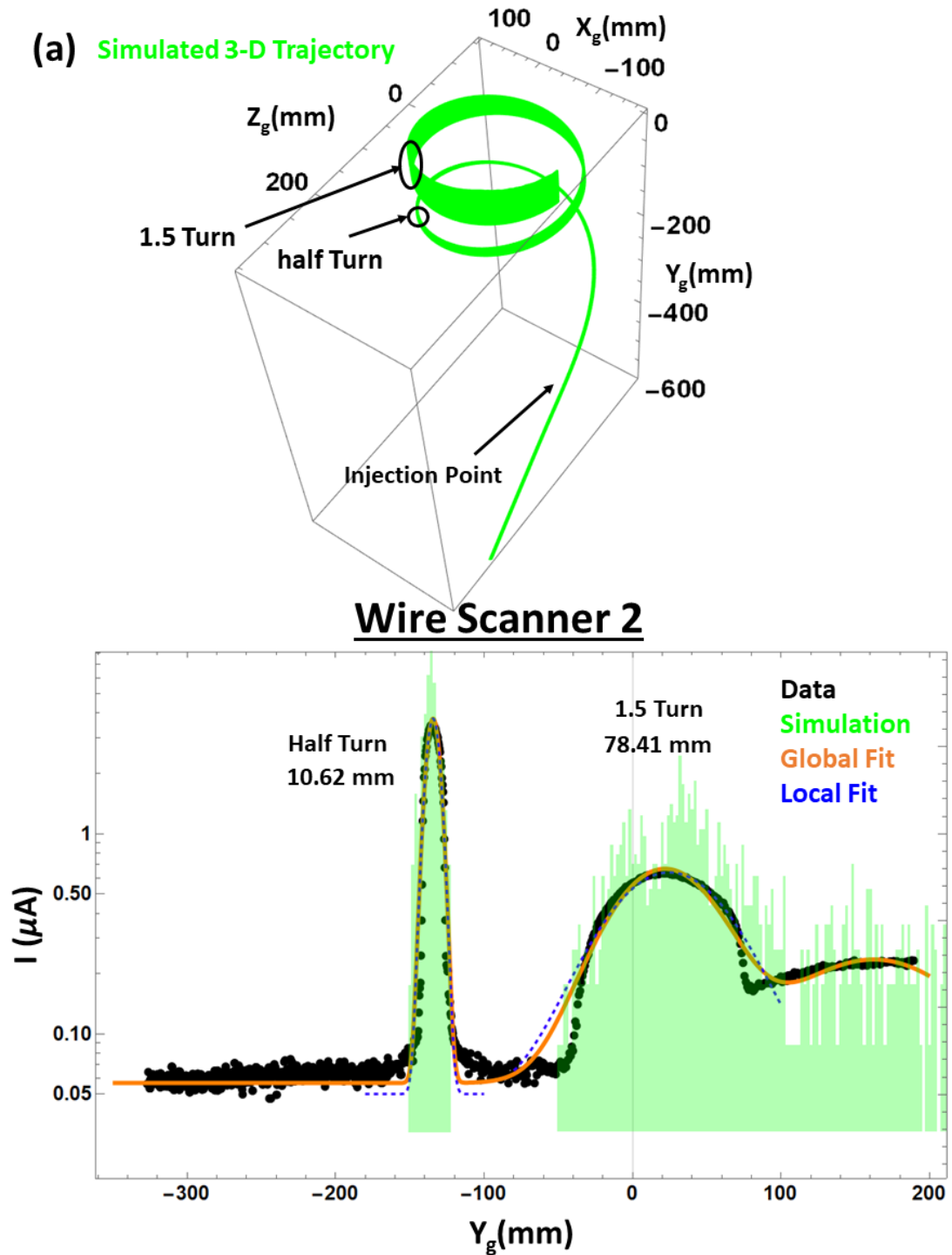


Figure 6.17: (a) The tracking simulation of the beam injection (CST-PS) into the storage magnet without phase-space matching. The black open circle shows the points at which the beam sizes were measured. (b) The black points are the wire scanner 2 data. The green histogram is a simulation result of CST-PS. The orange line is the fit to experimental data. The wire scanner 2 is located at 180 Degree away (cyclotron period) from the wire scanner 1 position.

6.4.2 Injection with Normal Quadrupole Magnets

In this case, the beam phase only with the Twiss parameters as mentioned in the Table 6.3 assumed and coupling parameters were set to zero, in order to reveal the effect of only Twiss parameter matching on the beam vertical size in the storage magnet. Figure 6.18 (a) shows the beam phase-space at the injection point. Figure 6.18 (b) illustrate the tracking in CST-PS with the beam phase space as mentioned in the Figure 6.18 (a), as the beam traverse through the storage magnet beam blow-up drastically in the vertical direction. It shows that the most xy-coupling to beam cross section is the most important parameter to controls the vertical beam spread in the solenoidal-type storage magnet.

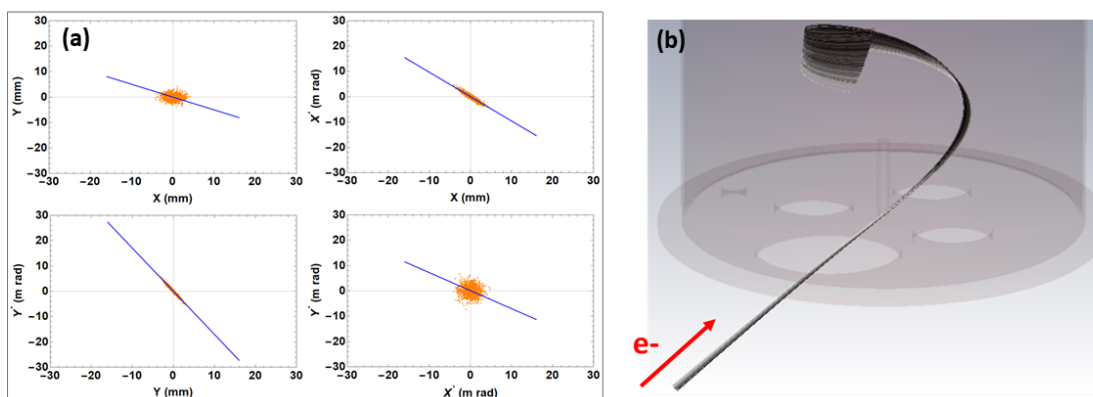


Figure 6.18: (a) The beam phase-space at the injection point with the Twiss parameters as listed in the Table 6.3 , but coupling parameters were set to zero. (b) Particle Tracking with the beam phase-space as mentioned in the in (a) as the beam traverse through the storage magnet beam blow-up drastically in the vertical direction. It signifies that the xy-coupling to the beam cross section is the most important parameter to controls the vertical beam spread in the solenoidal-type storage magnet.

6.4.3 Injection with Rotatable Quadrupole Magnets

In this section, the effect of the rotatable quadrupole magnets on the beam size growth in the storage magnet will be described.

Gas Monitor Results

The gas monitor result of the beam injection into the storage magnet with rotation quadrupole magnet setup as given in Table 6.7 is shown in Fig. 6.19 (above). The false colors were added to the photo for better visualization. The beam enters into the storage magnet from the injection hole and starts taking a spiral path into the storage magnet. Figure 6.19 (below) presents the horizontal projection of the above picture at a position highlighted in a thin line in Fig. 6.19 (above). The three turns can be visualized easily from this data. As anticipated from the simulation, the vertical beam blow-up significantly decreases with the appropriate setting of three rotatable quadrupole magnets.

Wire Scanner Results

Figure 6.20 (a) shows the beam tracking simulation with the beam phase-space as shown in the Fig. 6.12, the black open circle presents the positions where beam size was measured by the wire scanner. Figure 6.20 (b) shows the vertical beam size measured by using a wire scanner with the rotatable quadrupole magnets set up. Note that the vertical axis is the log scale. The black points are the wire scanner 1 data and the red histogram is a simulation result of CST-PS. The orange line is the multi-peak Gaussian fit to experimental data and dashed blue lines correspond to the local fit to each peak.

The wire scanner 2 simulation and data is shown in Figure 6.21. The wire scanner 2 is located at 180 Degree away (half cyclotron period) from the wire scanner 1 position. Figure 6.20 (b) represents the vertical beam size measured by using a wire scanner 2. The red histogram is a simulation result of CST-PS. The orange line is the fit to experimental data. As the beam traverse through the storage magnet, the amplitude of the peak decrease but the area under the curve ($A = \int I dy$, A is the area and I is the beam current) remains the same. In the wire scanner 1 data, the area under the first peak (injection point), second peak (first turns), and third peak (second turn) is $A = \int I dy = 41.91 \text{ A mm}$, 40.31 A mm , and 39.69 A mm respectively. From injection point to second turn the area under the curve changes 5.3%. This decrease could be due to some lost particles as the beam moves through the storage magnet.

The wire scanner results clearly show that the vertical beam blow-up reduced dramatically with the rotatable quadrupole magnets. The vertical beam size at the injection point ($Y_g = -344.30 \text{ mm}$) was $2.51 \pm 0.02 \text{ mm}$. When the beam reaches near to the kick point ($Y_g = -82.61 \text{ mm}$), the vertical beam size becomes to $8.06 \pm 0.21 \text{ mm}$. This value of vertical beam size at the kick point will provide 81% of the injection efficiency. This reduction in vertical beam size blow-up confirms our beam phase-space matching strategy.

The horizontal beam profile also has been measured by rotating vertical wire on the wire scanner 1. Please refer to the Section 4.2.1 of Chapter 4 for the detailed mechanism of horizontal beam size measurement monitor. Since the only one rotary actuator was available, therefore, horizontal beam profile had been measured only at the wire scanner 1 position. In order to extract the horizontal beam size, the vertical wire was placed at the fixed vertical position, and the wire scanner support bar was rotated at its own axis by the rotary actuator. As vertical wire rotates it provides the information of horizontal beam position and horizontal beam size.

Figure 6.22 (a) presents the 2-D projection of the beam profile in the storage magnet. The positive X_g -axis corresponds to the wire scanner 1 location and negative show the wire scanner 2 location. The black histogram is the CST-PS simulation and gray color show the experimental data. Figure 6.22 (b) is the zoom up view of the wire scanner 1 location. The horizontal beam profile at different vertical positions is shown in Fig. 6.23. The black points are the experimental data, the red histogram is the simulation, and the orange line is a fit to the experimental data. As explained earlier solenoid-type storage magnet has an intrinsic focusing effect in the horizontal direction, therefore, a horizontal beam does not grow in the storage magnet as the beam traverse through the storage magnet. The average horizontal beam profile form first turns to the second turn was 0.65 mm (1σ).

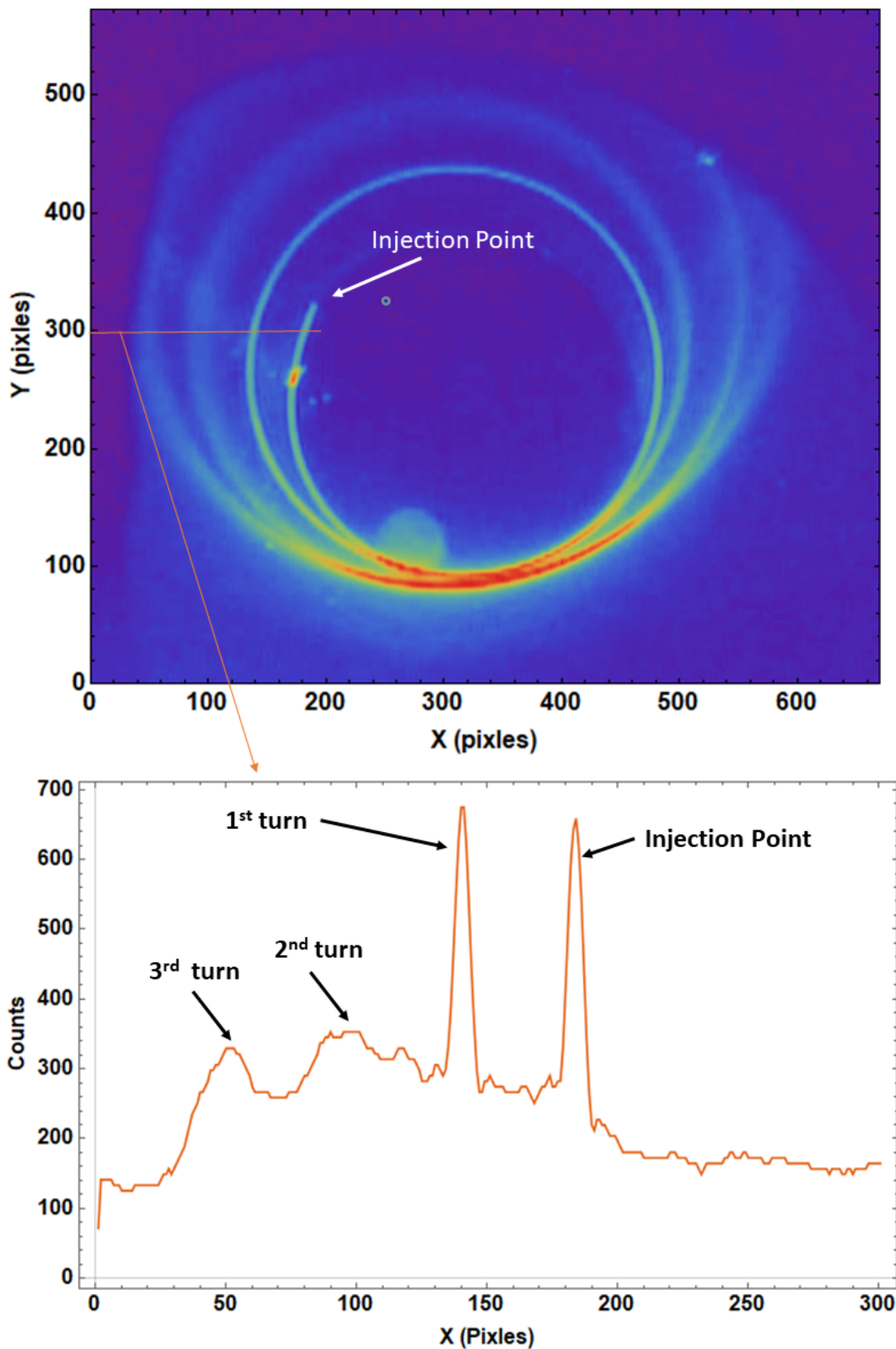


Figure 6.19: Above: The gas monitor results of the beam injection into the storage magnet with rotation quadrupole magnets set up as mentioned in Table 6.7. Below: The horizontal projection of the above picture. The three turns can be visualized easily from this data.

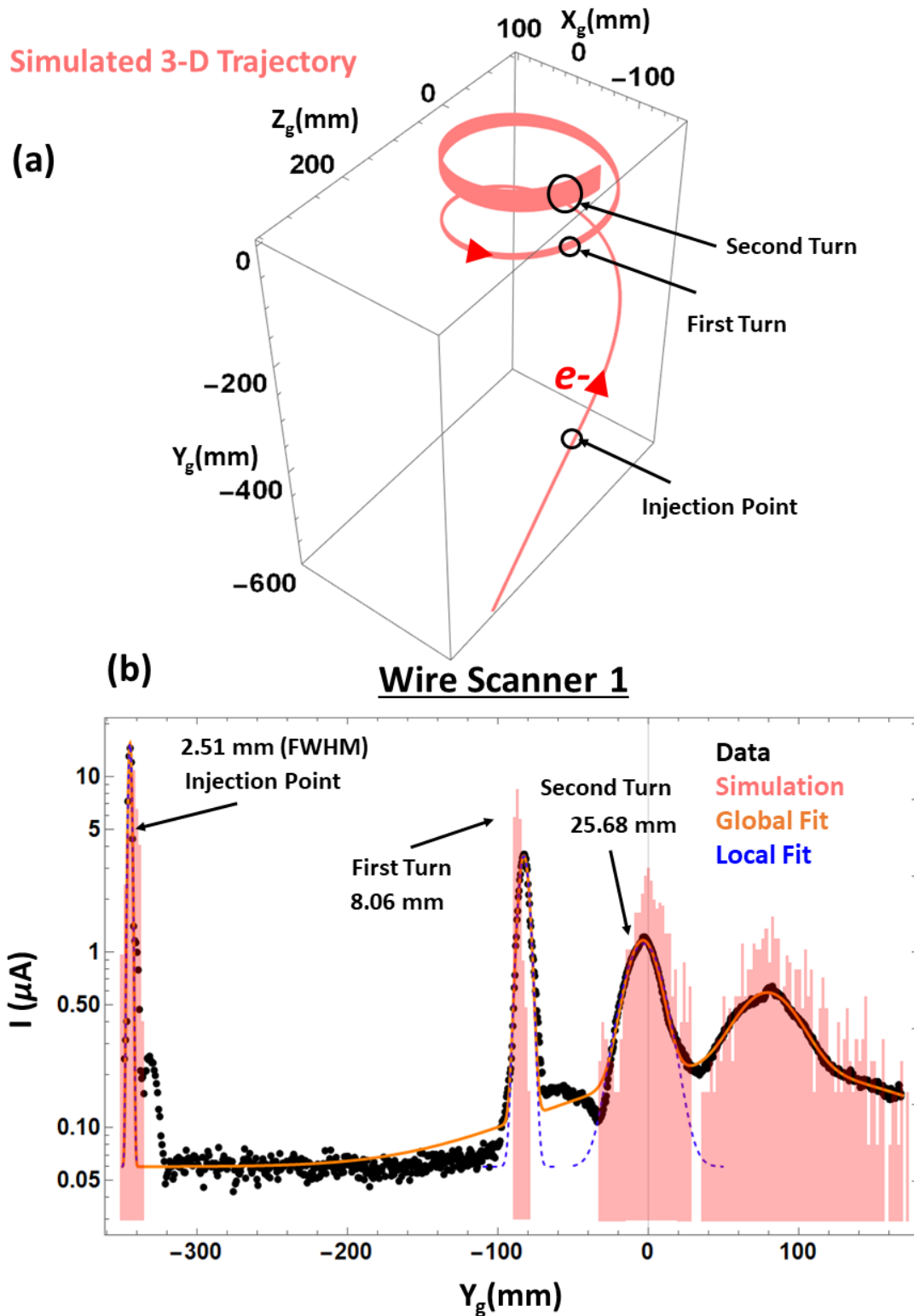


Figure 6.20: (a) The tracking simulation of the beam injection (CST-PS) into the storage magnet without phase-space matching. The black open circle shows the points at which the beam sizes were measured. (b) The vertical beam size is measured by using a wire scanner. The black points are the wire scanner 1 data. The red histogram is a simulation result of CST-PS. The orange line is the global fit to experimental data.

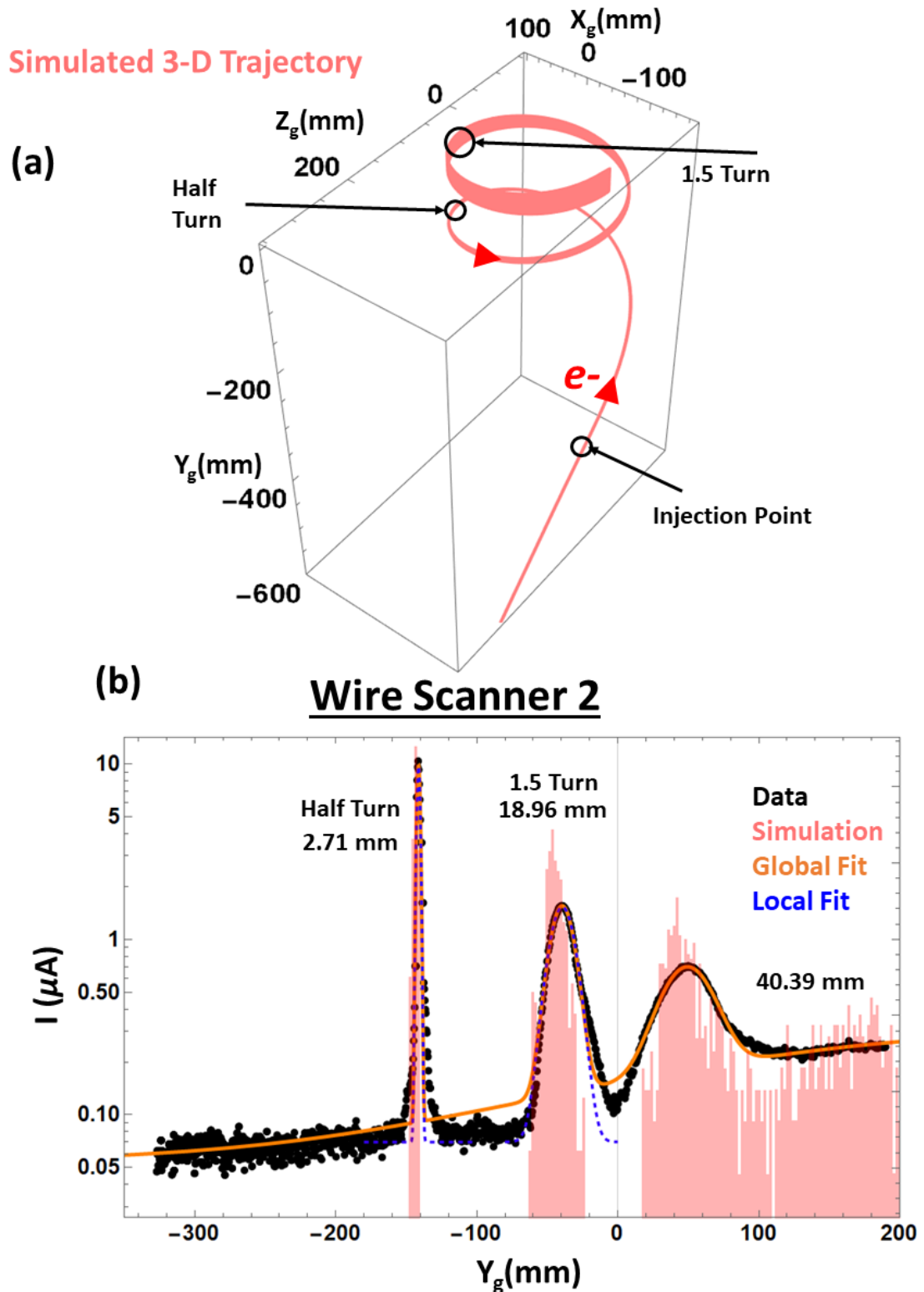


Figure 6.21: (a) The tracking simulation of the beam injection (CST-PS) into the storage magnet without phase-space matching. The black open circle shows the points at which the beam sizes were measured. (b) The vertical beam size was measured by using a wire scanner. The black points are the wire scanner 2 data. The red histogram is a simulation result of CST-PS. The orange line is the fit to experimental data. The wire scanner 2 is located at 180 Degree away (half cyclotron period) from the wire scanner 1 position.

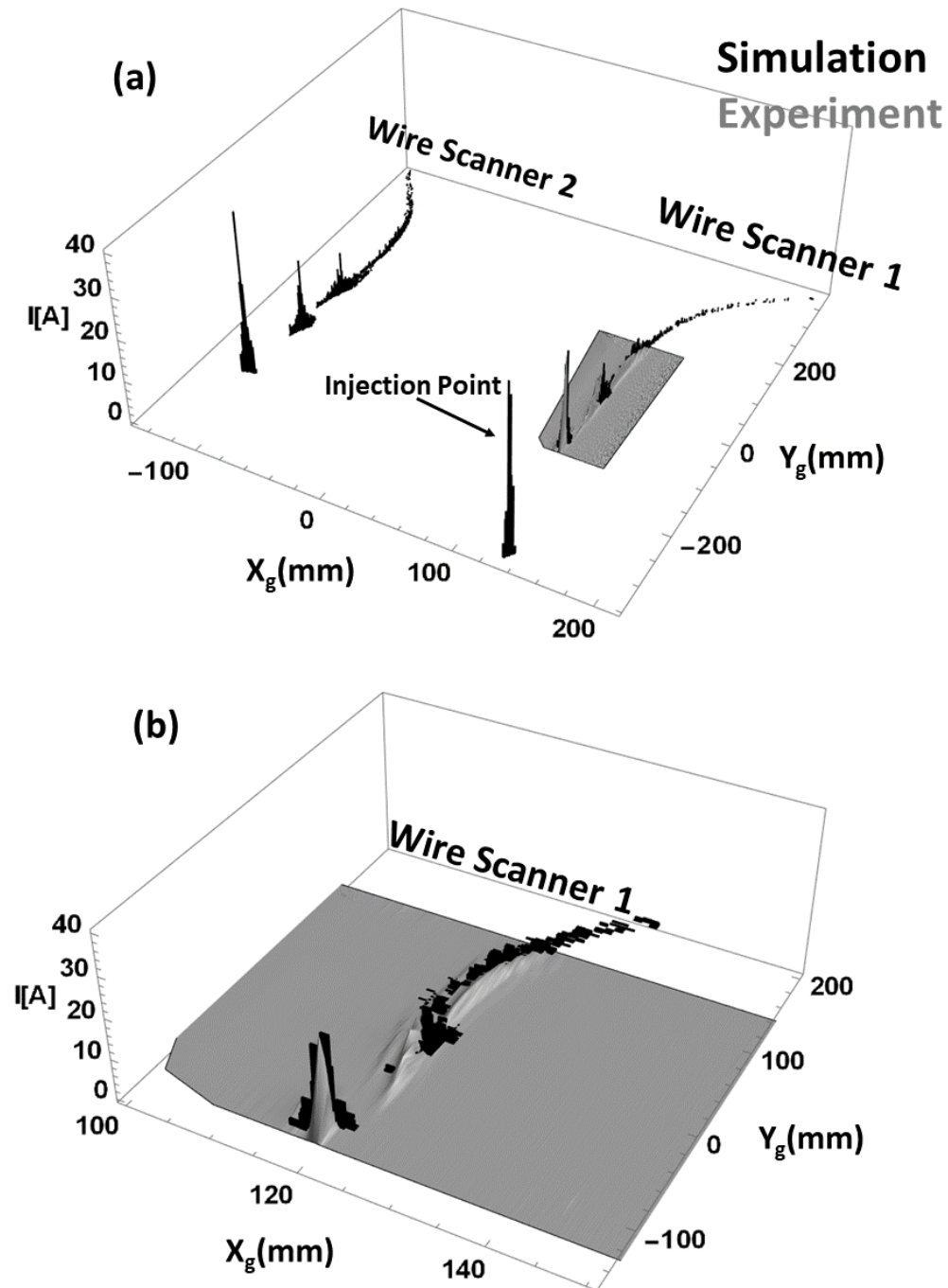


Figure 6.22: (a) The 3-D plot of the 2-D projection of the beam profile in the storage magnet. The positive X-axis corresponds to the wire scanner 1 location and negative show the wire scanner 2 location. The black histogram is the CST-PS simulation and grey plot show the experimental data. (b) The zoom up view of the wire scanner 1 location.

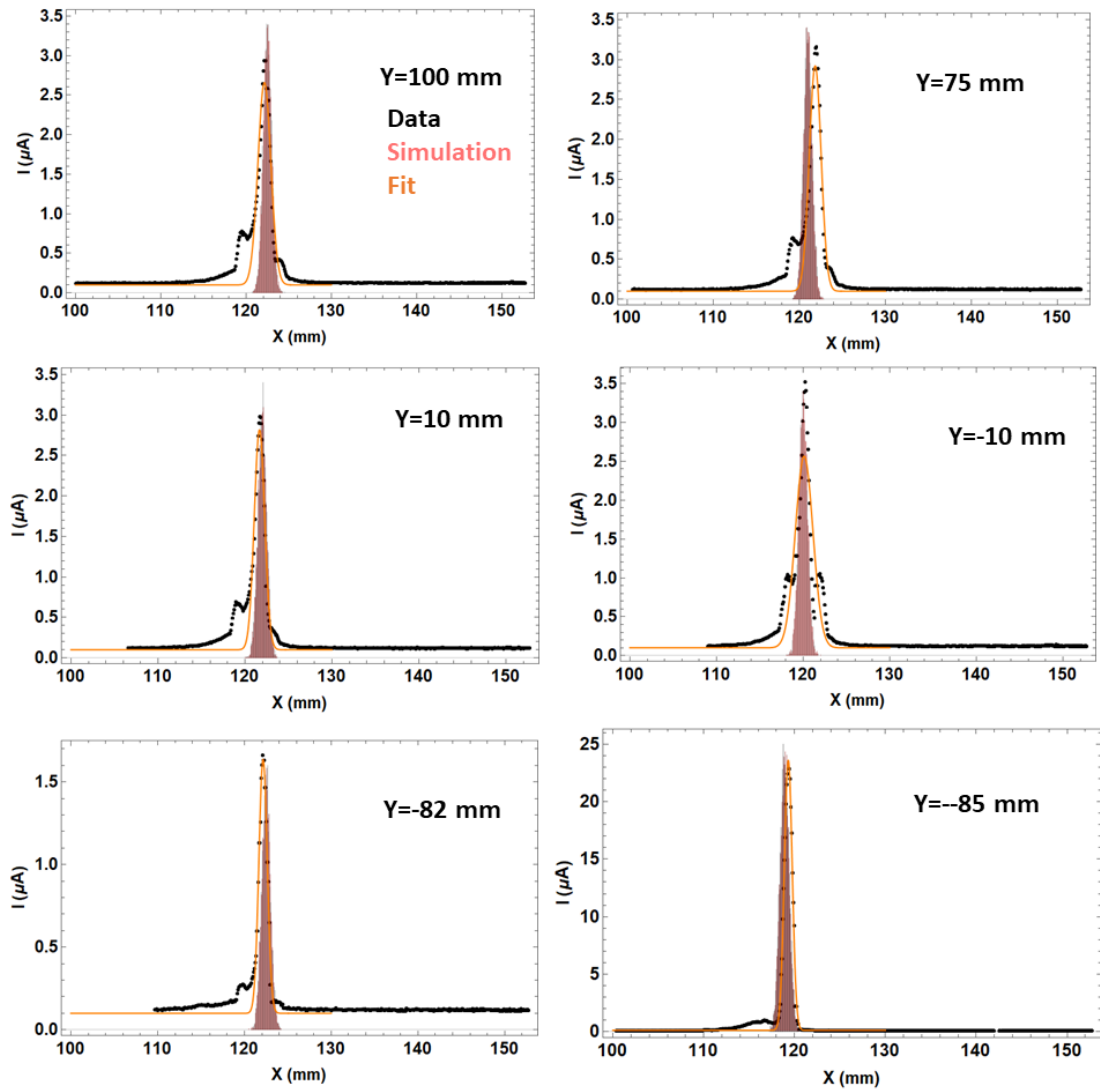


Figure 6.23: The horizontal beam profile at different vertical positions. Average horizontal beam profile from first turn to the second turn was 0.65 mm (1σ)

6.5 Discussions and Summary

The dramatic reduction in the vertical beam size was observed with the appropriate setting of three rotatable quadrupole magnets. Without any beam phase-space matching, the beam size grows to 31.25 ± 0.21 mm (FWHM) at the kick point of the storage magnet. The vertical beam blow-up was reduced to 8.06 ± 0.21 mm (FWHM) at the kick point with the appropriate combination of the three rotation quadrupole magnets. The horizontal beam size does not grow as beam moves through the storage magnet. The horizontal beam size was estimated 0.65 mm (1σ). In conclusion vertical beam size reduce to $3\times$ with the three rotatable quadrupole magnets as compared to the beam injection without any rotatable magnets. The charged particle tracking simulation in CST-PS and experimental results are in good agreement with each other.

Figure 6.24 shows the comparison of the beam vertical beam size growth as a function of the axial position of the storage magnet among different cases. The comparison between numerical values is given in the Table 6.9. Even in the case of the perfect matching the vertical beam size grows to the 6.3 mm (FWHM), whereas in the case of the partial matching vertical beam increases up to 8.06 ± 0.21 mm. In the case of the SITE, we choose the high value of field index 1.65×10^{-2} , this field index provides the focusing in the region of $Y = \pm 50$ mm. Therefore, partial matching of the beam phase-space is enough to store nearly 81% of the beam. In the next chapter, this topic will be discussed in detail.

Table 6.8 provides the comparison between ideal slope and measured slope of the $X - Y$.

Table 6.8: The Comparison of the Beam Slopes between the Simulation and Measured from the Beam Profile Monitor.

Correlation	Ideal Slope	No quads (Slope)	With Quads (Slope)
X-Y	0.40	0	0.35

Table 6.9: The Vertical Beam Sizes as a function of the Vertical Position of the Storage Magnet

Without Quads		With rotation Quads	
Y_0 [mm]	FWHM [mm]	Y_0 [mm]	FWHM [mm]
-345.46	1.4 ± 0.02	-344.30	2.51 ± 0.04
-134.34	10.62 ± 0.23	-141.34	2.71 ± 0.03
-59.57	31.25 ± 0.21	-82.61	8.06 ± 0.21
21.36	78.41 ± 0.83	-39.49	18.96 ± 0.14
86.558	122.45 ± 1.11	-3.47	25.68 ± 0.31
		49.22	40.39 ± 0.81

In order to completely stop the vertical motion of the beam in the storage magnet, a vertical kick is needed. To kick the beam appropriately the pitch angle at the kick point must reduce to

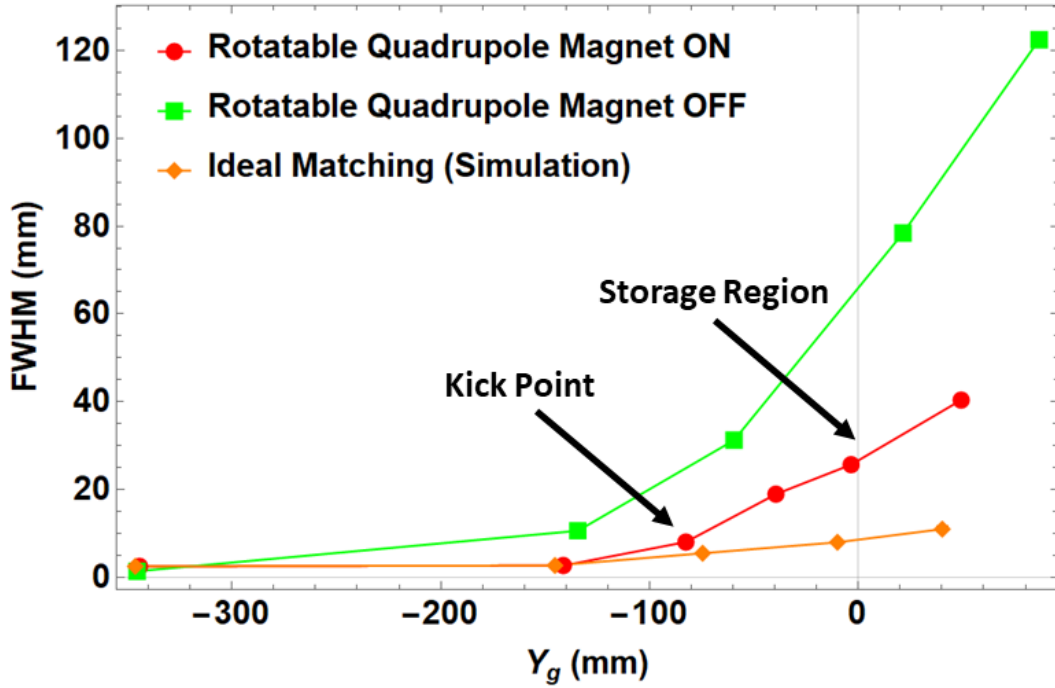


Figure 6.24: The comparison of the vertical beam sizes growth in the storage magnet without phase-space matching, with appropriate combination of rotatable quadrupole magnets and simulated perfect matching.

5-3 Degree. The small pitch angle reduces the high power and fast timing constraints of the kicker power supply. As shown in Fig. 6.24 with partially matched beam pitch angle at $Y = -82.6$ mm reduces to 3.37 Degree. Hence in the case of the partially matched beam injection, we can kick the beam appropriately. The following formula can be used to compute the pitch angle of the beam:

$$\psi \approx \tan^{-1}\left(\frac{p}{\pi D}\right) \quad (6.15)$$

where p is the pitch distance between two consecutive turns and D is the diameter of the spiral trajectory. Figure 6.25 shows the pitch angle of the beam as it traverses through the storage magnet. The comparison between the numerical values of the pitch angle between unmatched and partially matched beam is given in the Table 6.10. Note that the pitch angle at the kick point can be controlled by the injection angle.

Table 6.10: The Pitch Angel as a Function of the Vertical Position of the Storage Magnet

Without Quads		With rotation Quads	
Y_0 [mm]	ψ [Degree]	Y_0 [mm]	ψ [Degree]
-342.12	19.47	-344.30	15.06
-75.53	8.43	-141.34	4.45
36.34	13.73	-82.6	3.27

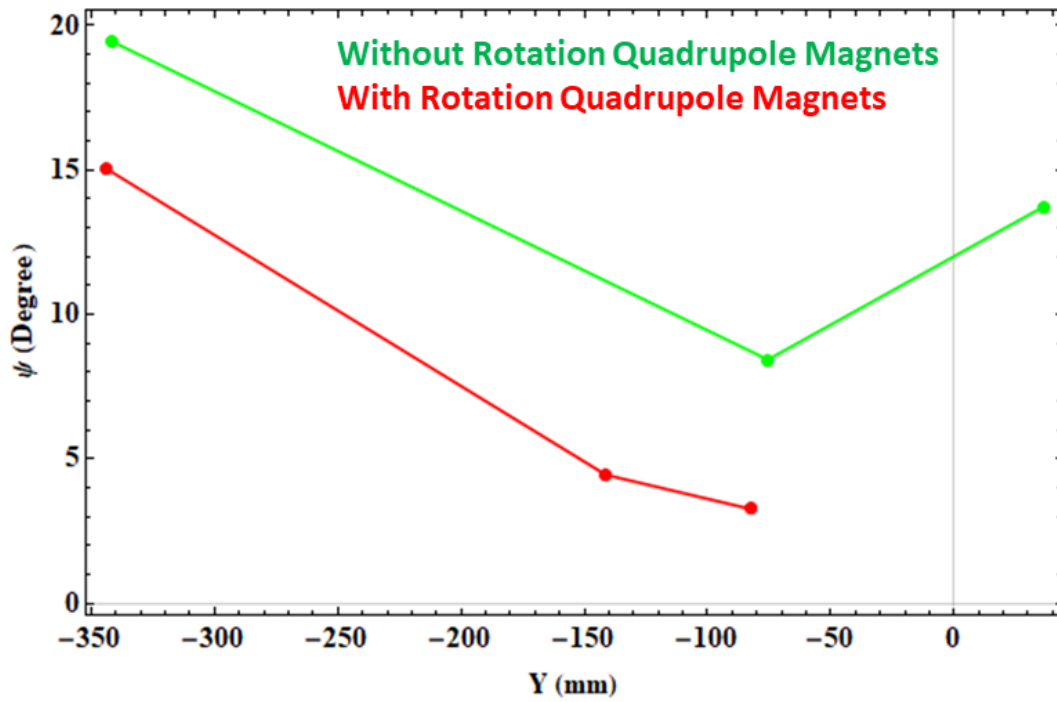


Figure 6.25: The comparison of the pitch angle between without phase space matching and with appropriate combination of rotatable quadrupole magnets.

Chapter 7

Kicker System for SITE

To store the beam at the center of the storage magnet, the vertical spiral motion of the beam must be completely stop, as it reach to the storage plane. Or in other words the pitch angle of the beam must reduce to around 0° as it reach to the storage plane. The remaining small pitch angle (in the range of few mrad) of the beam will be compensated by the designed weak focusing field at the storage plane. A pulsed vertical kicker will be utilized to stop the vertical motion of the beam at center of the storage magnet. The vertical kicker will generate the pulsed radial field of magnitude of few gauss and several cyclotron periods, to gradually reduced the pitch angle the beam. Figure 7.1 presents the concept of the kicker. The black dashed trajectory shows the motion of the beam inside the storage magnet without a kicker; it is observed that the injection angle of the beam reduced due to the radial fringe field but does not decrease to zero. The beam passed through the middle region of the storage magnet without getting stopped. When the appropriate kick is applied to the beam, as shown in the black solid trajectory, the pitch angle is reduced to zero.

In this Chapter, the following studies for the SITE kicker will be described

- Basic concept and design for the SITE kicker
- Tracking studies to determine the kicker requirements
- Eddy current consideration for kicker system

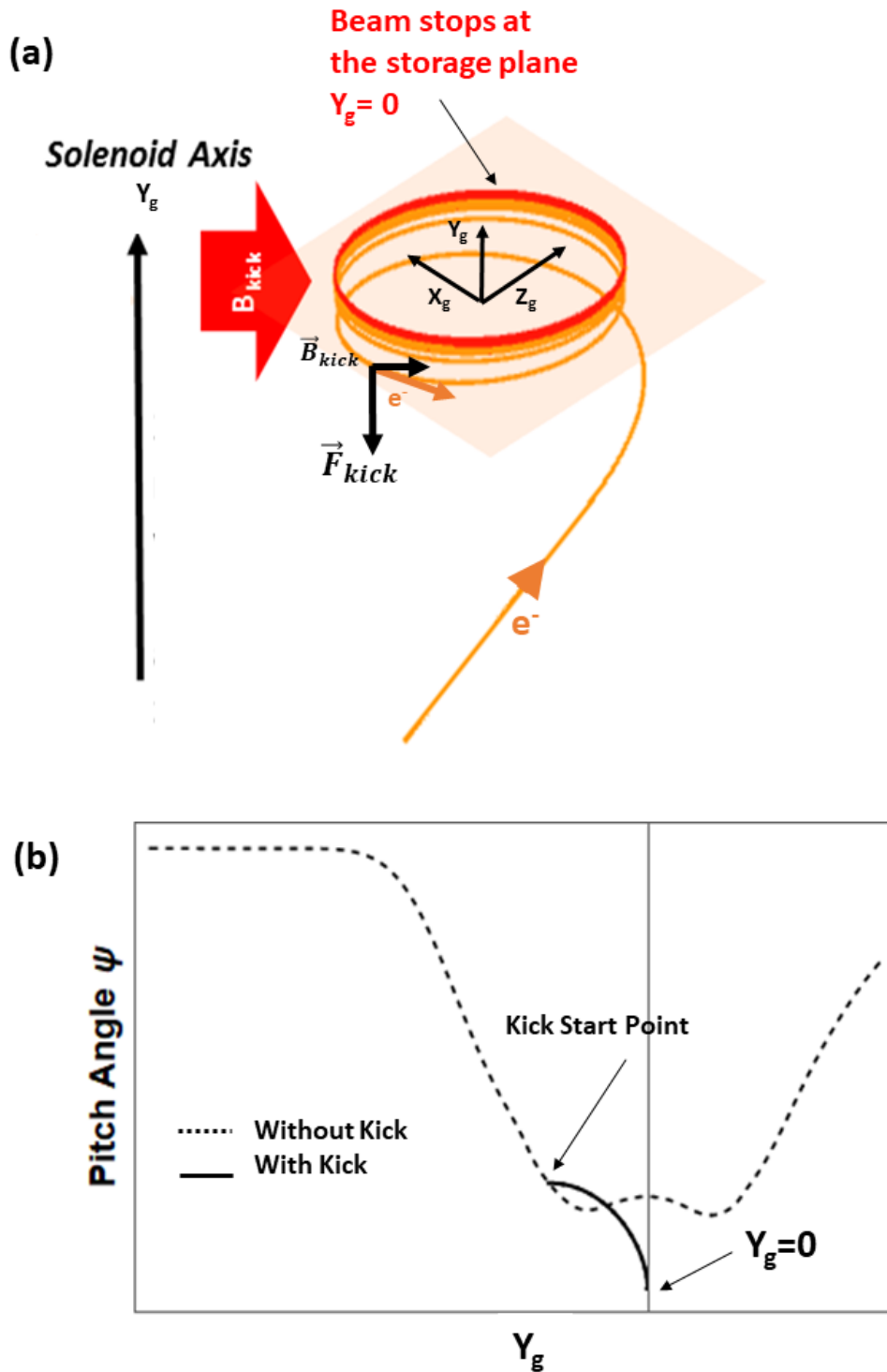


Figure 7.1: (a) The concept of the vertical kicker. The beam enters in the storage magnet at 40 Degree and radial field of the storage magnet reduce the injection to 4-5 Degree as it approaches the boundary of the weak focusing field. At $Y_g = -100$ mm a vertical kick applied to the beam to gradually reduce the pitch angle of the beam to the zero. (b) The pitch angle of the injected beam. And its reduction due to the radial field of the storage magnet and kicker field.

7.1 Vertical Magnetic Kicker for SITE

In the case SITE following two kinds of kickers were considered

- Symmetrical Kicker
- Localized Kicker

In symmetrical type kicker, the kick field will be applied to the beam throughout the region of the kick point to the stop position (storage plane). The pitch angle reduces continuously in the case of the symmetric kick. Figure 7.2 shows the symmetrical kick. The beam is injected into the storage magnet at 0.7 rad. The orange line in Fig.7.2 shows the reduction of the injection angle (pitch angle) due to the radial field of the storage magnet. The pitch angle reduces to 51.14 mrad at vertical position of -98.70 mm. At this point, the kick will be applied to the beam. The motion of the particles in the time-varying kicker field was simulated by the 4-th order Runge-Kuta method in Mathematica [37]. The half-sine type pulse shape of width 50 ns was considered for this simulation. The longer pulse width decrease stringent requirement of the power supply. The blue curve in Fig. 7.2 shows the decrease in the pitch angle to 0 rad as it reaches the storage plane, due to the symmetrical kick.

In the case of the SITE, the value of the field index (n : Weak Focusing Strength) is set to 1.65×10^{-2} . The corresponding separatrix¹ for this field index value are plotted in the Fig. 7.3. The closed circles show the stable regions and hyperbolic curves show the unstable regions. As far as the particles arrive in the closed contours they will trap in the weak focusing field and perform the simple harmonic motion. As described in the last chapter the beam size grows to the 25.68 mm. Therefore, the weak focusing trap is big enough to store 81% of the beam. The red contours in Fig. 7.3 show the stable storage orbit of $Y_g = \pm 30$ mm.

In a localized type kicker, the kick field will be applied to the beam only in the limited region of the kick point to the stop position (storage plane). The pitch angle reduces in steps in the case of the localized kick. Figure 7.4 shows the character of the localized kick. The pulse width is 50 ns and one cyclotron period is 5 ns, hence beam has to pass $\times 10$ through the localized kicker before pitch angle reduced to the zero at the storage plane. The orange line in Fig.7.4 shows the reduction of the injection angle (pitch angle) due to the radial field of the storage magnet. The pitch angle reduces to 57.14 mrad at vertical position of -101.60 mm. The black step-curve in Fig. 7.4 shows the decrease in the pitch angle to 0 rad as it reaches the storage plane, due to the localized kicker. Figure 7.5 represents the localized kick and separatrix. The decrease in steps is due to the limited region of the kicker. Table 7.1 shows the beam position and pitch angle at the kick point for the symmetrical and localized kicker.

The oscillation of the stored beam (vertical direction and pitch angle) in the weak focusing potential is shown in Fig. 7.8 and Fig.7.9. The horizontal and vertical tune of the beam are as

¹A phase-curve which connects the stable and unstable regions [80]

following:

$$\nu_x = \sqrt{1-n} = 0.9919, \quad \nu_y = \sqrt{n} = 0.1284 \quad (7.1)$$

Table 7.1: The beam position and pitch angle at kick point.

Parameters	Symmetrical kicker	Localized kicker
Injection Angle [rad]	0.70	0.70
Kick Position [mm]	-98.70	-101.60
Pitch Angle at kick point [mrad]	51.14	57.59
Kick duration [nsec]	50	50
Field Index (n)	1.65×10^{-2}	1.65×10^{-2}

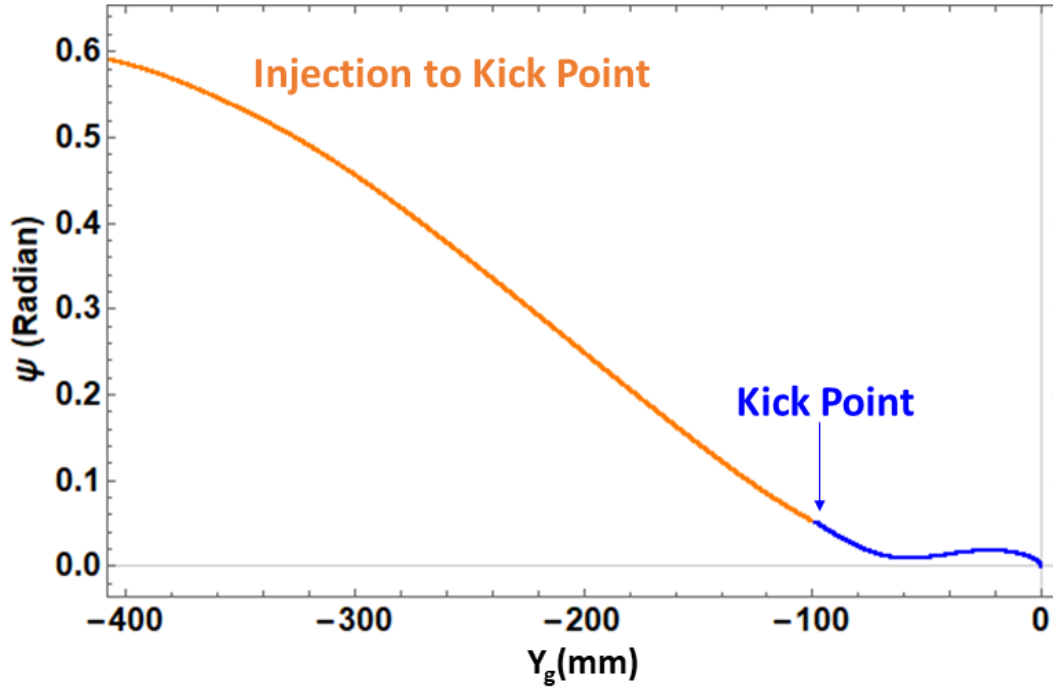


Figure 7.2: The character of the symmetrical kicker. The orange line shows the reduction in the pitch angle of the beam from the injection point to the kick point. The blue curve shows the kick due to the symmetrical kicker, the pitch angle of the beam reduces smoothly in the of the symmetrical kicker. After applying kick the pitch angle reduces to the zero.

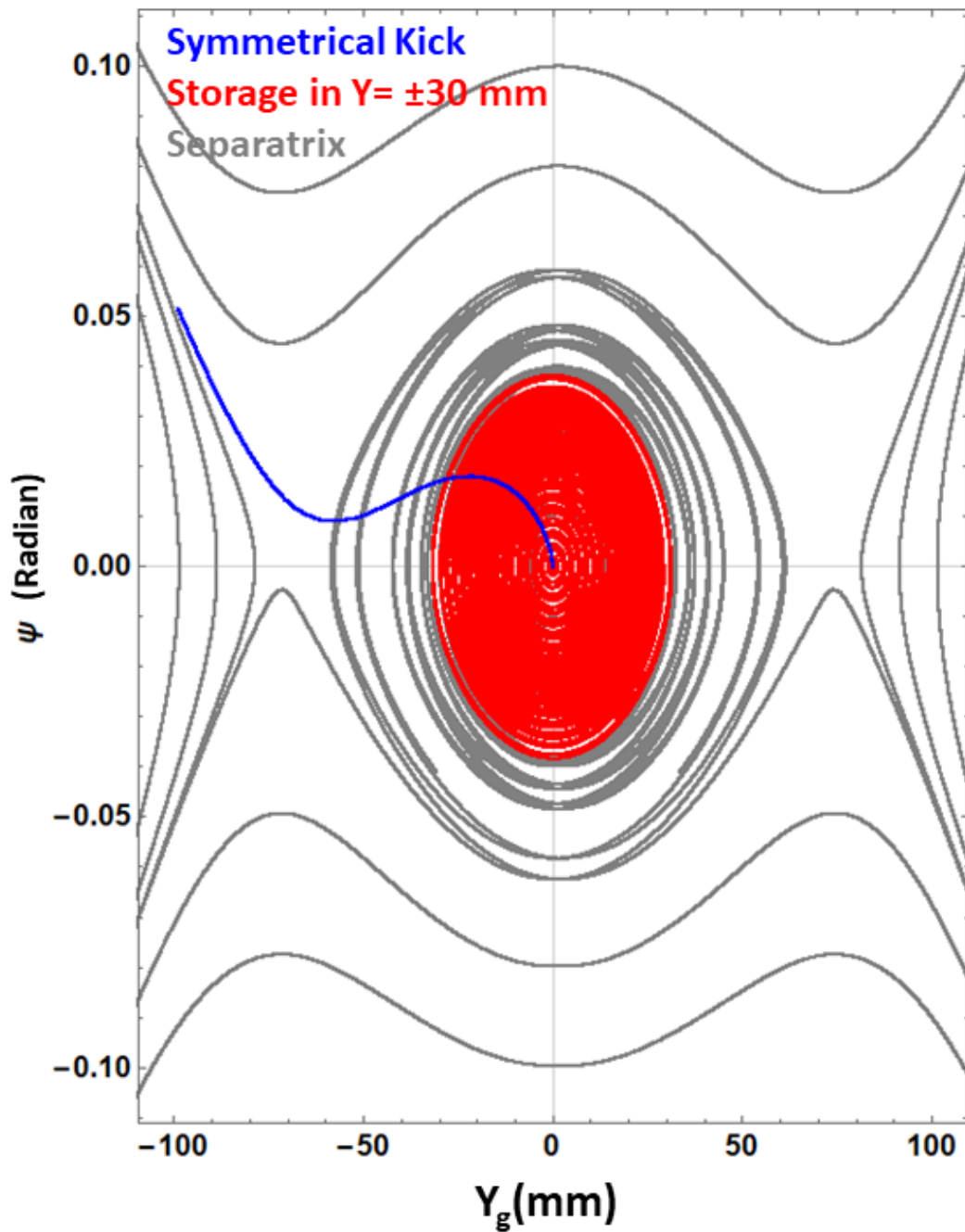


Figure 7.3: The symmetrical kick and separatrix. The blue curve is the symmetrical kick. The closed circles shows the stable storage orbit. If the particles lands on the closed circle after the kick the will get store. Th red circles shows the storage orbit for $Y_g = \pm 30$ mm.

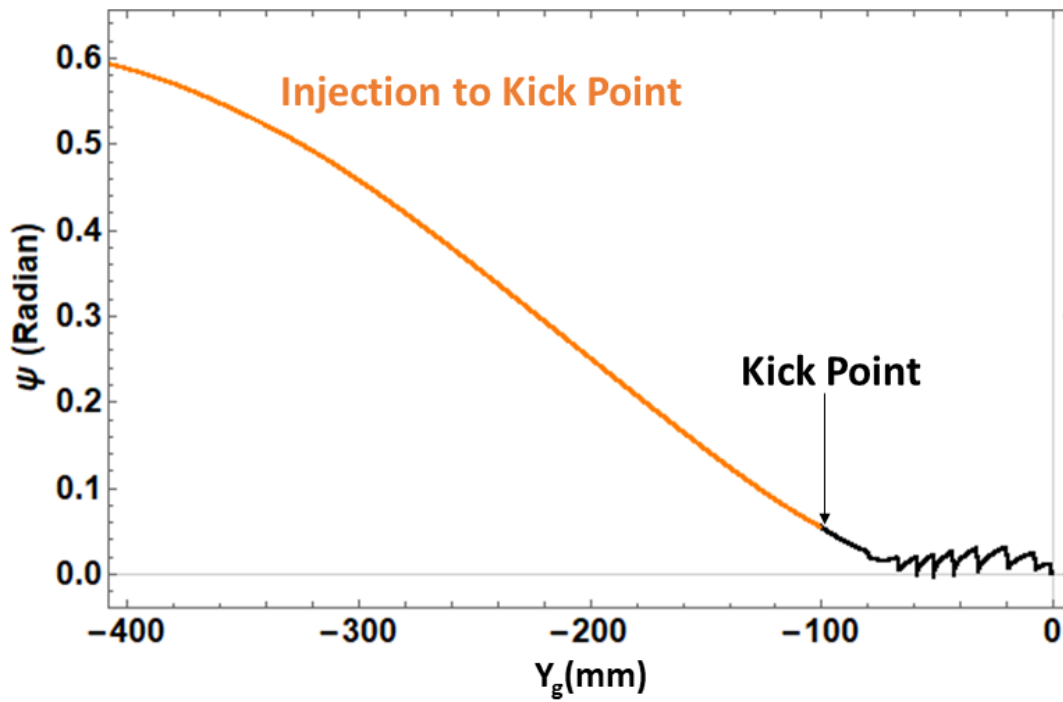


Figure 7.4: The character of the localized kicker. The orange line shows the reduction in the pitch angle of the beam from the injection point to the kick point. The black curve shows the kick due to the localized kicker, the pitch angle reduces to zero in 10 steps.

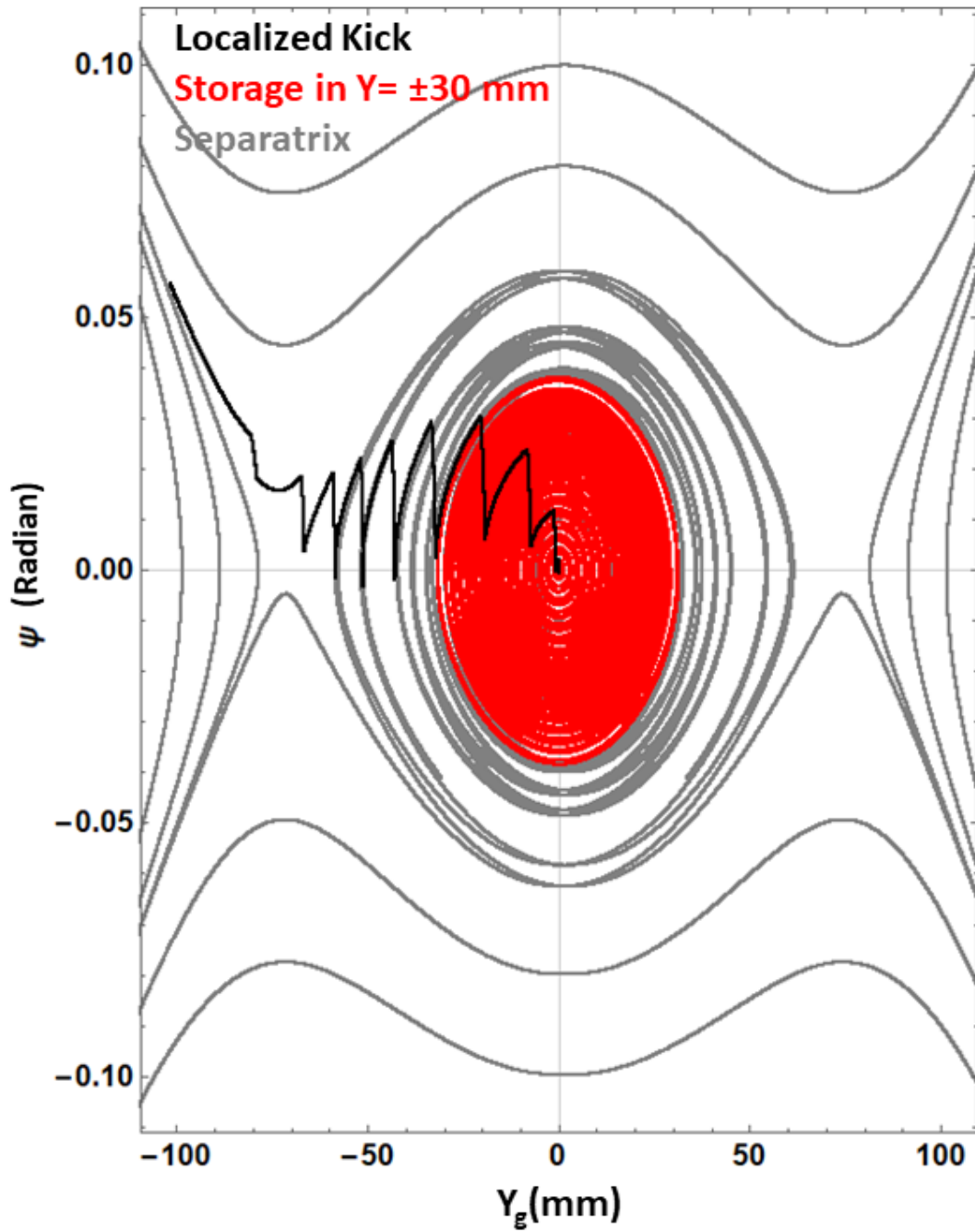


Figure 7.5: The localized kick and separatrix.

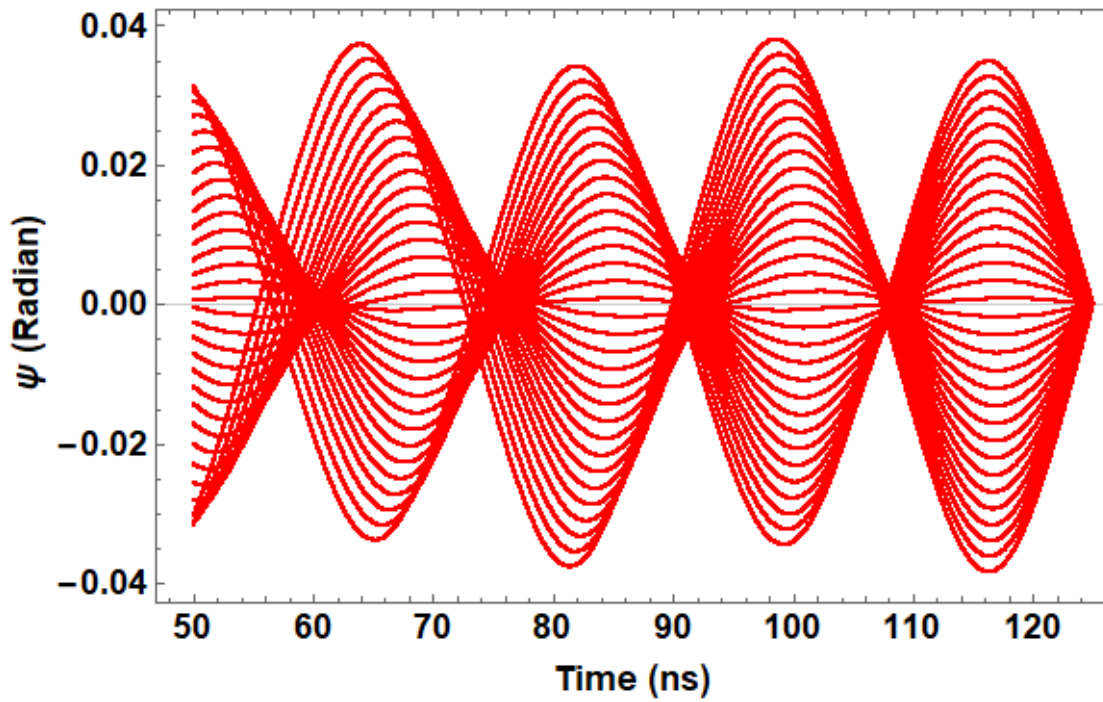


Figure 7.6: The oscillation of the pitch angle in the weak focusing field.

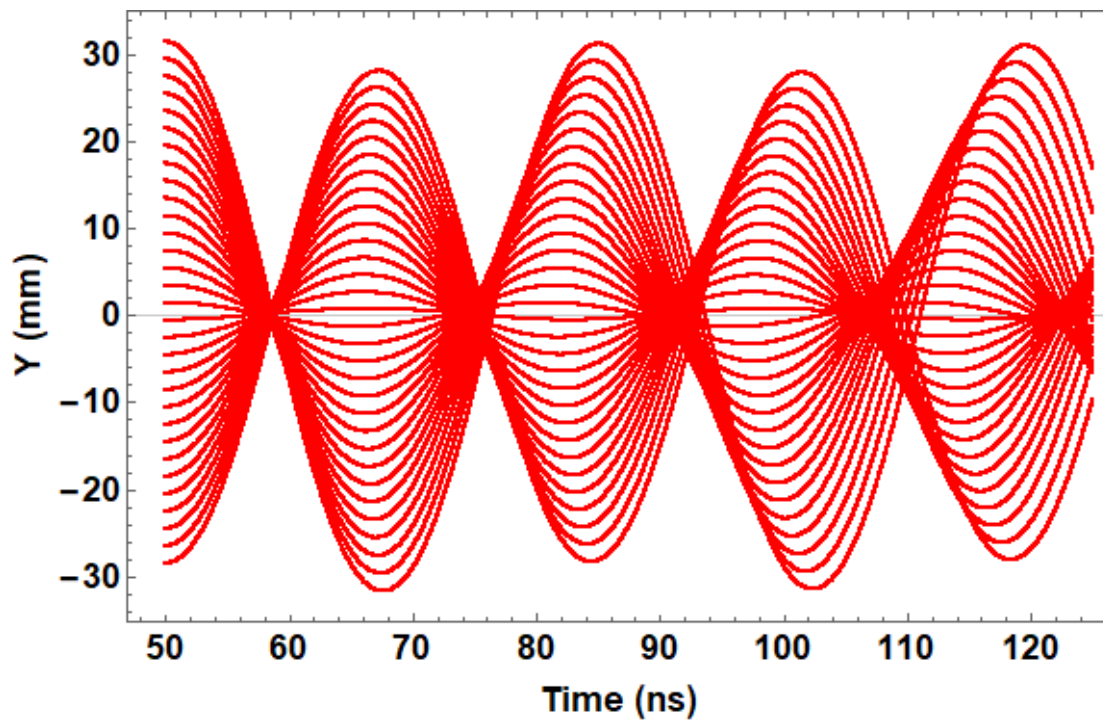


Figure 7.7: The oscillation of the beam in the vertical direction in the weak focusing field.

7.2 Design of the kicker Coils

A pair of circular coils with the current in the opposite directions can generate the radial field. This kind of coil configuration can be used to produce symmetrical kick for the beam. Figure 7.8 above shows the symmetrical kicker coil design. The diameter of these coils is 220 mm and their mutual distance is 240 mm. The radial magnetic field profile at the radius 120 mm along the axial direction is shown in Fig. 7.8. The total current required to produce the appropriate symmetrical kick is 15 A. Table 7.2 shows the parameters for the symmetrical kicker coils. The inductance of each coil is 0.67 μH . If they are connected in parallel then total inductance of the coils will become $L_T = 0.34 \mu\text{H}$.

$$L_T = \frac{L_1 L_2}{L_1 + L_2} \quad (7.2)$$

Table 7.2: Symmetrical Kicker Coil Parameters.

Parameters	Values
Diameter [mm]	220
Mutual Distance [mm]	240
Inductance of each coil [μH]	0.67
Current [A]	15

A dipole coil can serve as a localized kicker for 3-D spiral injection. Figure 7.9 represents the localized kicker coil design. The blue circles in Fig. 7.9 represent the beam trajectory. Figure 7.9 below shows the localized kicker field at the $Y_g = 0$ mm. The field direction is perpendicular to beam motion. Hence, this field can be used to produce a kicker field. The geometrical and electrical parameters of the localized kicker are shown in Table 7.3. The kicker coils were designed in CST-MS [36].

Table 7.3: Localized Kicker Coil Parameters.

Parameters	Values
Width [mm]	62
Gap [mm]	20
Height [mm]	175
Inductance of each coil [μH]	0.44
Current [A]	16

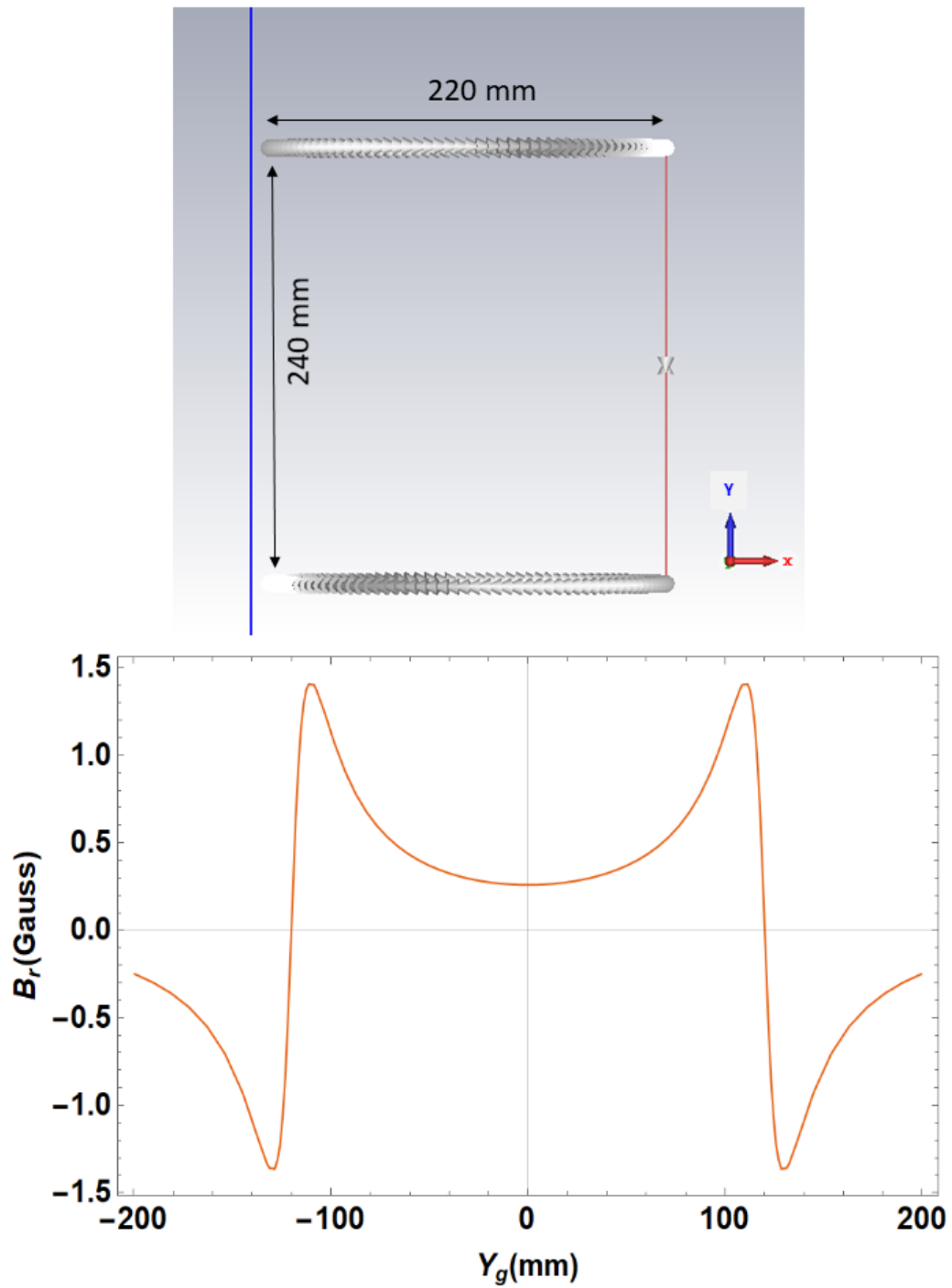


Figure 7.8: Above: The design of the symmetrical kicker. Below: The radial magnetic field of the symmetrical kicker coils.

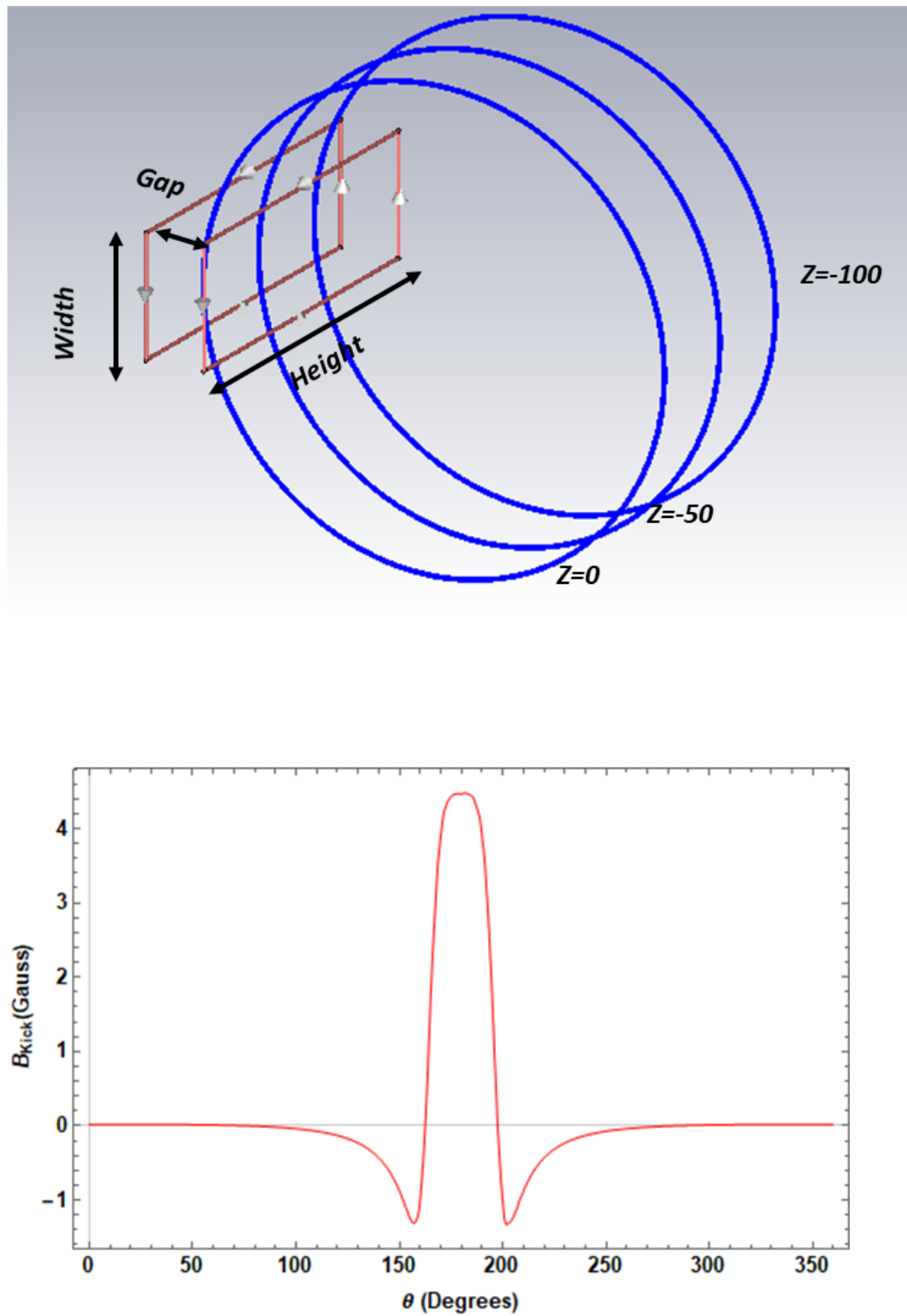


Figure 7.9: Above: The design of the localized kicker. Below: The kicker field of the localized kicker coils.

7.3 Eddy Current Considerations

According to Faraday's law of induction the change in the magnetic field produce loops of electric current or Eddy current in the conductor. The kicker coils are the transient device and produce eddy current in the wall of the vacuum chamber. The eddy current flow in the wall of the vacuum chamber can reduce the magnitude of the kicker field. In addition, it can also cause a thermal load for the vacuum chamber. In order to estimate the Eddy current effect, a simulation in the CST-LT [36] was conducted.

The vacuum chamber is made of SUS316. And the conductivity of SUS316 is 1.334×10^6 S/m. Figure 7.10 shows a vacuum chamber with the symmetrical kicker coils model. Figure 7.11 shows the contours plot of the average ohmic loss in the wall of the vacuum chamber due to Eddy current. The ohmic loss follows the shape of the current pulse. The maximum power loss in the case of the symmetrical kicker at the wall vacuum chamber is 1.1 Watt. Figure 7.12 shows the vacuum chamber with localized kicker and Fig. 7.13 shows the average ohmic loss in the case of the localized kicker. The maximum power loss in the case of the localized kicker is 0.49 Watt.

Figure 7.14 represents the power losses as a function of the kicker duration for symmetrical (Blue) and localized (Black) kicker coil. Note that the power loss is small in the case of the localized kicker due to the smaller and confined volume of the localized kicker coil. Whereas in the case of symmetrical kicker large area is exposed to the surface of the vacuum chamber and hence results in more power loss. Figure 7.15 and 7.16 show the decrease in the magnetic field due to the eddy current in the symmetric and localized kicker coils respectively. In the case of symmetric kicker field strength reduce nearly 30% and in the case of localized kicker reduction is only 4%.

The power loss of 1.1 Watt and 0.4 Watt can not cause any significant thermal load. Therefore, this kicker field reduction due to the Eddy current can be easily compensated by the increase of current from power.

Table 7.4: Power loss due to the Eddy Current.

Parameters	Symmetrical kicker	Localized kicker
Power Loss [Watt]	1.10	0.49
Field reduction	30%	4%

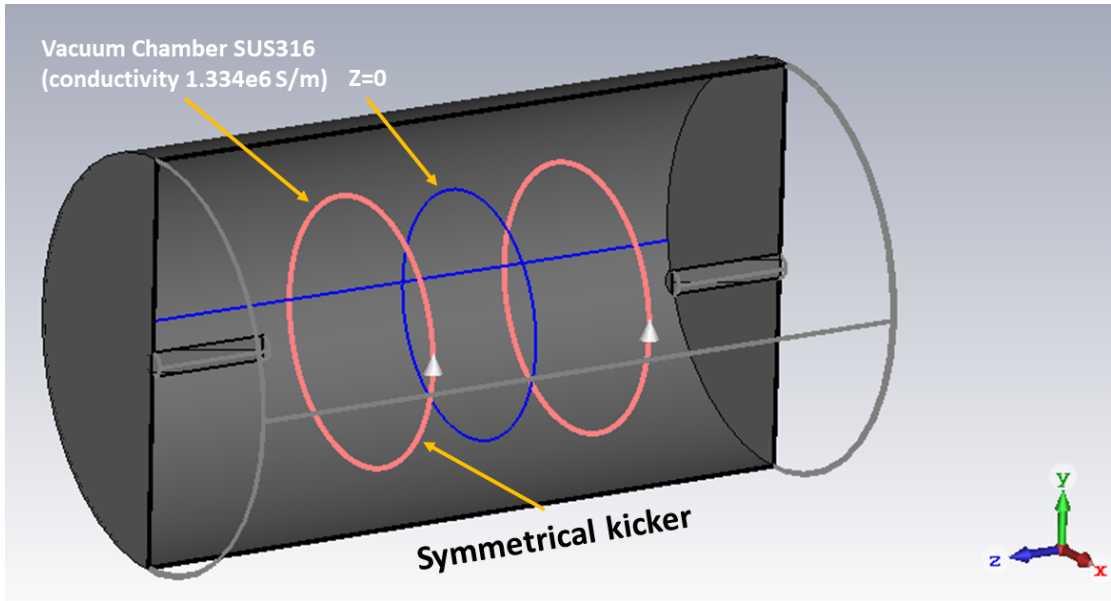


Figure 7.10: The vacuum chamber and kicker symmetrical kicker coils.

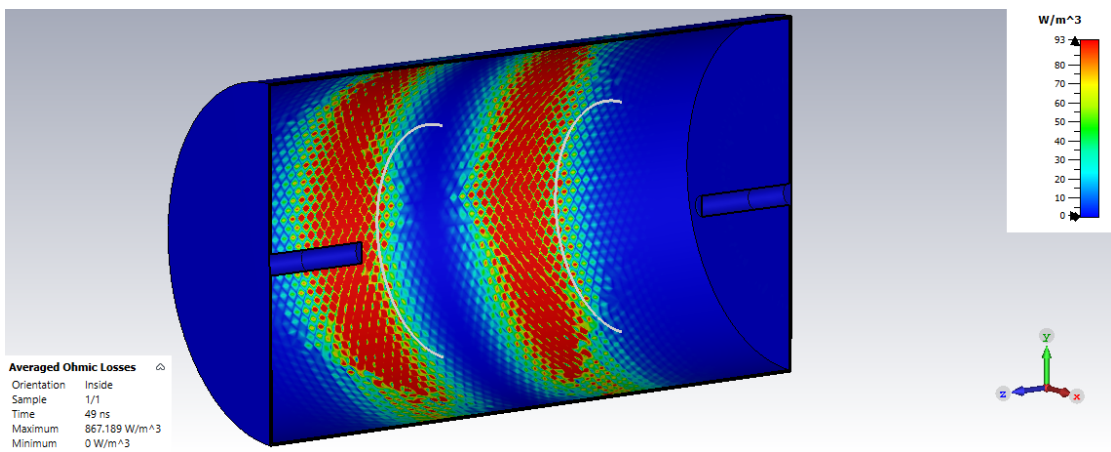


Figure 7.11: The average ohmic losses in the wall of the vacuum chamber due to the symmetrical kicker coils.

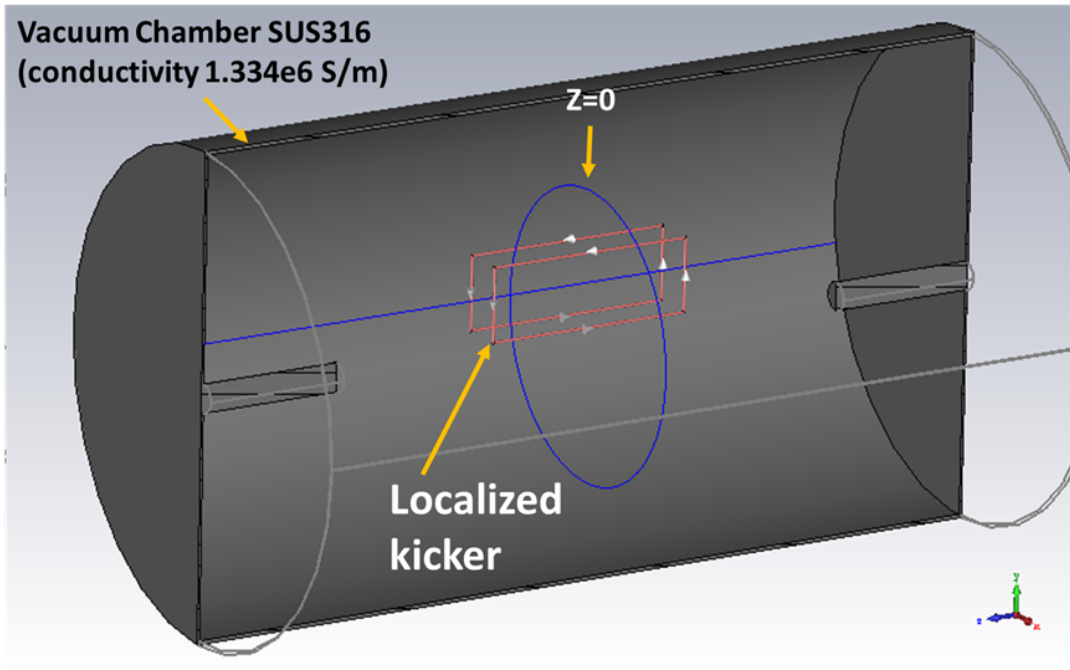


Figure 7.12: The vacuum chamber and kicker localized kicker coils.

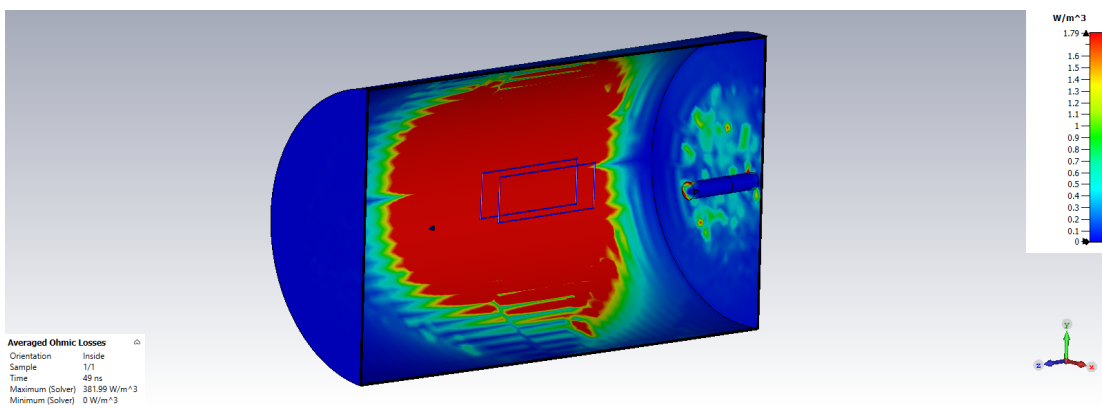


Figure 7.13: The average ohmic losses in the wall of the vacuum chamber due to the localized kicker coils.

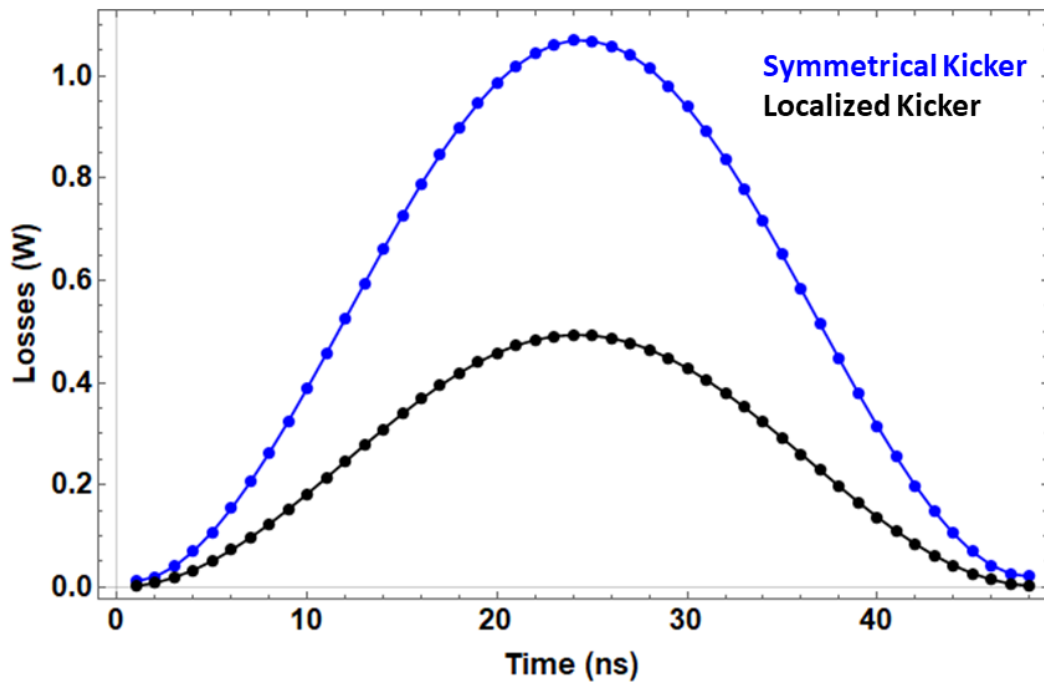


Figure 7.14: The power loss in the wall of the vacuum chamber due to the symmetric and localized kicker coils.

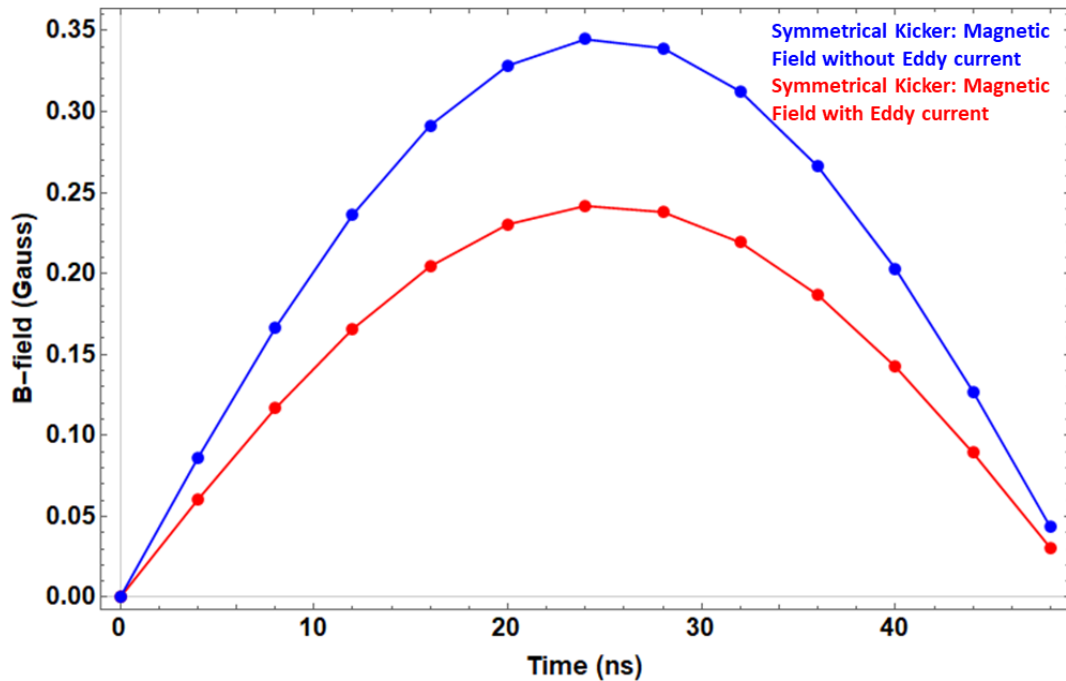


Figure 7.15: The magnetic field reduction in the case of symmetrical kicker due to eddy current flow in the wall of the vacuum chamber.

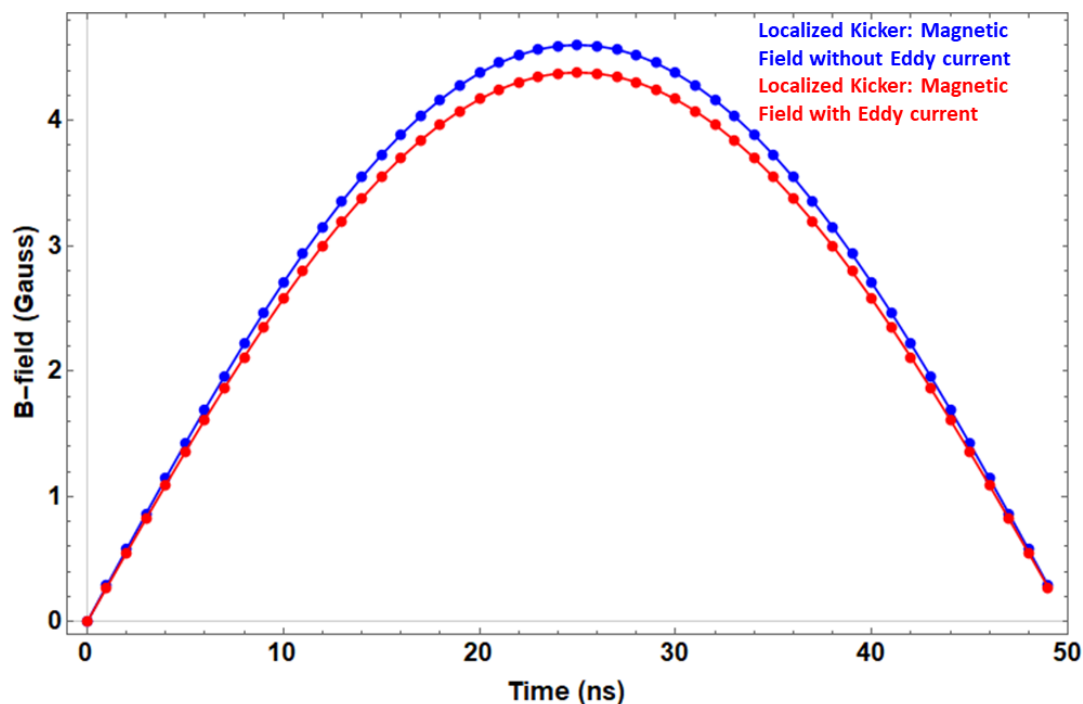


Figure 7.16: The magnetic field reduction in the case of localized kicker due to eddy current flow in the wall of the vacuum chamber.

7.4 Kicker Power Supply

The kicker power supply was designed and built-in collaboration with the private company 'Pulsed Power Japan Laboratory Ltd' [81]. Table 7.5 represents the parameters of the kicker power supply. The required voltages and capacitance for the kicker power supply can be computed as follow:

$$C = \frac{\left(\frac{T}{\pi}\right)^2}{L} \quad (7.3)$$

$$V = I\sqrt{\frac{L}{C}} \quad (7.4)$$

$$T = \pi\sqrt{LC} \quad (7.5)$$

The MicroCap [82] software was used to design the kicker power supply. Figure 7.17 (a) shows circuit diagram of the kicker power supply. Figure 7.17 (b) and (c) represents the current through kicker coils and voltage across kicker coils respectively.

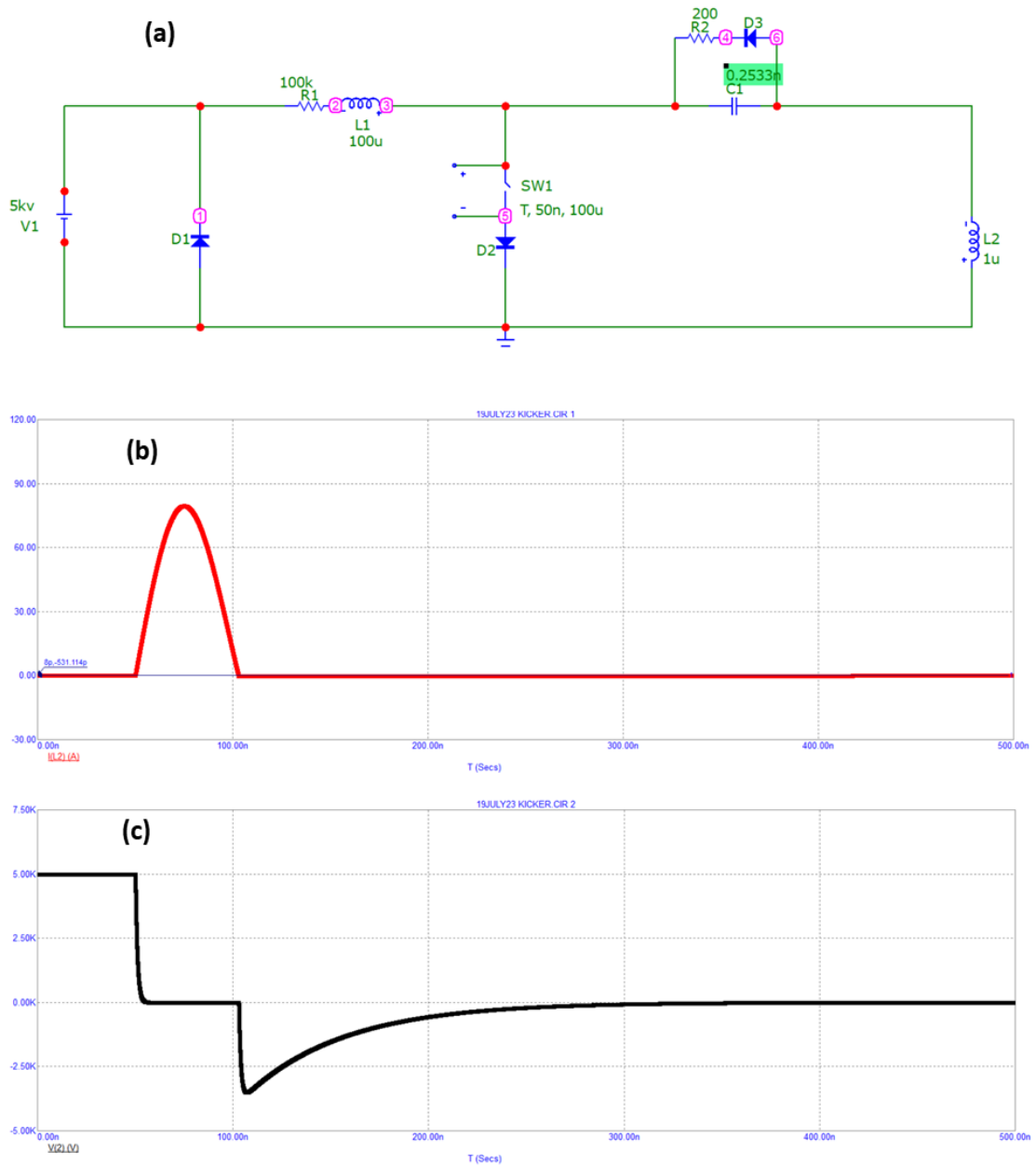


Figure 7.17: (a) The circuit diagram of the kicker power supply. (b) The current through kicker coils. (d) The voltage across kicker coils.

Table 7.5: Kicker Power supply Parameters.

Parameters	Values
Inductance [μH]	1 (including Cables)
Capacitance [nF]	0.2533
High Voltage [kV]	5
Current [A]	20
Frequency [Hz]	50
Pulse Width (half sine) [nsec]	50

7.5 Injection Efficiency

In order to determine the injection efficiency multi-particle tracking had been performed with different vertical initial phase-space conditions at the kick point. Figure 7.18 shows the beam vertical phase-space with different conditions at the kick point. In Fig. 7.18 (a) shows the vertical phase-space acceptance of the kicker in the case of $n = 1.65 \times 10^{-2}$, (b) is the vertical phase-space at the kick point with phase-space matching that can be achieved with the three rotatable quadrupole magnets, (c) presents the same vertical phase-space as mentioned in (b) except flipped it to the focusing, and (d) shows the vertical phase-space at the kick point without any phase-space matching.

The multi-particle simulation with 100 samples in the transient field of the kicker and weak focusing index $n = 1.65 \times 10^{-2}$ was carried out. In the case of, no phase space matching (no XY-coupling) vertical beam phase-space completely mismatch with the acceptance of the kicker and only a few stray particles get trapped in the weak focusing potential. In this case, the injection efficiency is only 12%.

The red points and ellipse in Fig. 7.18 presents the vertical phase-space at kick point point, achieved by three rotation quadrupole magnets. In this case, the vertical phase-space partially matched with the kicker acceptance. Figure 7.19 shows the kicker tracking with this vertical phase-space (XY-coupled) to estimate the injection efficiency. The closed red contours presents the stored beam and open hyperbolas are lost particles. In this case injection efficiency is 81%.

The blue points in the Fig. 7.18 presents the ideal vertical phase-space at the kick point. It is the same vertical phase-space as mentioned in (b) except flipped it's sign to the focusing. This situation has been simulated to show the injection efficiency in the case of the ideal case. Figure 7.20 shows the kicker tracking with flipped XY-coupled phase space to estimate the injection efficiency. The closed blue contours represents the stored beam. In this case injection efficiency is 100%.

The injection efficiency with different vertical phase spaces is summarized in Table 7.6.

Table 7.6: Injection Efficiency

ID	Condition	Stored/Total	Injection Efficiency
(b)	XY-coupled	81/100	81%
(c)	Flipped XY-coupling (Ideal)	100/100	100%
(d)	No XY-coupling	12/100	12%

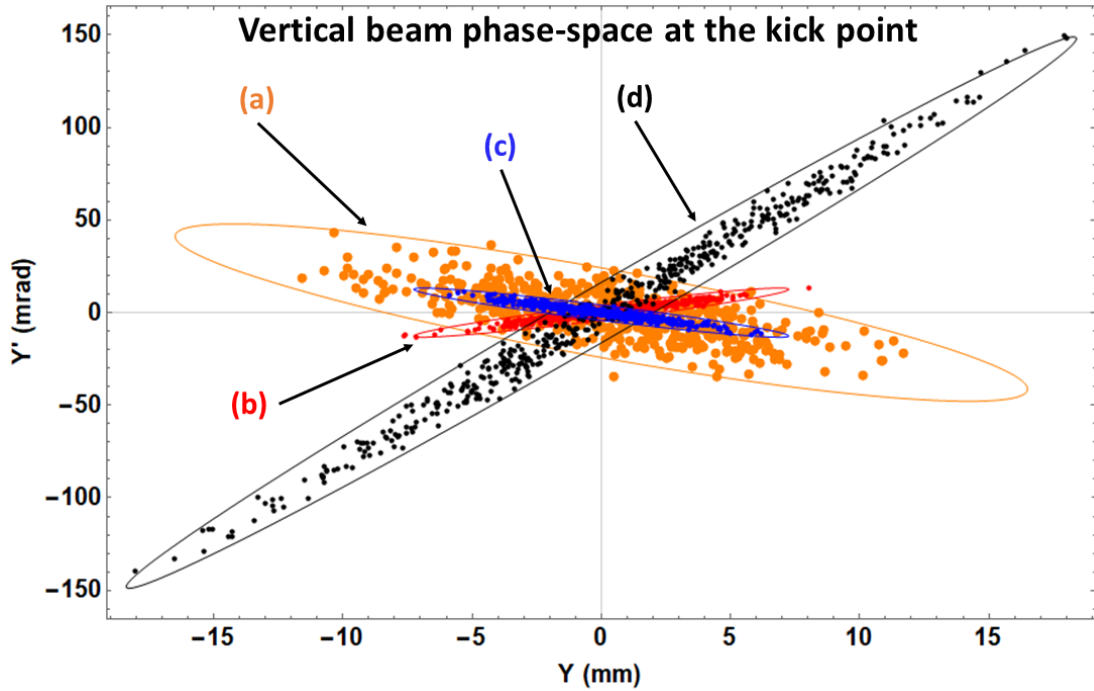


Figure 7.18: The beam vertical phase-space at the kick point. (a) The vertical phase space acceptance of the kicker. (b) The vertical phase-space at the kick point with phase-space matching. (c) The same vertical phase-space as mentioned in (b) except flipped it's sign to the focusing. This case has been simulated in order to show the injection efficiency in the ideal beam phase-space at the kick point. (d) The vertical phase-space at the kick point without any phase-space matching.

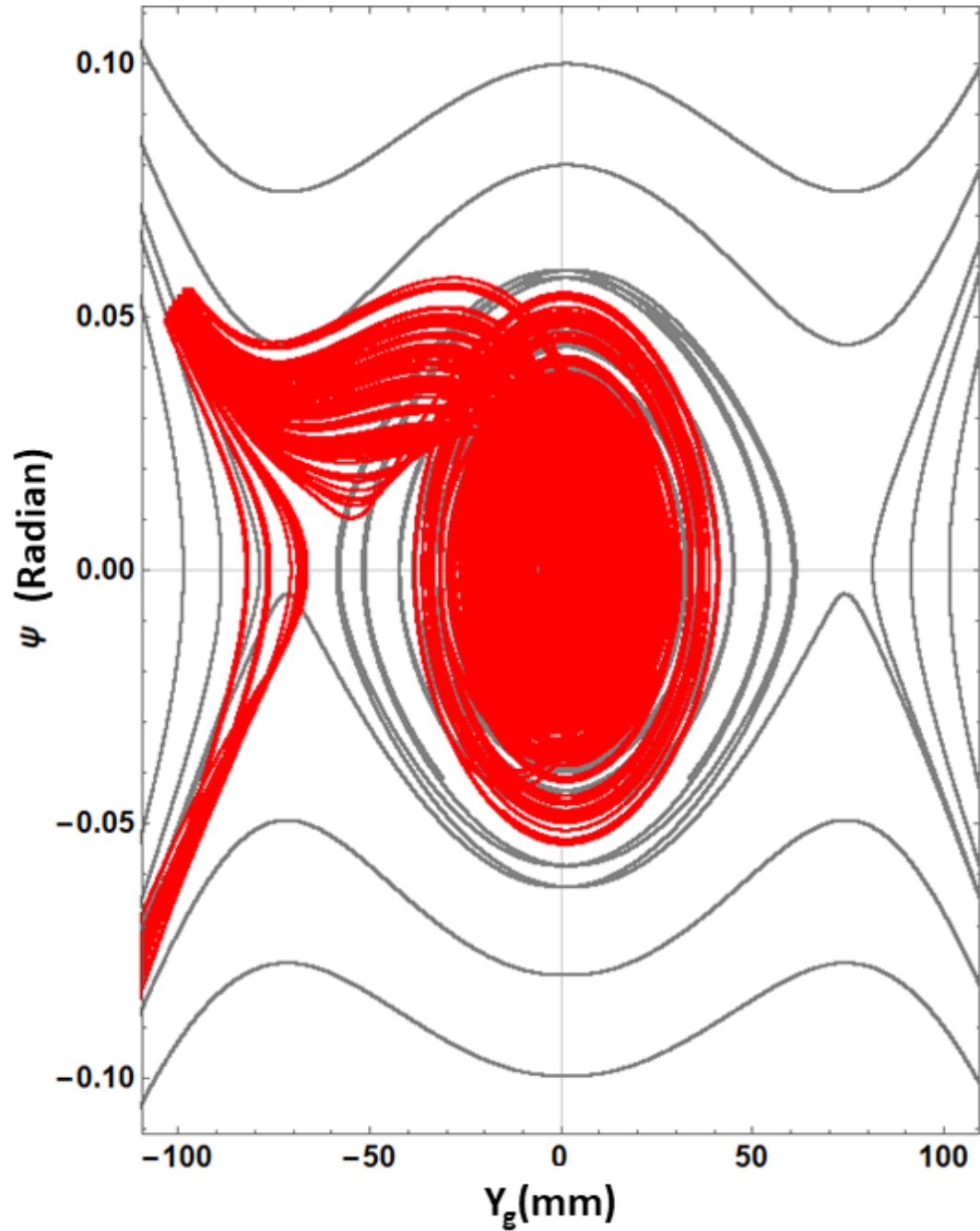


Figure 7.19: The kicker tracking with the phase-space matching (XY-coupled) to estimate the injection efficiency. The grey lines show the separatrix for the field index 1.65×10^{-2} . The closed contours present the stable region and open hyperbolas show the unstable region. The red closed lines present the stored beam, whereas, open lines show the lost particles.

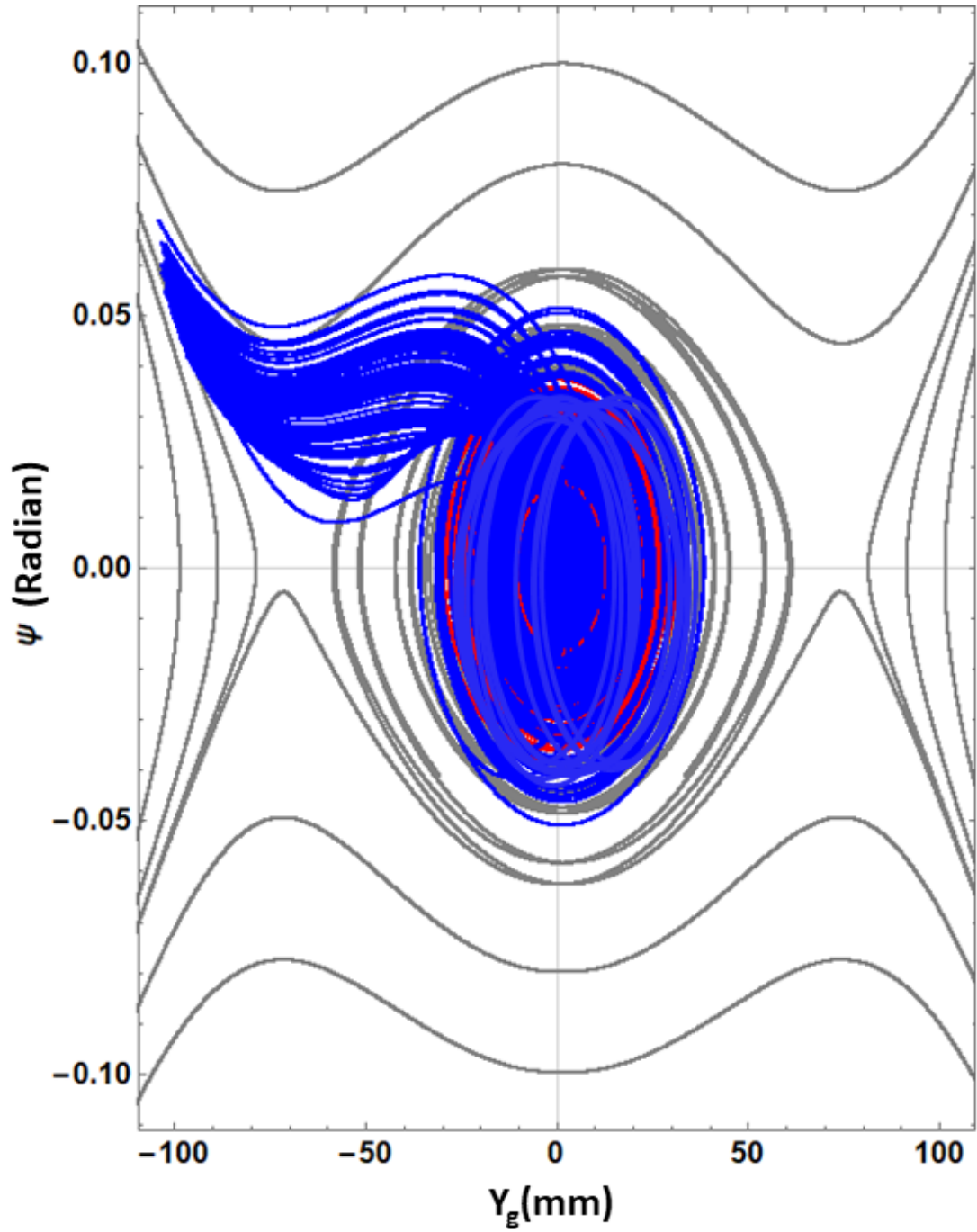


Figure 7.20: The kicker tracking with flipped XY-coupled phase space. The closed blue contours represents the stored beam. In this case 100% beam get stored.

7.5.1 Injection Inefficiencies

The most probable reasons for the injection inefficiencies are following:

- Vertical beam size at the kick point
- Energy spread
- The beam pulse length

The major reason for the injection inefficiency is the bigger vertical beam size at the kick than the acceptance of the the weak focusing index. As shown in the the previous section, in the case of no phase-space matching beam size grows to the 31 mm at the kick point and injection efficiency is only 12%. In the case of phase-space matching with three rotatable quadrupole magnets the vertical beam size reduces to the 8.06 mm at the kick point and approximately 80% beam gets stored in this case.

The other cause of the injection inefficiency could be the beam energy spread. The energy spread (ΔE) is associated to the accelerating voltage of the electron gun. The better stability of accelerating voltage results in the lower energy spread. For the SITE's electron gun the energy spread from the accelerating voltage stability was estimated about 0.01% ($\Delta E/E = 6 \times 10^{-5}$). This small value of the energy spread does not cause any effect on the injection efficiency. In order to reveal the effect of the energy spread on the injection efficiency a factor of large energy spread was assumed ($\Delta E/E = 6 \times 10^{-4}$). In this scenario, the injection efficiency reduce to 67%. Figure 7.21 presents the tracking of the beam in transient field of the kicker with the energy spread of $\Delta E/E = 6 \times 10^{-4}$.

The beam of 2 ns pulse length will be generated by the electric chopper system. In order to show the effect of beam pulse length on the injection inefficiency, tracking simulation with 2 ns. The kicker duration is 50 ns. Because kicker duration is enough longer as compared to the beam pulse length of 2 ns, therefore, it has no effect on the injection efficiency.

7.6 Summary

The symmetrical and localized types of kickers are designed for the SITE. The transient tracking simulation had been done by the custom made program (4th order Runge-Kutta method) to simulate the characteristics of the beam in the kicker field. The beam acceptance and storage volume was also computed by the tracking simulation.

The realistic design of both types of kickers coils was presented. In the case of symmetrical kick an Anti-Helmholtz type kicker will serve the purpose, whereas in the case of the localized kicker a simple dipole coil can produce the required kick field.

The power losses due to Eddy current in the wall of the vacuum chamber was also estimated. It was found that the losses due to the Eddy current is minor and can be compensated by simply increasing the current of the kicker power supply.

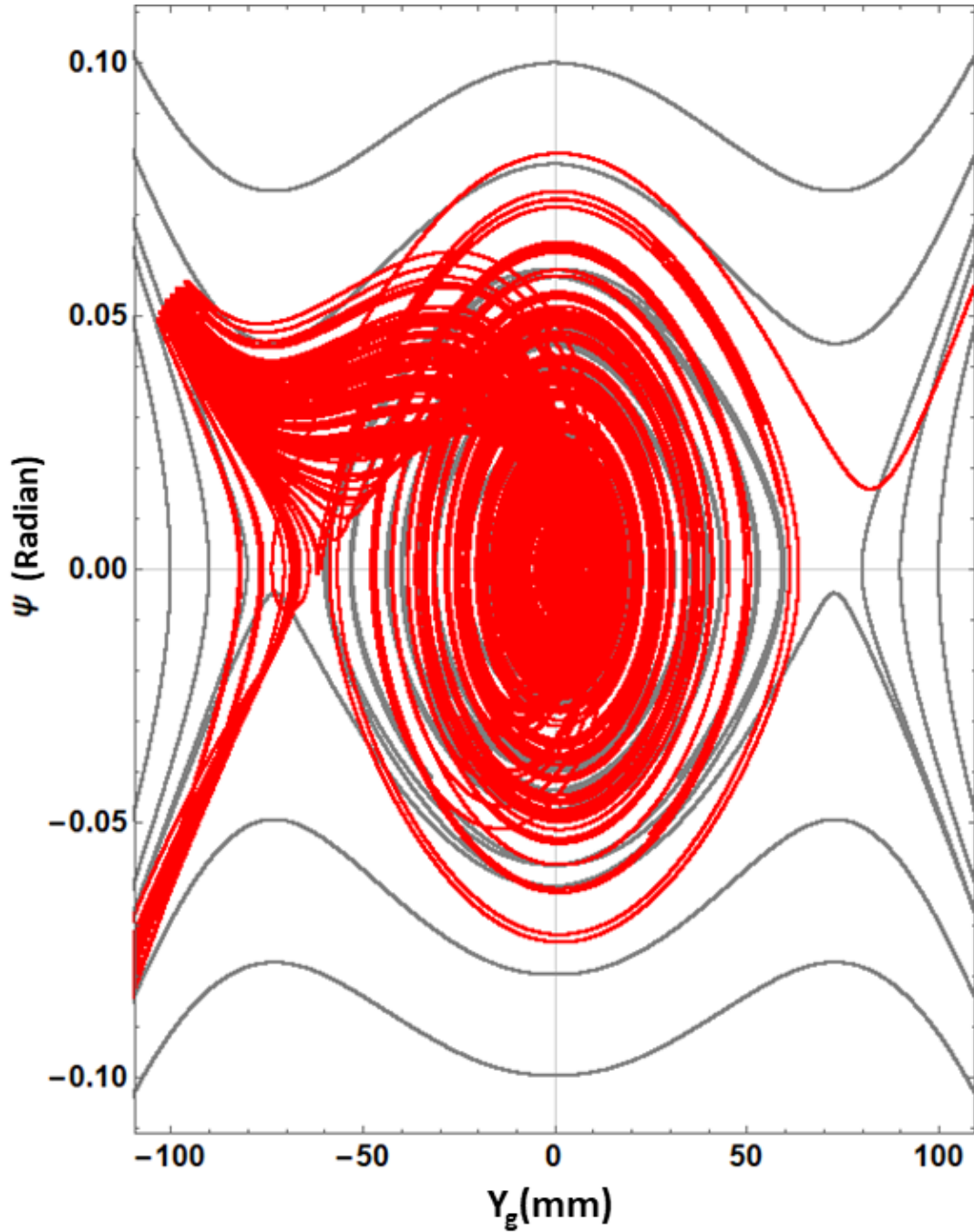


Figure 7.21: The tracking of the beam in transient field of the kicker with the energy spread of $\Delta E/E = 6 \times 10^{-4}$. In this scenario, the injection efficiency reduce to 67%.

7.6. SUMMARY

The kicker power supply had been designed and manufactured in collaboration with a private company. The test of the kicker power supply also has been performed.

Chapter 8

Conclusions

The muon anomalous magnetic moment $(g-2)_\mu$ is one of the most important measurements in elementary particle physics. The most recent measurement of $(g-2)_\mu$ at Brookhaven National Laboratory (BNL) results in more than 3σ discrepancy compared with the equally precise Standard Model prediction. This disparity could be indicative of new physics beyond the standard model. To resolve this discrepancy, a new muon's $g-2$ /EDM (E34) experiment at J-PARC aims to measure $(g-2)_\mu$ to a precision of 0.1 ppm and electric dipole moment (EDM) down to the sensitivity of 1.5×10^{-21} e.cm. The key objective of measuring $(g-2)_\mu$ is to store spin polarized μ^+ beam in a magnetic field and evaluate the evolution of the spin precession vector. In the E34 experiment, a muon beam with an emittance less than 0.5π mm mrad and a momentum of 300 MeV/c from a muon accelerator will be injected into a compact 3-T solenoid magnet. The muon beam will be stored on a 0.66 m diameter orbit. The solenoid magnet will provide an unprecedented local field uniformity of 0.1 ppm (peak to peak).

A new three-dimensional spiral injection scheme has been invented to inject the beam into a compact solenoid magnet. This new injection scheme will enhance injection efficiency and overcome technical challenges related to the small storage orbit diameter. In the spiral injection scheme, the beam will be injected at a vertical angle into the storage magnet. The radial component of the fringe field of the solenoid magnet will decrease the vertical angle of the beam as it approaches the midplane of the magnet. Finally, a magnetic pulsed kicker will guide the beam to the storage volume where the beam will be stored under a weak focusing field. However, the injection of the accelerated beam into such a small storage orbit is unprecedented; therefore, a demonstration experiment to establish the feasibility of this new injection scheme is inevitable.

The purpose of this research was to develop a scale down Spiral Injection Test Experiment (SITE) with an electron beam to demonstrate the ideology behind this new injection scheme.

An electron beamline of a length of 2 m has been designed and constructed for the SITE. The beamline consists of a triode-type thermionic electron gun with a **LaB₆** cathode to generate a DC electron beam of 80 keV with a beam current of approximately 100 μ A. Subsequently, a magnetic lens was placed to prevent the growth of the beam. A collimator with a diameter of 3 mm and

a length of 5 mm was placed at a distance of 0.7 m from the exit of the electron gun. A pair of air-core steering coils has been installed to control the transverse position of the 80 keV electron beam. Next, three rotation quadrupole magnets were installed to control the beam phase space for the spiral injection. An electron beam in a straight beam line was successfully commissioned and confirmed at several locations via fluorescent screen monitors. The emittance of the electron beam after collimation was measured by the quadrupole scan method. The emittance value in the horizontal direction was estimated 0.61 ± 0.05 mm mrad and in the vertical direction, it was 0.41 ± 0.04 mm mrad. In order to estimate the beam transverse coupling strength a simple procedure was developed. The coupling strength of the beam after the collimator was estimated to 0.17 ± 0.6 . This small value of coupling means decoupled beam after the collimator.

A normal conducting solenoid-type storage magnet of field strength 82.5 Gauss was designed and constructed to store the electron beam in an orbit with a diameter of 0.24 m. In the case of SITE, the field index value n (strength of weak focusing: $0 < n < 1$) of 1.65×10^{-2} was set. This higher value of the field index relaxes the phase space requirement and vertical kicker parameters for SITE.

A non-invasive gas monitor was used to detect the electron beam track in the storage magnet. A charge-coupled device (CCD) camera was used to observe fluorescent light originating from the gas monitor. An electron beam track of four turns in the vacuum chamber of the storage magnet was confirmed by this gas monitor, which is a good qualitative tool to efficiently verify the electron beam track inside the storage magnet. However, a gas monitor lacks the ability to provide quantitative information about the position of the beam and the profile in the storage magnet. Therefore, a special type of a wire scanner for determining the beam position and measuring the profile in the solenoid magnet was designed, constructed and successfully commissioned for SITE. Two wire scanners were installed on the storage magnet to measure the beam profile and beam evolution in the storage magnet.

Due to the axial symmetric field of the solenoid magnet, a strongly XY-coupled beam is required. To produce the required phase space for the solenoid-type storage magnet, a beam transport line consisting of three rotatable quadrupole magnets has been designed and built for SITE. The vertical beam size reduction by means of phase space matching and other geometrical information have been successfully measured by the wire scanners and confirmed by the simulation. The vertical beam size had been reduced to 25.68 ± 0.31 mm with the phase matching as compared to vertical beam growth of 78.41 ± 0.83 mm without any rotatable quadrupole magnets.

To store the beam at the center of the storage magnet, a pulsed magnetic kicker was designed and simulated. From simulation studies, the best design parameters for the magnetic kicker have been determined. As explained earlier in the case of SITE, the field index value of 1.65×10^{-2} was used. This value of the field index allowed to use pulse width of 50 ns for the kicker. In addition, it also provides a weak focusing trap of ± 50 mm at storage region. A tracking simulation with the best beam phase space that can be achieved by the three rotatable quadrupole magnets has

been performed. And it was estimated that injection efficiency of 81% can be achieved for SITE.

The purpose of this study was to prove the ideology of 3-D spiral injection scheme with the electron beam. The qualitative and quantitative details of the vertical and horizontal beam profiles and positions inside the solenoid storage magnet are one of the most important requisites for the successful 3-D spiral injection. Therefore, a wire scanner type beam position and profile monitor was developed for the SITE. The knowledge and experience of wire scanner development to extract the beam profile and position for the SITE storage magnet greatly helped to understand the beam behavior inside the solenoid storage magnet. Moreover, it paved the way for the development of a similar quantitative monitor for the successful 3-D spiral injection in the case of E34. The method to measure the transverse beam coupling developed at the SITE will also be implanted at E34 to estimate the coupling strength at the matching point.

Hence, evidence from this study concludes that the novel 3-D spiral injection scheme can be applied to the E34 storage magnet with the appropriate phase space matching and a quantitative monitor for the solenoid type storage magnet.

Acknowledgment

There are so many people I wish to thank who have in one way or another made this thesis possible. I would like to express my sincere gratitude to my supervisor Prof. Kazuro Furukawa for his constant support, guidance, and motivation academically and otherwise. The door to Prof. Kazuro Furukawa's office was always open whenever I ran into a trouble spot.

I would like to express my deepest gratitude to Prof. Hiromi Iinuma for her patient guidance, enthusiastic encouragement and useful critiques of my research work.

I wish to give special thanks to my Co-supervisor Prof. Tsutomu Mibe for his incredible support and encouragement.

I am much obliged to Prof. Satoshi Ohsawa for his support academically and in my daily life. His teaching and support were indispensable for the completion of this thesis.

I would like to thank Prof. Hisayoshi Nakayama. He has been supportive since the days I began my work at the experiment.

I am indebted to Mr. Hiromi Hisamatsu for his kind help during the experiment and for providing us many crucial vacuum components. I would also like to thank Prof. Tohru Honda for his special interest and care about my research project.

I am grateful to Prof. Naohito Saito for giving me many constructive comments and suggestions during weekly meetings. I would also like to thank all Saito's lab members: Mr. Ce Zhang, Mr. Taha Youssef, Mr. Hiromasa Yasuda, Mr. Takahiro Ushizawa, Dr. Yutaro Sato.

I am thankful to Mr. Hirohiko Someya for kindly letting me use his laboratory for coil winding. I am much obliged to Prof. Toshiyasu Higo and Prof. Izumi Mochizuki for their generous support for this project.

I am greatly indebted to KEK LINAC (e^-/e^+) staff for their support and help for SITE.

I gratefully acknowledge the support of the SOKENDAI office Ms. Harumi Michikawa, Ms. Noriko Yamamura, Ms. Minami Ono, and Ms. Kimura.

I am grateful to Dr. Sigit B Wibowo, Dr. Emy Mulyani, Dr. Na Liu, Mr. Di Wang, and Mr. Du Baiting for their friendship and being awesome office mates.

Finally, I must express my gratitude to my mother and siblings for their prayers and countless love for me.

Appendix A

Appendix

A.1 Wire Scanner Data Acquisition System Code (C#)

A GUI program in *C#* was developed for data acquisition and online plotting of wire scanner data. Figure A.1 is the screenshot of the control program.

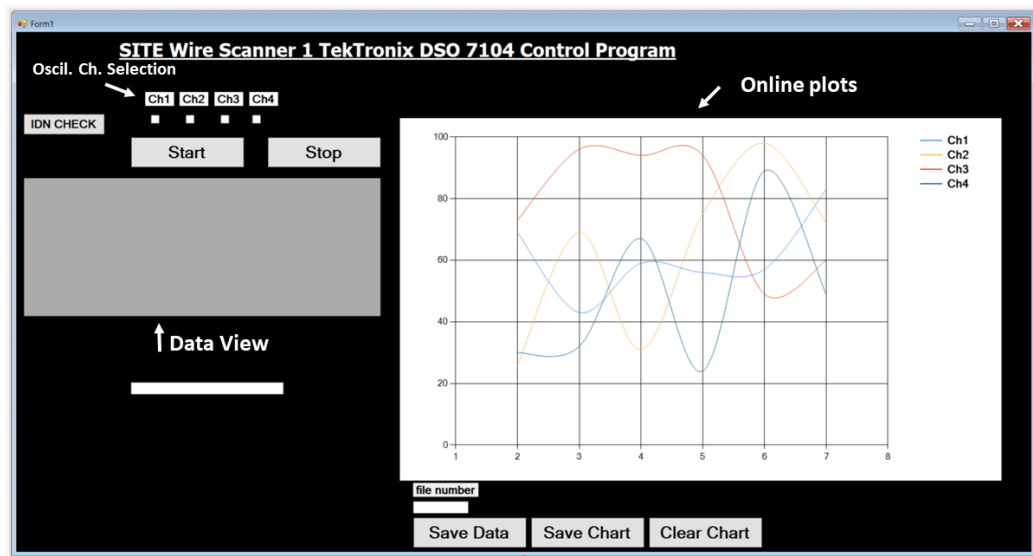


Figure A.1: The screenshot of the DPO-7104 oscilloscope control program.

Listing A.1: C# code for Tektronix DPO-7104 Oscilloscope

```
1 using System;  
2 using System.Collections.Generic;  
3 using System.ComponentModel;  
4 using System.Data;  
5 using System.Drawing;  
6 using System.Linq;  
7 using System.Text;
```

```

8 using System.Threading.Tasks;
9 using System.Windows.Forms;
10 using TekVISA.NET;
11 using TekInstrMgr;
12 using VISAInstallCheckLib;
13 using System.Collections;
14 using System.Diagnostics;
15 using System.IO;
16
17 namespace DPO7104_Control_WinForm
18 {
19     public partial class Form1 : Form
20     {
21         bool flag;
22         private const string OSCILLOSCOPE = "TCPIP::169.254.138.160::INSTR";
23         public Form1()
24         {
25             InitializeComponent();
26         }
27         private void Button1_Click(object sender, EventArgs e)
28         {
29             string response;
30             ArrayList resources = new ArrayList();
31             VISA tekVISA = new VISA();
32             tekVISA.FindResources("?* ", out resources);
33             Console.ForegroundColor = ConsoleColor.Green;
34             tekVISA.Open(resources[0].ToString());
35             tekVISA.Write("*IDN?");
36             bool status = tekVISA.Read(out response);
37             if (status)
38             {
39                 MessageBox.Show("Instrument *IDN? query returned:
40                 \n" + response.ToString(), "Device Connection
41                 Test");
42             }
43         }
44         private void Button2_Click(object sender, EventArgs e)
45         {
46             DataTable dt1;
47             dt1 = new DataTable();
48             dt1.Columns.Add("#ID");
49             dt1.Columns.Add("time (ms)");
50             dt1.Columns.Add("Ch1_V_Mean");
51             dt1.Columns.Add("Ch2_V_Mean");
52             dt1.Columns.Add("Ch3_V_Mean");
53             dt1.Columns.Add("Ch4_V_Mean");
54             dataGridView1.DataSource = dt1;
55
56             DataRow r1;

```



```

106         Application.DoEvents();
107     }
108 }
109
110 if (checkBox2.Checked)
111 {
112     tekVISA.Write("MEASUREMENT:MEAS2:TYPE MEAN");
113     tekVISA.Write("MEASUREMENT:MEAS2:SOURCE1 CH2");
114     tekVISA.Write("MEASUREMENT:MEAS2:STATE ON");
115     ///write command to read RMS
116     tekVISA.Write("MEASUREMENT:MEAS2:VALUE?");
117     string response1 = "";
118     ///read data
119     tekVISA.Read(out response1);
120
121     r1[3] = response1.ToString();
122     double rv2 = Convert.ToDouble(response1);
123
124     if (rv2 < 99.0000E+36)
125     {
126         this.chart1.Series["Ch2"].Points.AddXY((v
127             * (t / 1000)) * 1000, response1);
128     }
129 }
130 if (checkBox3.Checked)
131 {
132     tekVISA.Write("MEASUREMENT:MEAS3:TYPE
133     MEAN");
134     tekVISA.Write("MEASUREMENT:MEAS3:SOURCE1
135     CH3");
136     tekVISA.Write("MEASUREMENT:MEAS3:STATE
137     ON");
138     ///write command to read RMS
139     tekVISA.Write("MEASUREMENT:MEAS3:VALUE?");
140     string response2 = "";
141     ///read data
142     tekVISA.Read(out response2);
143     //textBox1.Text = response2.ToString();
144     r1[4] = response2.ToString();
145     double rv1 = Convert.ToDouble(response2);
146
147     if (rv1 < 99.0000E+36)
148     {
149         this.chart1.Series["Ch3"].Points.AddXY((v
150             * (t / 1000)) * 1000, response2);
151     }
152 }
153 if (checkBox4.Checked)
154 {

```

```

155         tekVISA.Write("MEASUREMENT:MEAS4:TYPE
156         MEAN");
157         tekVISA.Write("MEASUREMENT:MEAS4:SOURCE1
158         CH4");
159         tekVISA.Write("MEASUREMENT:MEAS4:STATE
160         ON");
161         ///write command to read RMS
162         tekVISA.Write("MEASUREMENT:MEAS4:VALUE?");
163         string response3 = "";
164         ///read data
165         tekVISA.Read(out response3);
166         // textBox1.Text = response3.ToString();
167         double rv = Convert.ToDouble(response3);
168
169         if (rv < 99.0000E+36)
170         {
171             r1[5] = response3.ToString();
172
173             this.chart1.Series["Ch4"].Points.AddXY((v
174             * (t / 1000)) * 1000, response3);
175         }
176     }
177
178     num++;
179     dt1.Rows.Add(r1);
180     Application.DoEvents();
181 }
182 s.Stop();
183 }
184 }
185
186 private void Button3_Click(object sender, EventArgs e)
187 {
188     flag = false;
189 }
190
191 private void Button5_Click(object sender, EventArgs e)
192 {
193     SaveFileDialog savechart = new SaveFileDialog();
194     savechart.Filter = "JPeg Image|*.jpg|Bitmap Image|
195     *.bmp|Gif Image|*.gif";
196     savechart.Title = "Save the Chart";
197     savechart.ShowDialog();
198     if (savechart.FileName != "")
199     {
200         System.IO.FileStream fs =
201         (System.IO.FileStream)savechart.OpenFile();
202         this.chart1.SaveImage(fs,
203         System.Drawing.Imaging.ImageFormat.Jpeg);

```

```

204         string path =
205             System.IO.Path.GetFullPath(savechart.FileName);
206         MessageBox.Show("Pol1 Saved" + path);
207     }
208 }
209
210 private void Button6_Click(object sender, EventArgs e)
211 {
212     chart1.Series["Chane11"].Points.Clear();
213     chart1.Series["Chane12"].Points.Clear();
214     chart1.Series["Chane13"].Points.Clear();
215     chart1.Series["Chane14"].Points.Clear();
216 }
217
218 private void Button4_Click(object sender, EventArgs e)
219 {
220     double num;
221     num = double.Parse(textBox2.Text);
222     // textBox5.Text = "Waveform format: BYTE";
223     StreamWriter writer = new StreamWriter
224         (@":\\Users\\M. A. Rehman\\Desktop\\Tek_data\\
225         \tek_meas_data_ws1_
226         + num.ToString() + ".txt");
227
228     for (int i = 0; i < dataGridView1.Rows.Count - 1; i++)
229     {
230         for (int j = 0; j < dataGridView1.Columns.Count;
231             j++)
232         {
233             writer.Write("\t" +
234                 dataGridView1.Rows[i].Cells[j].Value.ToString()
235                 + "\t");
236         }
237         writer.WriteLine("");
238     }
239     writer.Close();
240     MessageBox.Show("Data Exported");
241 }
242 }
243 }
244 }

```

Appendix B

Appendix

B.1 The beam Injection with other settings

In this section, the wire scanner results with settings other than the best run, with the three rotation quadrupole magnets are shown. In Fig. B.1 (a) and (b) (X, Y) , and (X, X') were matched preferentially while (Y, Y') was ignored. Figure B.1 shows the wire scanner 1 and 2 results with beam phase-space setting as shown in Fig.B.1. Figure B.3 presents the comparison of the vertical beam sizes growth in the storage magnet with the phase space settings as shown in Fig. B.1.

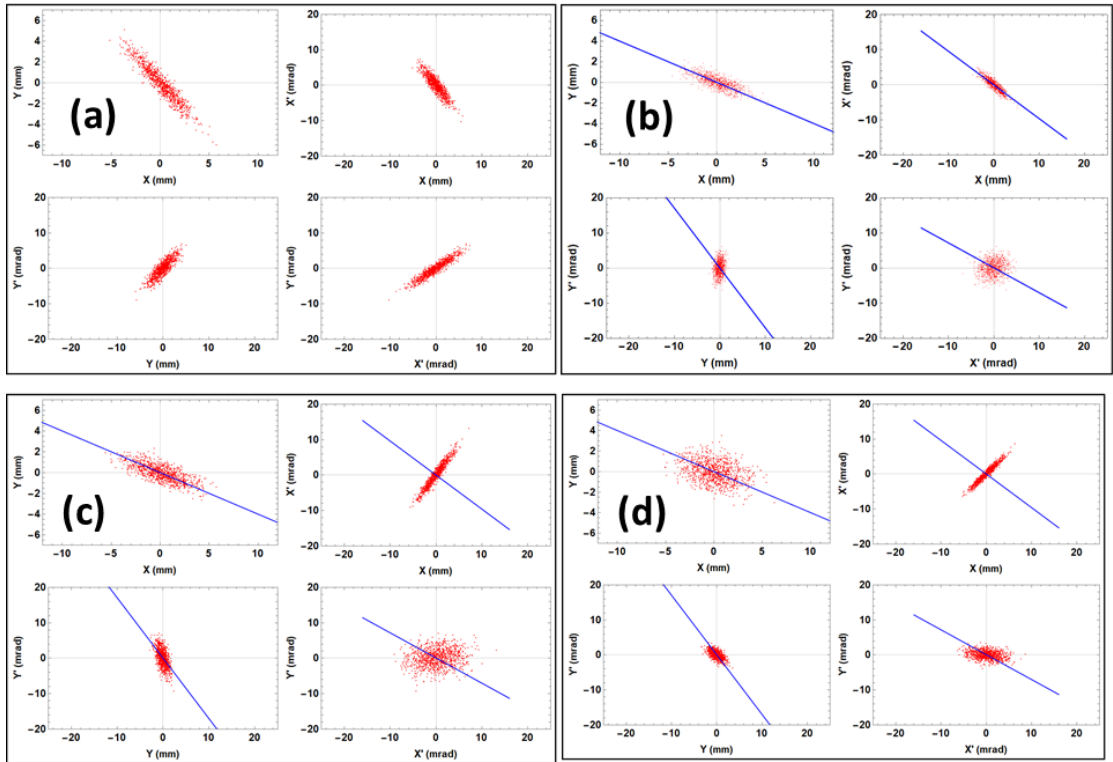


Figure B.1: The beam phase space with setting others than best run are shown. In (a) and (b) (X, Y) , and (X, X') were matched preferentially while (Y, Y') was ignored.

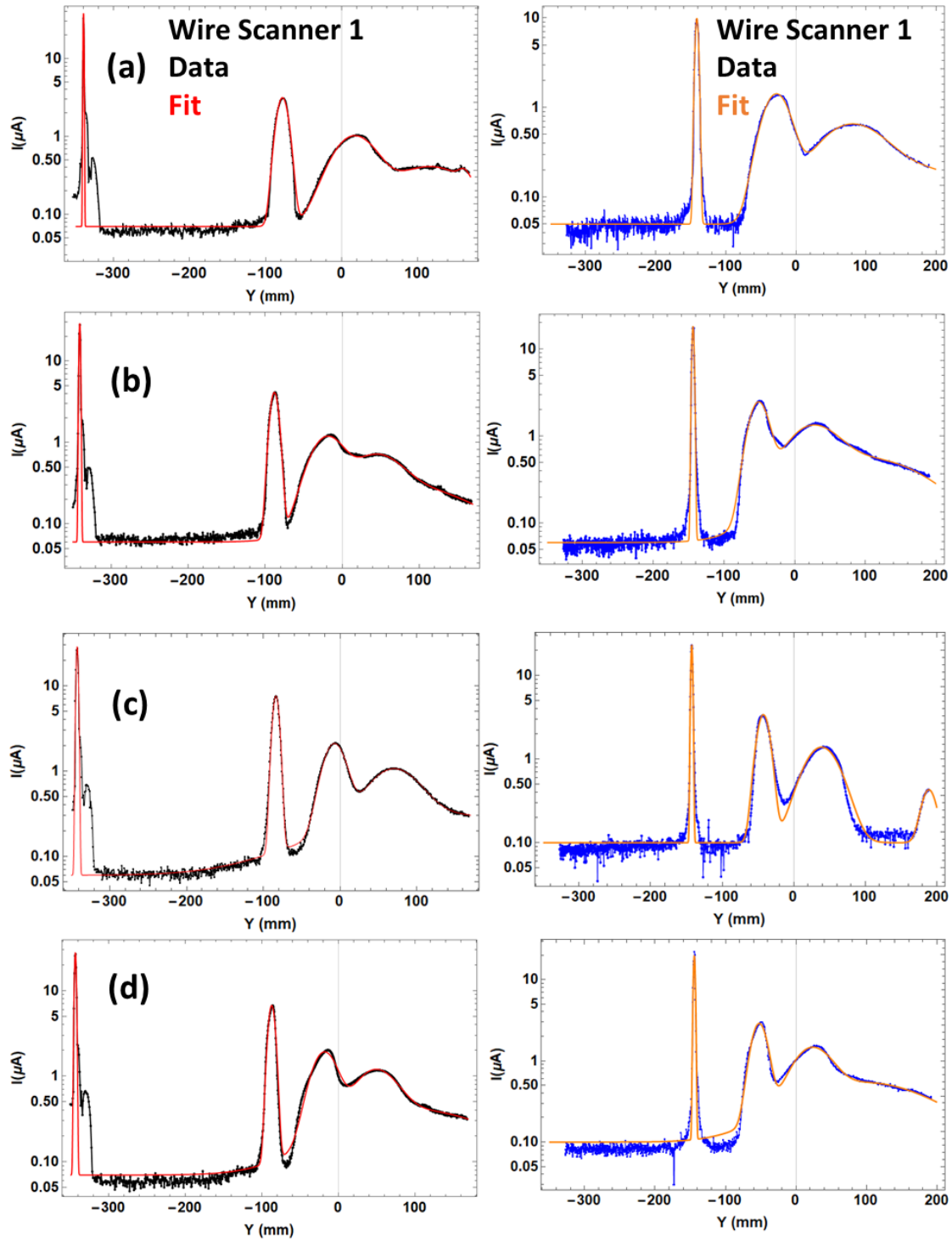


Figure B.2: The wire scanner a and 2 results with beam phase-space setting as shown in Fig.B.1.

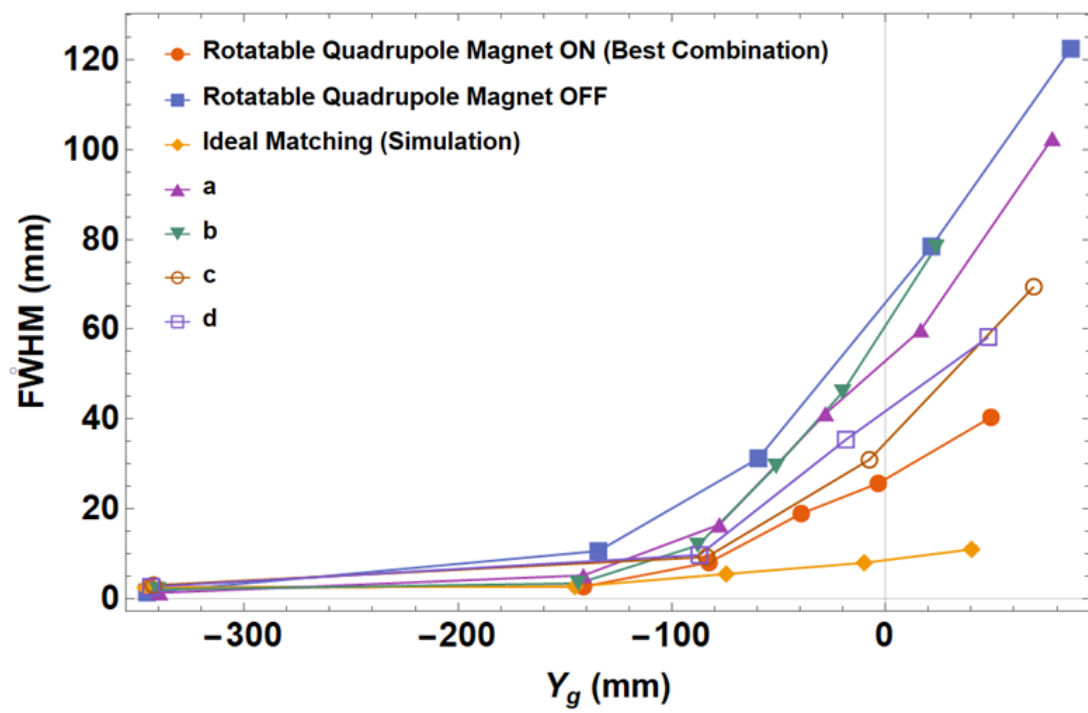


Figure B.3: The comparison of the vertical beam sizes growth in the storage magnet with the phase space settings as shown in Fig. B.1.

Appendix C

Appendix

C.1 Pulsed Magnetic Kicker Tracking Code (Mathematica)

This is the code developed for the particle tracking in the time varying field of the kicker.

Listing C.1: Example code

```
1 (*Time Doamin Tracking*)
2 Bz = Import[NotebookDirectory[] <> "6bz.txt", "Table"];
3 Bx = Import[NotebookDirectory[] <> "6bx.txt", "Table"];
4 BzD = Dimensions[Bz][[1]];
5 BxD = Dimensions[Bx][[1]];
6 oscil = 0; t11 = 100;
7
8 kick = Import[NotebookDirectory[] <> "currentpath_inner coil_10A.txt",
9 "Table"];
10 z1 = Table[i, {i, -300, 300, 1}];
11
12 Tf = t11 10-9; dt =
13 1 10-12; ttime = (Tf/dt); runT = (Tf/dt)/2 + oscil;
14 ParallelEvaluate [
15 MultiPart[xi0_, yi0_, zi0_, \[Theta]0_] :=
16 Module[{xi = xi0, yi = yi0, zi = zi0, \[Theta] = \[Theta]0},
17 z = Table[i, {i, -350, 350, 1}];
18 BTa =
19 Table[{z[[i]], 0.979 Bz[[i, 2]], -0.979 Bx[[i, 2]]}, {i, 1,
20 BzD - 1}];
21 br = Table[{z1[[i]], 1.98 kick[[i, 2]]}, {i, 1,
22 Dimensions[kick][[1]] - 1}];
23 (*RK-4 Method half sine shape pitch angle \[Theta]=
24 2.12 Degree*)
25
26 q = 1.6 10-19; k = 80; c = (3 108) 103;
27
```

```

28 Tf = t11 10^-9; dt = 1 10^-12; ttime = (Tf/dt);
29 Br = (0.571 10^-4);(*\[Theta]=0.5Degree;*)
30 er = 511;
31 et = k + er; \[Gamma] = et/er; \[Beta] =
32 Sqrt[1 - (1/\[Gamma]^2)] // N; m = 9.1 10^-31 \[Gamma];
33 vt = -\[Beta] c // N;
34 vxi = vt Cos\[Theta];
35 vyi = vt 0.;
36 vzi = vt Sin\[Theta];
37 t = t11 10^-9;
38 mat = {};
39
40 nnn = (Tf/dt)/2;
41 Clear[K, l, M, n, o, P];
42 { While[nnn >= 0 \[And] zi < 300 \[And] zi > -300, t = t - dt;
43 k1 = q / m (vyi BTA[[Position[BTA, Round[zi]][[1, 1], 2]] -
44 vzi ( If [nnn >= 0,
45 br[[ Position [br, Round[zi]][[1, 1], 2]] Cos[
46 ArcCos[xi/Sqrt[xi^2 + yi^2]] Sin[t (2 \[Pi])/Tf],
47 0] + BTA[[Position[BTA, Round[zi]][[1, 1], 3]] Cos[
48 ArcCos[xi/Sqrt[xi^2 + yi^2]]]) dt; l1 = vxi dt;
49 k2 = q / m ((vyi + k1/2) BTA[[Position[BTA, Round[zi]][[1, 1],
50 2]] - (vzi + k1/
51 2) ( If [nnn >= 0,
52 br[[ Position [br, Round[zi]][[1, 1], 2]] Cos[
53 ArcCos[xi/Sqrt[xi^2 + yi^2]] Sin[t (2 \[Pi])/Tf],
54 0] +
55 BTA[[Position[BTA, Round[zi]][[1, 1], 3]] Cos[
56 ArcCos[xi/Sqrt[xi^2 + yi^2]]]) dt;
57 l2 = (vxi + k1/2) dt;
58 k3 = q / m ((vyi + k2/2) BTA[[Position[BTA, Round[zi]][[1, 1],
59 2]] - (vzi + k2/
60 2) ( If [nnn >= 0,
61 br[[ Position [br, Round[zi]][[1, 1], 2]] Cos[
62 ArcCos[xi/Sqrt[xi^2 + yi^2]] Sin[t (2 \[Pi])/Tf],
63 0] + BTA[[Position[BTA, Round[zi]][[1, 1], 3]] Cos[
64 ArcCos[xi/Sqrt[xi^2 + yi^2]]]) dt;
65 l3 = (vxi + k2/2) dt;
66 k4 = q / m ((vyi + k3) BTA[[Position[BTA, Round[zi]][[1, 1],
67 2]] - (vzi +
68 k3) ( If [nnn >= 0,
69 br[[ Position [br, Round[zi]][[1, 1], 2]] Cos[
70 ArcCos[xi/Sqrt[xi^2 + yi^2]] Sin[t (2 \[Pi])/Tf],
71 0] + BTA[[Position[BTA, Round[zi]][[1, 1], 3]] Cos[
72 ArcCos[xi/Sqrt[xi^2 + yi^2]]]) dt; l4 = (vxi + k3) dt;
73 K = 1/6 (k1 + 2 k2 + 2 k3 + k4);
74 l = 1/6 (l1 + 2 l2 + 2 l3 + l4);
75 vxf = vxi + K; xf = xi + l;
76 m1 =

```

```

77     q / m (vzi ( If [nnn >= 0,
78         br [[ Position [br, Round[zi ]][[1, 1]], 2]] Cos[
79             ArcCos[xi/Sqrt[xi^2 + yi^2]] Sin[t (2 \[Pi])/Tf],
80         0] + BTa[[Position[BTa, Round[zi ]][[1, 1]], 3]] Cos[
81             ArcCos[xi/Sqrt[xi^2 + yi^2]]) -
82     vxi BTa[[Position [BTa, Round[zi ]][[1, 1]], 2]] dt;
83 n1 = vyi dt;
84 m2 = q / m ((vzi + m1/
85     2) ( If [nnn >= 0,
86     br [[ Position [br, Round[zi ]][[1, 1]], 2]] Cos[
87         ArcCos[xi/Sqrt[xi^2 + yi^2]] Sin[t (2 \[Pi])/Tf],
88     0] + BTa[[Position[BTa, Round[zi ]][[1, 1]], 3]] Cos[
89         ArcCos[xi/Sqrt[xi^2 + yi^2]]) - (vxi + m1/2) BTa[[
90     Position [BTa, Round[zi ]][[1, 1]], 2]] dt;
91 n2 = (vyi + m1/2) dt;
92 m3 = q / m ((vzi + m2/
93     2) ( If [nnn >= 0,
94     br [[ Position [br, Round[zi ]][[1, 1]], 2]] Cos[
95         ArcCos[xi/Sqrt[xi^2 + yi^2]] Sin[t (2 \[Pi])/Tf],
96     0] + BTa[[Position[BTa, Round[zi ]][[1, 1]], 3]] Cos[
97         ArcCos[xi/Sqrt[xi^2 + yi^2]]) - (vxi + m2/2) BTa[[
98     Position [BTa, Round[zi ]][[1, 1]], 2]] dt;
99 n3 = (vyi + m2/2) dt;
100 m4 = q / m ((vzi +
101     m3) ( If [nnn >= 0,
102     br [[ Position [br, Round[zi ]][[1, 1]], 2]] Cos[
103         ArcCos[xi/Sqrt[xi^2 + yi^2]] Sin[t (2 \[Pi])/Tf],
104     0] + BTa[[Position[BTa, Round[zi ]][[1, 1]], 3]] Cos[
105         ArcCos[xi/Sqrt[xi^2 + yi^2]]) - (vxi + m3) BTa[[
106     Position [BTa, Round[zi ]][[1, 1]], 2]] dt;
107 n4 = (vyi + m3) dt; M = 1/6 (m1 + 2 m2 + 2 m3 + m4);
108 n = 1/6 (n1 + 2 n2 + 2 n3 + n4);
109 vyf = vyi + M; yf = yi + n;
110 o1 =
111     q / m (vxi ( If [nnn >= 0,
112         br [[ Position [br, Round[zi ]][[1, 1]], 2]] Sin[
113             ArcSin[yi/Sqrt[xi^2 + yi^2]] Sin[t (2 \[Pi])/Tf],
114         0] + BTa[[Position[BTa, Round[zi ]][[1, 1]], 3]] Sin[
115             ArcSin[yi/Sqrt[xi^2 + yi^2]]) -
116     vyi ( If [nnn >= 0,
117         br [[ Position [br, Round[zi ]][[1, 1]], 2]] Cos[
118             ArcCos[xi/Sqrt[xi^2 + yi^2]] Sin[t (2 \[Pi])/Tf],
119         0] + BTa[[Position[BTa, Round[zi ]][[1, 1]], 3]] Cos[
120             ArcCos[xi/Sqrt[xi^2 + yi^2]]) dt; p1 = vzi dt;
121 o2 = q / m ((vxi + o1/
122     2) ( If [nnn >= 0,
123     br [[ Position [br, Round[zi ]][[1, 1]], 2]] Sin[
124         ArcSin[yi/Sqrt[xi^2 + yi^2]] Sin[t (2 \[Pi])/Tf],
125     0] + BTa[[Position[BTa, Round[zi ]][[1, 1]], 3]] Sin[

```

```

126      ArcSin[yi/Sqrt[xi^2 + yi^2]]) - (vyi + o1/
127      2) ( If [nnn >= 0,
128      br [[ Position [br, Round[zi ]][[1, 1]], 2]] Cos[
129      ArcCos[xi/Sqrt[xi^2 + yi^2]] Sin[t (2 \[Pi])/Tf],
130      0] + BTa[[Position[BTa, Round[zi ]][[1, 1]], 3]] Cos[
131      ArcCos[xi/Sqrt[xi^2 + yi^2]]) ) dt;
132 p2 = (vzi + o1/2) dt;
133 o3 = q /m ((vxi + o2/
134      2) ( If [nnn >= 0,
135      br [[ Position [br, Round[zi ]][[1, 1]], 2]] Sin[
136      ArcSin[yi/Sqrt[xi^2 + yi^2]] Sin[t (2 \[Pi])/Tf],
137      0] + BTa[[Position[BTa, Round[zi ]][[1, 1]], 3]] Sin[
138      ArcSin[yi/Sqrt[xi^2 + yi^2]]) - (vyi + o2/
139      2) ( If [nnn >= 0,
140      br [[ Position [br, Round[zi ]][[1, 1]], 2]] Cos[
141      ArcCos[xi/Sqrt[xi^2 + yi^2]] Sin[t (2 \[Pi])/Tf],
142      0] + BTa[[Position[BTa, Round[zi ]][[1, 1]], 3]] Cos[
143      ArcCos[xi/Sqrt[xi^2 + yi^2]]) ) dt;
144 p3 = (vzi + o2/2) dt;
145 o4 = q /m ((vxi +
146      o3) ( If [nnn >= 0,
147      br [[ Position [br, Round[zi ]][[1, 1]], 2]] Sin[
148      ArcSin[yi/Sqrt[xi^2 + yi^2]] Sin[t (2 \[Pi])/Tf],
149      0] + BTa[[Position[BTa, Round[zi ]][[1, 1]], 3]] Sin[
150      ArcSin[yi/Sqrt[xi^2 + yi^2]]) - (vyi +
151      o3) ( If [nnn >= 0,
152      br [[ Position [br, Round[zi ]][[1, 1]], 2]] Cos[
153      ArcCos[xi/Sqrt[xi^2 + yi^2]] Sin[t (2 \[Pi])/Tf],
154      0] + BTa[[Position[BTa, Round[zi ]][[1, 1]], 3]] Cos[
155      ArcCos[xi/Sqrt[xi^2 + yi^2]]) ) dt; p4 = (vzi + o3) dt;
156 o = 1/6 (o1 + 2 o2 + 2 o3 + o4);
157 P = 1/6 (p1 + 2 p2 + 2 p3 + p4);
158 vzf = vzi + o; zf = (zi + P);
159 AppendTo[
160 mat, {t, xf, yf, zf, vxf, vyf, vzf, Sqrt[
161 vxf^2 + vyf^2 + vzf^2],
162 Sqrt[(BTa[[Position [BTa, Round[zi ]][[1, 1]], 3]] Cos[
163 ArcCos[xi/Sqrt[xi^2 + yi^2]])^2 + (BTa[[
164 Position [BTa, Round[zi ]][[1, 1]], 3]] Sin[
165 ArcSin[yi/Sqrt[xi^2 + yi^2]])^2],
166 If [nnn >= 0,
167 Sqrt[(br [[ Position [br, Round[zi ]][[1, 1]], 2]] Sin[
168 ArcSin[yi/Sqrt[xi^2 + yi^2]] Sin[
169 t (2 \[Pi])/Tf]^2 + (br [[
170 Position [br, Round[zi ]][[1, 1]], 2]] Cos[
171 ArcCos[xi/Sqrt[xi^2 + yi^2]] Sin[t (2 \[Pi])/Tf]^2],
172 0], BTa[[Position [BTa, Round[zi ]][[1, 1]],
173 2]], ((BTa[[Position [BTa, Round[zi ]][[1, 1]], 3]] Cos[
174 ArcCos[xi/Sqrt[xi^2 + yi^2]]) + (BTa[[

```

```
175      Position [BTa, Round[zi ]][[1, 1], 3] Sin [
176      ArcSin[yi/Sqrt[xi^2 + yi^2]] ) ]; vxi = vxf; vyi = vyf;
177      vzi = vzf; xi = xf; yi = yf;
178      zi = zf; nnn--, mat}}];
```


Bibliography

- [1] Carl D. Anderson and Seth H. Neddermeyer. Cloud chamber observations of cosmic rays at 4300 meters elevation and near sea-level. *Phys. Rev.*, 50:263–271, Aug 1936. doi: 10.1103/PhysRev.50.263. URL <https://link.aps.org/doi/10.1103/PhysRev.50.263>.
- [2] Paul Adrien Maurice Dirac and Ralph Howard Fowler. The quantum theory of the electron. *Proceedings of the Royal Society of London. Series A, Containing Papers of a Mathematical and Physical Character*, 117(778):610–624, 1928. URL <https://royalsocietypublishing.org/doi/abs/10.1098/rspa.1928.0023>.
- [3] M. Tanabashi et al. Review of particle physics. *Phys. Rev. D*, 98:030001, Aug 2018. doi: 10.1103/PhysRevD.98.030001. URL <https://link.aps.org/doi/10.1103/PhysRevD.98.030001>.
- [4] Tatsumi Aoyama, Toichiro Kinoshita, and Makiko Nio. Revised and improved value of the qed tenth-order electron anomalous magnetic moment. *Phys. Rev. D*, 97:036001, Feb 2018. doi: 10.1103/PhysRevD.97.036001. URL <https://link.aps.org/doi/10.1103/PhysRevD.97.036001>.
- [5] C. Gnendiger, D. Stöckinger, and H. Stöckinger-Kim. The electroweak contributions to $(g-2)_\mu$ after the higgs-boson mass measurement. *Phys. Rev. D*, 88:053005, Sep 2013. doi: 10.1103/PhysRevD.88.053005. URL <https://link.aps.org/doi/10.1103/PhysRevD.88.053005>.
- [6] Alexander Keshavarzi, Daisuke Nomura, and Thomas Teubner. Muon $g-2$ and $\alpha(M_Z^2)$: A new data-based analysis. *Phys. Rev. D*, 97:114025, Jun 2018. doi: 10.1103/PhysRevD.97.114025. URL <https://link.aps.org/doi/10.1103/PhysRevD.97.114025>.
- [7] Alexander Keshavarzi, Daisuke Nomura, and Thomas Teubner. $g-2$ of charged leptons, $\alpha(M_Z^2)$, and the hyperfine splitting of muonium. *Phys. Rev. D*, 101:014029, Jan 2020. doi: 10.1103/PhysRevD.101.014029. URL <https://link.aps.org/doi/10.1103/PhysRevD.101.014029>.
- [8] G. W. Bennett et al. Final report of the e821 muon anomalous magnetic moment measurement at bnl. *Phys. Rev. D*, 73:072003, Apr 2006. doi: 10.1103/PhysRevD.73.072003. URL <https://link.aps.org/doi/10.1103/PhysRevD.73.072003>.

- [9] Keisuke Harigaya, Tsutomu T. Yanagida, and Norimi Yokozaki. Muon $g - 2$ in focus point susy. *Phys. Rev. D*, 92:035011, Aug 2015. doi: 10.1103/PhysRevD.92.035011. URL <https://link.aps.org/doi/10.1103/PhysRevD.92.035011>.
- [10] Andrzej Czarnecki and William J. Marciano. Muon anomalous magnetic moment: A harbinger for “new physics”. *Phys. Rev. D*, 64:013014, Jun 2001. doi: 10.1103/PhysRevD.64.013014. URL <https://link.aps.org/doi/10.1103/PhysRevD.64.013014>.
- [11] A.D. Sakharov. Violation of cp invariance, c asymmetry, and baryon asymmetry of the universe. *JETP Lett. (USSR)(Engl. Transl.)*, 5: 24-7(Jan. 1, 1967)., 1 1967.
- [12] Jonathan L. Feng, Konstantin T. Matchev, and Yael Shadmi. Theoretical expectations for the muon’s electric dipole moment. *Nuclear Physics B*, 613(1):366 – 381, 2001. ISSN 0550-3213. doi: [https://doi.org/10.1016/S0550-3213\(01\)00383-2](https://doi.org/10.1016/S0550-3213(01)00383-2). URL <http://www.sciencedirect.com/science/article/pii/S0550321301003832>.
- [13] G. W. Bennett et al. Improved limit on the muon electric dipole moment. *Phys. Rev. D*, 80: 052008, Sep 2009. doi: 10.1103/PhysRevD.80.052008. URL <https://link.aps.org/doi/10.1103/PhysRevD.80.052008>.
- [14] R. L. Garwin, D. P. Hutchinson, S. Penman, and G. Shapiro. Accurate determination of the μ^+ magnetic moment. *Phys. Rev.*, 118:271–283, Apr 1960. doi: 10.1103/PhysRev.118.271. URL <https://link.aps.org/doi/10.1103/PhysRev.118.271>.
- [15] Julian Schwinger. On quantum-electrodynamics and the magnetic moment of the electron. *Phys. Rev.*, 73:416–417, Feb 1948. doi: 10.1103/PhysRev.73.416. URL <https://link.aps.org/doi/10.1103/PhysRev.73.416>.
- [16] G. Charpak, F. J. M. Farley, R. L. Garwin, T. Muller, J. C. Sens, V. L. Telegdi, and A. Zichichi. Measurement of the anomalous magnetic moment of the muon. *Phys. Rev. Lett.*, 6:128–132, Feb 1961. doi: 10.1103/PhysRevLett.6.128. URL <https://link.aps.org/doi/10.1103/PhysRevLett.6.128>.
- [17] G. Charpak, F.J.M. Farley, R.L. Garwin, T. Muller, J.C. Sens, and A. Zichichi. A new measurement of the anomalous magnetic moment of the muon. *Physics Letters*, 1(1):16 – 20, 1962. ISSN 0031-9163. doi: [https://doi.org/10.1016/0031-9163\(62\)90263-9](https://doi.org/10.1016/0031-9163(62)90263-9). URL <http://www.sciencedirect.com/science/article/pii/0031916362902639>.
- [18] J. Bailey and W. Bartl. Precision measurement of the anomalous magnetic moment of the muon. *Physics Letters B*, 28:287 – 290, 1968. doi: [https://doi.org/10.1016/0370-2693\(68\)90261-X](https://doi.org/10.1016/0370-2693(68)90261-X). URL <http://www.sciencedirect.com/science/article/pii/037026936890261X>.
- [19] R. L. Garwin, D. P. Hutchinson, S. Penman, and G. Shapiro. Final report on the cern muon storage ring including the anomalous magnetic moment and the electric dipole moment of

- the muon, and a direct test of relativistic time dilation. *Nuclear Physics B*, 150:1 – 75, 1979. doi: [https://doi.org/10.1016/0550-3213\(79\)90292-X1](https://doi.org/10.1016/0550-3213(79)90292-X1). URL <http://www.sciencedirect.com/science/article/pii/055032137990292X>.
- [20] A Yamamoto et al. The superconducting inflector for the bnl g-2 experiment. *Nuclear Instruments and Methods in Physics Research Section A: Accelerators, Spectrometers, Detectors and Associated Equipment*, 491(1):23 – 40, 2002. ISSN 0168-9002. doi: [https://doi.org/10.1016/S0168-9002\(02\)01232-9](https://doi.org/10.1016/S0168-9002(02)01232-9). URL <http://www.sciencedirect.com/science/article/pii/S0168900202012329>.
- [21] G.T. Danby et al. The brookhaven muon storage ring magnet. *Nuclear Instruments and Methods in Physics Research Section A: Accelerators, Spectrometers, Detectors and Associated Equipment*, 457(1):151 – 174, 2001. ISSN 0168-9002. doi: [https://doi.org/10.1016/S0168-9002\(00\)00704-X](https://doi.org/10.1016/S0168-9002(00)00704-X). URL <http://www.sciencedirect.com/science/article/pii/S016890020000704X>.
- [22] Efstratios Efstathiadis, Y.Y Lee, Jian lin Mi, Chien Pai, Jonathan M Paley, B.Lee Roberts, Ralph T Sanders, Yannis K Semertzidis, and David S Warburton. A fast non-ferric kicker for the muon ($g-2$) experiment. *Nuclear Instruments and Methods in Physics Research Section A: Accelerators, Spectrometers, Detectors and Associated Equipment*, 496(1):8 – 25, 2003. ISSN 0168-9002. doi: [https://doi.org/10.1016/S0168-9002\(02\)01627-3](https://doi.org/10.1016/S0168-9002(02)01627-3). URL <http://www.sciencedirect.com/science/article/pii/S0168900202016273>.
- [23] R Prigl, U Haeberlen, K Jungmann, G zu Putlitz, and P von Walter. A high precision magnetometer based on pulsed nmr. *Nuclear Instruments and Methods in Physics Research Section A: Accelerators, Spectrometers, Detectors and Associated Equipment*, 374(1):118 – 126, 1996. ISSN 0168-9002. doi: [https://doi.org/10.1016/0168-9002\(96\)37493-7](https://doi.org/10.1016/0168-9002(96)37493-7). URL <http://www.sciencedirect.com/science/article/pii/0168900296374937>.
- [24] The e821 muon ($g-2$) home page, 2004. URL <https://www.g-2.bnl.gov/pictures/g2magnet2.jpg>.
- [25] L.H. Thomas B.A. I. the kinematics of an electron with an axis. *The London, Edinburgh, and Dublin Philosophical Magazine and Journal of Science*, 3(13):1–22, 1927. doi: 10.1080/14786440108564170. URL <https://doi.org/10.1080/14786440108564170>.
- [26] John David Jackson. *Classical electrodynamics; 2nd ed.* Wiley, New York, NY, 1975. URL <https://cds.cern.ch/record/100964>.
- [27] W. Liu, M. G. Boshier, S. Dhawan, O. van Dyck, P. Egan, X. Fei, M. Grosse Perdekamp, V. W. Hughes, M. Janousch, K. Jungmann, D. Kawall, F. G. Mariam, C. Pillai, R. Prigl, G. zu Putlitz, I. Reinhard, W. Schwarz, P. A. Thompson, and K. A. Woodle. High precision measurements of the ground state hyperfine structure interval of muonium and of the muon

- magnetic moment. *Phys. Rev. Lett.*, 82:711–714, Jan 1999. doi: 10.1103/PhysRevLett.82.711. URL <https://link.aps.org/doi/10.1103/PhysRevLett.82.711>.
- [28] Strasser, P. and others. New precise measurements of muonium hyperfine structure at j-parc muse. *EPJ Web Conf.*, 198:00003, 2019. doi: 10.1051/epjconf/201919800003. URL <https://doi.org/10.1051/epjconf/201919800003>.
- [29] M Abe et al. A new approach for measuring the muon anomalous magnetic moment and electric dipole moment. *Progress of Theoretical and Experimental Physics*, 2019(5), 05 2019. ISSN 2050-3911. doi: 10.1093/ptep/ptz030. URL <https://doi.org/10.1093/ptep/ptz030>. 053C02.
- [30] Naritoshi Kawamura, Masaharu Aoki, Jacob Doornbos, Tsutomu Mibe, Yasuhiro Miyake, Fumiaki Morimoto, Yohei Nakatsugawa, Masashi Otani, Naohito Saito, Yoshihiro Seiya, Koichiro Shimomura, Akihisa Toyoda, and Takayuki Yamazaki. New concept for a large-acceptance general-purpose muon beamline. *Progress of Theoretical and Experimental Physics*, 2018(11), 11 2018. ISSN 2050-3911. doi: 10.1093/ptep/pty116. URL <https://doi.org/10.1093/ptep/pty116>. 113G01.
- [31] P. Bakule, G.A. Beer, D. Contreras, M. Esashi, Y. Fujiwara, Y. Fukao, S. Hirota, H. Iinuma, K. Ishida, M. Iwasaki, T. Kakurai, S. Kanda, H. Kawai, N. Kawamura, G.M. Marshall, H. Masuda, Y. Matsuda, T. Mibe, Y. Miyake, S. Okada, K. Olchanski, A. Olin, H. Onishi, N. Saito, K. Shimomura, P. Strasser, M. Tabata, D. Tomono, K. Ueno, K. Yokoyama, and S. Yoshida. Measurement of muonium emission from silica aerogel. *Progress of Theoretical and Experimental Physics*, 2013(10), 10 2013. ISSN 2050-3911. doi: 10.1093/ptep/ptt080. URL <https://doi.org/10.1093/ptep/ptt080>. 103C01.
- [32] G. A. Beer, Y. Fujiwara, S. Hirota, K. Ishida, M. Iwasaki, S. Kanda, H. Kawai, N. Kawamura, R. Kitamura, S. Lee, W. Lee, G. M. Marshall, T. Mibe, Y. Miyake, S. Okada, K. Olchanski, A. Olin, H. Ohnishi, Y. Oishi, M. Otani, N. Saito, K. Shimomura, P. Strasser, M. Tabata, D. Tomono, K. Ueno, E. Won, and K. Yokoyama. Enhancement of muonium emission rate from silica aerogel with a laser-ablated surface. *Progress of Theoretical and Experimental Physics*, 2014(9), 09 2014. ISSN 2050-3911. doi: 10.1093/ptep/ptu116. URL <https://doi.org/10.1093/ptep/ptu116>. 091C01.
- [33] S. Bae, H. Choi, S. Choi, Y. Fukao, K. Futatsukawa, K. Hasegawa, T. Iijima, H. Iinuma, K. Ishida, N. Kawamura, B. Kim, R. Kitamura, H. S. Ko, Y. Kondo, S. Li, T. Mibe, Y. Miyake, T. Morishita, Y. Nakazawa, M. Otani, G. P. Razuvaev, N. Saito, K. Shimomura, Y. Sue, E. Won, and T. Yamazaki. First muon acceleration using a radio-frequency accelerator. *Phys. Rev. Accel. Beams*, 21:050101, May 2018. doi: 10.1103/PhysRevAccelBeams.21.050101. URL <https://link.aps.org/doi/10.1103/PhysRevAccelBeams.21.050101>.

- [34] Hiromi Iinuma, Hisayoshi Nakayama, Katsunobu Oide, Ken ichi Sasaki, Naohito Saito, Tsutomu Mibe, and Mitsushi Abe. Three-dimensional spiral injection scheme for the $g=2$ /edm experiment at j-parc. *Nuclear Instruments and Methods in Physics Research Section A: Accelerators, Spectrometers, Detectors and Associated Equipment*, 832:51 – 62, 2016. ISSN 0168-9002. doi: <https://doi.org/10.1016/j.nima.2016.05.126>. URL <http://www.sciencedirect.com/science/article/pii/S0168900216305277>.
- [35] Muhammad Abdul Rehman, Hiromi Iinuma, Satoshi Ohsawa, Hisayoshi Nakayama, Kazuro Furukawa, Tsutomu Mibe, and Hiromi Hisamatsu. Development of the pulsed magnetic kicker for the spiral injection test experiment. In *Proc. 15th Annual Meeting of Particle Accelerator Society of Japan August 7-10, 2018, Nagaoka, Japan*, number 29, pages 768–772. JACoW Publishing, Jan. 2018. URL https://www.pasj.jp/web_publish/pasj2018/proceedings/PDF/THP0/THP006.pdf.
- [36] CST Studio Suite 3d EM simulation and analysis software. <https://www.3ds.com/products-services/simulia/products/cst-studio-suite/>.
- [37] Wolfram Mathematica: Modern Technical Computing. <https://www.wolfram.com/mathematica/>.
- [38] Muhammad Abdul Rehman, Hiromi Iinuma, Satoshi Ohsawa, Hisayoshi Nakayama, Kazuro Furukawa, Tsutomu Mibe, and Hiromi Hisamatsu. Progress of the Novel Three-dimensional Spiral Injection Scheme Test Experiment. In *Proc. 29th Linear Accelerator Conference (LINAC'18), Beijing, China, 16-21 September 2018*, number 29 in Linear Accelerator Conference, pages 717–720, Geneva, Switzerland, Jan. 2019. JACoW Publishing. ISBN 978-3-95450-194-6. doi: doi:10.18429/JACoW-LINAC2018-THPO017. URL <http://jacow.org/linac2018/papers/thpo017.pdf>.
- [39] Muhammad Abdul Rehman, Hiromi Iinuma, Satoshi Ohsawa, Hisayoshi Nakayama, Hiromi Hisamatsu, Kazuro Furukawa, and Tsutomu Mibe. *Three-dimensional Spiral Injection Scheme Test Experiment*. doi: 10.7566/JPSCP.25.011029. URL <https://journals.jpss.jp/doi/abs/10.7566/JPSCP.25.011029>.
- [40] D. W. Kerst. Acceleration of electrons by magnetic induction. *Phys. Rev.*, 58:841–841, Nov 1940. doi: 10.1103/PhysRev.58.841. URL <https://link.aps.org/doi/10.1103/PhysRev.58.841>.
- [41] D. W. Kerst and R. Serber. Electronic orbits in the induction accelerator. *Phys. Rev.*, 60:53–58, Jul 1941. doi: 10.1103/PhysRev.60.53. URL <https://link.aps.org/doi/10.1103/PhysRev.60.53>.
- [42] Helmut Wiedemann. *Single Particle Dynamics*, pages 177–211. Springer International Publishing, Cham, 2015. ISBN 978-3-319-18317-6. doi: 10.1007/978-3-319-18317-6_7. URL https://doi.org/10.1007/978-3-319-18317-6_7.

- [43] Michiko G. Minty and Frank Zimmermann. *Transverse Beam Emittance Measurement and Control*, pages 99–131. Springer Berlin Heidelberg, Berlin, Heidelberg, 2003. ISBN 978-3-662-08581-3. doi: 10.1007/978-3-662-08581-3_4. URL https://doi.org/10.1007/978-3-662-08581-3_4.
- [44] K. Oide. Introduction to beam dynamics, in Japanese. 1992. doi: 10.1103/PhysRev.123.2084. URL <https://www-jlc.kek.jp/2003oct/subg/ir/lib/DOC/japanese/Lecture.beam.dynamics.pdf>.
- [45] K. Kubo. How to calculate 'intrinsic' emittances from 4-dimensional beam matrix. *ATF Internal Report*, 99-02, 1999.
- [46] Muhammad Abdul Rehman, Hiromi Inuma, Satoshi Ohsawa, Hisayoshi Nakayama, Kazuro Furukawa, Tsutomu Mibe, and Hiromi Hisamatsu. Test experiment of 3-d spiral injection scheme using electron beam for new g-2/edm experiment at j-parc. In *Proceedings of the 13th Annual Meeting of Particle Accelerator Society of Japan August 8-10, 2016, Chiba, Japan*, pages 7004–1007. JACoW Publishing, Aug. 2016. URL https://www.pasj.jp/web_publish/pasj2016/proceedings/PDF/TUP0/TUP056.pdf.
- [47] Muhammad Abdul Rehman, Hiromi Inuma, Satoshi Ohsawa, Hisayoshi Nakayama, Kazuro Furukawa, Tsutomu Mibe, and Hiromi Hisamatsu. Development of three-dimensional spiral injection by using electron beam for muon g - 2/edm experiment. In *Proceedings of the 14th Annual Meeting of Particle Accelerator Society of Japan August 1-3, 2017, Sapporo, Japan*, pages 114–117. JACoW Publishing, Aug. 2017. URL https://www.pasj.jp/web_publish/pasj2017/proceedings/PDF/WEOM/WEOM01.pdf.
- [48] Takashi Sugimura, Satoshi Ohsawa, and Mitsuo Ikeda. Performance of an electron gun for a high-brightness X-ray generator. *Journal of Synchrotron Radiation*, 15(3): 258–261, May 2008. doi: 10.1107/S0909049507066769. URL <https://doi.org/10.1107/S0909049507066769>.
- [49] C.R. Crowell. The richardson constant for thermionic emission in schottky barrier diodes. *Solid-State Electronics*, 8(4):395 – 399, 1965. ISSN 0038-1101. doi: [https://doi.org/10.1016/0038-1101\(65\)90116-4](https://doi.org/10.1016/0038-1101(65)90116-4). URL <http://www.sciencedirect.com/science/article/pii/0038110165901164>.
- [50] Irving Langmuir. The characteristics of tungsten filaments as functions of temperature. *Phys. Rev.*, 7:302–330, Mar 1916. doi: 10.1103/PhysRev.7.302. URL <https://link.aps.org/doi/10.1103/PhysRev.7.302>.
- [51] Button operated mv1000/mv2000 — yokogawa electric corporation. <https://www.yokogawa.com/solutions/products-platforms/data-acquisition/portable-data-acquisition/button-operated-mv1000-mv2000/>.

- [52] I. Pinayev. beam based alignment of solenoid. *BNL-114488-2017-CP*, 117(778):610–624, 1928. URL <https://www.bnl.gov/isd/documents/95489.pdf>.
- [53] Helmut Wiedemann. *Dynamics of Coupled Motion**, pages 669–697. Springer International Publishing, Cham, 2015.
- [54] Vector/magnitude gauss meter model vgm - alphalab, inc. <https://www.alphalabinc.com/product/vgm/>.
- [55] R. H. Hughes, J. L. Philpot, and C. Y. Fan. Spectra induced by 200-keV proton impact on nitrogen. *Phys. Rev.*, 123:2084–2086, Sep 1961. doi: 10.1103/PhysRev.123.2084. URL <https://link.aps.org/doi/10.1103/PhysRev.123.2084>.
- [56] Peter Strehl. *Beam Profile Measurements*, pages 105–153. Springer Berlin Heidelberg, Berlin, Heidelberg, 2006. ISBN 978-3-540-26404-0. doi: 10.1007/3-540-26404-3_4. URL https://doi.org/10.1007/3-540-26404-3_4.
- [57] M.A Plum, E Bravin, J Bosser, and R Maccaferri. N₂ and Xe gas scintillation cross-section, spectrum, and lifetime measurements from 50 MeV to 25 GeV at the CERN PS and booster. *Nuclear Instruments and Methods in Physics Research Section A: Accelerators, Spectrometers, Detectors and Associated Equipment*, 492(1):74 – 90, 2002. ISSN 0168-9002. doi: [https://doi.org/10.1016/S0168-9002\(02\)01287-1](https://doi.org/10.1016/S0168-9002(02)01287-1). URL <http://www.sciencedirect.com/science/article/pii/S0168900202012871>.
- [58] Peter Sigmund. *Particle Penetration and Radiation Effects Volume 2*, volume 179. 01 2014. doi: 10.1007/978-3-319-05564-0.
- [59] Bethe formula - wikipedia. https://en.wikipedia.org/wiki/Bethe_formula.
- [60] mks. gm50a-mass-flow-controller. URL <https://www.mksinst.com/f/gm50a-mass-flow-controller>.
- [61] Hamamatsu. Hamamatsu, b/w chilled CCD camera: C5985 series. <https://camera.hamamatsu.com/jp/en/index.html>. (Discontinued Product).
- [62] H416-pentax-c mount. <https://uniel-denshi.co.jp/RICOH/PENTAX/H416.html>.
- [63] shibuya opt. Light exclusion / absorption sheets. URL https://www.shibuya-opt.co.jp/eng/super_black_top.html.
- [64] araldite. araldite-rapid-2-x-15ml-tube. URL <http://www.go-araldite.com/products/epoxy-adhesives/araldite-rapid-2-x-15ml-tube>.
- [65] Muhammad Abdul Rehman, Hiromi Iinuma, Satoshi Ohsawa, Hisayoshi Nakayama, Kazuro Furukawa, Tsutomu Mibe, and Hiromi Hisamatsu. Beam control and monitors for the spiral injection test experiment. *Journal of Physics: Conference Series*, 1350:012151, nov 2019.

doi: 10.1088/1742-6596/1350/1/012151. URL <https://doi.org/10.1088%2F1742-6596%2F1350%2F1%2F012151>.

- [66] Magnetically coupled rotary/linear feedthrough — pfeiffer vacuum. <https://www.pfeiffer-vacuum.com/en/products/chambers-components/manipulators/standard-manipulators/magnetically-coupled-rotary-linear-feedthrough/10531/magnetically-coupled-rotary-linear-feedthrough-dn-40-cf>.
- [67] THK. ES series linear actuator. URL <https://www.thk.com/>.
- [68] Item # dgm130r-arac, hollow rotary actuator on oriental motor japan. <https://catalog.orientalmotor.com/item/all-categories/all-categories-components-hollow-rotary-actuators/dgm130r-arac>.
- [69] Dpo7000 — tektronix. <https://www.tek.com/oscilloscope/dpo7000-digital-phosphor-oscilloscope>.
- [70] Visual studio 2019 ide - programming software for windows. <https://visualstudio.microsoft.com/vs/>.
- [71] Helmut Wiedemann. *Particle Beams and Phase Space*, pages 213–251. Springer International Publishing, Cham, 2015. ISBN 978-3-319-18317-6. doi: 10.1007/978-3-319-18317-6_8. URL https://doi.org/10.1007/978-3-319-18317-6_8.
- [72] Isd-2500hd ultra low light color hd camera – ikegami japan – english. <https://www.ikegami.co.jp/en/archives/menu9/isd-2500hd>.
- [73] S Y Lee. *Accelerator Physics*. WORLD SCIENTIFIC, 3rd edition, 2011. doi: 10.1142/8335. URL <https://www.worldscientific.com/doi/abs/10.1142/8335>.
- [74] Eduard Prat and Masamitsu Aiba. Four-dimensional transverse beam matrix measurement using the multiple-quadrupole scan technique. *Phys. Rev. ST Accel. Beams*, 17:052801, May 2014. doi: 10.1103/PhysRevSTAB.17.052801. URL <https://link.aps.org/doi/10.1103/PhysRevSTAB.17.052801>.
- [75] C. Xiao, M. Maier, X. N. Du, P. Gerhard, L. Groening, S. Mickat, and H. Vormann. Rotating system for four-dimensional transverse rms-emittance measurements. *Phys. Rev. Accel. Beams*, 19:072802, Jul 2016. doi: 10.1103/PhysRevAccelBeams.19.072802. URL <https://link.aps.org/doi/10.1103/PhysRevAccelBeams.19.072802>.
- [76] C. Xiao, O. K. Kester, L. Groening, H. Leibrock, M. Maier, and P. Rottländer. Single-knob beam line for transverse emittance partitioning. *Phys. Rev. ST Accel. Beams*, 16:044201, Apr 2013. doi: 10.1103/PhysRevSTAB.16.044201. URL <https://link.aps.org/doi/10.1103/PhysRevSTAB.16.044201>.

- [77] Alexander Wu Chao, Karl Hubert Mess, Maury Tigner, and Frank Zimmermann. *Handbook of Accelerator Physics and Engineering*. WORLD SCIENTIFIC, 2nd edition, 2013. doi: 10.1142/8543. URL <https://www.worldscientific.com/doi/abs/10.1142/8543>.
- [78] Symplectic matrix - wikipedia. https://en.wikipedia.org/wiki/Symplectic_matrix.
- [79] Sad home page. <http://acc-physics.kek.jp/SAD/>.
- [80] Separatrix – from wolfram mathworld. <https://mathworld.wolfram.com/Separatrix.html>.
- [81] Technical support for generation and control of pulsed power, prototype prototyping, collaborative research — pulsed power japan laboratory ltd. <http://www.mypj.com/en/>.
- [82] Spectrum software - micro-cap 12. analog simulation, mixed mode simulation, and digital simulation software. spice and pspice® compatible circuit simulator. <http://www.spectrum-soft.com/index.shtm>.